



Real Time Temperature Distribution Monitoring of SOFC Cathode and Contributing Parameters

by

Erdogan GUK

Doctoral Thesis

Submitted in partial fulfilment of the requirements for the award of
Doctor of Philosophy of Loughborough University, School of
Automotive, Aeronautical, Chemical and Material Engineering

June 2018

Supervisor: Prof. Lisa Jackson

Acknowledgement

I wish to express my sincere gratitude to my previous supervisor Prof. Lisa Jackson, and co-supervisors Dr. Jung-Sik Kim and Dr. Houzheng Wu for their excellent supervision, advise, encouragement, support, and especially insight and guidance given to my studies throughout the research. . Their contribution, support and co-operation towards completion of the thesis were invaluable. I would like to thank Dr Jung-Sik for the friendly and co-operative atmosphere that he has created within our group which markedly facilitated the research, together with frequent one to one meetings.

I wish to extend my sincere gratitude to my colleagues Mr. R.A. Manoj Prasanna Ranaweera, Mr. Indae Choi, Mr. Vijay Venkatesan and Yunus Sayan for their invaluable support in my studies.

Finally, I wish to thank every single person who directly or indirectly helped me finalise this study.

Abstract

The solid oxide fuel cell (SOFC) as an energy conversion device is considered as a promising technology due to its high operating efficiency, fuel flexibility and relatively low emissions. However high operating temperature related issues such as availability and durability of the materials to operate at that high temperature and for long-time thermal cycling need to be understood and overcome. These are vital areas for research to ensure availability and durability measures are maximised subject to minimising SOFC system cost. To obtain the desired power output, especially for industrial applications, several cells are linked together to form a stack and the stacks are linked together to form a SOFC power generating system. There are two ways to overcome these issues, first; to reduce the operating temperature and second; to have better thermal management of the systems. Decreasing the operating temperature however can lead to a reduction in overall performance of the system due to an increase in the resistance in the cell as well as the electrodes becoming less active. Thus, thermal management of SOFCs is significant for minimising performance losses and maximising cell/stack lifetime.

Due to the harsh operating conditions of the SOFC, numerical analysis based works have been widely studied for predicting the temperature distribution of the SOFC under certain simplified operating conditions. While the conventional experimental way for SOFC temperature monitoring involves using thermocouples at the inlet/outlet of the gas channel. In this study, a recently developed multi-array thermal sensor was applied for in-situ monitoring of the temperature distribution of the SOFC, which is measured directly from the cell electrode surface with little or negligible disturbance to the SOFC operating environment. The sensor can be fabricated in both thin film (by depositing directly onto the cell electrode) and wired array/grid form and requires fewer thermo-elements for the same number of sensing points compared to conventional thermocouples. The focus during this study has been i) performance durability of the implemented sensor; ii) determination of an effective way/platform for sensor integration to the cell especially for electrical signal collection; iii) establishing an effective mechanism for temperature distribution monitoring of the cell with higher temporal and spatial resolution, and

iv) understanding the parameters contributing to the monitored temperature distribution.

The performance in terms of mechanical durability and oxidation state of the thin film thermo-elements of the thermocouple array on the porous SOFC cathode is investigated. A thin-film multi-junction thermocouple array was sputter deposited using a magnetron sputter coater. Scanning electron microscopy (SEM) and X-ray photoelectron spectroscopy (XPS) characterisation techniques were carried out to understand characteristics of the thin film before and after temperature measurement (20 °C-800 °C). Micro-scale cracks on the thin film surfaces and oxidation through its thickness are revealed by using SEM imaging and XPS depth profiling, respectively.

A new concept of packaging external wire attachments to the thin film/thin wire sensor is described to enable the integration of the sensor in the SOFC system. This testing unit comprises SOFC elements (50 mm × 50 mm NextCell, Fuel Cell Materials), fuel-supply pathways and channels, a thermal control system (incl. sensor), electrical and fluidic connections, as well as mechanical support. It has been demonstrated that the external wire attachment was successful in maintaining the required electrical connections throughout and after the experiments, under SOFC operating temperatures ranging from 700 °C to 800 °C. The contribution of thermal and contact resistance is also identified.

The temperature distribution of the SOFC cell (50 mm × 50 mm NextCell, Fuel Cell Materials) is monitored during real operation and the result is validated with the use of conventional thermocouples. It is revealed that the implemented sensor has greater capability to detect the temperature variation occurring along the entire cell surface during operation than the conventional thermocouples. A temperature distribution map of the cell cathode surface was monitored under loading and OCV conditions. Electrochemical reactions were observed as the dominant factor for the observed cathode temperature gradient, while cooling effect, fuel/air starvation and fuel distribution are observed as other contributors to the gradient.

The impact of the parameters including furnace operating temperature, supplied fuel amount and drawn current on the cell average temperature and cell temperature gradient are individually monitored. In addition to this, the characteristic of their

impact is also identified by generating the cell's surface temperature map for each parameter separately from the sixteen individual sensing points of the inserted sensor. This measurement is carried out under OCV, and different loading conditions with varying flow rate at different furnace temperatures. Work has demonstrated that it is necessary to enhance the capability of monitoring at cells surface to give greater granularity to temperature understanding.

Publications

Journal papers

E. Guk, M. Ranaweera, V. Venkatesan, and J. -S. Kim, , Performance and Durability of Thin Film Thermocouple Array on a Porous Electrode, *Sensors*, 16(9), p.1329, 2016.

Y. Sayan, V. Venkatesan, **E. Guk**, H. Wu, J.-S. Kim, “Single-step fabrication of an anode supported planar single- chamber solid oxide fuel cell,” *Int J Appl Ceram Technol*, no.1–13, 2018.

E. Guk, V. Venkatesan, Y. Sayan, L. Jackson, and J.-S. Kim, “Spring Based Connection of External Wires to a Thin Film Temperature Sensor Integrated Inside a Solid Oxide Fuel Cell,” *Sci. Rep.*, vol. 9, no. 1, p. 2161, 2019.

E. Guk, V. Venkatesan, S. Babar, L. Jackson, and J. S. Kim, “Parameters and their impacts on the temperature distribution and thermal gradient of solid oxide fuel cell,” *Appl. Energy*, vol. 241, no. February, pp. 164–173, 2019.

Conferences

E. Guk, M. Ranaweera, V. Venkatesan, and J. -S. Kim, “Thin Film Thermocouple Array for Cathode Temperature Gradient of SOFC,” in *European Fuel Cell Forum*, 2016, no. July, pp. 1–8.

E. Guk, M. Ranaweera, V. Venkatesan, J. S. Kim, “Thin Film Thermocouple Array for Temperature Gradient and flow distribution of SOFC Cathode” *3rd International Conference on Nanotechnology, Nanomaterials & Thin Films for Energy Applications* held in Liverpool, UK, 27th July 2016. (Abstract only)

E. Guk, M. Ranaweera, V. Venkatesan, Y. Sayan, S. Babar, J. S. Kim, L. Jackson, “New Platform Enabling Signal Collection for Temperature Measurement via Thin Film Sensor from a Solid Oxide Fuel Cell” *H2FC SUPERGEN (the hydrogen and fuel cell research hub) held in St. Andrews*, UK, 13-15th Dec 2017. (Abstract only)

Table of Contents

Acknowledgement	II
Abstract.....	III
Publications.....	VI
Table of Contents	VII
List of Figures.....	XII
List of tables.....	XV
Abbreviations	XVI
Nomenclature.....	XVIII
Introduction	1
1.1 Motivation	1
1.1.1 Fuel cell technologies	1
1.1.2 Fuel cell types	2
1.2 Solid Oxide Fuel Cells (SOFCs)	4
1.2.1 Background.....	4
1.2.2 Applications.....	6
1.2.3 Degradation issue in SOFCs	7
1.2.3.1 Actual performance.....	7
1.2.3.2 Degradation mechanisms in SOFCs	8
1.2.4 Monitoring methods.....	9
1.3 Aim and Objectives	11
1.4 Thesis Outline.....	12
Understanding SOFCs – Literature Review.....	14
2.1 Solid Oxide Fuel Cells	14
2.1.1 Introduction and working principles.....	14
2.1.2 Cell components	16

2.1.2.1	Electrolyte	16
2.1.2.2	Anode	18
2.1.2.3	Cathode	20
2.1.2.4	Interconnect.....	23
2.1.3	Cell configurations.....	24
2.1.3.1	Planar.....	25
2.1.3.2	Tubular	27
2.1.3.3	Micro-tubular	29
2.1.4	Applications.....	30
2.1.4.1	SOFCs for transportation and portable applications (20W-10kW).....	31
2.1.4.2	Stationary applications of SOFCs	33
2.1.5	SOFC thermodynamic and heat sources.....	35
2.1.5.1	Thermodynamics.....	35
2.1.5.2	Heat sources	36
2.1.5.2.1	Heat correlated with chemical reactions	36
2.1.5.2.2	Heat correlated with electrochemical reactions	37
2.1.5.2.3	Joule heating or ohmic heat loss	38
2.2	SOFC Degradation Mechanism.....	39
2.2.1	Soft failure	39
2.2.2	Hard failure	40
2.3	SOFC Temperature Measurement.....	41
2.4	Chapter Summary	48
Experimental methodology		49
3.1	Overview	49
3.2	Materials	50
3.3	Methods	55
3.3.1	Temperature sensing.....	55

3.3.2	Characterisation	60
3.3.3	Workflow and design of the testing	61
3.4	Chapter Summary	64
Viability of Thin Film Sensor for Temperature Distribution Monitoring		65
4.1.	Introduction	65
4.2.	Experimental Details	65
4.2.1.	Material selection and sensor fabrication	66
4.2.2.	External wires connection.....	68
4.3.	Results and Discussions	70
4.3.1.	Temperature reading.....	70
4.3.2.	Film characterisation tests	73
4.3.2.1.	SEM analysis.....	73
4.3.2.2.	XPS analysis	74
4.4.	Chapter Summary	76
Spring Integrated Connection Method for Signal Acquisition		78
5.1	Introduction	78
5.2	Background and Concept of the Technique	79
5.2.1	Currently applied method for external wire attachment to a thin film sensor.....	79
5.2.2	Description of the designed SOFC manifolds	81
5.3	Spring Based Connection (SBC) for Wire Attachment to a Thin Film Sensor.....	83
5.4	Experimental Procedure	86
5.5	Results and Discussions	88
5.5.1	Results for SBC without silver paste	88
5.5.2	Results for SBC with application of silver paste	94
5.6	Chapter Summary	98
Experimental Investigation of Temperature Distribution of SOFC Electrode..		99

6.1.	Introduction	99
6.2.	Experimental Process	100
6.2.1.	Materials	100
6.3.	SOFC Anode Reduction and Operation	102
6.4.	Results and Discussions	104
6.5.	Chapter Summary	123
Parameters and Their Impacts on the Temperature Distribution and Thermal Gradient of SOFC		124
7.1	Introduction	124
7.2	Experimental Preparation and Operating Conditions.....	125
7.3	Results and Discussions	127
7.3.1	Operating temperature effect on temperature increment and its distribution across the cell.....	127
7.3.2	Fuel rate effects.....	130
7.3.2.1	Thermodynamic approach to temperature increase due to anode reduction and variation in fuel flow rate	133
7.3.2.2	SSPs and TCs response to the heat released by direct oxidation of leaked H ₂	137
7.3.3	Loading Effect on Cell average temperature and cell temperature gradient.....	140
7.3.3.1	Thermodynamic approach to temperature increase due to loading ...	144
7.4	Effect of the Applied Sensor on Cell Performance	151
7.5	Chapter Summary	155
Conclusions and Future Works		158
8.1	Conclusions	158
8.2	Contributions	160
8.3	Limitations.....	161
8.4	Future Research.....	162

Appendix.....	164
A. Thin film sensor testing under operating SOFC condition	164
B. Fuel spectra atomic percentage of the thermoelement samples for both intact and used.....	167
Bibliography	169

List of Figures

Fig. 1. Comparison of specific power density and specific energy range [21].....	5
Fig. 2. Theoretical and actual polarization curves for theoretical cell voltage	7
Fig. 3. Representation of the Solid Oxide Fuel Cell working process	15
Fig. 4. Oxygen ions transportation through the electrolyte [57]	17
Fig. 5. Schematic representation of anode and the effect of electrolyte materials [48]	20
Fig. 6. Schematic of oxidation reaction at the cathode TPBs region	22
Fig. 7. Schematic representation of cell interconnect configuration.....	23
Fig. 8. Planar SOFC single cell and the stack	25
Fig. 9. Schematic of the design of the stack configuration of planar SOFCs [58]	26
Fig. 10. Representation of different cell configurations of the SOFC [90].....	27
Fig. 11. Demonstration of a single (a) and stack (b) tubular SOFC [90]	28
Fig. 12. Fabricated MT-SOFC before (a) and after (b) sintering.....	30
Fig. 13. SOFC power generator integrated truck by Delphi	31
Fig. 14. Illustration of APU mobile power (10 kW) generator	32
Fig. 15. Demonstration of Rolls Royce SOFC power plant [104]	34
Fig. 16. Stack assembly with three cell and inserted TCs [130]	44
Fig. 17. Placement of the inserted thermocouples on the anode interconnect [36] ...	45
Fig. 18. a) TCs inserted stack and b) location of the inserted TCs [132].....	46
Fig. 19. a) Planar anode supported and b) electrolyte supported SOFC with their cross sectional SEM views.....	51
Fig. 20. House-made Macor SOFC manifold bottom (left) and upper (right) parts ..	52
Fig. 21. Alumel and chromel thin wires in different diameters, mica shape cut gasket and calibrated conventional TCs	53
Fig. 22. Set up for a sample placed sputtering machine.....	54
Fig. 23. Schematic of conventional thermocouple structure.....	55
Fig. 24. Architecture of thin film (a) N+1 and (b) grid structured and thin wire (c) N+1 and (d) grid (P represents connection pads while S refers to sensing points)....	57
Fig. 25. Basic building block of multi-junction array	58
Fig. 26. Exaggerated view of the intermediate junction	59
Fig. 27. Illustration of (a) SEM and (b) XPS	61

Fig. 28. Workflow of the design of experiment with different sensor configuration	62
Fig. 29. Schematic view of sputter-deposited 500 nm thick sensor thin film thermocouple array architecture.....	67
Fig. 30. External wires attached to the thin film thermo-element pads	69
Fig. 31. Temperature profiles of two thermocouples and 4 sensing point of the sensor	71
Fig. 32. SEM images of (a, b) 500 nm thick thin film thermo-elements before and (c) after thermal cycling at 800 °C	74
Fig. 33. Atomic percentage profiles of nickel and oxygen before and after the experiment.....	75
Fig. 34. Structured (a) RTD and (b) RSG sensors and their connection mechanism [153], [154]	80
Fig. 35. Schematic view of (a) lower (anode side) and (b) upper (cathode side) of the cell holder.....	82
Fig. 36. Illustration of (a) sensor patterned cell (onto bottom part) and corresponding external wires (onto upper part) configuration and (b) its assembly	85
Fig. 37. Top view of the external wires attached manifold.....	88
Fig. 38. Temperature measurements with spring-based connection without silver paste.....	89
Fig. 39. (a) SSPs and TC average temperature from the given temperature range and the differences between them separately for heating, dwelling, and cooling segment with (b) SD deviation of TC and SSPs ave.....	90
Fig. 40. Results from spring based connection with small amount of silver paste	95
Fig. 41. SSPs and TC average temperature (a) from the given temperature range and the differences between them separately for heating, dwelling, and cooling segment with (b) SD deviation of SSPs and TC	96
Fig. 42. Schematic representation of cell-sensor configuration.....	102
Fig. 43. Experimental set up	103
Fig. 44. Temperature monitoring from sixteen sensing point and two TCs	105
Fig. 45. Increment in temperature with the increase in flow rate under OCV condition.....	107
Fig. 46. Variation of local regions temperature during polarisation	110
Fig. 47. Temperature distribution under constant loading condition.....	113
Fig. 48. Temperature distribution across the cell with loading.....	114

Fig. 49. Obtained average temperature increment under varying conditions	121
Fig. 50. Schematic view of the sensor integrated cell-manifold configuration	126
Fig. 51. OCV _{exp} , CTG and increment in CTA at varying operating temperature with 50 mL min ⁻¹ constant flow rate	128
Fig. 52. Temperature distributions after anode reduction at OCV condition at different operating temperature.....	130
Fig. 53. Obtained CTA and CTG with OCV under varying flow rate.....	131
Fig. 54. Temperature profile of the cell with varying fuel rate.....	133
Fig. 55. Analytically and experimentally calculated temperature increment.....	137
Fig. 56. Schematic view of cross section of the manifold-cell-sensor integration ..	138
Fig. 57. Comparison of temperature increment between the TCs and SSPs.....	138
Fig. 58. Timely temperature response of SSPs and TCs to the varying flow rate ...	140
Fig. 59. Cell temperature increment with resulted gradient with corresponding voltage	141
Fig. 60. Temperature profile of the cell under OCV and loading conditions	143
Fig. 61. Experimentally and analytically obtained temperature increment by time	146
Fig. 62. Cross view of the cell-manifold configuration	147
Fig. 63. Timey temperature increment of SSPs _{center} , TCs, S13, S1 at 0.2V	148
Fig. 64 Comparison of the polarisation curves	152
Fig. 65. The EIS data obtained from the cell with and without sensor integration..	154
Fig. 66. Equivalent circuit for the behaviour of the obtained impedance elements shown in Fig. 65.....	154
Fig. 67. Temperature response of SSPs, TC1 and TC2 to the varying fuel flow rate under OCV condition of SOFC.....	165
Fig. 68. Atomic percentage of the intact sample for full spectrum.....	167
Fig. 69. Atomic percentage of used thermoelement	168

List of tables

Table 1 Reactions and corresponding heat released in SOFC system [110].....	39
Table 2 Pros and cons of the methods used for SOFC temperature sensing	47
Table 3 Chapters with corresponding experimental set ups.....	64
Table 4 Sputtering parameters	68
Table 5 Measured resistances of the four sensing points before and after the heating process.....	72
Table 6 Failure initiations of SSPs.....	91
Table 7 Initial resistance of SSPs and TC.....	92
Table 8 Regions and their corresponding SSPs	111
Table 9 flow rate of supplied gases and percentage of the excess gases	118
Table 10 Variations in ACT and CTG with varying operating temperature.....	127
Table 11 Variations in CTA, CTG, OCV_{expr} and OCV_{theor} with varying flow rate .	132
Table 12 Parameters used for computing heat convection coefficient	135
Table 13 Cell temperature increment with resultant gradient under OCV and loading condition.....	141
Table 14 Parameters and their impact on total temperature increment (5.5 °C).....	149
Table 15 Experimentally obtained value for the elements given the equivalent circuit	155

Abbreviations

SOFC	– Solid oxide fuel cell
AFCs	– Alkaline fuel cells
EU	– European Union
PAFCs	– Phosphoric acid fuel cell
MCFCs	– Molten carbonate fuel cells
PEMFCs	– Polymer electrolyte membrane fuel cells
CH ₄	– Methane
CO	– Carbon monoxide
SO ₂	– Sulfur dioxide
NO _x	– Nitrogen oxides
APU	– Auxiliary power unit
UUV	– Unmanned undersea vehicle
ISO	– International Organization for Standardization
OCV	– Open circuit voltage
TPB	– Triples phase boundaries
YSZ	– Yttria stabilised zirconia
GDC	– Gadolinia doped ceria
ESB	– Erbium bismuth oxide
DWSB	– Dysprosium-tungsten bismuth oxide
Bi ₂ O ₃	– Bismuth based electrolytes
CTE	– Coefficient thermal expansion
LSM	– Strontium-doped-lanthanum manganite
BSCF	– Ba _{0.5} Sr _{0.5} Co _{0.8} Fe _{0.2} O _{3-δ}
LSCF	– La _{0.6} Sr _{0.4} Co _{0.2} Fe _{0.8} O _{3-δ}
MIEC	– Mixed ionic electronic conducting

LaCrO ₃	– Lanthanum chromite oxide
MT-SOFC	– micro-tubular
SWP	– Siemens Westinghouse power
SECA	– Solid State Energy Conversion Alliance
DOE	– Department of energy
CHP	– Combined heat power
CFD	– Computational fluid dynamics
TCs	– Thermocouples
EMF	– Electromotive force
V_{emf}	– Seebeck voltage
S_i	– Seebeck coefficient
XPS	– X-Ray Photoelectron Spectroscopy
SEM	– Scanning electron microscope
SBC	– Spring-based connection
SSPs	– Sensor sensing points
RTD	– Resistance temperature detectors
RSG	– Resistance strain gauges
SD	– Standard deviation
CTA	– Cell temperature average
CTG	– Cell temperature gradient

Nomenclature

ΔG	– Gibbs free energy
n	– Number of moles of electrons,
F	– Faraday constant (96,487 C/mol)
T	– Operating temperature
E_{r-ner}	– Reversible (Nernst) voltage
ΔH	– Changes of enthalpy
R	– Gas constant
E_{cell}	– Cell voltage
Q_i	– Released/sink heat amount
$T\Delta S_r$	– Entropy change
J	– Current density
R	– Electrical resistance
ρ	– Resistivity
p	– Density
k	– Thermal conductivity
I	– Thermal inertia
c	– Specific heat capacity
R_{th}	– thermal resistance
R_c	– Contact resistance
P_{H_2}, P_{O_2} and P_{H_2O}	– Partial pressure of reactants and product
F	– Faraday constant
E°	– Potential at standard condition
A	– Surface area
m	– Weight
V	– System volume

h	– Heat transfer coefficient
Nu	– Nusselt number
Re	– Reynolds number
Pr	– Prandtl number
u	– Steam velocity
ν	– Kinematic viscosity

Chapter 1

Introduction

1.1 Motivation

1.1.1 Fuel cell technologies

There has been an increasing demand for energy to support human being's lives. This demand has been enlarged significantly with the technological development of industrial applications especially in the transport sector. For instance, around 30% of the total energy has been consumed for transportation purposes alone, with this sector contributing 20% to the total emissions in last 10 years in the European Union (EU) [1]. Also more than 90% of the energy required for transportation is still been provided by fossil fuels, typically oil [2]. In this regard, fossil fuels have been extensively used as a main energy source due to their high energy density and historical availability compared to other renewable energy sources. Thus, even though fossil fuels have disadvantages, such as current limited resources and damaging environmental results, some believe that these harmful fuels shall still remain as the integral energy sources worldwide for the next few generations [3].

Great efforts have been made recently for the purpose of the alteration of current energy policies which mainly depend on non-renewable sources, such as fossil fuels, to utilise some renewable energy sources [2]. This drive is due to fossil fuels having both directly or indirectly a hazardous impact on the environment, not to mention humankind itself. For instance, air pollution, climate change and greenhouse gas emissions are considered as being major issues that humans have had to face over the last few decades. With the high technological development in industrial applications, the rate of greenhouse gases released into the air has also been increasing due to the high fossil fuel consumption in industrial processes [4].

The increasing demand for energy and the issues with current energy sources clearly prove that there is an undeniable need for new, clean and high efficient energy

suppliers. In this regard, fuel cell technology can be considered to be an attractive alternative energy system with high energy transformation performance and almost zero pollution. Fuel cell technology, which typically uses hydrogen as the fuel, is considered as a promising alternative to fossil fuel based energy systems due to its high efficiency, zero emission and air pollution characteristics [5].

1.1.2 Fuel cell types

Fuel cells are energy conversion devices that convert the chemical energy of the fuels into electrical energy without direct combustion. The basic working principles are almost the same for all fuel cells and are similar to batteries. However, in some respects, there are also differences between fuel cell and batteries. For instance, batteries work as energy storage devices which require recharging or replacing when the energy inside is totally consumed, whilst fuel cells have the capability to work continuously as long as the fuel and oxygen are supported. Compared to combustion engines, fuel cell devices are more environmentally friendly because there are no combustion-type chemical reactions taking place during the fuel cell operation [6]. A fuel cell consists of anode and cathode electrodes which sandwich an electrolyte membrane. Even though there can be a variation in charge species migrating via the electrolyte, there is oxidation of hydrogen and reduction of oxygen occurring at the anode and cathode electrodes, and the generated electricity is transferred externally in all fuel cell systems. Although there are similarities in terms of working principles and construction amongst fuel cells, they are separated generally due to the materials of their electrolyte.

- *Alkaline fuel cells (AFCs)* which use potassium hydroxide as the electrolyte material are the earliest generation of fuel cell amongst the others. It has been used by the National Aeronautics and Space Administration (NASA) for a space mission on the space shuttle. It operates at 80 °C in which H₂ and O₂ are used as the fuel (reactant) during the operation while electricity, heat, and water are produced as reaction products [7].
- *Phosphoric acid fuel cell (PAFCs)* consumes H₂, O₂ and air as fuels and produces electricity, heat and steam. The operating temperature is about

200 °C and a liquid phosphoric acid is used as the electrolyte material. It can be used in both stationary and portable application [8].

- *Molten carbonate fuel cells (MCFCs)* which have relatively higher operating temperatures (~600 °C) can use hydrocarbons and biogas as fuel. A carbon based material which allows carbonates ions' mitigation is used as the electrolyte material. They have already been used in stationary applications and portable applications such as ship services specifically for auxiliaries of differing scales up to several MWs [9].
- *Polymer electrolyte membrane fuel cells (PEMFCs)* also known as proton exchange membrane fuel cells were initially developed as power sources for military application. It uses a polymer membrane as the electrolyte material while purified H₂ and O₂ are used as fuels at relatively lower operating temperatures (~80 °C). It is the most developed fuel cell technology, especially for transportation application [10]. However, these fuel cells cannot use the hydrocarbons as fuel directly due to their relatively low operating temperature [11], [12].
- *Solid oxide fuel cells (SOFCs)* which use a thin ceramic layer as the electrolyte material which allows oxide ion transfer. They have the highest operating temperature (800 °C-1000 °C) among other fuel cell types. Due to its high operating temperature they have the flexibility that they can use a variety of hydrocarbons such as methane (CH₄ and carbon monoxide (CO)) and biogases without requiring expensive novel catalyst material. Its efficiency can reach up to 75% by combining with other energy generating system which require heat to operate, such as gas turbines [13]. SOFCs have been used in stationary power applications and auxiliary applications as power sources. SOFCs technology has been a growing interest not only for researchers but also companies such as Bloom Energy, DELPHI, FuelCell Energy, Protonex (USA), Catator (Sweden), Ceres power (UK), SOFCMAN (China), POSCO (South Korea), MHI (Japan) [14]. However, there is a performance degradation issue standing as a major obstacle preventing SOFCs technology to fully commercialisation. Therefore, SOFCs technology, and their high temperature correlated degradation issues will be

further discussed and analysed with a proposed method as the main focus of this study.

1.2 Solid Oxide Fuel Cells (SOFCs)

1.2.1 Background

Solid Oxide Fuel Cells (SOFCs) as an energy conversion device is considered a promising technology for electricity generation due to its high conversion efficiency ($> 50\%$) and important environmental benefit [15], [16]. SOFCs use a solid ceramic electrolyte with electronically and ionically conductive mixed anode and cathode electrodes. Conversion of energy directly from chemical fuels to electrical energy and fuel flexibility due to high operation temperature ($800\text{ }^{\circ}\text{C} - 1000\text{ }^{\circ}\text{C}$) of SOFCs promote its usage for electricity generation [17]. In addition to this, there is also a way to further increase its efficiency up to 75% when the released heat is harnessed into useful energy by combining the SOFC with other systems that requires heat. Another strong advantage of SOFCs is the possibility of using hydrocarbon based fuels such as hydrogen, methane and carbon monoxide without requiring expensive catalyst material due to the high operating temperatures. Some key advantages of SOFCs are explained as follows:

- **High efficiency:** SOFC system has an opportunity to be combined with another bottoming system, such as a turbine, due to its high operating temperature ($800\text{-}900\text{ }^{\circ}\text{C}$). In the literature, the efficiency of just the SOFC is mentioned between $40\text{-}50\%$ fuel efficiency; when the SOFC is combined with a turbine (35%) then the overall efficiency of the system can reach up to 75% [18].
- **Low emission:** SOFC is a sustainable energy generation platform with low or zero emissions, with negligible harmful pollutants including SO_2 (Sulfur dioxide) and NO_x (nitrogen oxides); these low emission can be decreased further by utilizing the exhaust gas in conjunction with another system requiring high temperature gas, such as gas turbine [19].

- **Fuel flexibility:** A strong advantage of SOFC is the possibility of using hydrocarbon based fuels such as hydrogen, methane and carbon monoxide. The fuel flexibility provides the opportunity to use the SOFC system in various applications including some mobile applications, stand alone, remote and automotive axillary power systems [20].
- **Modularity:** Generally the characteristics of almost all fuel cell applications are similar in terms of modularity. As a result, more cells can be used in a stack and more stacks can be used in a unit for a desired power output to be satisfied. Therefore the feasibility of the fuel cell systems is increased by its flexibility and scalability [21].

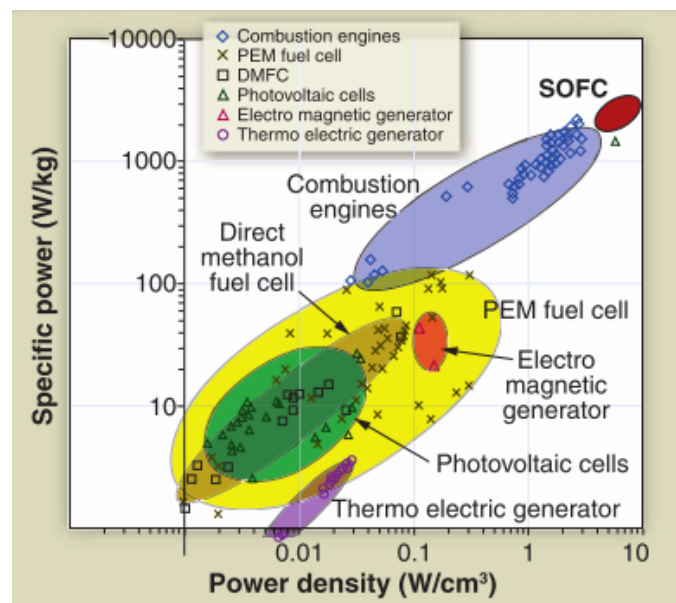


Fig. 1. Comparison of specific power density and specific energy range [21]

As seen from Fig. 1 SOFC has advantages in terms of specific power compared to other devices including combustion engines, PEM fuel cells, direct methanol fuel cells, electromagnetic generator, photovoltaic cells and thermoelectric generators owing to the availability of being micro sized with negligible weight. Combustion engines are the second effective devices in terms of specific power and power density. It is important to have higher gravimetric and volumetric power densities especially for portable and transportation applications due to limited available space. Availability of having different sizes of SOFC makes it a versatile technology that

can be used for many applications with very high system efficiency especially at the intermediate temperature SOFC [21].

However, there are some limitations mostly correlated with high operating temperature: longer start up and shutdown process, robust construction, materials that can resist the operating temperature. In connection to these limitations, there are performance degradation issues of SOFCs which are hindering SOFC technology to be fully commercialized.

1.2.2 Applications

SOFCs are intensively used in stationary power generation with an off-grid power output of a few hundred kW [20].

In terms of stationary power generation, Bloom Energy (USA) has been using SOFC as a stationary power generation system since 2001 with an electrical power output of 250 kW from a power module. Convion (Finland) on the other hand use SOFCs for distributed power sources with a power range of 50-300 kW while Hexis (Swiss) uses SOFC based combined heat power CHP unit as a stationary power generation with an expected efficiency of 95% [14].

The capability of using a wider range for fuel of the SOFCs system, increase its applicability for transport technologies especially for hybrid vehicles [22]. For instance, fuel cells auxiliary power units (FC-APU) has been developing a SOFC involved heavy duty truck by further improving the SOFC fuel usage [14]. FuelCell Energy (FEC) (USA) has been focusing on SOFC powered portable device development such as unmanned undersea vehicle (UUV) [14].

As mentioned, SOFCs have been growing as a power generation technology for both stationary and mobile devices. However, the technology has been facing with thermal management correlated issues which will be further addressed in this study.

1.2.3 Degradation issue in SOFCs

1.2.3.1 Actual performance

Electrical efficiency of a cell has a strong relation with cell performance. The cell performance is determined as cell voltage (volt) which is directly affected by polarization losses. There are three important polarization losses; ohmic losses, activation and concentration losses. These polarizations, mainly due to the materials used, design and microstructure, cause a decrease in the efficiency of the SOFC system as shown in Fig. 2 [23].

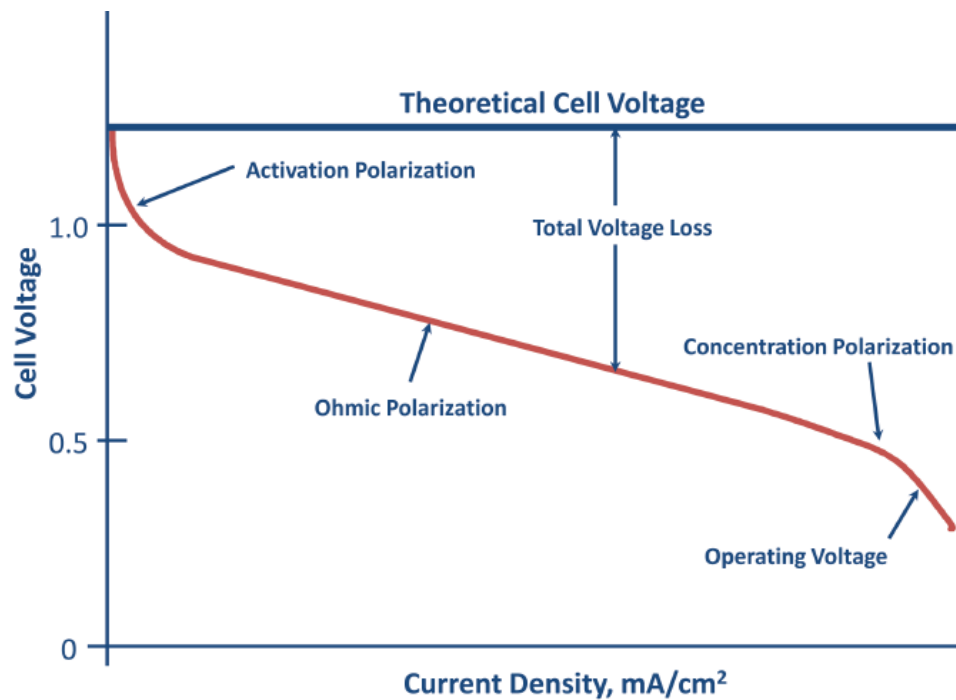


Fig. 2. Theoretical and actual polarization curves for theoretical cell voltage

- **Activation polarization**

Activation losses are mainly brought about by specific reactions which occur at both electrodes. Microstructure, electrocatalytic characteristic, reactant activities of fuel composition and temperature variations of the electrodes are considered as the main reasons for activation losses. Catalytic activity of the used materials can make strong

positive contribution to decrease in loss due to activation polarization of the cell which leads to an increase in the overall performance [23] .

- **Ohmic polarization**

Ohmic polarization depends on the materials and stack design and generally results from ionic resistance in the electrolyte, electronic resistance in the cathode and the resistance comes from the contact point between interconnector and current collector. The magnitude of the ohmic losses is increased when the current density increases while it decreases with an increase in temperature. Active cell area widely referred to as area specific resistance (ASR) is the key parameter to optimise ohmic polarisation. This is the more dominant polarization type compared to other polarization types [24], since it involves all electronic and ionic transfer correlated losses and can occur within all parts of the cell components including anode, cathode and electrolyte.

- **Concentration polarisation**

Concentration losses are generated by mass transport related activities occurring through the cell. The reactant, fuel rate, current density and materials and their design can also directly affect the concentration polarizations [24].

1.2.3.2 Degradation mechanisms in SOFCs

The lifetime expected from a SOFC (especially for stationary power generation SOFCs units) to be fully commercialised is about 40000 hours (h) with a degradation rate of 0.25% per 1000 h [25]. Currently SOFCs performance is sufficient (i.e. it meets these targets) especially when it used at intermediate temperatures, however there is still degradation occurring in the SOFCs which affects performance during the operating time period. The degradation rate has been achieved with high temperature SOFCs (>800 °C) [26], though it is still important to reduce the rate of the degradation which can have considerable power losses with prolonged cell/system operation especially with stationary applications. Additionally, the decrease in operating temperature leads to an increase in ohmic and electronic losses. At high temperatures on the other hand there are failures that can occur related to

both materials and structural aspects. The degradation can be classified as a soft failure (e.g. material related) or as a hard failure (typically structural). Soft failure relates to the degradation occurring in the materials of the cell components such as changes in material composition or poisoning, whilst there is mechanical degradation such as cell cracks or delamination resulting in total system failure in the case of a hard failure.

1.2.4 Monitoring methods

Mechanical durability and degradation caused by high operating temperatures stand as the fundamental barriers to SOFC performance and prevent the complete commercialization of SOFC at industrial scales [27]. Owing to limited available techniques, the temperature distribution of SOFC cell electrodes has not been understood fully. Additionally, the limited available funding and lack of facilities to be able to study this system in detail experimentally and computationally are another important boundary that hindering the full understanding of SOFC thermal behaviour. Therefore, it is important to monitor real-time surface temperature in order for operators to understand the real temperature gradient along the SOFC electrode. Understanding the temperature characteristics of the cell provides significant information that could be used to understand stress distribution, current density distribution, flow distribution as well as leakage related failure mechanisms. The three most common methods used to measure the SOFC temperature are numerical analysis (modelling tools), optic methods and experimental measurement (TCs).

There are a crucial number of studies focused on modelling of the temperature changes, along with the cell's performance, during operations [28]–[32]. Some software has been developed to model the temperature characteristics of the cell with the cell's or stack's performance. For instance, Pacific Northwest National Laboratory developed a software tool to observe the relationship between SOFC operating temperature and its performance. Additionally, there are some computational fluid dynamics (CFD) modelling works carried out for the temperature profile of SOFCs [33]–[35]. However compared to computational studies less research is available from the literature focused on experimental

measurements of SOFCs temperature profile due to the harsh operating environments and limited available space within the SOFC system [36].

Electrochemical (electrochemical impedance spectroscopy (EIS), voltammetry) and optical technologies, Raman spectroscopy and Fourier transform infrared spectroscopy (FTIR) are also used for temperature monitoring purposes of SOFC. However the harsh operating conditions, is a limiting factor for many of the mentioned optical measurement technologies, and a second factor, limited space, also restricts the measurement with sensory technologies [37]. Furthermore most of the optical techniques focus only on an electrochemical reaction correlated analysis however the cells chemical reactions are also an important contributor to the heat release/sink in SOFC systems [38]. Advances with the integration of Sagnac interferometric optical set up and infrared thermometer (IR) was developed and used for SOFC surface *in-situ* temperature and deformation measurement at 800 °C [16]. Nevertheless, the system required more instrumentation and the obtained spatial resolution was related to the proximity of the measurement location which was poor. It is important to obtain high spatial and temporal characteristics to reach a more realistic measurement, which is related to the time dependent response from the sensing. Most recently, infrared radiation (IR) imaging with integrated Matlab coding was performed to monitor SOFC temperature during operation under different operating conditions [39]. The limitation of accessibility of the electrode for optical imaging was noted as a challenge for stack level SOFC operations.

Although the SOFC system is challenging for implementation of sensory techniques within the cell or stack during operation, TCs are still the most common experimental technique serving temperature gradient measurement purposes [40], [41]. The measurement with TCs is generally made by placing the TCs into flow channel through the interconnect material [36]. Even though TCs are sufficient to capture the temperature changes with great accuracy (± 2 International Organization for Standardization (ISO)) and with their wider operating temperature range (up to 1200 °C) especially with K-type TCs, there is still doubt on the reliability of the obtained temperature of SOFCs with TCs due to possible disturbance of external parameters such as fuel flow temperature [42]. Thus, in this study temperature distribution of SOFCs will be experimentally monitored with a thermal array sensor directly from the cell surface.

1.3 Aim and Objectives

In high temperature SOFCs, the performance of the cell can be altered by the variation in the cell operating temperature along the entire cell as well as in a stack. As temperature gradient induced stress contributes to performance degradation issues faced in an SOFC system, resulting in a decrease in cell performance, understanding the temperature distribution characteristics of the SOFC is necessary. This will allow the identification of any high temperature related degradation mechanisms at both a cell and stack level. In this respect, the *aim* of this research is to investigate the parameters contributing to temperature distribution through in-situ monitoring of the SOFC electrode, especially at the cell level, under real operation.

To achieve the intended aim, the requirement is for a technique to be used to facilitate in-situ monitoring. A recently developed thin film/wire sensor, which is offering more benefits compared to other temperature measurement techniques including thermocouple and thermistor, shall be investigated for the temperature measurement. The objectives of the research, to meet the aim are:

1. *Review of limitations of current temperature distribution methods:*

The pitfalls of existing experimental and computational methods are required to establish the knowledge gap.

2. *Investigation of thin film sensor technique for monitoring:*

The current sensor characteristics need to be understood alongside the methods of application, for example the sensor can be used in both thin film and thin wire form by considering spatial and temporal resolution. Considering these resolutions will allow greater sensitivity to smaller temperature changes. Having high spatial and temporal resolution is a key factor for accurate measurement and is specifically focused on in this research to understand the temperature gradient along the cell electrode. A sputtering technique will be investigated as a method of application alongside appropriate sensor patterns for efficient temperature detection.

3. *Determining optimal sensor architecture:*

For any temperature distribution collection the sensor needs to have physically durable and chemically stable thin film sensor elements, and for the wire attachment to have mechanically and electrically effective external wire connection for signal collection. Using the sensor in thin wire form can eliminate the connection related challenges while it requires placement within the manifold and to be bonded to the cell surface without damaging the cell electrode. Investigation of the optimal architectures will be investigated to facilitate having high spatial and temporal resolution.

4. Cell temperature distribution monitoring:

Monitoring sensitively the cell electrode temperature gradient directly from the cell surface during operation via experiments is proposed. This requires a mechanism for data collection and specific experimental set ups for sensor placement.

5. Knowledge elicitation of cell temperature distribution:

Understanding different parameters and their effects on temperature gradient locally within the cell is required. Therefore temperature distribution will be *in-situ* monitored under varying operating conditions and the obtained readings will be compared with those analytically calculated via the data for validation purposes.

1.4 Thesis Outline

The thesis consists of eight chapters. In the first chapter, the introduction, an overview of the research background, novelty and impact of the research as well as a detailed explanation of the aims and objectives of the thesis are explained. A literature review on SOFC technology in terms of the main types, its working principles, main components including electrodes, electrolytes, and polarization losses as well as current studies about temperature of SOFC are provided in chapter 2. Furthermore, thermodynamics and electrochemistry of SOFC systems are also outlined in the same chapter.

The third chapter includes the methodology. The materials used and the applied techniques are described in this chapter. The characteristics of the recently developed sensor and its architecture are described. Furthermore brief explanations about the experimental set up used for each research chapter are also described in chapter 3.

The fourth chapter is devoted to the study of integration of the thin film sensor and also its durability on a porous cell electrode while the method for the external wire attachment to thin film sensor pattern is explained in chapter five. Results and discussions of the both experiments were also included in the related chapters.

The sixth chapter includes in-situ temperature gradient mapping of the working SOFC under conditions of OCV and also with some current drawn. Results and discussions from the experiment are provided and analysed in terms of the thermodynamics of the SOFC. Chapter 7, on the other hand, focuses on the parameters, including current density, fuel rate and operating temperature, to identify their contribution to cell temperature gradients under different operating conditions.

In the last chapter, the conclusions resulting from the thesis are discussed with recommendations for future work.

Chapter 2:

Understanding SOFCs — Literature Review

2.1 Solid Oxide Fuel Cells

2.1.1 Introduction and working principles

There are three main components in a SOFC system: two porous electrodes (cathode and anode) and a ceramic electrolyte which is a metallic oxide [16], [43]. A SOFC has a crucial advantage of utilizing a wide range of fuels including hydrogen (H_2), methane (CH_4) and carbon monoxide (CO) compared to other low temperature fuel cell systems [44]. As a high temperature fuel cell (600-1000 °C) SOFC offers high efficiency (>50%) [22], [45]–[47] and is an environmentally friendly power source to meet society's growing demand [48], [49]. Even though, stationary and heat generation applications are considered as the main areas for SOFC usage, it is a convenient power source for transportation and portable devices [50].

A SOFC has simple operation principles. At the anode, fuel (generally H_2) is diffused from the outer surface of the anode to the anode-electrolyte interface by diffusing through the pores. At this point, which is the connection point of the electrically conductive anode, referred to as the triples phase boundaries (TPB), the oxygen ion donor electrolyte and pore (fuel source) meet the oxygen ions transferred from the cathode, as illustrated in Fig. 3 [51]. Then, the electrochemical reactions take place at the anode and cathode as represented in equation 1 and 2 for the cathode and anode respectively [52].

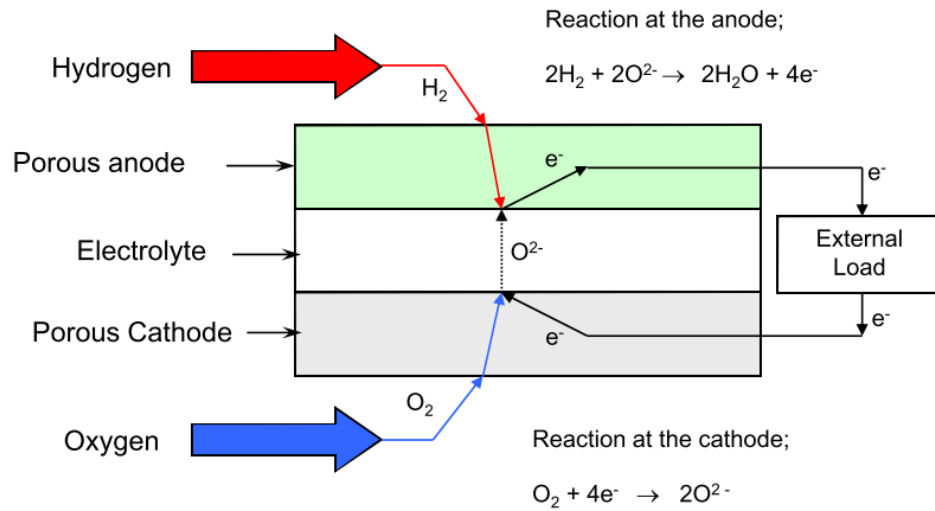
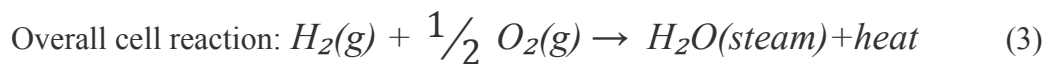
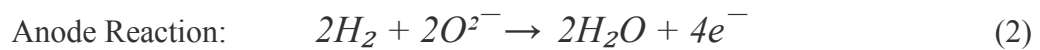
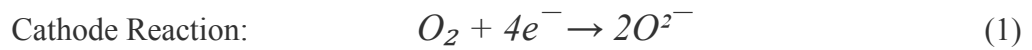


Fig. 3. Representation of the Solid Oxide Fuel Cell working process

The negative electrons produced from the reaction at the anode side are transferred to the cathode side by an external circuit while the reaction products of H_2O are diffused back to the outer surface in order to mix with the fuel stream. A similar protocol is also followed at the cathode side where the air from the outer surface of the cathode is diffused towards the electrolyte triple phase boundaries (TPB) including the cathode (electronic conductor), electrolyte (oxygen ion acceptor) and pore interphase where the reduction reaction of oxygen occurs at this point, as in equation 1. The cathode is working as a mixing conductive region comprising electronic and ionic conductivity this is due to the ease of transport for electrons diffused by the anode side and transportation of oxygen ions to the electrolyte [53]. Eventually there is water steam and heat generated as products from the overall reaction (equation 3).



2.1.2 Cell components

2.1.2.1 Electrolyte

The electrolyte plays an important role in SOFC operation. The key characteristics expected from an electrolyte material are high ionic conductivity for oxygen ions migration, high density to prevent any gas leakages and low electronic conductivity [54]. Oxygen ions from the cathode are transferred through the electrolytes while other gas transfer is inhibited. As seen in the Fig. 4 the electrochemical reactions occur at the TPBs between anode and electrolyte. The transferred oxygen ions meet with the fuel (H_2) supplied to the anode electrode while the generated electrons are transferred externally. Yttria stabilised zirconia (YSZ) and gadolinia doped ceria (GDC) are considered as the main candidates for electrolyte material with relative higher ionic conductivity about 0.01 S/cm at 500 °C [50]. On the other hand, there is a potential of obtaining reasonable power output from the proton-conduction electrolytes which is where positively charged ions (H^+) is transferred through electrolyte. The proton conducting electrolytes, i.e. Indium doped $CaZrO_3$, have advantages of providing good conductivity at intermediate temperature (400 °C - 700 °C) [55]. However their instability issue in CO_2 and steam atmosphere and difficulties of sintering process are hindering the practical application of proton conducting electrolyte [56]. YSZ has some promising advantages including excellent chemical stability, chemical inertness, reasonable ionic conductivity and high fracture toughness. Chemical stability and inertness are required to prevent any interaction between the electrode and electrolyte material which reduces both electrode and electrolyte performance. In contrast, GDC offers better ionic conductivity with higher electronic conductivity but lower thermodynamic stability under reducing conditions which is where the number of oxygen atoms in a molecule is reduced [54]. The higher electronic conductivity of GDC can be an advantage whilst it is used as active layer at high temperature or as an electrolyte at intermediate temperature due to its great ionic conductivity at cooperatively low temperature. In other words, the higher electronic conductivity of GDC electrolyte has a disadvantage of being electronically conductive which allow electron transfer via electrolyte eventually reduction in performance. In the case of using a CDO

based electrolyte in a reducing atmosphere, the ceria-based electrolyte is reduced (from CeO_2 to $\text{CeO}_{2-\delta}$).

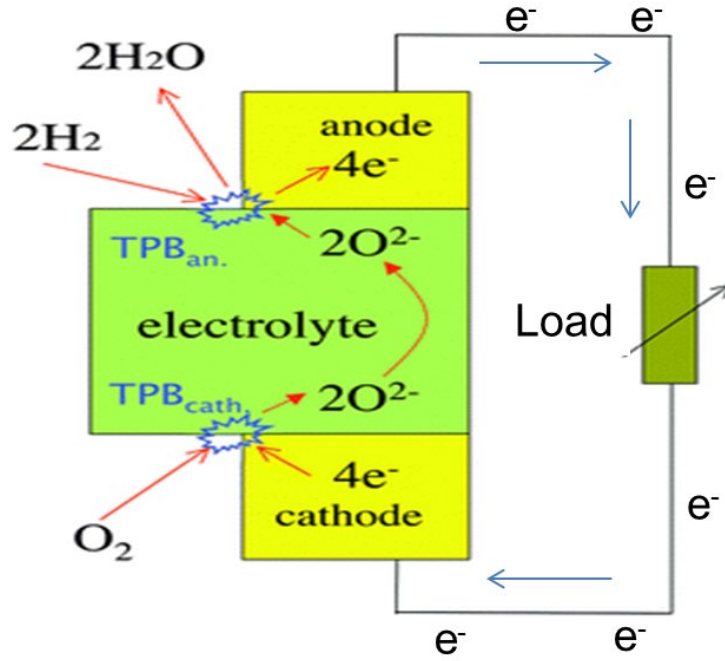


Fig. 4. Oxygen ions transportation through the electrolyte [57]

Stabilized bismuth oxides including erbium bismuth oxide, ESB, ($\text{Er}_{0.4}\text{Bi}_{1.6}\text{O}_3$) and dysprosium-tungsten bismuth oxide, DWSB, ($\text{Dy}_{0.08}\text{W}_{0.04}\text{Bi}_{0.88}\text{O}_{1.56}$) are other promising candidates as an alternative to GDC and YSZ owing to their higher ionic conductivity at an intermediate temperature as seen in [21]. However, bismuth based electrolytes (Bi_2O_3) become electronically conductive due to decomposition of Bi_2O_3 at relatively high temperatures which leads to a decrease in overall cell performance [21]. Therefore, YSZ and GDC are considered as the most promising candidates amongst the others for SOFC electrolyte materials owing to their chemical and electrochemical stabilities.

Oxygen ions which are generated from the oxygen reduction reaction at the cathode transfer via vacancies in the electrolyte. Thus, YSZ is aerated by doping zirconium dioxide (ZrO_2) with generally 8 % mole Y_2O_3 and vacant O^{2-} is occurred [58]. Increase in the vacant ions which provide transportation of oxide ions leads to an increase in ionic conductivity in the same defined range of the doping limit (should

be 6-8 % of Y_2O_3) [59]. GDC, instead, is obtained by doping ceria (CeO_2) with a second aliovalent lanthanide metal. There is a strong relation between ionic conductivity and concentration of dopant ions where the ionic conductivity proportionally increases with the increase in dopant. However, there is a doping limitation percentage where after some certain percentage range the conductivity decreases by the increasing of doping percentage due to the unwanted reaction between the doping material and vacancies ions. It is vitally important to add a dopant which is similar to the host ions in pore size to preserve the crystalline shape of the essential metals, as there can be a failure due to the mismatch between dopants and main materials [60].

Overall, YSZ and GDC are both promising electrolyte materials where GDC is more preferable at relatively lower temperatures (600 °C-800 °C) whilst YSZ is mostly preferred for high temperature SOFCs. The operating temperature is helping to reduce the resistance mainly during charge transfer which leads to increase in total power output while it is a main limiting factor for the availability of different materials to be used as SOFC components such as electrolyte with desired efficiency.

2.1.2.2 Anode

The anode is where hydrogen molecules catalytically react with oxygen ions transferred from the cathode. Released electrons which are transported to the external circuit, water and heat are produced as products from the anode reaction. Redox stability, tolerance of transients, easy expedition of oxide ions, catalytic activity and sufficient porosity are the main requirements for the anode material [58]. Higher catalytic activity leads to an increase in reaction rate and a decrease in activation losses resulting in higher SOFC performance while the higher the porosity is the more the TPBs which causes higher fuel utilisation and eventually increases the cell performance. Furthermore, the anode must protect its electrochemical functionality and structural coherence at high working temperatures to prevent the occurrence of soft and hard failure of the system, respectively [61].

Considerable amount of study has been carried out on a wide range of materials to produce the most efficient anode with a maximum performance and minimum risks for failure [62]–[64]. Precious metals such as platinum have been considered physically and chemically unstable even though they provide perfect catalytic activity [65], [66]. There is a consensus between researchers in the literature that in terms of stability and catalytic activity, nickel cermet and YSZ composition are the most efficient anode materials for SOFC application [67]. Nickel (Ni) provides not only catalytic activity for the oxidation reaction but also creates pathways for electron conduction from TPB to the current collector [67]. The composition of Ni-YSZ consists of a zirconia cermet mixture with ceramic and nickel due to its high electronic conductivity and catalytic activity at high temperatures [68].

Even though Ni has advantages of being economically viable compared to other novel catalyst materials such as platinum or gold, the high electrically conductive, low adhesion performance, redox instability and issues during sintering process due to its different CTE compared to YSZ is considered as the main drawback [24]. Zirconia prevents the sintering of the metal particles and induces coefficient thermal expansion (CTE) mismatch. Due to different material properties of the zirconia and Ni, there can be adhesive correlated issues raised during sintering the anode electrode. This leads to some intrinsic stress between these two materials which appear as a soft material issue during the SOFCs operation.

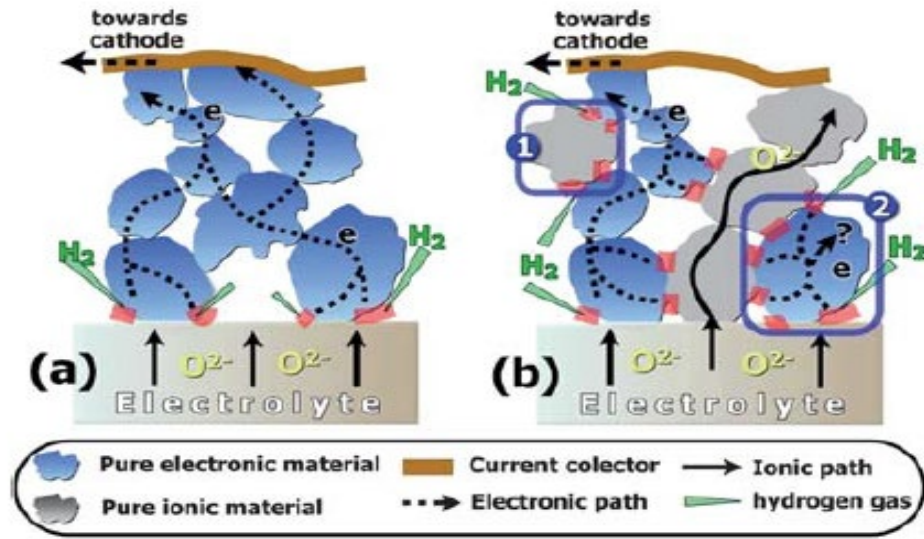


Fig. 5. Schematic representation of anode and the effect of electrolyte materials [48]

Fig. 5 shows the anodic reaction points (pink dots) at the TPBs of the Ni/YZS when a pure ionically conductive material (fig. 5(a)) or the mixture of both ionically and electronically conductive material (fig. 5(b)) are used as anode materials. Ionic conductor (electrolyte), electronic conductor (electrode) and gas phase are connected to each other at the TPBs. A pure electrode (Fig. 5 (a)) with a limited electrode-electrolyte interfaces results in fewer TPBs with them being located only in the vicinity of electrolyte. While the anode with the material composition of the mixture of ionic and electronic conductor provides more TPBs.

2.1.2.3 Cathode

The oxygen reduction process occurs at the cathode which is a crucially important part of the SOFC that directly affects cell performance [69]. High catalytic activity for the oxygen reduction process which reduces the activation losses, electronic and ionic conductivity which increase the cell performance, compatibility with adjacent components which reduces risks for CTE related failure, and porosity for oxygen diffusion are the main requirements for the cathode material choices [70]. Additionally, having a smooth surface and small thickness are the key factors to increase cell performance [71]. In the past, platinum due to its high catalytic

properties was used as the cathode material [72]. However, platinum is an expensive novel material therefore alternative cathode materials have been studied as a substitute for platinum.

Ionic and electrically conducting ceramic materials have begun being used widely as cathode materials. The most common cathode materials are perovskites based materials such as strontium-doped-lanthanum manganite (LSM) [58]. This material, $\text{La}_{0.8}\text{Sr}_{0.2}\text{MnO}_{3-\delta}$ (LSM), offers good compatibility with the YSZ electrolyte and has high chemical and thermal stability [73]. On the other hand, $\text{Ba}_{0.5}\text{Sr}_{0.5}\text{Co}_{0.8}\text{Fe}_{0.2}\text{O}_{3-\delta}$ (BSCF) and $\text{La}_{0.6}\text{Sr}_{0.4}\text{Co}_{0.2}\text{Fe}_{0.8}\text{O}_{3-\delta}$ (LSCF) have been also widely used as a cathode material [74]. However, low conductivity and thermal mismatch are the main issues for BSCF while LSCF offers the best electrical and ionic conductivity with reasonable compatibility [70]. The composite cathode materials such as mixed ionic electronic conducting (MIEC) cathodes offers better compatibility with electrolyte and interconnect and has perfect ionic and electronic conductivity [75]. Overall, LSFC cathode material is considered as the most preferable choice due to its sufficient stability with high electronic and ionic conductivity. LSM is more preferable in terms of its compatibility with the electrolyte [23]. In other words, LSCF offers higher performance with higher risk of coefficient of thermal expansion (CTE) mismatches, with related failures whilst LSM provides more stability with relatively less performance.

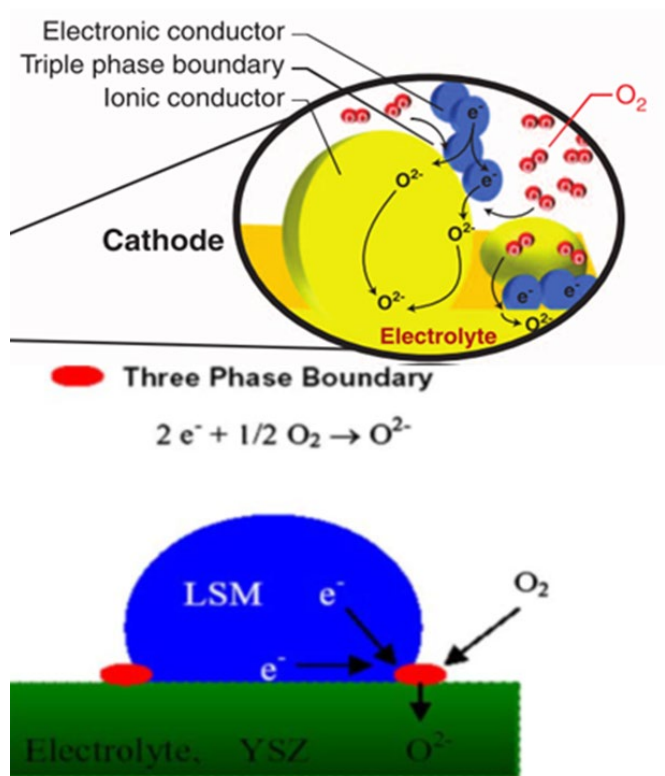


Fig. 6. Schematic of oxidation reaction at the cathode TPBs region

[21]

Fig. 6 shows the basic operation mechanism of a cathode which is where the electronic conductors (blue coloured), gas phase and ionic conductor (yellow coloured) exist at the same time at the TPBs. As the TPBs are the region where the electrode has electronic conductivity, electrolyte ionic conductivity and gas interphase exist at the same time and the chemical reaction occurs [76].

In order to enhance cathode performance, improvements in catalytic activity and long-term stability of the materials is vital to prevent material and performance related degradation occurrence, especially at the TPBs [77]. Density of TPBs are strongly depends on the morphology characteristics and electrochemical catalytic activity of the materials [78]. The enlargement in TPB leads to an increase in the current accommodation function [52]. In order to increase the TPB region, cathode materials are enhanced either by the addition of an interlayer between the cathode and electrolyte, such as Ceria gadolinium oxide (CGO), or changes in the chemical modification of the perovskites materials by introducing some materials such as Ga (gadolinium) , La (Lanthanum) , and Mn (manganese) [48].

Chromium poisoning, caused usually by the interconnect material when chromium-containing alloys are used, is considered as the most dangerous degradation mechanism of the SOFC cathode [79], [80]. The deposition of the chromium on the cathode surface can block the oxygen diffusion from outside to inside which leads to a significant decrease in cell performance [76].

2.1.2.4 Interconnect

SOFCs can be a single cell or combined in a stack of several cells. Moreover it can be a module by combining several stacks for the purpose of obtaining a higher useable power output. In stack configurations the planar cells (which will be discussed in the next section) are placed on top of each other in which interconnect materials are required to provide an electronic connection between these cells. Interconnect covers the central place in the SOFC stack design. As shown in Fig. 7, a cell (green coloured) is sandwiched between two interconnects (grey coloured) where they are connected to each other through the contact layers.

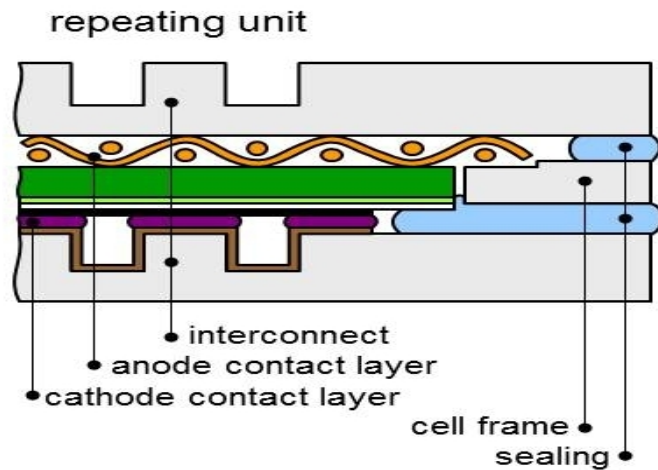


Fig. 7. Schematic representation of cell interconnect configuration

There are a wide variety of critical tasks that have to be performed by this interconnect since it provides the electrical connection between an anode of one cell and a cathode of another cell [81]. Therefore it is required to meet both cathode and anode electrode characteristics. High thermal and electrical conductivity, chemical

stability, low permeability, excellent resistance to sulphur and carbon poisoning are the main requirements for interconnect materials [59]. Interconnects are usually made of ceramic and metallic materials. Among these, the ceramic interconnects provide better stability and compatibility with a reasonable electronic conductivity. Ferritic stainless with the Cr composition ranged between 20-25% is used as a metallic interconnect. Moreover, different metallic alloys such as Crofer 22 APU and Crofer 22 H have also been developed by improving the material composition or coating with different materials to increase its performance [81]. Metallic interconnects offer higher electronic conductivity, blockage of Cr evaporation and ion diffusion and thermal diffusivity with reasonable compatibility with the cell electrodes.

Lanthanum chromite oxide (LaCrO_3) is the most common ceramic interconnects [81]. It provides effective chemical stability, thermal expansion coefficient matching with low ionic conductivity, which can be increased by the addition of calcium (Ca), and high oxygen permeation, which can be improved by the addition of magnesium (Mg) and strontium (Sr) [82]. However, it is hard to machine and relatively expensive compared to metallic interconnects. On the other hand, metal interconnects are composed of chromium metal alloys which provide higher electrical conductivity, mechanical stability without any oxygen permeation, and uniform temperature distribution due to its high thermal conductivity [83], [84]. The thermal expansion mismatch with the YSZ electrolyte and chromium poisoning which causes electrical activity degradation in the cathode are the main issues for these interconnect materials but still they are generally preferred especially for intermediate temperature SOFCs (600 °C-800 °C) [85].

2.1.3 Cell configurations

As aforementioned, especially for power generation for industrial applications, cells are stacked. The cells can be arranged in different ways where the cells shape influences the set up. SOFCs have been classified as planar, tubular, and micro-tubular (MT-SOFC) [82]. The planar SOFCs can either have square or circular geometries while the tubular SOFCs are formed in different sizes. Fabrication methods of the SOFCs vary depending on the types of SOFCs.

2.1.3.1 Planar

In planar cell types, the cell components are designed as flat plates and the electrical connectivity is obtained in a series set up, as shown in Fig. 8. The utilisation of planar type SOFCs has increased due to advances in ceramics which leads to easier fabrication and processing of planar SOFCs [86]. Due to their flat shape, it is easy to stack planar SOFCs by the placement of an interconnect between each cell which helps gas diffusing across the cell surface.

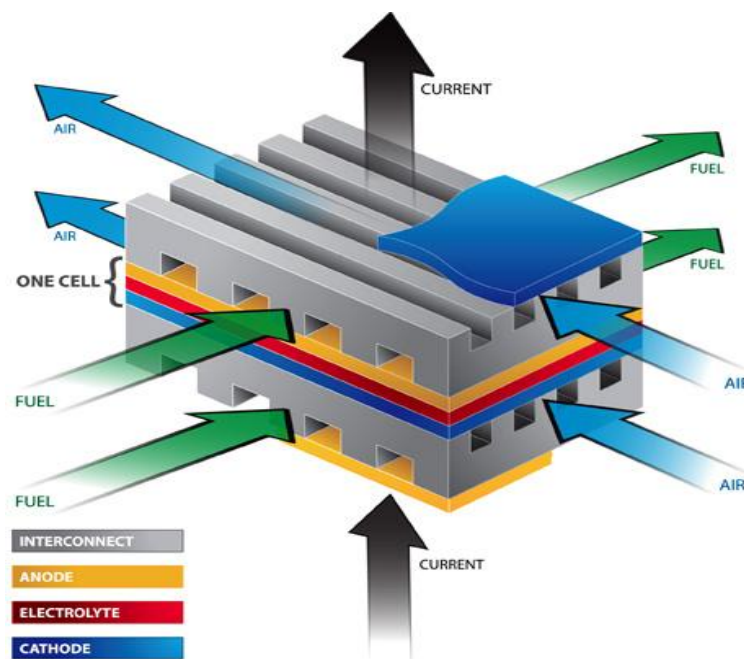


Fig. 8. Planar SOFC single cell and the stack

The power density of the planar cell can reach up to 1 W cm^{-2} which varies depending on the cell material and configuration (i.e. an anode supported cell produces more power) and operating condition such as operating temperature and fuel utilisation [87]. The power density obtained from a planar cell is higher than the power density produced by the tubular types owing to the short transportation pathway of the planar cell (20-50 μm for electrode supported, a few hundred μm for electrolyte supported) from the anode to the cathode side [32], [86]. However, thermal stability and gas sealing at high temperatures are the main challenges. Two

common planar SOFC configurations mainly applied in industry are: short stack planar (Julich). The key requirements from the planar SOFC are;

- *Electrical and electrochemical performance*
- *Thermal management*
- *Mechanical and structural integrity*

The stack configuration of the planar SOFCs including Z-flow, serpentine, radial-flow and spiral flow is generally designed depending on the gas flow/interconnect configuration (Fig. 9). This is due to the geometry of the interconnect configuration which has an impact on stack performance [88]. As the interconnect fulfils the mission of fuel distribution across the cell surface it thus affects fuel utilisation and eventually cell performance, cell thermal stress and its cooling etc. The flow channels designed to have uniform gas distribution and positive contribution to heat and mass transport and also promote electrical connectivity either for a single cell or in a cell stack [89].

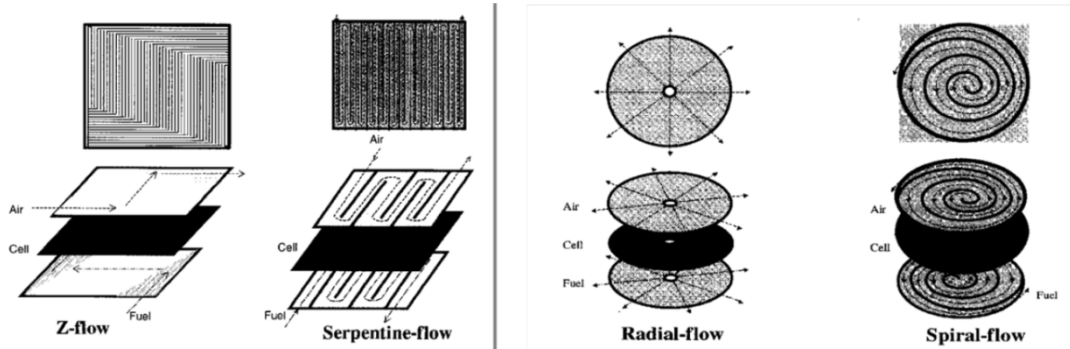


Fig. 9. Schematic of the design of the stack configuration of planar SOFCs [58]

SOFCs have been based on electrolyte supported, anode supported and cathode supported, as well as inert supported based on its cell configuration [90]. When the cell is designed as electrolyte supported Fig. 10 (a), the thickness of the electrolyte ranges from 80 to 250 μm , whilst it is about 50 μm for thin porous anode and cathode supported. In the case of fabrication of the electrolyte supported cell; first the thickest part (electrolyte) is fabricated then the thinner anode and cathode electrodes are deposited on both sides of it [86]. The same fabrication process is also

followed for the anode and cathode supported configurations (as seen Fig. 10 (b) and (c), respectively).

A thicker electrolyte increases the ohmic resistance which leads to a decrease in overall cell performance [91], while a thicker electrode leads to an increase in cell performance due to the increase in TPBs [92]. The inert support material (Fig. 10 (d)) serves as a mechanical supporter only thus it does not contribute to cell performance.

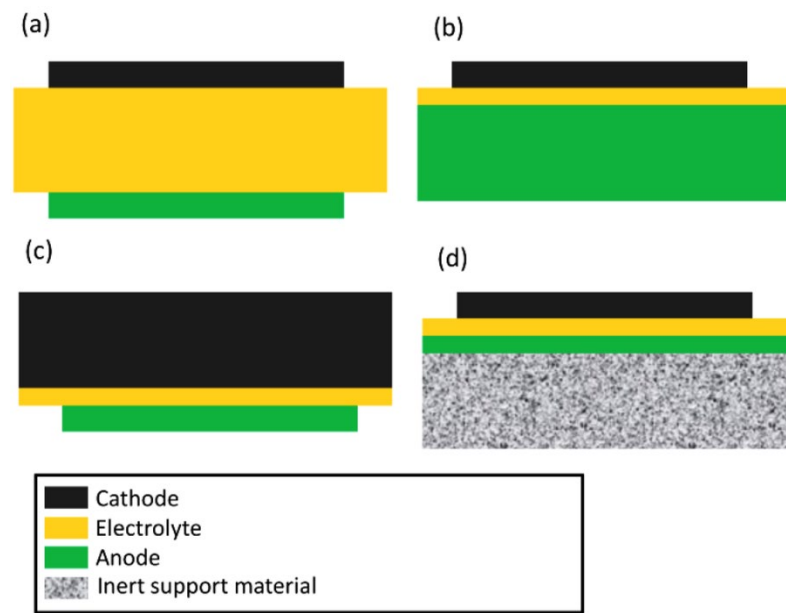


Fig. 10. Representation of different cell configurations of the SOFC [90]

2.1.3.2 Tubular

Tubular SOFC is one of the most commercialised types after planar [93], [94]. Additionally in terms of mechanical and thermal stability and the absence of sealing problems the tubular design is preferable compared to the planar SOFC [93]. The main reason for this is the possibility of having larger sizes of tubular cells due to its sufficient mechanical stability resulting in easy handling. Another reason making the tubular design more attractive is the minimised sealing problems where sealing is only required at the free ends whilst all the edges of the planar type cell are required to be gas tight. In some of tubular design such as Siemens design, it is deliberately allowed to have imperfect sealing to let the combustion reaction to use the released

heat to warm up the provided air. However, in many cases there is a sealing required between the metal frame and ceramic tube. Brazing and ceramic glue is the mostly applied technique for sealing of tubular SOFC cell [95].

The configuration of the tubular cell which is developed by Siemens Westinghouse Power (SWP) can be either supported by an external component or by itself. LG and Rolls Royce have also been developing a flat strip tubular cell where all cell components patterned onto a tubular porous ceramic (fuel supplied) in a required integration from the electrical point of view. When the tubular SOFC is supported by itself, it can be either anode supported or cathode supported. For instance, an anode supported cell (Ni-YSZ) coated with a thin YSZ electrolyte (green coloured) and a thin LSM cathode (purple coloured in the inner side) is shown in Fig. 11 (a) for single cell and (b) for a stacked configuration of the cells [93]. The buffer layer provides mechanical support and the Ni felt is used for electronic connection between the electrodes (Fig. 11 (b)).

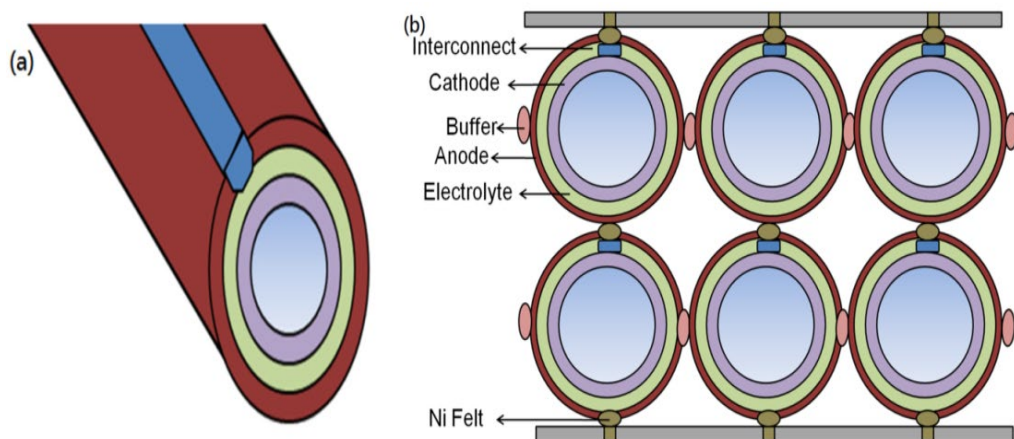


Fig. 11. Demonstration of a single (a) and stack (b) tubular SOFC [90]

The power density of tubular cells ranges from $0.35\text{--}0.6\text{ W cm}^{-2}$ depending on its operating conditions, including operating temperature and supplied fuel rate [96]. Even though there is limited information about the cell fabrication process of the tubular SOFC, the extrusion method is generally applied. Once the mixture of the material composition for a supporting cell component (for instance this is the cathode for the tubular cell shown in Fig. 11) then the extrusion is carried out through a die to fabricate the desired tube. A support tube is fabricated with

extrusion to provide mechanical support. Eventually, the other thinner components of the cell (anode, cathode & electrolyte) are deposited on the support parts [82].

2.1.3.3 Micro-tubular

MT-SOFC is similar to tubular types in terms of its fabrication process and constructions (stacking) however they are smaller in size. Micro tubular SOFC has advantages of having quicker start up capability, higher power output density which can reach up to $0.5\text{-}0.8\text{ W cm}^{-2}$ [97], and feasible portable characteristics in comparison to planar and tubular SOFCs [82]. However, the MT-SOFC is required to have effective mechanical supporting components which are not easy to fabricate due its smaller size. MT-SOFC performance has been further improved by reducing the cell size, making it micro scale, resulting in higher power density and better thermal stability with negligible long path problems. This results in less ohmic losses compared to the tubular configurations [98] since the longer the path for charge transfer the more the ohmic losses. There is also the possibility to design the MT-SOFC as self-supported where the supporting part is around $80\text{-}250\text{ }\mu\text{m}$ thick whilst the thicknesses of other parts are $50\text{ }\mu\text{m}$. Fig. 12 shows a fabricated MT-SOFC with three different diameter sizes before (Fig. 12 (a)) and after (Fig. 12 (b)) the sintering process. The diameter size of the fabricated cell further reduces after sintering as the components of the cell are becoming denser. The supporting material provides mechanical strength and stability to the system, in other words it leads to a compact SOFC system. Compared to the electrolyte supported configuration of the MT-SOFC system, an anode or cathode supported system can provide better performance due to the thinner electrolyte design which causes lower ohmic losses and faster transportation to the electrons [82].

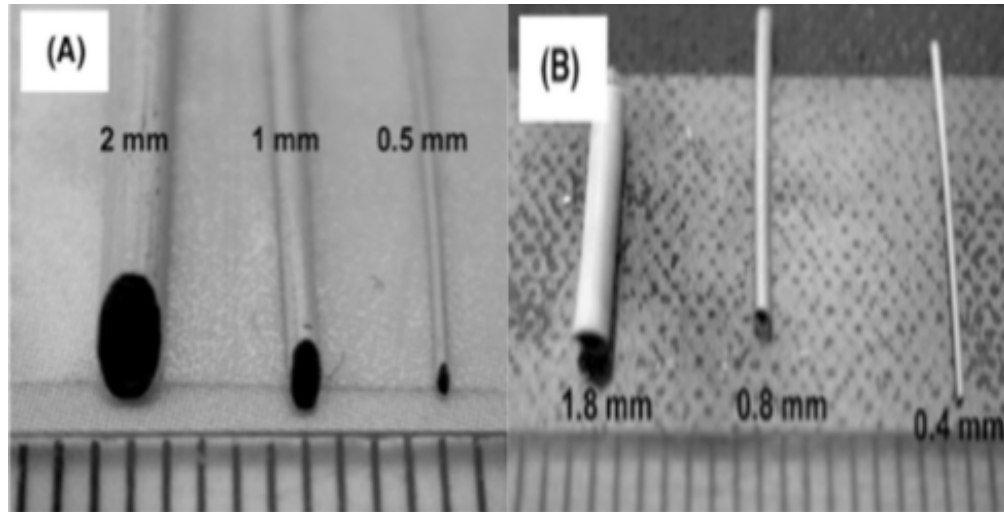


Fig. 12. Fabricated MT-SOFC before (a) and after (b) sintering

Overall, compared to other two types of SOFC, the planar SOFC has higher power density due to the low volume of the cell with the advantages of short distance between electrodes resulting in easy transport for electrons and ions. However, thermal stability and gas sealing due to the high operating temperature still remains the main challenging issue requiring solution compared to tubular designed SOFCs. Tubular and MT-SOFC on the other hand offer more mechanical stability and negligible sealing issue however with less power output. Thus due to its sufficient power density, planar SOFC temperature related issues, including sealing and thermal stability, through improvements in its thermal management are important to make this configuration more preferable for industrial application. Temperature distribution monitoring of an anode supported planar cell offers less possibility of a cell hard failure due to intrinsic stress and cell performance is the main focus in this study.

2.1.4 Applications

SOFCs have a wide variety of application potential depending on the size of the power output requirement of the proposed system. Also the range of applications has been increasing with the development in SOFC technology. The applications of SOFCs can be gathered as portable, transportation and stationary [22], [99]. Depending on the required power output, different modular structures can be created

as the power ranges from 100W for portable devices to MW for stationary systems [100].

2.1.4.1 SOFCs for transportation and portable applications (20W-10kW)

A great amount of effort has been made by the FuelCell Energy (FCE, US) company which supports a key project under the US Department of Energy (DOE) Solid State Energy Conversion Alliance (SECA) to improve the application of SOFCs for transportation [14]. The main target of the project is to introduce low emission highly efficient SOFC integrated system with a power output scale of MWs. While Delphi (US) which has been working on SOFC for a few decades developed a power unit for trucks that works independently from the main engine and provides power for the in-cab electrical accessories and also for the fan to cool down the engine as shown in Fig. 13 [14].



Fig. 13. SOFC power generator integrated truck by Delphi

As mentioned earlier transportation is one of the most important applications of SOFC technology as it can be applied as a potential energy source to reduce the significant emissions caused by transportation [22]. Other fuel cell technologies such as Proton Exchange Membrane (PEM) fuel cells have been studied to be an emission

free power generation system for transportation applications. However, SOFCs seem more feasible in terms of the required fuel, system cost and process management than the PEM [45]. For example, PEM requires pure H_2 which is costly and there are limited processes to obtain pure H_2 while SOFC systems are capable of running with H_2 and CO compositions [101]. In addition to this, there is no need with a SOFC system for the noble catalysts for the electrochemical reactions that take place during operation due to the high operating temperature (600 °C-900 °C) which leads to a decrease in cost.

Portable devices such as battery chargers or mobile power units, as shown in Fig. 14 are generally aimed at use in military purposes. In this regards, an Auxillary Power Unit (APU) has been developed by AVL (Austria) especially for such applications with a power output ranging from 20W to 10 kW. They have made great efforts to meet the power demand of portable devices and automobile auxiliary systems for mobile and transportation applications (5kW-10kW) [100]. This system can be integrated into a vehicle and operate with conventional diesel, used for anti-idling purposes of truck to prevent from low efficiency idle operation or power sources for some portable devices such as providing electricity.



Fig. 14. Illustration of APU mobile power (10 kW) generator

The potential of SOFCs application for portable devices and transportation can be further increased by solving the problem regarding long start-up times, and temperature related degradation especially in the case of using planar type SOFCs

[99]. Thus SOFCs for transportation applications have been developing but are not fully commercialised yet.

2.1.4.2 Stationary applications of SOFCs

Larger developments have been achieved in stationary application of SOFCs together with a growing interest paid by companies and their allies, governments, and researchers. Siemens Westinghouse, as a leading company for stationary applications of SOFCs, fabricated a 100 kW size system by using the tubular arrangement. Additionally a 250 kW SOFC-gas turbine hybrid power system which is supported by Southern California Edison is also fabricated by Siemens Westinghouse. Bloom Energy which is a large manufacturer of SOFCs with a generation potential of 75 MW [102] is another leading company in SOFC systems. Siemens Westinghouse uses tubular and micro-tubular configurations, fabricating SOFC units with the power output ranging from 100kW-500kW for distributed stationary power generation [103]. A huge installation has been made in Japan through the Ene-Farm programme where 40,000 SOFCs integrated into a CHP (combined heat power) system have been built in homes to provide power for their electricity and hot water [102]. Electrical efficiency of the SOFC (~50%) is increased when it is combined with CHP unit. CHP makes important contribution to SOFC for distributed energy application. Also, LG fuel cell systems which are a group of companies including Rolls Royce systems, Rolls Royce group and LG group focused to develop a 1-10 MW sized system [80]. The process from fuel into power out of the Roll Royce fuel cell system is represented in Fig. 15 (with exaggerated view of SOFC unit). After air and natural gases are processed to clean the raw natural gas to make it ready for SOFC use, they are sent to the SOFC unit where the gas chemical energy is converted into electrical energy, and finally the produced useful power is connected to a grid system.

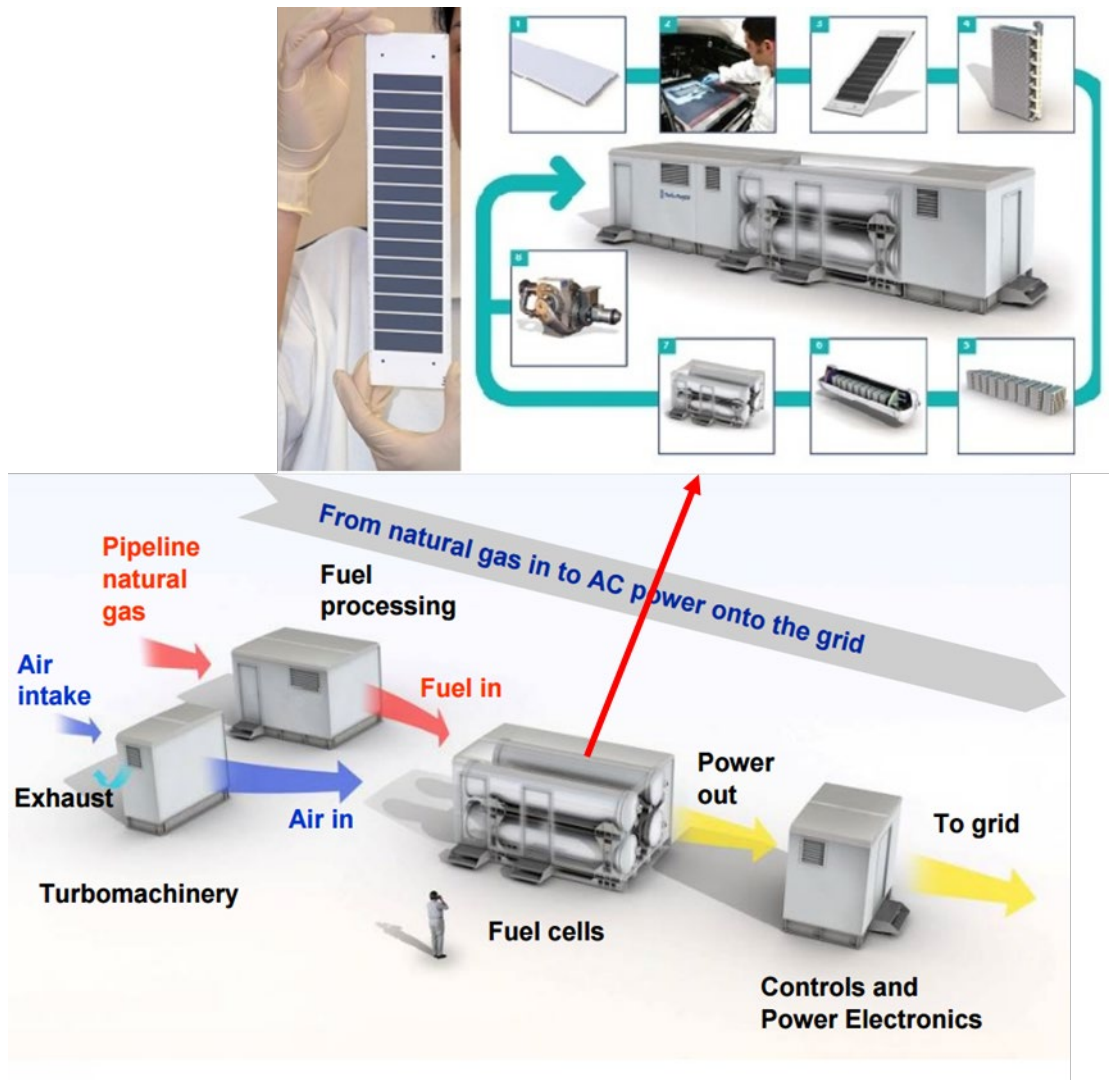


Fig. 15. Demonstration of Rolls Royce SOFC power plant [104]

There is always the possibility to increase the power output of the SOFCs application when the system is combined with another system such as turbines. The power output can reach several MW when the Rolls Royce based configuration is combined with another power generating system.

Bloom energy which generally uses planar type SOFCs, is seen as one of the biggest SOFC companies playing a key role in for the commercialisation of SOFCs for stationary power generation while APU and Delhi are considered as suppliers in the niche market for the commercialisation of portable and transportation application of SOFCs. Additionally Rolls Royce and LG have been working to further increase the power range of stationary applications. There is large number of companies

including Panasonic, Toshiba, Aisin, Bosh and GM that have been focusing on integration of SOFCs as a power generating system for their technologies [14].

2.1.5 SOFC thermodynamic and heat sources

2.1.5.1 Thermodynamics

There is an energy balance expected in the energy conversion process of a SOFC including power generation, heat loss/sink, and chemical reactions. The overall fuel cell reaction given in equation (3) is the reaction which generates the maximum available power by converting the fuel chemical energy into electrical energy. This energy change is defined by Gibbs free energy equation (6) [59]:

$$\Delta G = -nFE_r \quad (6)$$

Where ΔG is the change in available free energy, n is the number of moles of electrons, F is the faraday constant (96,487 C/mol) and E_r is the reversible voltage (V). The obtained free energy varies depending on the states of the reactants and products. For instance, an increase in temperature leads to a decrease in Gibbs free energy as a result of changes in obtained reversible voltage E_r . The total energy of the reactants on the other hand can be given in the changes of enthalpy ΔH which is the amount of entire heat released due to the reaction. Thus the ideal/reversible efficiency of the reactions (ε_R) can be given in equation (7) [59].

$$\varepsilon_R = \frac{\Delta G}{\Delta H} \quad (7)$$

However, the state of the reactants and products of the reaction are not constant during SOFC operation. For instance, their partial pressure varies depending on their utilisation rate. In this regards, the Nernst equation is performed to obtain the corresponding reversible voltage as given in equation (8) [59].

$$E_r = E_o + \frac{RT}{2F} \ln \left(\frac{P_{H_2} P_{O_2}^{1/2}}{P_{H_2O}} \right) \quad (8)$$

Where E_0 is cell potential under standard conditions (1 atm at 25 °C), R is the gas constant (8.314 J. K⁻¹ .mol⁻¹), T is the operating temperature, and P_{H_2} , P_{O_2} and P_{H_2O} are the partial pressure of H₂, O₂ and H₂O respectively [105].

However the actual cell voltage E_{cell} can be defined as $E_{cell} = E_r - E_{loss}$ after the impact of all the irreversible losses/polarizations (mentioned in section 1.2.3.1) on E_r are taken into account.

2.1.5.2 Heat sources

2.1.5.2.1 Heat correlated with chemical reactions

As mentioned earlier different hydrocarbons including methane (CH₄) can be used as the fuel in SOFC system, and each individual reaction contributes to the heat balance of the system. Methane internal reforming and water-gas shift reactions, as shown in equation 9 and 10 respectively, are the main chemical reactions taking place during SOFC operation [106]. The supplied methane reacts with the steam at the anode and produces carbon monoxide and hydrogen as products. The produced carbon monoxide (CO) reacts with steam and produce hydrogen as well. The produced hydrogen reacts with oxygen ions and produce heat and electrical power. The internal reforming reaction and shift reaction can be shown, respectively, as follows:



Methane internal reforming is considered as the most dominant reaction associated with heat sink due to its endothermic reaction with steam while there is heat released during exothermic reactions [107]. There is more of a drop in temperature due to reforming observed at the fuel inlet of the anode electrode along the cell surface. At the anode current collector which is located on the cell surface which is parallel to anode catalyst layer between the anode and electrolyte where the electrochemical reaction takes place. In addition to this a little amount of methane reforming reaction can also take place in the fuel channel depending on the operating temperature which increases with the increase in temperature especially after 800 °C. The methane

reforming reaction is endothermic (enthalpy of reforming reaction $\Delta H_{ref} > 0$) while the shift reaction is an exothermic reaction (enthalpy of shifting reaction $\Delta H_{sh} < 0$). The heat released/sink from the chemical reactions can be computed by applying equation 11.

$$Q_c = R_{ref}\Delta H_{ref} - R_{sh}\Delta H_{sh} \quad (11)$$

Where Q_c is the volumetric chemical heat source as the released heat depends on the methane utilisation ($\text{J/m}^3\text{s}$), R_{ref} and R_{sh} are the rates of the reforming and shift reactions, respectively, based on the molar change of CH_4 and CO , and ΔH_{ref} and ΔH_{sh} are the corresponding enthalpy changes.

2.1.5.2.2 Heat correlated with electrochemical reactions

Hydrogen oxidation as the overall electrochemical reaction is the main reaction for power output and heat release from SOFC operation. Electrochemical reactions are key to understanding SOFC operation and the main sources for heat production [106], [108]. This is because the oxidation of hydrogen reaction which is earlier mentioned in equation 3 in section 2.1.1 is considered as the driving reaction for energy conversion in SOFC systems.

Even though the global approach regarding the heat associated with the electrochemical reaction is assigned to the anode side TPBs, actually there are two semi-reactions that take place [109]. First there is the hydrogen oxidation reaction at the anode TPBs (exothermic) and second the oxygen reduction reaction at the cathode TPBs (endothermic). The hydrogen oxidation and oxygen reduction semi-reactions have already been explained in equation 2 and 1 in section 2.1.1.

Overall the electrochemical reaction is assumed as the exothermic reaction due to the small effect of the anodic endothermic reaction [107]. Therefore the available work and the released heat from the electrochemical reaction can be calculated (shown in equation 12 and 13), respectively, as follows:

$$\Delta G_r = \Delta H_r - T\Delta S_r \quad (12)$$

$$Q_r = R_r\Delta H_r - 2FR_rE_{cell} \quad (13)$$

Where the subscript r refers to the electrochemical reaction and the term $(T\Delta S_r)$ is the entropy change related to the released heat as a result of the reaction, ΔG_r is the reaction Gibbs free energy and ΔH_r is enthalpy of the reaction while Q_r is the released heat, R_r is reaction rate E_{cell} is the potential of the reaction. The net heat is the difference between the total available heat (first term of equation 13) and the corresponding heat converted into electrical energy (second term of equation 13).

2.1.5.2.3 Joule heating or ohmic heat loss

Apart from the chemical and electrochemical reactions, there is another heat source known as joule heating. Due to resistance to the transformation of ion and electrons in the electrolyte, electrode and interconnect or current collector the heat produced, which is called joule heating or ohmic losses, contribute to the cell operating temperature [110]. It has less of an impact on the temperature gradient due to its smaller contribution compared to the heat related to the electrochemical and chemical reaction (Table 1). The heat due to ohmic losses can be written as shown in equation 14.

$$Q_{ohm} = \frac{1}{\sigma} j^2 \quad (14)$$

Q_{ohm} is the local heat source and j is the current density while σ represents the material conductivity.

In addition to the heat sources that have been mentioned above, the activation and concentration polarisation as irreversible losses as well as heat from the resistance to the current collection mechanisms are other contributors to the heat generation in an SOFC system. The activation losses which are negligible for high temperature SOFCs occur due to the barrier (resistance) of the electrochemical reactions while the concentration losses are related to the unbalance between the supplied and consumed fuel/air. The heat due to resistance to current collection mechanisms has not been involved as well due to high electrical conductivity of used silver mesh. The impact of the heat sources on the SOFC system are summarised and depicted in Table 1. As seen from the table electrochemical reaction is the more dominant contributor which is followed by chemical reaction and polarisation losses respectively while the lowest impact is made by ohmic losses.

Table 1 Reactions and corresponding heat released in SOFC system [110]

Mechanism	Location	Heat source/sink	% relative contribution
Chemical reaction	TPB anode side	Sink	33
Electrochemical reaction	TPB anode and cathode side	sink and source	47
Polarisation losses	Electrode reaction sides	Source	17
Ohmic heating	Solid cell component	Source	3

2.2 SOFC Degradation Mechanism

2.2.1 Soft failure

Cathode chromium (Cr) poisoning due to interconnect materials is the most widely known soft degradation mechanism for cathode which plays a key role for whole cell performance. While redox instability, carbon deposition and Ni agglomeration induced Ni-coarsening are the main soft degradation modes for Nickel (Ni) based anodes. The soft degradation mechanism can be reduced with the alteration of testing condition such as changing the rate of supplied gases. In the case of using a metallic alloy based interconnect material rather than a ceramic interconnect due to their higher electronic and thermal conductivity, there is oxidation occurring due to the high operating temperature of SOFCs [84]. Thus increasing the amount of Cr content is seen as a possible solution due to its higher resistance to oxidation. However, the interaction of the Cr^{+6} with gaseous and cell materials leads to serious degradation in the cathode material due to blockage of O^{2-} penetration [111].

Redox cycling is considered as an important limiting factor for SOFCs operating time range especially for long term operation. The impact of the redox cycle is more serious if the cell consists of a thick anode and a thin electrolyte. Since there is

shrinkage experienced the anode is reduced and then expansion occurs when the anode is re-oxidised. These volume changes in the anode electrode leads to micro-cracks in both the anode and electrolyte, especially in the case of using the Nickle yttria stabilised zirconia (N-YSZ) anode and the thin YSZ electrolyte, resulting in performance degradation [47].

As outlined earlier, the anode is another important component of the cell facing soft degradation issues. Carbon deposition as a result of segregation of contaminants is a serious issue for anode materials primarily for the anode active layer (TPBs) and also for stack components such as the interconnect and sealant [112]. Since the impurities penetrate through the anode active layer and accumulate in the vicinity of where the cell electrochemical reaction mostly takes place this leads to deterioration in the cell electrochemical activities. Eventually it negatively affects the reactant penetration due to changes in morphology of the electrode since the porosity of the electrode is reduced with the presence of impurities. Ni coarsening which is also known as Ni agglomeration is another detrimental degradation mechanism seen at the anode [113]. Due to the agglomeration of the Ni particles by diffusion of these particles or Ni movement in the gas phase the electrode suffers a Ni-Ni contact loss after operation. The impact of the agglomeration based degradation can be altered depending on the operation condition including changing the operating temperature or composition of the supplied fuels [114].

2.2.2 Hard failure

Apart from the soft failure mechanisms cracking and delamination of both the stack and the cell components are the main mechanisms for failure. The experiences of hard failures are generally irreversible and result in whole system failure. The hard failure mechanisms correlated with the cell components due to temperature related operating conditions is the main focus in this study. There are different driving factors leading to cracks in the cell components such as weaknesses of the used materials, uneven composition and sintering related parameters of the cell materials. These impacts are more severe at high operating temperatures. Delamination, on the other hand, generally occurs between two different layers when there is a thermal expansion mismatch and a thermal gradient occurs between the layers. Both failure

mechanisms, cracks and delamination, are directly affected by the operation temperature. Technical issues like mechanical durability, sealing, and thermal expansion mismatch are typically induced by the SOFC's high operational temperature including the lengthy heating and cooling periods during power on and off [115]. The significant challenge is the lack of control of the system during heating and cooling, these phases being when the likely cause of deterioration of the system's performance is observed and cause more severe irreversible damage to the cells/stacks that will ultimately fail the whole system. Therefore, better temperature management of the system from cell to stack level plays a key role in minimising temperature correlated performance deterioration. In this study, temperature characteristics of the SOFC will be investigated at the cell level under real operating conditions by using a nascent sensor.

2.3 SOFC Temperature Measurement

Why important?

Temperature management of the SOFC is of great importance so as to not sacrifice the benefits provided by high operating temperatures and prevention of the high temperature correlated performance degradation. Both soft and hard degradation mechanisms are directly and indirectly related with the high operating temperature. Furthermore the degradation is more severe especially for the hard degradation mechanisms in the presence of a thermal gradient across the cell, as well as between the cell components, which can lead to whole system failure. Thus understanding the temperature distribution of SOFC during operation is a key step for effective temperature management. For instance thermal stress, as a kind of hard failure degradation, induced by the high operating temperature and thermal gradient across the cell due to different CTE of the cell components leads to micro-scale cell component cracking and sealing related problems, and eventually results in performance degradation or system failure [116]. Numerous research efforts have been made on numerical modelling based work to predict the temperature distribution of the SOFC while only a limited number of experimental works is available in the literature [13].

Due to structural (cell components which are severely ductile especially for those in the planar configuration with a whole thickness of <1 mm) and operational limitations (limited access to the cell due to being a closed system), numerical modelling has become a commonly applied method for identifying the parameters in correlation with SOFC performance including prediction of temperature distribution during operation [117]–[121]. It is common in almost all modelling studies that there is a non-negligible intrinsic stress caused during the manufacturing process which affects the overall stress when the cell heated up [122]. Due to intrinsic stress there can be cell failure occurrence depending on the cell configuration thus this is an important parameter for determining the thickness of cell components. Fan et al. [120] studied the relationship of temperature stress on the positive electrode-electrolyte-negative electrode (PEN) by developing a 3D model based on finite element analysis (Abaqus). It used a stress calculation and computational fluid dynamics (CFD) for determining the governing equations including mass transport, momentum, species, energy and electrical potential methods. The model comprised different geometries with different types of induced polarisations in the case of both electrochemical and chemical reactions. They revealed that there is a uniform compressive stress (intrinsic) of -600 MPa over the electrolyte at room temperature while the anode experiences larger stress than the cathode. There is about a 20 % relaxation observed on the anode tensile stress (reduced by about 50 MPa) and electrolyte compression stress (reduced similar to the anode) after the anode reduction. There is negligible variation in the electrolyte and cathode intrinsic stress by increasing the anode thickness while detrimental stress changes occur on the anode by increasing the electrolyte thickness [122]. The maximum principle stress in the electrolyte is increased with the increase in temperature due to variations in CTE of the components with uniform temperature distribution. There is more tensile stress occurring on the electrolyte near the gas outlet due to higher temperatures since the temperature is higher at the outlet due to the exothermic reaction in the case of co-flow in which fuel and air are sent from same side. The maximum tensile stress is occurring at the fuel inlet when the counter-flow arrangement is used. This is shown clearly by the study that the temperature gradients across the cell surface affect the thermal stress of electrolyte.

Currently applied methods:

Xu et al. [123] also developed a simulation model to identify thermal stress fields caused by uneven cell temperature distribution due to electrochemical reaction in an anode supported planar SOFC by taking into account the governing equation for the parameters that have an impact on temperature distribution. According to the result of the simulation, reasonable compressive residual stress was observed in the thin electrolyte while small tensile stress was observed in the anode. The stress values found were greater with the counter-flow compared to the values with co-flow. This meant that the flow configuration (co-flow, counter-flow and cross-flow) have been identified as one of the important design parameters of SOFC as it has an important impact on its temperature distribution [124]. Depending on the flow type it might be possible to diminish the temperature gradient of the cell or even stack. In this regards, Fardadi et al. [125] also investigated the effect of traditionally used flow types and non-uniform air flow on the temperature gradient of the SOFC. The results agree with the results obtained from the previously mentioned studies that the highest temperature difference was observed with the cross flow configuration while the lowest distribution was obtained with counter-flow types. On the other hand, non-uniform air flow provides a smoother temperature profile with about 3% reduction in efficiency, a similar result observed earlier by Yuan and Liu [126].

The numerical studies provide key information for factors including current density and flow configuration as the main contributors to the temperature distribution of SOFC, as well as uneven temperature induced thermal stress. Additionally, the numerical analysis is required to validate the experimentally obtained data with the benefits of not requiring high cost or long-time duration [127]. However, Schlegl and Dawson [127] also emphasize the importance of the experimental validation of the results obtained from numerical analysis. This is because there is a difficulty of having reliable inputs including Young's modulus, Poisson's ratio, and the thermal expansion coefficient which can vary depending on the fabrication process for the numerical analysis. Aydin et al. [128] claim that further validations of the reliability of conventional I–V (current-voltage) curve based numerical studies are required. This is because some average values are used as the main parameters for investigating the relationship between temperature variation and current. Therefore the validation of the parametric numerical studies with experimentally obtained data

has vital importance underlying the need for experimental measurement of SOFC temperature distribution.

Temperature distribution measurement of SOFC cell or stack has been generally carried out by conventional TCs as an experimental method [129]–[131]. For example, Guan et al. [130] investigated the effect of gas flow on the temperature of a stack of three anode supported planar cells (active area of each cell is 100 cm^2) by placing five TCs into the cell unit throughout the sealing material as depicted in Fig. 16. The measuring probe of the TCs are pasted to interconnects where TC 1, 2 and 4 are located at the air inlet side of cell A, B, C respectively while TC 3 is located at the air outlet of cell B and TC 5 is located at the hydrogen outlet.

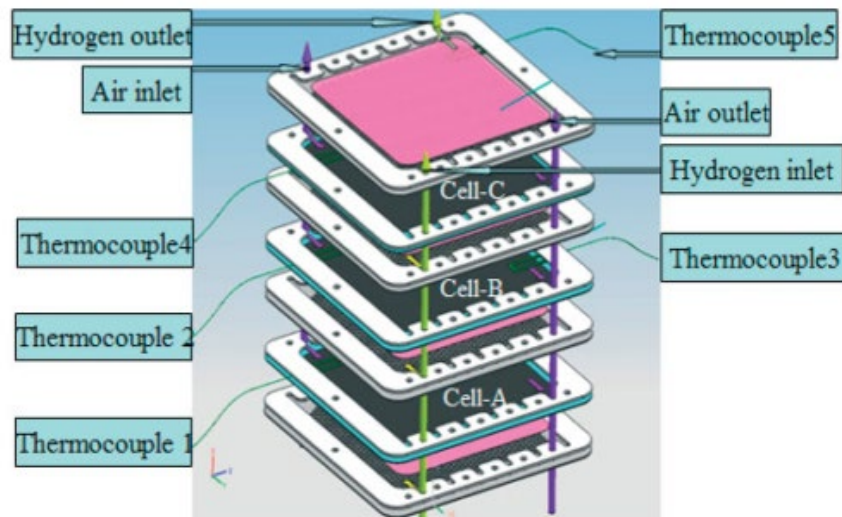


Fig. 16. Stack assembly with three cell and inserted TCs [130]

As a result of the experiment the highest temperature increment is monitored from TC 3 at the outlet when the system is not loaded since the gas is heated during its travel whilst the lowest temperature occurred at the inlet (TC 1) ($\sim 25 \text{ }^\circ\text{C}$ difference). When the system is loaded there is about a $200 \text{ }^\circ\text{C}$ temperature difference occurring between TC 3 and TC 5 especially for the transient condition before the system reaches steady-state condition. Thus it is pointed out from the study that the impact of the fuel flow is too small compared to the impact due to loading. Celik et al. [36] used five TCs to investigate the relationship between temperature and voltage-current characteristics of a short stack (less than three cells) with two different sized

cells (active area of the cells are 16 cm^2 and 81 cm^2). They inserted TCs through the anode interconnect at five different locations as seen in Fig. 17. In almost all experimental temperature measurement of SOFCs with TCs, the TCs are located near the interconnect either pasted on it or located in the flow channel due to limited available space in SOFCs system. TCs were also located in the flow channel of interconnects during the study conducted by Celik et al. [36].

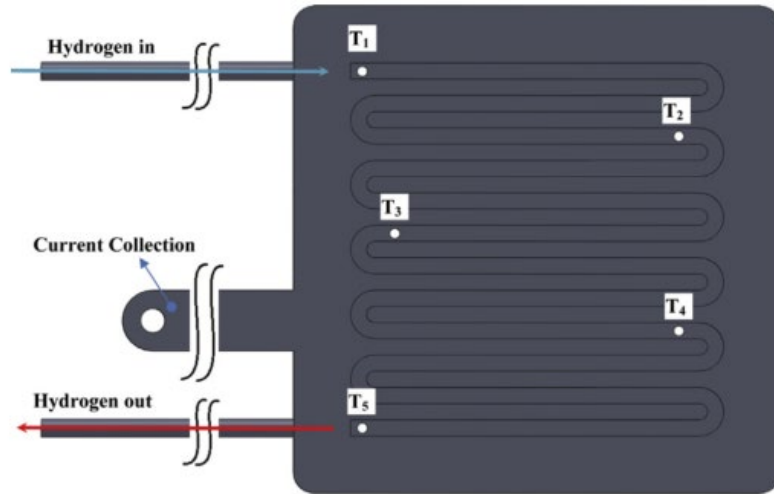


Fig. 17. Placement of the inserted thermocouples on the anode interconnect [36]

They investigated that there was no observed temperature gradient on the small cell (16 cm^2) whilst a higher temperature was obtained at the anode inlet compared to the cell's other parts ($11 \text{ }^\circ\text{C}$ difference) with the larger cell (81 cm^2) under the same experimental conditions with a current density of $0.25 \text{ A (amps) cm}^{-2}$.

Razbani et al. [132] studied the influence of oven temperature and current density on the temperature distribution of a stack consisting of six planar cells by inserting five TCs in the gas flow channels of an interconnect in the middle of the stack (Fig. 18 (a)). As shown in Fig. 18 (b), four TCs were placed at each corner whilst one of them was placed in the middle of the interconnect to monitor temperature variation at different locations of the cell.

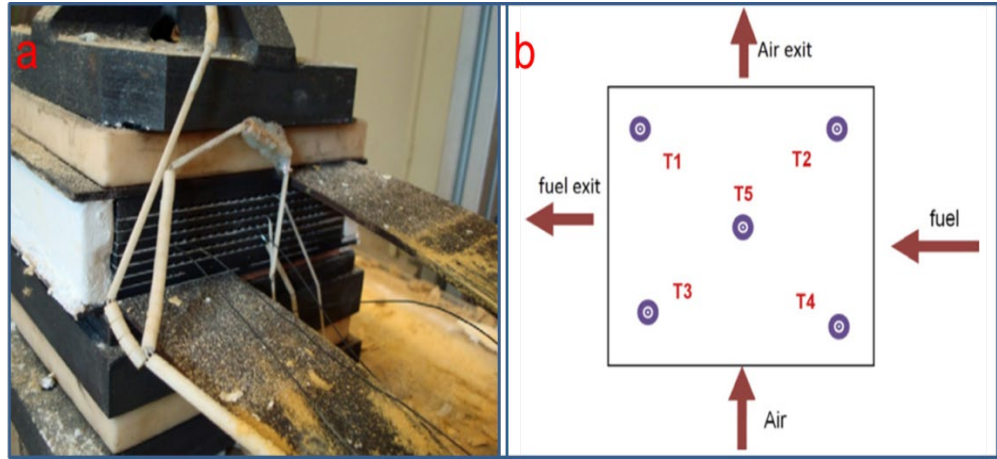


Fig. 18. a) TCs inserted stack and b) location of the inserted TCs [132]

It is determined from the study that there was a strong dependency of temperature distribution on current density where the temperature increased with the rise in current density. Maximum temperature was obtained by the T5 and T2 sensors located closer to the fuel inlet (a similar result found in study [36]). The temperature distribution along the cell surface, on the other hand, was diminished with the increase in oven temperature eventually turning into a more uniform cell surface temperature.

The main drawbacks in real-time temperature sensing with conventional TCs are limited available space in the SOFC stack, and the possibility of disturbance to the cell operating environment. Therefore, TCs are generally placed in the gas flow channels of the interconnect materials during measurement meaning that the TCs tips are 2-3 mm above the cell surface. This leads inevitably to a consideration of reliability of the obtained temperature distribution measurement [42]. In addition the individual contribution of parameters affecting the temperature distribution of the cell or stack cannot be easily identified and have not been fully experimentally investigated. In order to monitor temperature distribution of the SOFC during its operation, experimental set up and materials including manifolds used, temperature sensing sensors, signal collecting items or their functionalities need to be improved. These improvements can be a key factor to diminish the limitation caused by the SOFC harsh operating environment and its sensitive structural characteristics. In this regards, there is some attempt [133] made by applying a recently developed thin

film sensor array and analysing its durability at SOFC operating temperatures. In the study, thermocouple thermo-elements were directly deposited on the cell surface and their physical durability is analysed at SOFC operating temperatures. Crack formation on the deposited thin film thermo-elements were observed after the test.

Other experimental techniques also known as non-destructive methods including acoustic emission, X-ray computed tomography, and X-ray fluorescence, IR sensing/imaging have been considered for SOFC temperature measurement [39]. However, these techniques are only applicable in the case of ex-situ measurement and require specific modification of the SOFC stack [134]. It is also claimed that the achieved resolution with IR sensing for SOFC temperature measurement is poor and not effective at high operating temperatures ($> 500\text{ }^{\circ}\text{C}$) [135]. As a summary of the written information about the methods for temperature measurement, the advantages and weaknesses of the three generally applied methods including numerical analysis, experimental measurement with sensory techniques and experimental measurement with optical techniques is given in Table 2.

Table 2 Pros and cons of the methods used for SOFC temperature sensing

Methods	Advantages	Disadvantages
Numerical analysis [136], [127]	Inexpensive, easy, applicable for variety of shapes and sizes of cells	Some assumption used, needs further validations
Sensory method (TCs) [42]	In-situ measurement High resolution Inexpensive	Limited space for placement in SOFC system, some small modification required
Optic methods [39], [134], [135]	In-situ measurement Reasonable resolution	Limited access to the working cell, high modification is needed on the SOFC system, Expensive

2.4 Chapter Summary

The SOFC working principles and its main components have been explained in the current chapter. The specifications of the components including anode, cathode, electrolyte and interconnect; along with the materials used and their performance for those components were also discussed. It is found that the high temperature is a limiting factor for the material selection as well as for design of the SOFC system. Thus, SOFC thermodynamics and the heat sources in correlation with the electrochemical and chemical reactions have been explained. In addition to this, a literature study has been carried out to identify the current effort on temperature management of the SOFC as key factor to minimise SOFC temperature induced degradation. During the survey three methods were identified for temperature measurement: numerical; experimental using sensory methods; and experimental using optical methods. All methods have their own advantages and disadvantages which were also addressed. Even though a great number of studies have been made based on using a numerical analysis, a fewer number of studies have been conducted with sensory and optical methods. This is because of difficulties in application of the sensory method while the high cost for system modification and limited access to the working SOFC are the main barriers for the optic method. Furthermore there is still a lack of understanding of temperature distribution of an operating SOFC cell/stack by using TCs. The reason for this is the ineffectiveness of the implementation of the TCs which is generally placed in the flow channel of the interconnects. Hence the gap identified is the lack of an effective sensory technique to monitor the temperature distribution of SOFC with high temporal and spatial resolution without disturbance to the operating environment, which is the focus of the thesis. The implementation of the sensor as it will be directly applied to cell surface and the benefit from its architecture which it requires less number thermal elements even for the same number of sensing points compared to the conventional TCs are the two main novelty of the proposed measuring method.

Chapter 3:

Experimental methodology

3.1 Overview

SOFC electrode temperature distribution is required to be identified for better understanding of the temperature related degradation influencing SOFC performance. The main limitations of the currently available concept for in-situ temperature measurement of SOFCs by sensory methods (TCs) are the limited space available and difficulties in implementation of the TCs inside an SOFC system. Therefore, a recently developed multi-array sensor, which can be fabricated in either thin film or thin wire form, will be used in this study. Due to its architecture it reduces the required number of sensing points required over the number needed when using conventional TCs. The implementation of this sensory technique offers SOFC temperature distribution monitoring directly from the cell surface rather than from the flow channel. Using this implementation method it is proposed to increase both the temporal and spatial resolution of the obtained temperature. To achieve this, a new implementation concept was crucial due to the limited space available and harsh environment of the SOFC system during operation. The sensor will be fabricated firstly in the thin film form and secondly in the thin wire form. A sensor with thin film form offers potentially a faster response time resulting in better temporal resolution with the limitation of its durability on the porous cell surface. While the thin wire formed sensor produces a slower response time than the thin film form but still faster than the conventional TCs based sensing due to its improved implementation, being more closely embedded into the cell. Even though it is in thin wire form the sensing points will be in direct contact with the cell surface which leads to higher temporal and spatial resolution of obtained temperatures compared to the TCs based measurement. The developed experimental apparatus and new implementation methods are fully documented in the current chapter' subsections.

3.2 Materials

Commercially available 50 mm \times 50 mm sized anode supported (Fuelcellstore, US) square SOFC planar cells are used during SOFC operation in the study (Fig. 19 (a)). As mentioned in chapter 2, there is more risk for a crack based failure with an electrolyte supported cell due to the intrinsic stress in thin anode layer. Thus to minimise these failures caused by intrinsic stresses an anode supported cell is chosen the thickness of the anode means the electrolyte strength is enough to survive compression stresses. As seen from the cross sectional view shown in Fig. 19 (a) the cell consists of a thin electrolyte (20 μm) with relatively thick anode (600 μm) and cathode electrodes (60 μm). On the other hand an electrolyte supported cell (Fig. 19 (b)) is used for the thin film sensor durability test due to its higher strength without inserting the cell into the manifold. During this test the cell is used as a support material thus a mechanically more stable cell (electrolyte supported) is chosen. The sizes of the cell are the same for both anode and electrolyte supported cells with 16 cm^2 active area. There are two reasons for using such a sized cell. Firstly, this study is a continuation of work where a 50 mm \times 50 mm sized cell has been used. Secondly and more importantly this small cell size provides the benefits of having more difficult measurement characteristics (due to the size/space limitation) for temperature distribution acquisition. Thus it is envisaged that if this cell demonstrates measurement capabilities these capabilities should be realised in larger sized cells which do not have these space limitations. As seen from the cross sectional view of the electrolyte supported cell the thickness of the electrolyte is almost double the thickness of the electrodes (50 μm). In addition to this, once the thermal sensor is tested with electrolyte supported cell in terms of its implementation and stability, an anode supported cell with the same sizes will be tested due to the potential benefit of anode supported cell as early mentioned in the literature chapter. Anode supported cell with thin electrolyte will provide more chance to monitor thermal induced issues such as small crack, electronic and gas leakages related oxidations.

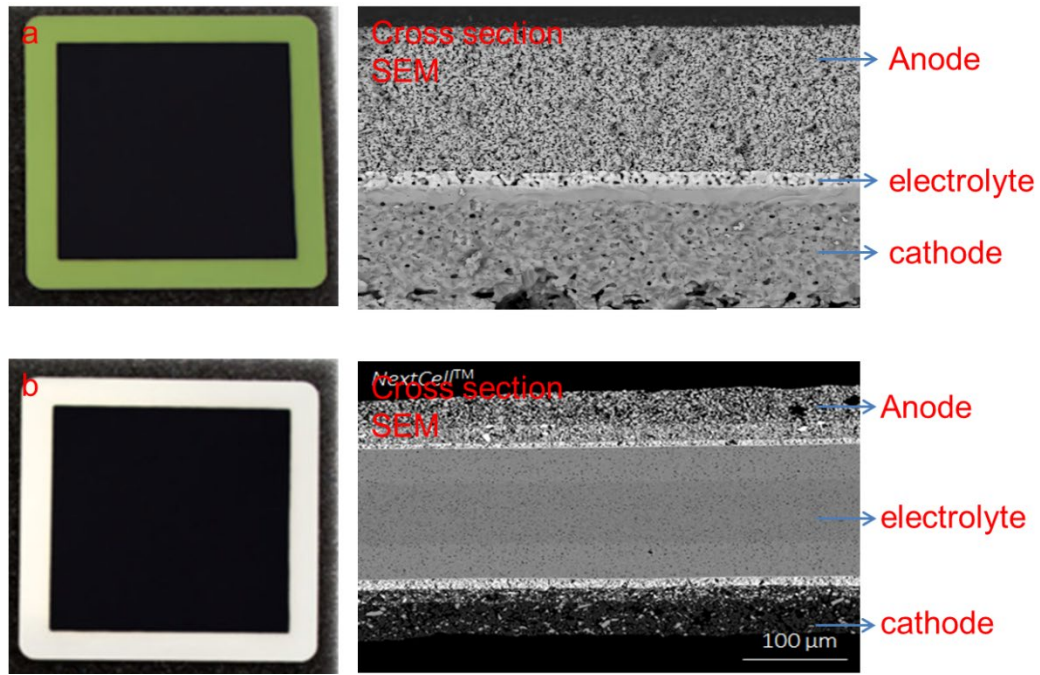


Fig. 19. a) Planar anode supported and b) electrolyte supported SOFC with their cross sectional SEM views

Fig. 20 shows the purpose designed manifold which has a unique feature of having more holes on the cathode side (machined by Precision Ceramic Company, UK). The manifold which is made of Macor and consists of upper and bottom parts is specifically designed for 50 mm × 50 mm square cells only and used with mica based gasket (Flexitallic Ltd., UK) to prevent gas leakages. The shapes of these gaskets are illustrated in Fig. 21. These gaskets, which contain glass powder, are specifically designed to serve SOFCs applications with low compression stress (less than 0.1 MPa), which is a characteristic of the chosen cell. The manifold-cell-sensor integration is explained in detail in chapter 5.

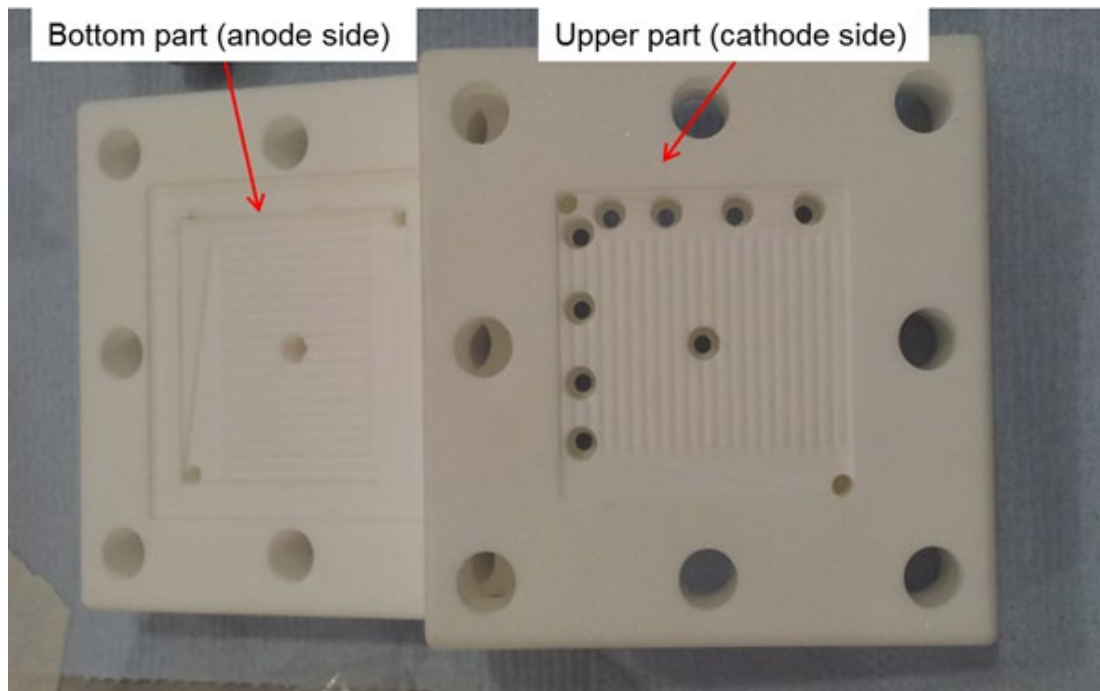


Fig. 20. House-made Macor SOFC manifold bottom (left) and upper (right) parts

The materials chosen to be used as sensor thermo-elements are alumel and chromel to form K-type thermal pairs. The wider operating temperature range, comparatively lower prices, higher and linear Electromotive Force (EMF) characteristics are the main reason for choosing the K-type thermocouple types (National Institute of Standards and Technology (NIST)). The conventional thermocouples (seen in Fig. 21) are used during operation together with implemented sensor for comparison and also for validation purposes of both sensor and TCs by comparing the obtained results at different temperatures. Furthermore, as mentioned earlier TCs are the generally applied sensory method for SOFC temperature sensing from the fuel flow channel. In this study the sensor will be mounted on the cell surface. By doing this, the effectiveness of the applied technique in terms of its measurement resolution will be monitored. Additionally the obtained temperature reading and the results from the conventional TCs will be compared.

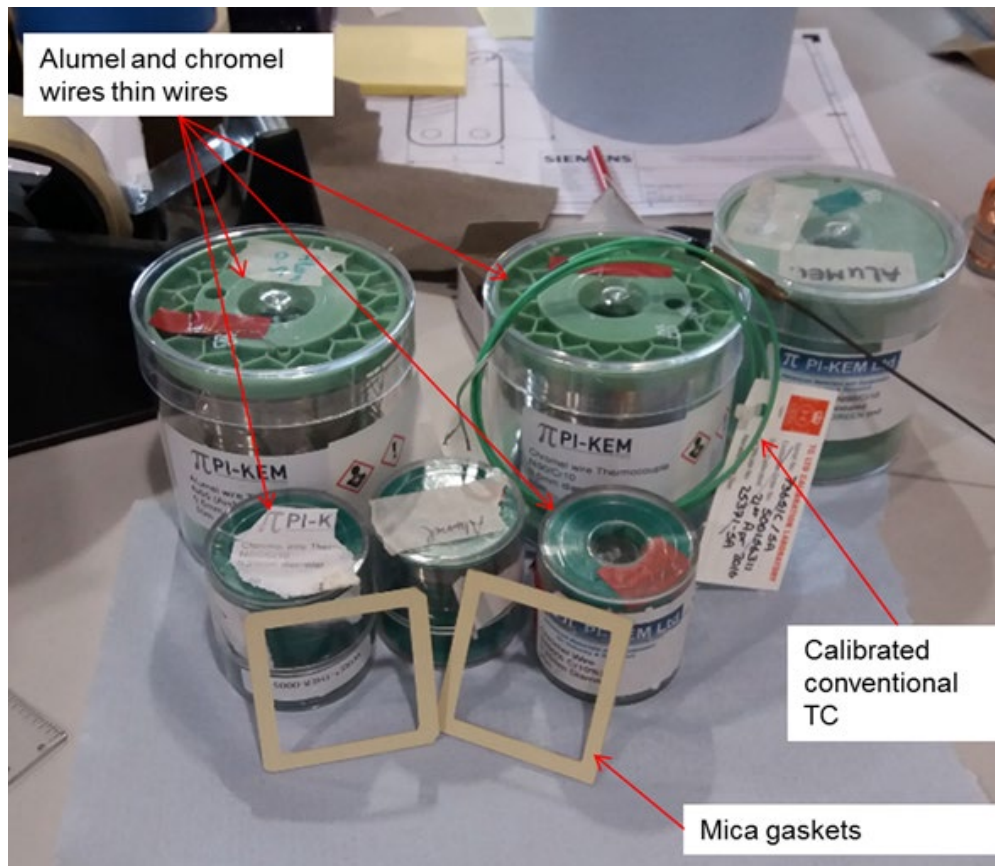


Fig. 21. Alumel and chromel thin wires in different diameters, mica shape cut gasket and calibrated conventional TCs

The desired architecture of the sensor in thin film form is achieved by performing a TS150 magnetron sputter (Quorum Technologies, UK) while the spot welding method is applied to fabricate the thin wire formed sensor. The sputtering is considered as an effective technique to have a uniform metal film deposition while spot welding (which has two small tips to weld/bold such thin wires) is generally applied to join the small sized wires. The alumel and chromel thermo-elements materials are sputtered from the alumel and chromel target material under vacuum conditions and a metal mask is used for shaping the structure of the sensor. The set up for the sample to be pattern deposited is shown in Fig. 22. The sample is placed in the vacuum chamber on a rotary support which rotates during sputtering to enable uniform film deposition. The touch screen is used for data entry of the specific target material while the sputtering head is where the target material is held. The spot welding machine, on the other hand, is used to create the multi-junction sensor array

by welding the thin alumel and chromel wires at the desired points to generate the desired sensor structure.

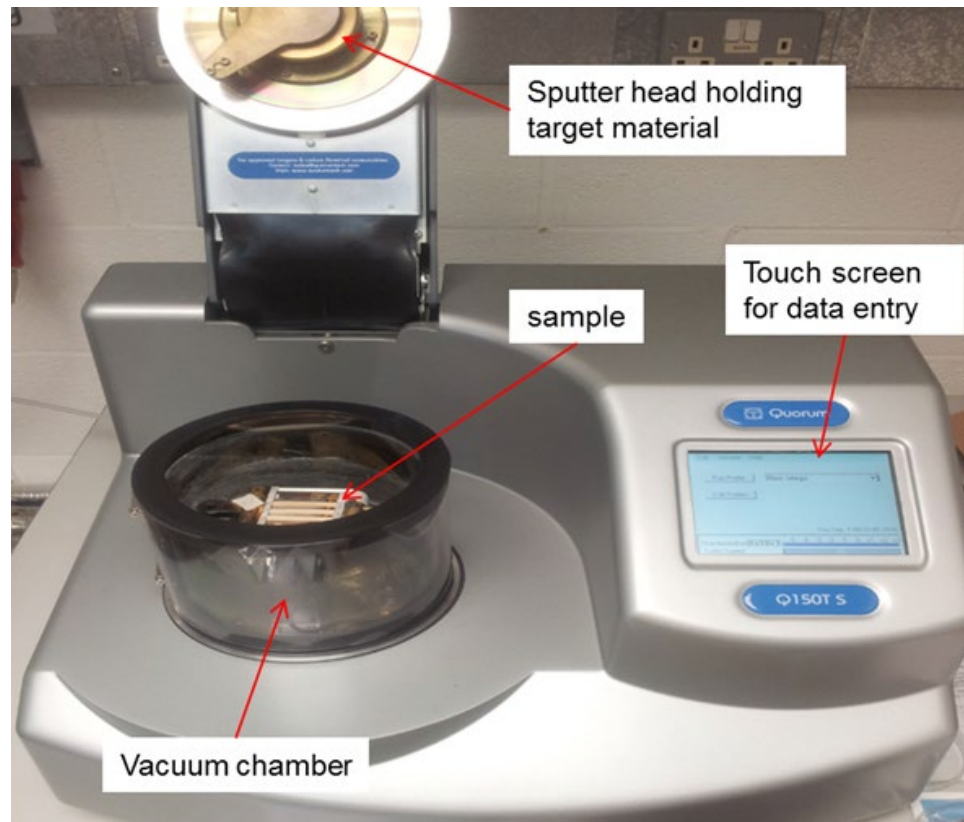


Fig. 22. Set up for a sample placed sputtering machine

To bond the wired sensor to the cell surface in the case of using thin wires as sensor thermo-elements and the external wires to the thin film sensor pads (pads and thermo-elements obtained by applying sputtering method), alumina paste (Ceramobond™ 552, Aremco Inc.) and silver paste (Pyro-Duct™ 597-A, Aremco Inc.) are used respectively. Silver paste and alumina paste are required to be cured at 100 °C over a 2 hour period then heated up to 350 °C. These are then dwelled for 2 hours to complete the alumina curing process. A manually controllable high temperature box and horizontal furnaces are used to heat the cell to the required SOFC operating temperature. For curing purposes these are used whilst a vertical furnace is used for gas preheating. The box furnace is generally used for curing purposes due to its larger inside volume whilst the horizontal furnace is used to heat the cell to operating temperature since the manifold is well suited due to the two open sides of the furnace which allows connection of gas pipes and electrical wires.

3.3 Methods

3.3.1 Temperature sensing

A recently developed thermocouple array sensor is used in this study together with commercially available TCs for SOFCs temperature monitoring. The sensor works according to the Seebeck theory which is similar to conventional TCs in terms of their working principles. According to the Seebeck theory if two dissimilar materials are joined at one end and the temperature is different at the terminal (temperature at the terminal, T_T) there is an electromotive force (Seebeck voltage, V_{emf}) created at the terminal as schematically shown in Fig. 23. The electrical connection is made at the terminal and at the joint (temperature at the joint, T_J) where temperature measurement is made.

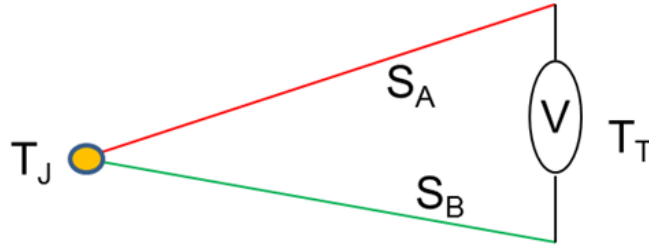


Fig. 23. Schematic of conventional thermocouple structure

Where, S_A and S_B are the Seebeck coefficients for materials A and B respectively. The Seebeck voltage (V_{emf}) for a basic TCs configuration (Fig. 23) is calculated as an definite integral of the difference between the Seebeck coefficients of two dissimilar materials with respect to temperature is given in equation (15). Equation (16) gives the relation between the Seebeck coefficient (S_i), temperature (dT) and voltage (dV) for a single material.

$$V_{emf} = \int_{T_J}^{T_T} (S_A - S_B) dT \quad (15)$$

$$S_i = \frac{dV}{dT} \quad (16)$$

Although the new sensor has similar working principles to the conventional TCs and the same thermoelectric laws are applicable, it is a multi-array sensor and different from TCs in terms of its architecture. It has a key advantage of requiring less thermo-elements even for the same number of sensing points which makes the sensor more applicable and a convenient technique for SOFC temperature sensing. This architecture thus addresses the fact that SOFCs have limited available space within the manifolds for sensor implementation for the cell level testing and within the stack for stack level testing. Different arrangements of the sensors are available:

- “N+1” : which requires “N+1” number of thermo-elements for “N” number of readings
- Grid structure which requires only “2N” number of thermo-elements for “N²” sensing points.

The arrangement of the architectures are shown in Fig. 24 with the connection pads which are larger in size for external wire attachments P_A to P_E for the N+1 architecture and P_A to P_F for the grid set up. Connection pads are where the electrical connection between the sensor and data collecting devices is made. Thus they were deposited larger in size to give some space to secure the connection of the external wires to the thin film.

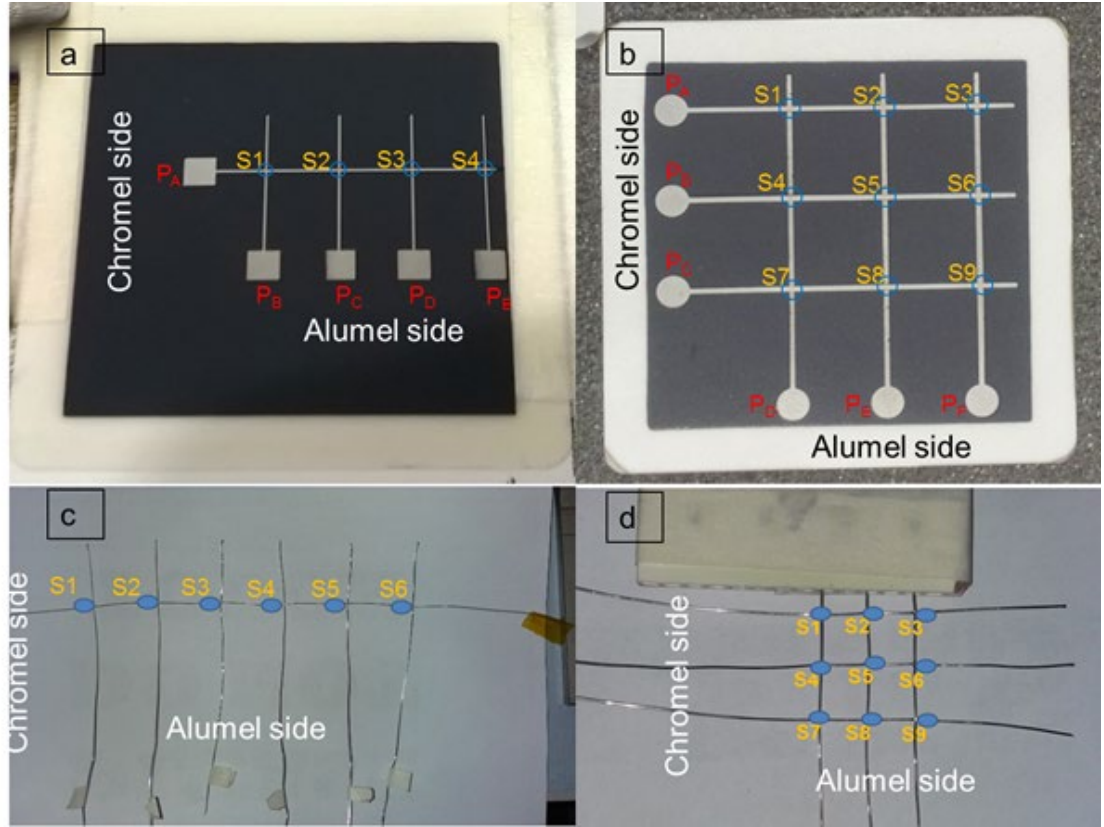


Fig. 24. Architecture of thin film (a) N+1 and (b) grid structured and thin wire (c) N+1 and (d) grid (P represents connection pads while S refers to sensing points)

As it can be seen from Fig. 24 the architecture (in both instances) is different from the conventional TCs structure (Fig. 23). One of the thermo-element is used as common thermo-elements such as chromel (Cr) line for N+1 shared with other thermo-elements (alumel lines) creating sensing points (S1-S4 for N+1). For the grid structure each one of the similar thermo-elements such as three chromel are shared with the three other alumel thermo-elements ((S1-S9 for grid) as depicted in Fig. 24 (d)). This provides more sensing points by minimising the required thermo-elements. The obtained voltage (V_{emf}) junctions are independent from each other due to the law of intermediate conductors [137]. According to this law the net absolute thermoelectric power generated between two dissimilar materials is zero if there is uniform temperature. The basic structure of a junction of the multi-junction sensor is demonstrated in Fig. 25 which illustrates the technical explanation of the sensor. T_0 is assumed as the known terminal temperature (temperature at the data logger) while T_1 and T_2 are the unknown temperature that can be calculated from the resultant

voltages between a-f and a-e respectively. T_0 is considered as the temperature near the data logger even though the external wires connection method is made at the cell surface. This has been deemed a valid assumption since the attached external wires are selected from the same corresponding thermo-elements materials to eliminate parasitic voltage contribution at the connection. Thus the effect of the isothermal zone is neglected since there is zero voltage generated due to the similarity of the Seebeck coefficients of the similar connected materials. This is only the case if the sensor used is in the thin film form. When the sensor is used in thin wire form, the wires thermo-elements are chosen to be long enough to reach the data logger without requiring any connection within the manifold. Two different thermo-elements which are represented with different colours are used in this measurement.

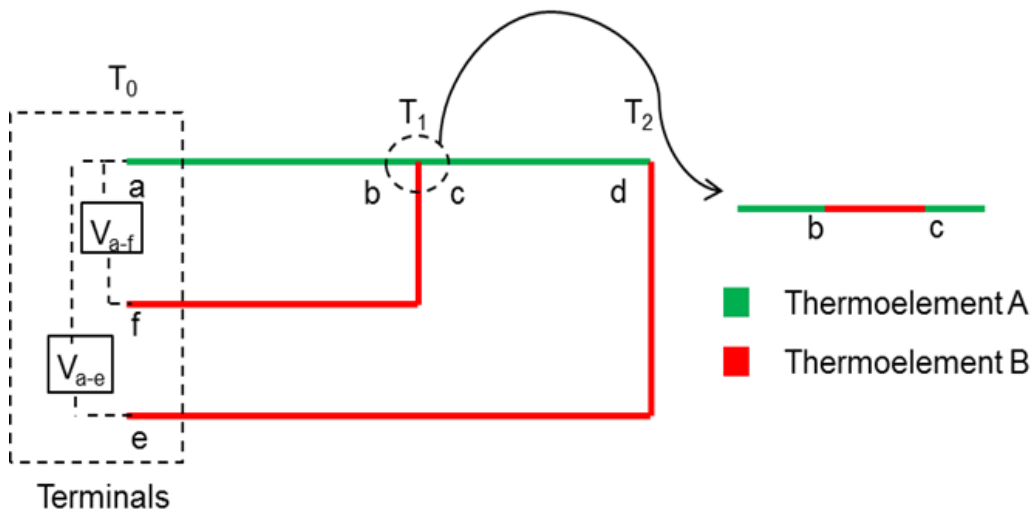


Fig. 25. Basic building block of multi-junction array

Technically, there is no effect from the inserted thermo-element from b and c between T_0 and T_2 as long as the temperatures are the same at point's b and c in which the distance between these two points is less than 0.2 mm. Therefore the temperature difference between these two points is assumed negligible.

The array structure is shown in Fig. 26 which is where the exaggerated view of the junction is presented with the materials Seebeck coefficient S_A , S_B and temperatures at inserted junction T_b and T_c . Without inserting b-c the architecture is a basic conventional TC block. Equation (17) and (18) show that there is no impact on the

obtained Seebeck voltage when another thermo-element is joined to the thermocouple junction in terms of thermoelectric's of the given thermal pairs.

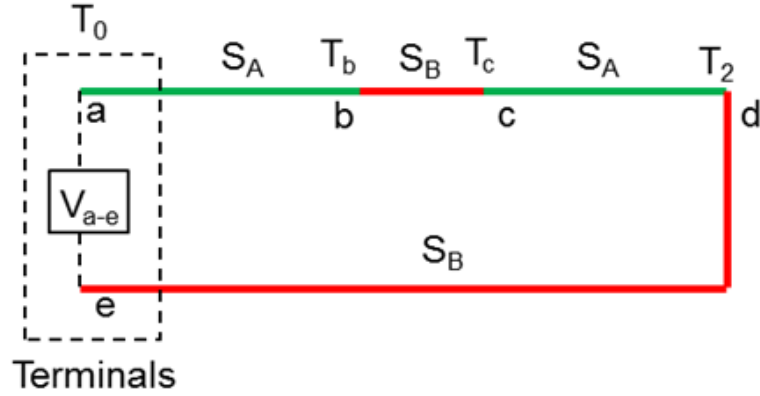


Fig. 26. Exaggerated view of the intermediate junction

$$V_{emf} = \int_{T_0}^{T_b} S_A dT + \int_{T_b}^{T_c} S_B dT + \int_{T_c}^{T_2} S_A dT + \int_{T_2}^{T_0} S_B dT \quad (17)$$

Where $V_{emf(a-e)}$ is the Seebeck potential between point “a” and “e” while “ S_A ” and “ S_B ” are the Seebeck coefficients for the related materials.

When the temperature for $T_b=T_c$ then the resultant Seebeck voltage is found as:

$$V_{emf} = \int_{T_0}^{T_2} S_A dT + \int_{T_2}^{T_0} S_B dT \quad V_{emf} = \int_{T_0}^{T_2} (S_A - S_B) dT \quad (18)$$

As seen from Fig. 26 and from equation (18) there is no impact on any other junction from the intermediate junction as long as the temperature is the same at the two sides of the added junction (The law of intermediate conductors). Since, according to the Law of intermediate conductors, the impact of the inserted material S_B depends on the temperature difference between T_b and T_c which is negligible due to small dimension (0.25 mm in dia.) of the inserted/joint thermoelement. Therefore it is vital to have the junction point as small as possible to avoid any possible thermal gradient at the junction point. In this respect, thin film deposited thermoelement comes into prominence because it gives the opportunity to have an efficient junction by adjusting the deposition techniques and the rate. The thickness of the used thermoelements were 500 nm with the width of 0.5 mm. Sputter operating temperature increase not more than 40 °C thus there was no chemical damage to cell

expected. The width of the deposited thermo-elements can be further reduced by considering its mechanical stability. As a result the minimum thickness where the thermos can survive needs to be determined to remove any junction related issues during operation at the harsh environment. Thickness of the used thermo-element and the position of the junction which should be perpendicular to the heat flow are the key parameters to reduce the impact of the heat transferred through the used thermo-elements. If there is a considerable amount of heat transferred via these thermoelements, this can lead to a considerable error in measurement. Thus the thin wire/film is used as the thermo-element for thin wire sensor fabrication in this study to minimise the error due to physical structure of the thermo-elements used. Additionally, the distance between each junction is kept as 10 mm which results in sixteen evenly distributed sensing points across the 40 mm x 40 mm cell electrode in the case of using a 4x4 grid architecture which is the number of maximum sensing points that the data logging system can accommodate. Moreover the temperature impact from one junction to another due to heat transfer via conduction or via thermo-element wires with a distance of 10 mm is calculated in the order of $10^{-4} \text{ W } \Delta K^{-1}$, i.e., negligible.

At this point using a thin wire (\varnothing 0.25 mm) provides benefits of having a mechanically and physically durable junction without requiring wire connection within the SOFCs system. Since there is no external wire attachment required to complete the electrical circuit between the sensor and data logging system when the sensor is used in thin wire form. The sensor is fabricated with 1 metre long wires' at one end and the other end of the wires is connected to the logger.

3.3.2 Characterisation

In order to visualise the surface features and oxidation rate through the thickness of the material used especially for the thin film sensor, some characterisation tests are carried out. Fig. 27 (a) shows the high resolution scanning electron microscope (SEM) used for surface characterisation of both deposited thin film sensor and cell electrode before and after operation. The porosity of the applied paste materials including alumina and silver paste for connection and electrical conduction purposes, respectively, and the cell electrode are also visually checked by applying the SEM.

In addition to this, X-Ray Photoelectron Spectroscopy (XPS) (Fig. 27 (b)) is used in element identification specifically for the oxidation state of the deposited intact and used thin film. The characterisation test helps to visualise the material physically in terms of its physical and chemical stability. Thus it will be proposed to visualise the oxidation state of the patterned thin film thermo-elements after its usage.

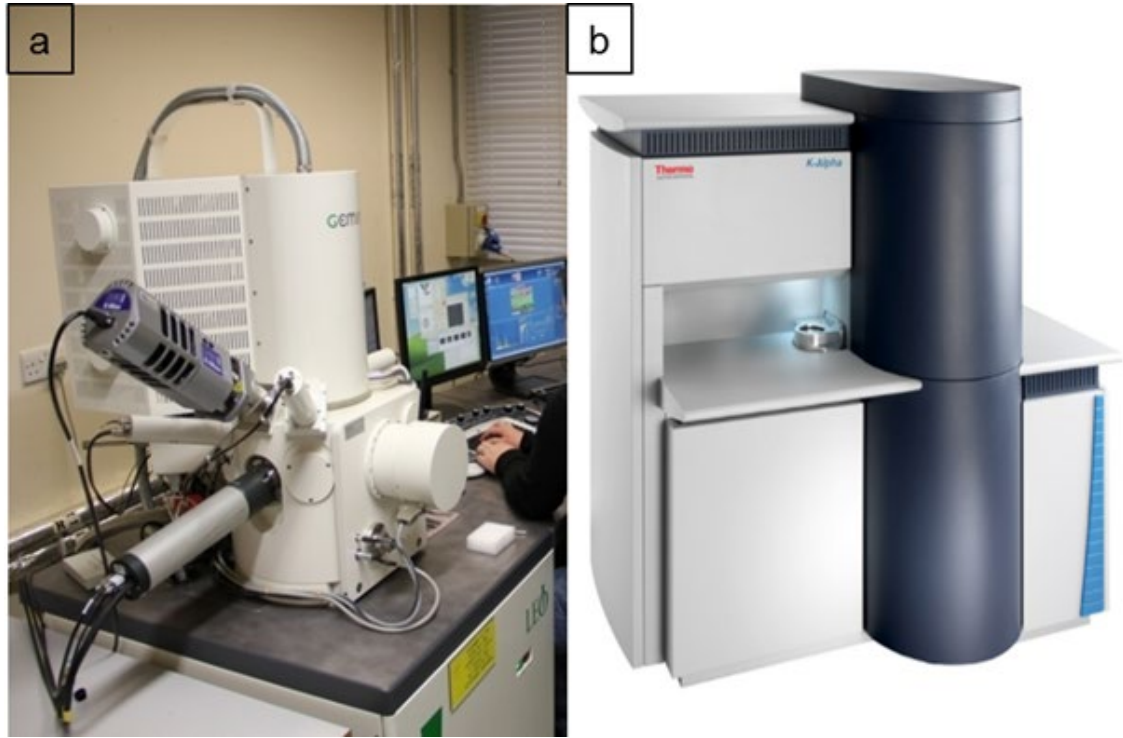


Fig. 27. Illustration of (a) SEM and (b) XPS

3.3.3 Workflow and design of the testing

The testing set ups vary slightly for the experiments with thin film or thin wired sensor array with their different architecture, the main workflow and assembly set ups are shown in Fig. 28. For instance there is no external wire attachment required for the testing carried out with the thin wire form while it is a key requirement for thin film formed sensor. So the arrangement of the set ups for these experiments will be different. The detailed explanation from cell fabrication to SOFC testing for each set up will be given in the chapter 4 and 5 for thin film and chapter 6 for thin wire.

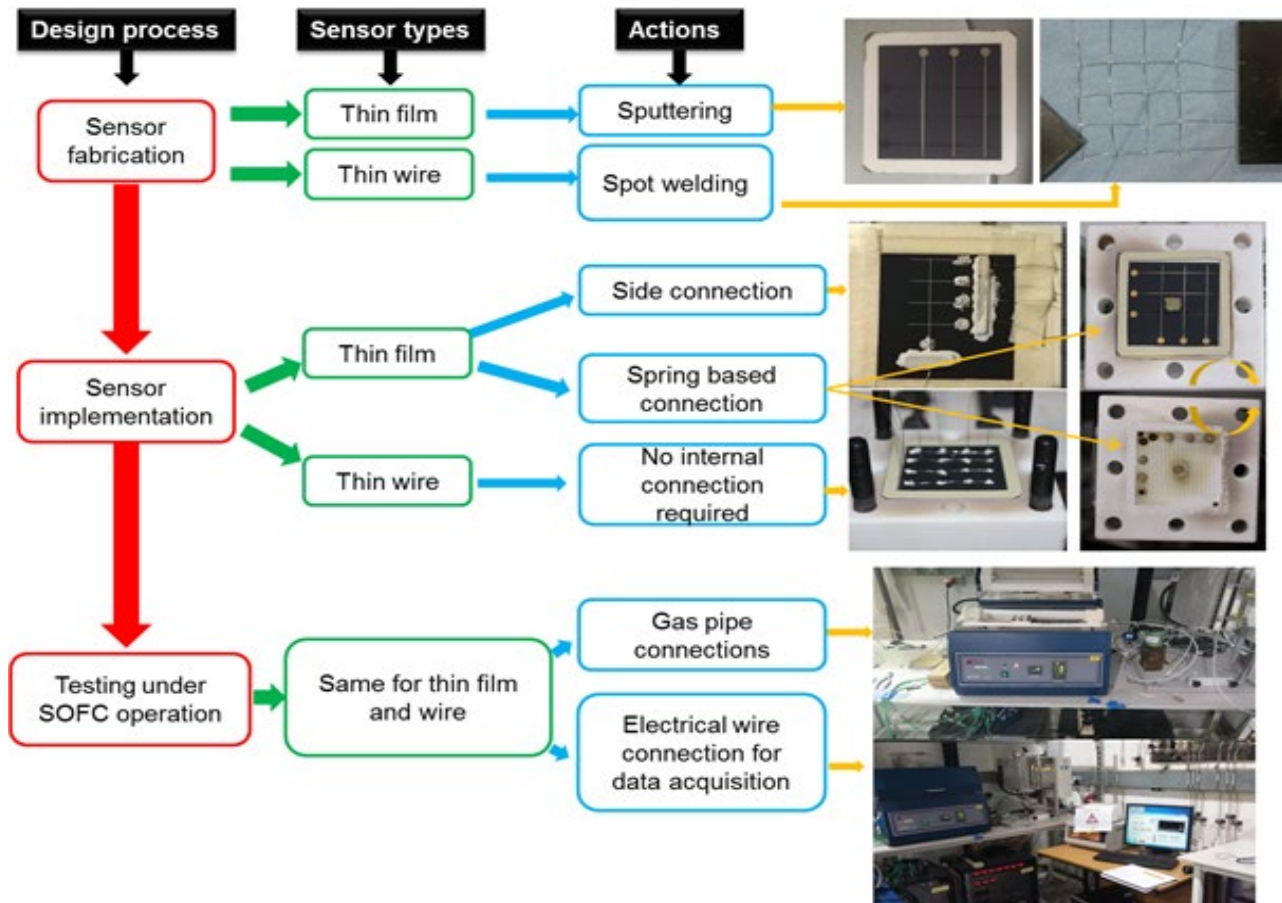


Fig. 28. Workflow of the design of experiment with different sensor configuration

Basically, once the sensors architecture is deposited/welded, the sensor attachment process is carried out. In the case of the thin film sensor, firstly the desired sensor pattern is sputtered, and then external wires are attached to complete the electrical circuits. The connection is carried out in two different ways i) side connection where the wire is attached through the support material surface (which is the cell in our case) ii) spring based connection where the external wires are sent through the upper part of the manifold and there is no physical contact with the cell apart from the connection pads (Table 3). When the side connection attachment is applied at the cathode side it has to be open to air. The detailed information about the connection mechanisms will be given in chapter 4. In the case of the thin wire sensor, the desired architecture of the sensor is achieved by welding the wires at the required points. As mentioned earlier there is no external wire connection required however the sensor is required to be bonded to the cell surface at each individual junction. Alumina paste is used to bond the metal elements to the cell surface since it is

electrically non-conductive and chemically inert. Once the electrical connections of the wires are completed the sensor integrated cell-manifold assembly is placed in the furnace for heating and testing. Durability of the thin film sensor thermo-elements on the porous cell electrode was the main concern in the case of using the thin film sensor which is explained in chapter 4. External wire attachment to the sensor pads was problematic with side connection (Fig. 28) due to the coverage size and its potential impact of the cell active area and hence providing ineffective electrical connection, as well as the concerns with the requirement of having a cathode side open air system. Thus, the spring based connection method was developed which requires less area with electrically, mechanically stable connection and allows the sensor to be used in a closed SOFC system (house-made manifold). The external wire only contact with the cell electrode at the connection pads is shown in Fig. 28 with gold coloured arrows. The designed cell holder consists of two parts: (i) an upper part which is where the oxidant is supplied (and contains an exit path), and also has holes for wire attachments for thin film sensors' electrical circuit connection, and (ii) a lower part in which the fuel is supplied, and has only a single hole for electrical connection for the current collection mechanism employed. The sensor integrated cell is placed in the manifold by being sandwiched by two gaskets. After all the assembly is completed the manifold is then placed in the high temperature furnace which is where the gas pipe connection is made. Temperature readings from the sensors and TCs are *in-situ* monitored using dedicated LabVIEW software. This was created in-house to perform the duties of collecting and recording the data throughout the experiment. Finally the furnace is heated to the SOFC anode reduction temperature by presenting N_2 to the anode side to prevent anode oxidation and chamber purification.

Table 3 Chapters with corresponding experimental set ups

Sensor forms	Thin film		Thin wire	
Chapters	Chapter 4	Chapter 5	Chapter 6	Chapter 7
External wire connection	Side connection	Spring based connection	Not required	Not required
Sensor types	N+1	Grid	Grid	Grid
Sensor thermo-elements materials	Alumel-chromel (k-type)	Alumel-chromel (k-type)	Alumel-chromel (k-type)	Alumel-chromel (k-type)
Method for Sensor fabrication	Sputtering	Sputtering	Spot welding	Spot welding

3.4 Chapter Summary

This chapter has introduced the materials which will be used for cell, sensor and testing set ups. Working principles of the proposed sensor and its fabrication and attachments on a cell for both thin film and thin wire form has also been explained. Techniques which will be used for surface characterisation especially for the applied sensor used in the thin film form have been introduced. Due to its architecture the sensor offers unique advantages of requiring less number of thermo-elements even for the same number of sensing points compared to using conventional TCs. In addition to this, the implementation of the sensor has the potential to provide higher temporal and spatial resolution with negligible disturbance to the nature of the SOFC operation. The specifications of the desired sensor forms together with their required testing conditions have been explained. A novel external wire connection method and its potential benefits have been introduced. Testing of the integrated thin film sensor for its durability and characterisation studies is given in following chapter 4. Two different methods i) traditional wire attachment to thin film elements ii) new method for wire attachment to a thin film especially for SOFC application with an external wire connection have been introduced. Advantages of the new connection method will be explained in chapter 5.

Chapter 4:

Viability of Thin Film Sensor for Temperature Distribution Monitoring

4.1. Introduction

The thin film formed multi-array sensor has two significant advantages over the traditionally available thermocouple as a means of temperature monitoring. Firstly, it decreases the number of thermo-elements used to create the sensing points due to its architecture. Secondly, it increases the spatial and temporal resolution due to being in thin film form and has less distortion to environmental factors [138]–[140]. The temporal resolution is high due to the reduced thermal inertia of the layers, which translates to providing a faster signal response compared to the use of conventional TCs [20]. Additionally, the spatial resolution is also higher due to the direct contact between the sensing system and the location of the temperature measurement.

However, the durability of the thin film thermo-elements on the porous electrode and the security of the external wire connection are concerns and have not been studied before. Thus, in this study, the performance of the thin film thermocouple array (N+1 types) fabricated directly on a porous substrate have been investigated at a temperature ranged from room temperature (20 °C) to SOFC operating temperature (800 °C). The aim is to monitor the capability of the thin film sensor array for physical durability and electrical security to provide signals related to temperature readings during SOFC operation, under normal operating temperatures.

4.2. Experimental Details

During this study, the “N+1” thin film (500 nm) sensor architecture has been patterned on an electrolyte supported cell. The external wire connection to the deposited sensor elements is connected via connection pads by applying a side connection (currently available method) method. The prepared cell has been tested in the high temperature furnace at elevated temperatures (from 20 °C to 800 °C). Two

conventional TCs which are located 2-3 mm above the cell surface have also been placed on the SOFC for calibration purposes, namely by comparing these obtained readings to those of the film sensor. There has been characterisation studies carried out by SEM and XPS for visualising the surface features of the thin film sensor used.

4.2.1. Material selection and sensor fabrication

A thin film thermocouple array sensor was fabricated on the cathode surface of a Next-Cell electrolyte-supported cell (FuelCellMaterials, US) as the schematic view depicts in Fig. 29. Standard K-type thermocouple materials alumel (500 nm) (Ni:Mn:Al:Si/95:2:2:1 by wt.) and chromel (500 nm) (Ni:Cr/90:10 by wt.) were the thermo-element materials employed to form the K-type desired sensor architecture. As seen from Fig. 29, there are five thermo-elements (A-D (alumel) E (chromel)) deposited on the cathode resulting in four individual sensing points. The K-type thermocouples have a design that operates in the temperature range covering the operating temperature of a typical SOFC (from 600 °C to 800 °C). The cathode, used as the substrate to fabricate the sensors on, has a porous structure with a thickness of 50 µm while the total cell thickness is approximately 0.17-0.2 mm (0.17 mm electrolyte and 50 µm anode electrodes), which offers enough strength to handle the substrate during both the sensor deposition and the annealing process. The focus of this study is on how the thin film sensor performs on a real SOFC electrode which has a porous media, in other words the cell will be used as substrate material to host the applied thin film sensor.

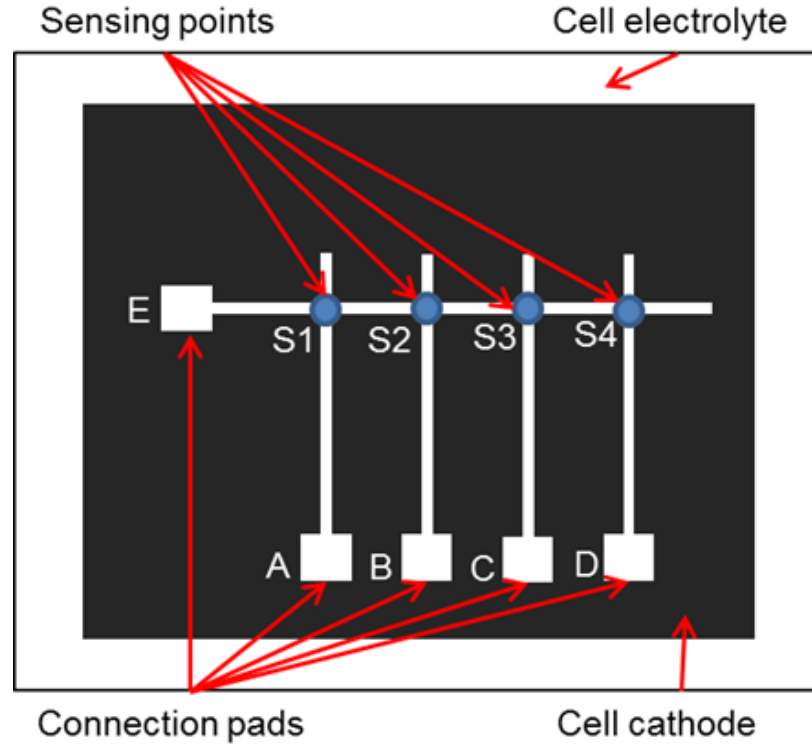


Fig. 29. Schematic view of sputter-deposited 500 nm thick sensor thin film thermocouple array architecture

Sputtering was selected as a deposition technique to fabricate the thin film thermo-elements on the cell cathode surface. Sputtering for thin film deposition is widely used due to low deposition temperature required, achievement of uniform film deposition and easy process controllability [141]. A Q150T S sputter coater was used for sputtering with the parameters for selected alumel and chromel material (same for both since they are Ni based materials) shown in Table 4. All the operating parameters for each element have already been set by the factory. Thus when the desired elements are chosen depending on the target materials, then the parameters are automatically applied. Alumel and chromel were used as target materials to deposit the corresponding alumel and chromel thermo-elements pattern (Fig. 29).

Table 4 Sputtering parameters

Temperature	<50 °C
Deposition rate	~14 nm/min
Current	140 mA

Four alumel and one chromel thermo-elements were deposited separately by using a patterned metal mask. The mask is made of metal (302-stainless steel) and was designed for alumel thermo-elements with four slits and chromel thermo-elements with one slit. A single horizontal line of chromel thermoelement (E) was fabricated, along with four corresponding vertical alumel thermo-elements (A, B, C, D), yielding four sensing points (S1, S2, S3, S4), as depicted in the Fig. 29. The numbers of sensing points were determined depending on the cell size which for this experiment cannot accommodate anymore thermo-elements. Furthermore there was no intention to increase to number of sensing points as the physical durability of the film sensor is the main focus

The size (area) of thin film thermo-elements were enlarged at the points A, B, C, D and E, designated as thin film pads in order to have enough surface area for external wire attachments. However, it is important to keep each connection area as minimum as possible to prevent blockage of the cell surface area during SOFC operation. The resulting array provides four sensing points using five thermo-elements only; for comparison, commercial thermocouples would have required 8 thermo-elements for the same number of sensing points.

4.2.2. External wires connection

Correspondingly four alumel external wires were connected to the thin film pads A, B, C and D and a chromel external wire was connected to thin film pad-E to form K-type thermocouple junctions (see Fig. 29 for pad positions and Fig. 30 for connections). Silver paste (Aremco-bond 597) was applied to provide electrical connections between the pads and external wires, due to possessing excellent electrical conductivity (6.30×10^7 S/m) up to 900 °C. However, silver paste is not capable of carrying the mechanical load induced by the wires attached to it.

Therefore, alumina strips, connected with alumina paste, were used to increase the mechanical strength of the connection and minimize unwanted external loads from the wires and beads depicted in Fig. 30. The alumina was cured at 250 °C for 2 hours, and the silver paste was cured at 90 °C for one hour (as defined in the manufacturer curing instructions).

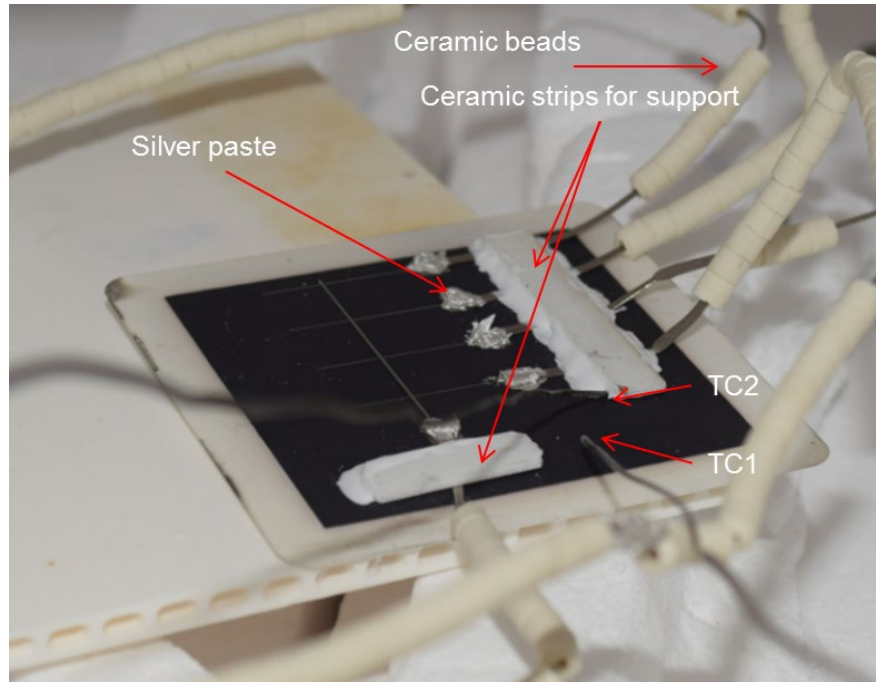


Fig. 30. External wires attached to the thin film thermo-element pads

Two commercial thermocouples (K-type) were also placed very close to the substrate surface to compare and validate the measurement obtained from the thin film array sensor. The number of TCs can be increased and the size can be reduced to obtain fast response even from the conventional TCs however still the main benefit from the applied sensor comes not only from size, it provides benefit due to its architecture.

Once experimental preparation for sensor integration to the cell surface had been completed, then the sensor integrated cell was placed in a high temperature box furnace. The furnace was heated to 500 °C with a 2 °C/min heating rate and dwelled 30 minutes at this point then heated to 800 °C with the same heating rate and dwelled 30 minutes at that temperature. Finally, the furnace cooled down with the same rate as was used for heating instead used for cooling. Random variations in furnace temperature have been applied to monitor the thin film sensor response to the varying operating temperature.

4.3. Results and Discussions

4.3.1. Temperature reading

The monitored temperature readings from the sensor array and commercial TCs are plotted in Fig. 31. From Fig. 31, it can be found that the temperature reading from the sensor array has good agreement in following the same trend as the commercial TCs during the 1st segment from room temperature to 500 °C. While a temperature difference is seen between the sensor average and TCs average temperatures, of about 10 °C, due to the difference in the cell bulk temperature and the inside furnace transient temperature. The minor temperature fluctuations from room temperature to 500 °C were due to furnace heating characteristics as the furnace inside temperature is not uniform and shows instant variation in temperature with applied power. During the heating process some overshooting is experienced from the furnace where the applied power is over the set power rate. One benefit of this response is that it allows monitoring of the sensor performance during sudden and repeating variations in temperature due to heating patterns. As depicted in Fig. 31 in the 1st segment, measurements from the sensors exhibit the same behaviour as the two K-type thermocouples. In the 2nd segment, in which continuous heating was introduced, the furnace temperature was increased from 500 °C to around 800 °C. The measurements from the two thermocouples and the sensor readings from the four sensing points produced even better agreement in this step compared to the previous segment. This is attributed to the reduction in furnace overshooting where the applied power rate of the furnace matches the set expected power rate.

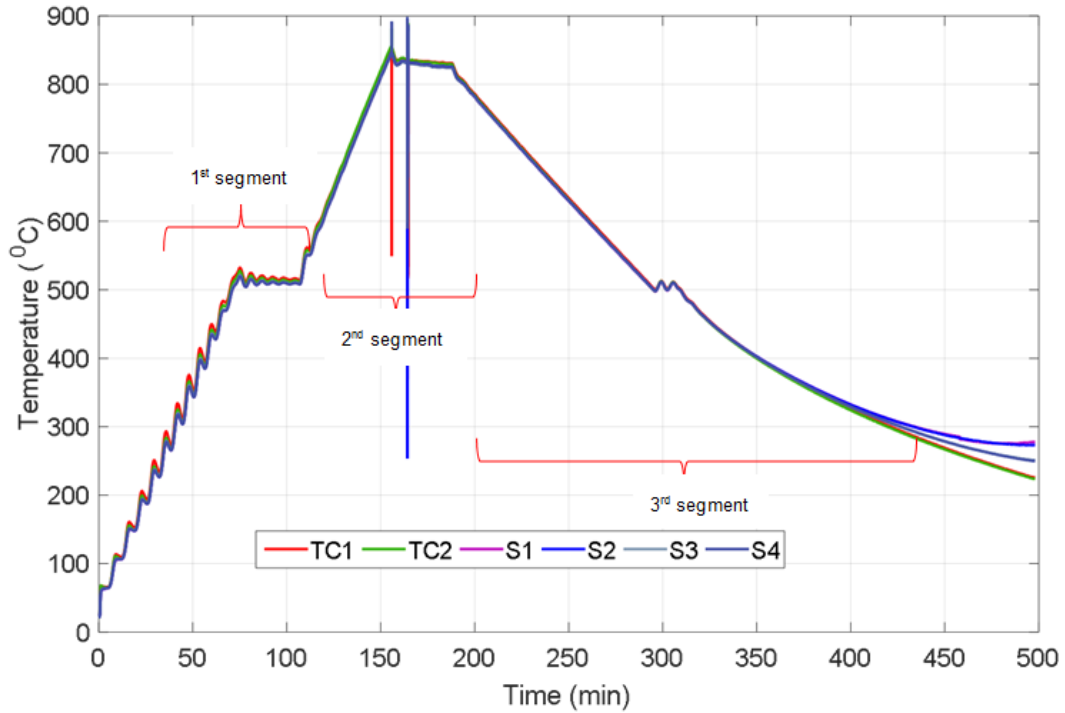


Fig. 31. Temperature profiles of two thermocouples and 4 sensing point of the sensor

During the 3rd segment from 800 °C to 500 °C, all the sensing points and thermocouples follow exactly the same trend, which coincides with the overlap of each set of readings, which appears to be a single line; this was followed by another dwelling phase at 500 °C for 30 minutes. The sudden drop observed in the readings from TC1 and S2 during dwelling at 800 °C are attributed to data logging based issues. The thermocouples and sensor points continue to follow the same trend down to 350 °C during cooling; however there is a diversion that starts after this temperature as shown in the latter sections of the x axis shown in Fig. 31. The two thermocouples kept slightly decreasing whilst the temperature readings from sensing points S1, S2 and S3 stopped their decrease and levelled out. Despite measurements from sensing point S4 continuing to decrease, it was not similar to the decrease observed in the thermocouples. After 500 minutes the temperature reading from all sensing points diverged from each other (see Fig. 31) and there was no reading obtained from the sensor while the thermocouples continued to provide readings down to room temperature. This disparity was deemed due to a failure of the sensing points. It is proposed that the reason leading to failure of the integrated array sensor could either be the high degree of resistance in the thermo-elements or be issues at the connection point between the external wires and thin film thermo-elements pads,

which is connected by silver paste. To investigate the potential reasons further initially resistances were evaluated and thin film characterisations tests were carried out.

Table 5 Measured resistances of the four sensing points before and after the heating process

Electrical Resistance	S1	S2	S3	S4
Before (Ω)	20	25	30	37
After ($M\Omega$)	6	8	1	2

Table 5 shows the difference between the electrical resistances of each of the sensing points before and after the heating cycle. The resistance of the corresponding thermal pairs for each sensing points (junction) were measured at the connection points by using a multi-meter. As is clearly seen from Table 5, there is a drastic increase in the resistance of the sensing points observed for S1-S4 from 20-37 Ω to a few $M\Omega$ respectively. This significant rise in resistance leads to variations in temperature readings resulting in a drift due to the metallurgical changes of the thermo-elements [140]. The resistance change coupled with observed temperature differences seem to correlate with research findings. However in this study there was not just a change in measurement but also no measurement. Oxidation of the thin film or external wire, thin film cracking, poor electrical contact or delamination and cracks in the silver paste during cooling have in the literature been considered as the reasons for the sharp increase in resistance, hence resulting in the failure of the temperature measurement [140]. Thermal expansion mismatch (between silver paste, external wires and substrate material at the connection point) which causes cracking in, and removal of, silver paste during cooling due to the tensile stress can be a potential reason for the failure. The sample has reheated after cooling down and some of the sensing points have provided reading while others not. Obtaining reading from some of them is a clue for removal of the connection but not enough to explain issue totally. Thus, SEM and XPS were carried out to examine the failed thin film sensor, and the results are presented and discussed in the following section.

4.3.2. Film characterisation tests

4.3.2.1. SEM analysis

In order to further investigate the reasons causing the failure mechanism, contributions from the thermo-element material mechanical and chemical stability point of view were investigated. Some characterisation tests were performed. Fig. 32 shows the SEM images of the longitudinal view of the thin film thermo-elements under different magnification before (a-500 and b-2k), and after (c-2k) the experiment. There were no micro-cracks generated on the thin film sensor during sputtering (Fig. 32 (a)), and hence no cracking was present before the heating cycles (Fig. 32 (b)). Transverse micro-scale cracks were observed after thermal cycling as seen from Fig. 32 (c). It is worth noting that the cracks only occurred on the deposited sensor film while there was no cracking observed on the substrate (the cathode) nearby to the deposited film (Fig. 32 (c)). Thermal expansion mismatches [140], [142] and different friction rates between the deposited thin film material and the substrate material are the main reasons proposed for the crack formed on the thin film [143]. Due to the higher thermal expansion coefficient of the fabricated thin film thermo-elements ($17 \times 10^{-6} \text{ K}^{-1}$), these elements experience more shrinkage than the cathode materials ($15 \times 10^{-6} \text{ K}^{-1}$). This in turn creates tensile stress, resulting in transverse cracks on the thin film thermo-element as shown in Fig. 32 (c). It is highly possible that the formed cracks will negatively contribute to the electrical potential drop between the two thermo-elements, leading to a significant increase in resistance; even so, it is not considered as a primary reason for signal losses due to the available path for electrical conduction throughout the thermo-elements. Hence it is concluded that though small cracks are evident their small size does not constitute failure such that no readings are obtained.

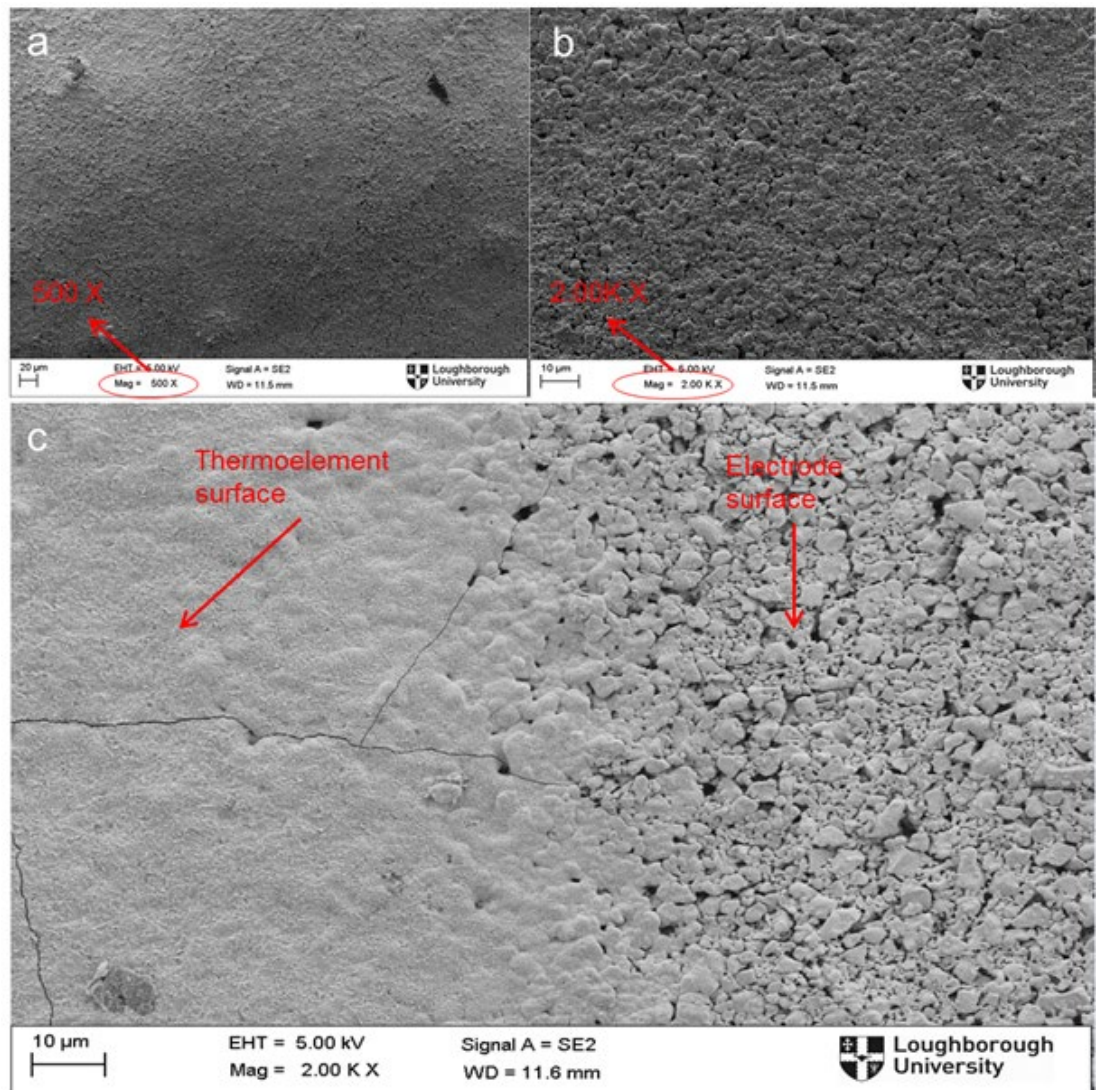


Fig. 32. SEM images of (a, b) 500 nm thick thin film thermo-elements before and (c) after thermal cycling at 800 °C

4.3.2.2. XPS analysis

XPS depth profiling analysis from the cell surface to its bulk was carried out to investigate the oxidation state of the thin film sensor thermo-elements before and after heating. The depth profiling provides information regarding about identification of the elements and oxidation state in a sample through its thickness. The etching rate was 0.15 nm/sec for 50 minutes (450 nm thickness) which is the factory set parameters for Ni. Nickel as the dominant material (95%) and oxygen in the thermo-elements are analysed before and after the heating cycle. The XPS characterization is carried out by a member of the Loughborough University material characterization center (LMCC) who, as an expert, determines all the parameters considering the

specification of the provided sample such as film thickness (500 nm) and material composition (Ni based).

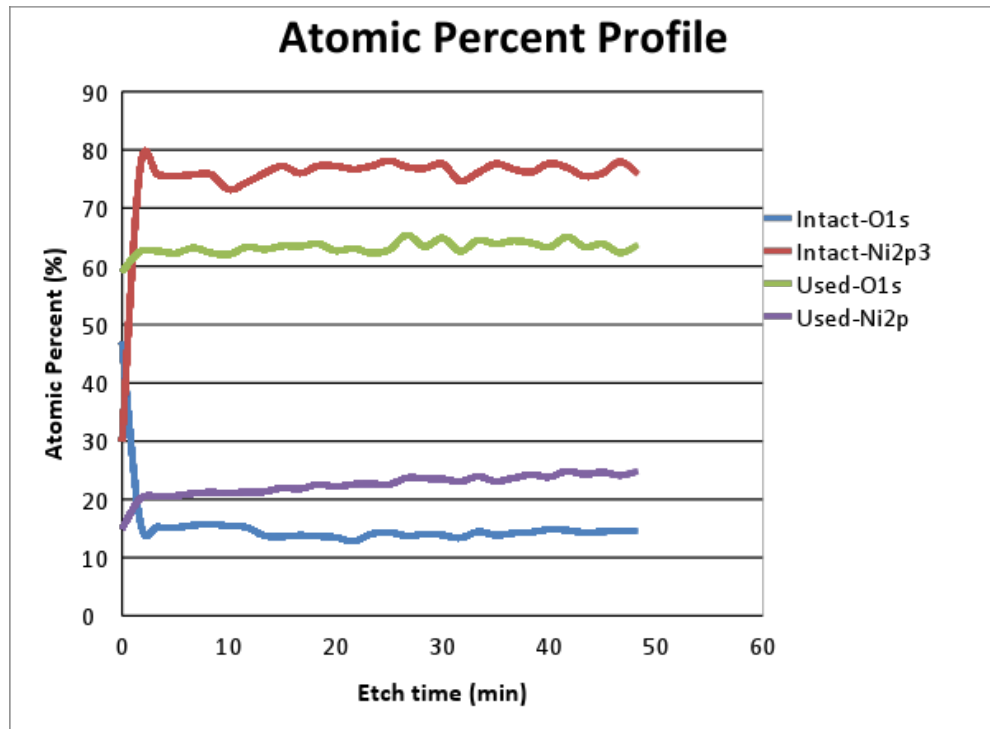


Fig. 33. Atomic percentage profiles of nickel and oxygen before and after the experiment

As seen from Fig. 33, XPS analysis of the top surface (~1 nm depth) of the thin film layer revealed considerable changes in the percentage of only dominant elements Ni and O₂ before and after the heating cycle (full spectra analysis of whole elements is provided in the appendix, section B, Fig. 69 for the intact and Fig. 70 for the used sample). As expected, the atomic percentage of nickel increased drastically from 30% to around 78%, while oxygen atomic percentage decreases from 48% to about 15% after 2 minutes of etching and both stay at the same level during the etching process for the intact sample. This can be due to surface (1-5 nm) oxidation of nickel based thermo-elements at room temperature [144]. The possible reason for the oxygen (15%) is the reasonably porous structure of the film (see Fig. 32 (b)) allowing oxygen penetration. On the other hand, there is no significant change revealed in the oxygen and nickel percentage between the surface and the thin film layer during etching for the thermo-elements used. It implies that there is a uniform oxidation state through the depth of the thermo-elements. Atomic percentage of both

nickel and oxygen increases by roughly 5% after 2 minutes of the etching process and remains stable throughout the etching process for the heat treated samples. A slight increase in nickel with increase in etching depth is observed due to the decrease in oxygen penetration with etching depth. Eventually, the thin film is oxidised significantly during the heating cycle, leading to an increase in resistance (see Table 5) [140]. Oxidation is one of the most important reasons for chemical degradation even for the ceramic materials in thin film thermo-elements [145]. As is shown from the XPS result, the thin film thermo-elements materials (Ni) oxidised significantly where the percentage of oxygen was found as 15% for the intact sample while it was observed as about 60% for the used sample.

There are two important disruptions that oxidation can cause, especially in metal thin film thermocouples. Firstly, it can lead to drift [138], [146] due to chemical changes in the material composition of the thermo-elements, which has a small effect (0.2-0.5 °C/hours) on the temperature reading under 1000 °C [145]. Drift, due to the metallurgical time-dependant changes in the thermocouple array thermo-elements, leads to incorrect readings being obtained over time. Secondly, rapid increase in the oxidation rate at high temperature causes morphology changes and leads to bubbling, resulting in delamination [147]. In this study, it is proven from the results obtained from the characterisation techniques (SEM and XPS) that insulation, or more stable thermo-elements such as ceramic based materials [140], [148] is a crucial requirement. This is vital to protect thin films from not only oxidation but also chemical interaction with the substrate material especially if there is a chemically active surface used as a support material [149]. However, oxidation and micro-scale cracks are not evaluated as the real reason for sensor failure due to their relatively light impact on the temperature reading compared to connection-related issues. Thus, it is reasoned that high resistance between the external wires, silver paste and thin film pad at the connection point is the primary mechanism leading to sensor failure, as supported by the literature [146].

4.4. Chapter Summary

The novel N+1 type's thin film (500 nm) thermal array sensor architecture designed and implemented, which was fabricated directly on an SOFC cell cathode electrode,

was tested in air at 800 °C. Temperature readings from the four sensing points were obtained. Temperature readings from the two commercially available thermocouples (placed near the sensing points) and those from the thin film sensor were generally in agreement throughout the heating segments down to 350 °C during the cooling segment. Sensor failure occurred at around 350 °C resulting in divergent readings henceforth no readings obtained.

Significant difference was noticed between the resistances measured before and after the experiment for each sensing point (S1-S4). High resistance is proposed as the main reason for sensor failure. SEM and XPS characterisation techniques were performed to understand the main source for this high resistance and the failure mechanism of the sensor. As a result of the characterisation tests, transverse cracking and high oxidation throughout the thin film layer were obtained. Even though micro-scale cracks and oxidation states contribute negatively and lead to drift in temperature readings, these are not considered as the main sources for sensor failure due to total loss of the readings. The resistance at the connection pads between external wires, thin film pad and silver paste is proposed as a more convincing and impactful reason for sensor failure. This is deemed the reason as there can be a partial removal of the applied silver paste from the cell surface at the connection during cooling due to its higher CTE which experiences more shrinkage with reducing temperature. It is seen from the study that the implemented sensor has the potential to provide temperature readings with fewer thermo-elements from the electrode surface if the implementation is improved. Temperature sensing by the thin film sensor (grid architecture) from the cell surface with an improved connection method will be studied in the next chapter. It has also been highlighted from the study that the thin film sensor elements require a protecting layer to minimise the cracking and oxidation based issues. The oxidation is clearly due to the air atmosphere while the most likely contributor to cracking is by the porous media both due to its different material and physical structure. Thus alumina as a protecting layer can be a potential candidate due to its chemical and physical stability together with the expectedly good compatibility with ceramic based cells.

Chapter 5

Spring Integrated Connection Method for Signal Acquisition

5.1 Introduction

In the previous chapter, the thin film (N+1) array sensor architecture was tested as a potential application for SOFC temperature sensing due to its advantageous features including minimal intrusion to the cells working nature and the mechanically self-supporting components not requiring too much machining [43]. The persisting challenge is to ensure that, as this is still fundamentally an analogue electrical method, the external wiring and connections, which are critical for signal acquisition, are made reliable, conductive and robust. From the previous experiment issues identified were cracks on the sensor elements, oxidation and external wire attachment to the thin film thermo-elements. Among these, wire connection based issues were attributed as the main reason for whole signal losses. Hence a reason for new wire attachments was needed with better implantation but still with as little disturbance to the cell surface.

In this study, a technique for wire attachment, designated as a spring-based connection (SBC) has been investigated at practical SOFC operating temperatures. This technique offers direct electrical connection to the thin films' sensor pads without touching any other parts of the cell resulting in fewer disturbances to the cell area compared to the connection applied in the previous chapter. To achieve this type of connection a commercially available cell holder which accommodates a SOFC planar cell and its main components in relation to the wire connection method is altered and elaborated to fulfil the requirements of connection. A detailed explanation about the designed manifold will be given in the following section 5.2.2. The cell used in this experiment is similar to the cell that has been used in the previous experiment in chapter 4 due to both its higher mechanical strength and to maintain consistency between the two studies, facilitating effective comparison of the results. A description of the external wire connection mechanism to the sputtered

thin film sensor pads is provided. Temperature measurements have been carried out with the proposed method. The results are discussed and the parameters affecting the monitored readings are identified. Following on from the initial experimentation the creation of a design that allows robust and reliable temperature monitoring is needed. In the previous chapter thin film has connection related issues resulting in no temperature reading during cooling process. The advantages of the new method of attachment are explained and the results from the experiment carried out with new method are discussed.

5.2 Background and Concept of the Technique

5.2.1 Currently applied method for external wire attachment to a thin film sensor

For those sensors including resistance temperature detectors (RTD), thermistors, resistance strain gauges (RSG), and TCs used in the thin film form, external wire connection plays a key role as a step in the determinant pathway for accurate and constant signal collection [145]. Additionally, the intrusions to signal properties, especially due to aging, parasitic thermal voltages and internal resistance, all have a direct correlation with the connection mechanism. Furthermore, these mechanisms typically occur slowly and hence are not easily noticeable, resulting in ‘drift’ and inaccurate sensor readings [150]. Since the connection point acts as a third party in making a bridge between thin film thermo-element and corresponding electrical external wire resulting in a completed electrical circuit. Therefore, it is paramount to have a mechanically stable and electrically conductive connection. However, conventional wire connection techniques such as welding and soldering are not applicable for certain applications due to their sensitive material characteristics and high working/treatment temperature. In SOFC, welding is not applicable due to the brittle ceramic behaviour of the used cell while soldering is generally applied for low temperature application (less than 200 °C). Thus, external wires are generally bonded to the thin film sensor by using conductive metal paste as shown in Fig. 34 (a, b). In Fig. 34 (a) external wire connection to a thin film with RTD is shown while Fig. 34 (b) shows external wire connection to a thin film using RSG.

There can be two particular difficulties that arise with this connection method, especially when the sensor is used in SOFC system. Firstly, it is essential to hold the wires in a position of stability and continuous contact; otherwise a small external load from the wires (e.g. tension forces or weight) or expansion of the wires themselves, may lead to removal of the wire from the thin film surface, eventually resulting in failure of the connection [145]. Secondly, the connection can cover a significant amount of area which is larger than the area that is taken up by the sensors themselves, as illustrated by Fig. 34 (a, b). The total connection area for RTD (in the blue rectangle) is similar to the area covered by the sensor architecture (shown in the red rectangle) (Fig. 34 (a)) while the area used for the connection (in the blue rectangle) is much larger than the area covered by the sensor pattern (in the red rectangle) for RSG (Fig. 34 (b)). Signal acquisition in the form of a temperature reading via a thin film sensor directly sputtered onto a conventional SOFC cell has been studied in the previous chapter and published in [151], [152]. To complete the electrical circuit shown in Fig. 34, the usually applied technique is to attach a wire to a thin film [153], [154].

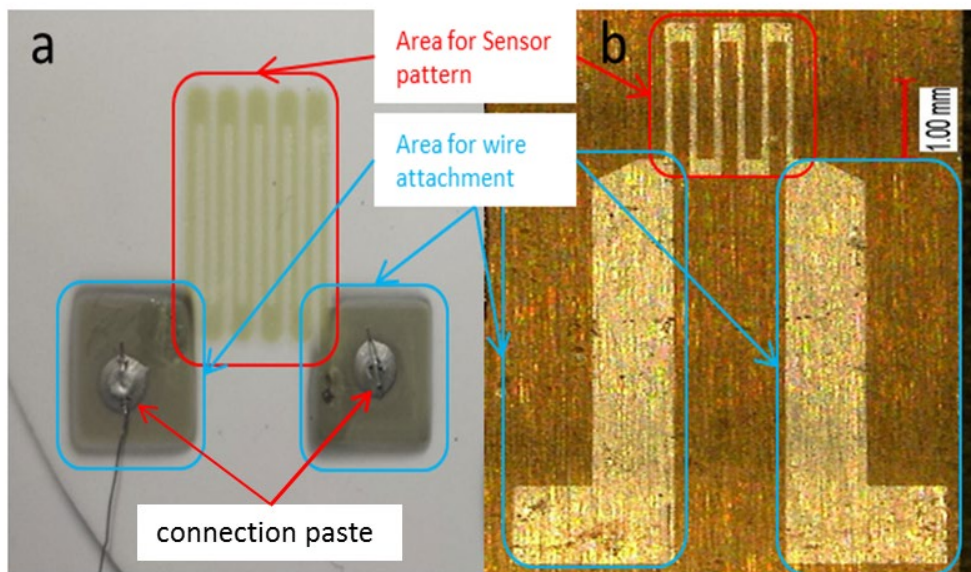


Fig. 34. Structured (a) RTD and (b) RSG sensors and their connection mechanism [153], [154]

Further to the difficulties in the wire attachment to the thin film sensor, the surface of the cell is electrochemically and chemically active and a larger active surface area is one of the key factors to maximise SOFC performance [155]. Moreover, the SOFC should ideally be a gas-tight closed system, which makes external wire connections

even more challenging. By considering the SOFC requirements for thin film sensor integration; these include:

- minimum disturbance to the nature of operation and its requirements
- minimum space for wire attachment and connection
- no requirement of machining on SOFC cell

To overcome the difficulties for wire connection namely:

- requiring sufficient space;
- extra support to provide constant mechanical strength to hold wires in position;

a new wire connection technique has been developed

5.2.2 Description of the designed SOFC manifolds

A multifunctional lab-scale (in-house) cell holder (manifold), comprising flow channels (bed), holes for fuel and oxidant inlets and outlets, and orifices for wire connection, was developed as shown in Fig. 35. The main requirement for designing a new manifold rather than using a commercially available one is that the commercial manifolds do not have features such as holes that allow adaptation of the proposed connection method. Thus based on the parameters already accounted within commercial manifolds, the new manifold is designed by the addition of some new features for coupling with the proposed connection mechanism. Macor as a machinable ceramic was used as the manifold material. Aside from its coefficient of thermal expansion being compatible with most metals and sealing materials, it also provides great electrical insulation even at high temperatures (up to 1000 °C) [156]. Manifold design and its functionality is an important aspect that helps the fuel and oxidant to be uniformly distributed, positively impacting on SOFC performance [157], [158]. The designed manifold consists of two parts: (i) an upper part (Fig. 35 (b)) which is where the oxidant is supplied (and contains an exit path), and also has holes for wire attachments for thin film sensors' electrical circuit connection, and (ii) a lower part (Fig. 35 (a)) in which the fuel is supplied, and has only a single hole for electrical connection for the current collection mechanism employed.

The lower part (anode side) of the cell holder, as shown in Fig. 35 (a), has two main sections: (i) a flow bed (blue coloured) including a triangular enlarging inlet, parallel

flow channels in the middle and a flow outlet which has a similar structure to the flow inlet; (ii) a cell bed (green coloured), where the cell electrolyte with sealing materials rests.

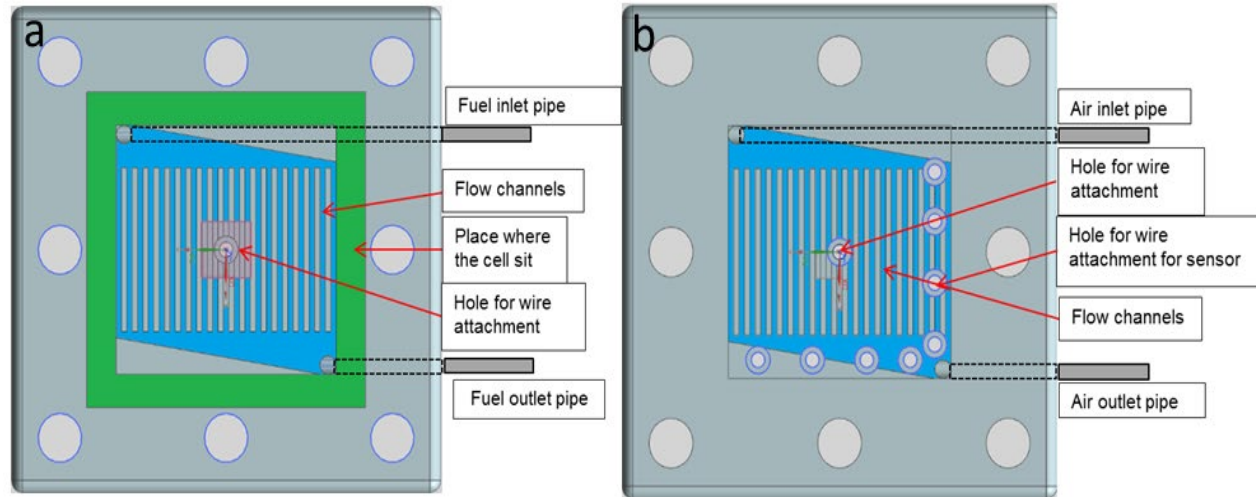


Fig. 35. Schematic view of (a) lower (anode side) and (b) upper (cathode side) of the cell holder

On the cell bed, the cell is placed between two gaskets for chemical sealing. The electrolyte is therefore sandwiched flush with the upper and lower holder parts, to prevent fuel leakage from the anode side to the cathode side (or vice versa).

In this case, the cell will be sandwiched between two gaskets which will be compressed safely. The bores on the outer side of the bottom part are for fasteners (threaded rod/nut type) to connect the two parts of the cell holder with the required tightness (~ 1 Nm). This can be modified to apportion the appropriate number and type of fasteners to ensure requisite pressure/screw torque if mechanical gaskets are employed.

The upper part (cathode side) of the cell holder as shown in Fig. 35 (b) also consists of one main sections, namely a flow bed to determine the flow direction which has having the same geometric configuration as the bottom part as per the previous paragraph. The hole in the centre is to be used for cell current collection and the holes on the outer side of the flow bed are to be used for sensors' electrical connection. The holes are placed on the outer side to further minimise disturbance to the operating environment. This is accompanied by a cell bed designed to accommodate the electrolyte of the cell. The manifold is specifically designed for a

50 mm × 50 mm planar cell with an allowance for different configurations such as electrolyte, anode or cathode supported cell. The configuration of the external wire attachment via the designed manifold is proposed by applying a new spring based connection.

5.3 Spring Based Connection (SBC) for Wire Attachment to a Thin Film Sensor

A thin film sensor with grid architecture is used, which has similar working principles as an N+1 sensor and commercially available TCs as already explained in the methodology part, chapter 3. As aforementioned, with a grid structured sensor, “ N^2 ” number of independent sensing points can be obtained with only “ $2N$ ” number of thermo-elements. Due to the benefits provided by the new method, there is no extra space required for six point connection hence the grid structure is used yielding nine sensing points and six connection points. Increase in connection points increase the feasibility of connection testing since the testing will be made upon six connection points rather than four. The thin film sensor sputtered cell with the corresponding external wire end is shown in Fig. 36 (a) and (b). The sensor-integrated cell is placed onto the lower part and the required corresponding spring-loaded external wires were placed into holes built-in on the upper part. The enlarged end of the external alumel (A1-A3) and chromel (C1-C3) wires and the corresponding alumel and chromel connection pads were gold plated to minimise oxidation and facilitate better electrical connection. Gold was used since it is chemically stable with a very high resistance to oxidation.

In the current chapter nine sensing points (red dotted) were created by applying a grid structured thin film sensor with three alumel and three chromel. The number of sensing points can be further increased to higher the resolution of measurement such as sixteen sensing points in a 4x4 grid structure being the maximum sensing points that can be reached with the current manifold which will be studied in following chapter 6. The sensing resolution is not focused on in this study instead the effective connection mechanisms to overcome the issues addressed in the previous studies. As previously mentioned in the methodology chapter alumel and chromel thermoelements were selected to form K-type TC junctions due to its wider working temperature range up to 1200 °C and lower material cost [130]. The sensor thermo-

elements were encased with an alumina protecting layer to prevent any detrimental harm such as cracking due to mismatches of CTE from the working environment. To achieve the protecting alumina layer, even though there is not enough temperature for formation of a true alumina layer, thermal oxidation of aluminum (Al) has been carried out under the air atmosphere at 900 °C. This is not a high enough temperature for proper aluminum oxidation to form alumina [159]. However we could not go beyond this temperature, since the cell components can be damaged beyond this temperature. Meanwhile, the high chemical stability is not expected from the alumina layer since the cell will not be chemically active during connection testing. For an operating cell there is a proper alumina layer needed as a protecting layer for the sensor which can possibly be achieved by direct physical deposition of an alumina layer rather than thermal oxidation of aluminum. First, Al is sputtered onto the cell surface from an Al target material and oxidised. Then the sensor thermo-elements are deposited onto the oxidised Al alumina layer, with the same oxidation process repeated to obtain the alumina top layer to complete the encasing process. Additionally, the deposited alumina and gold thin film at the connection pads blocks the penetration of the applied connection paste material into the porous cathode (in the case when using conductive silver (Ag) paste for wire bonding) as the surface of the sputtered film is more dense than the surface of the electrode. However the impact of this is minimal due to the small width (narrow) of the used alumina layer and can be further narrowed at industrial level production.

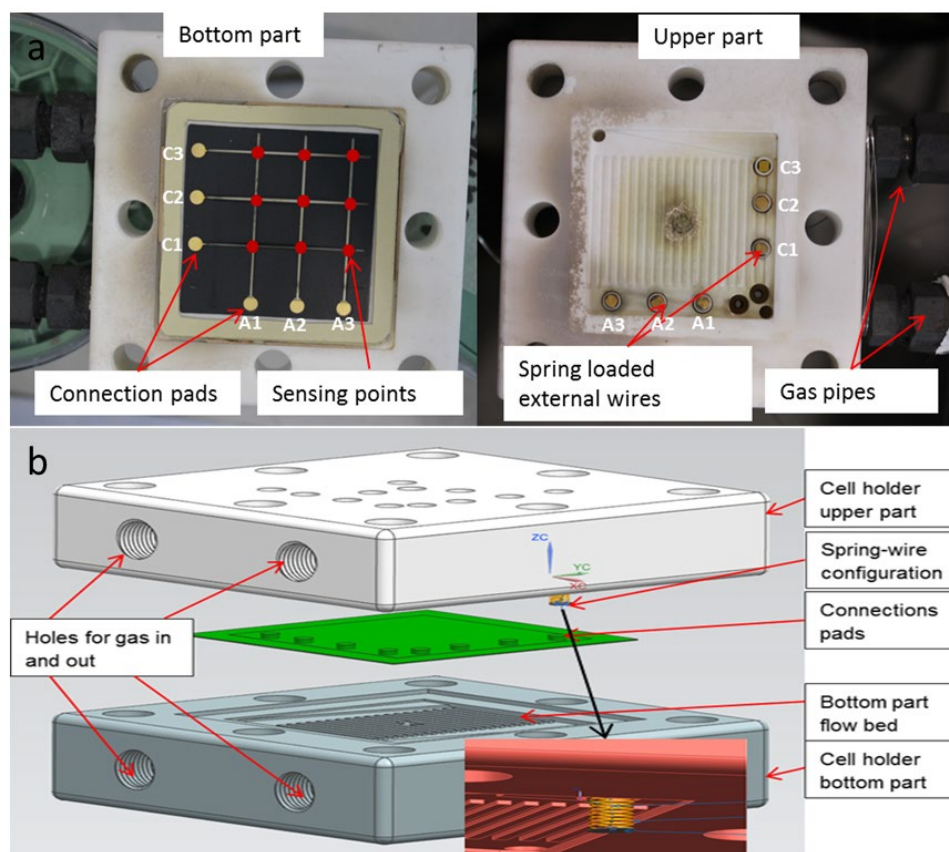


Fig. 36. Illustration of (a) sensor patterned cell (onto bottom part) and corresponding external wires (onto upper part) configuration and (b) its assembly

Fig. 36 (b) shows the schematic of the assembly of the manifolds' upper and lower parts with integrated spring, wires, and cell configuration. A spring (stainless steel) is placed within the built-in holes contained in the upper part of the manifold for sensor integration, to exert a normal load at the connection point. The external wires are sent from outside the upper part of the cell holder to the interior (through the aforementioned spring located in the hole), to contact with the pads at the connection point. The spring used is a stainless steel spring with a compression rate of 0.18N/mm and wire diameter of \varnothing 0.25 mm. Even though the spring is not produced for the high temperature applications over 250 °C, it has still been used to provide mechanical compression in the study. It has been considered that the spring does not lose its compression during heating and dwelling since there is an expansion expected with elevated temperature which can be enough to hold the external wires in contact with the pads. Due to limited availability of such small sized springs which work at the desired high operating temperature and high cost, it was not

deemed applicable in this instance to use a high temperature spring for the connection mechanism testing experiment.

The key point here is that the mask used to generate the desired shape of the sensor and connection pads is well aligned with the holes where the external wires come through. The pads were located at the edge of the cell active area (shown in Fig. 36 (b)) minimising disturbance to the cell active surface. An \varnothing 1 mm thick wire is pressed and enlarged to \varnothing 3 mm diameter and cut as a circle shape similar to the shape of thin film pads to match at the connection points. Then an \varnothing 0.25 mm small wire is connected to the obtained circler piece on one side for electrical connection between the circler shape and data logging where the other side of the circler shape is in connection with the corresponding pad.

The diameter of the enlarged edge of the wires (\varnothing 3 mm) is larger than the diameter of the spring (2.95 mm in Dia.) and less than the holes' diameter (4 mm in Dia.). With this configuration, the spring applies a compressing load to the connection depending on the free length and the compression rate of the spring employed. When the two parts of the cell holder are joined the free length of the spring is compressed to the channel wall level which is where the cell surface is in contact. The aim and intent with this connection configuration is to limit disturbance (including flow distribution, gas penetration and electrochemical reactions) to the operating conditions whilst simultaneously keeping the wires in continuous contact with the thin film sensor pads.

5.4 Experimental Procedure

Two different set ups were prepared and applied for the experiment: one with silver paste and another one without silver paste as a conductive connection material. Since, at this stage, there is no guarantee that the new connection method will work properly without silver paste hence two set ups are prepared. Even though the connection mechanism is improved with SBC, the disturbance to the working nature is further minimised having connection without silver paste. Therefore two set ups are performed. In the first case, the external wires were directly attached between the enlarged end of the wires and connection pads without any paste, and for the second instance the external wires were attached with a very small amount of silver paste. For both cases, the SBC technique was applied.

The thin film sensor-integrated cell was placed in the lower part of the cell holders' while the external wires' connection set up was placed onto the upper part. The cell was sandwiched by two gaskets. The gaskets, which provide the mechanical sealing mechanism, were placed in the cell beds of the upper and lower parts. The material used was Thermiculite 866 LS (Flexitallic Ltd.), cut as a hollow square, with outer dimensions approximately 52 mm x 52 mm, and inner dimensions of 40 mm x 40 mm to couple with the electrolyte outer side.

When the sensor and its external wire connection is completed the upper and lower part of the manifold are assembled. Then the manifold was placed within a high temperature furnace. No gas apart from nitrogen was supplied during the heating process and throughout the experiment. In other words, there were no chemical or electrochemical reactions expected during the experiment; as the effectiveness of the connection technique that enables insertion of a thin film sensor within the SOFC system is the main focus of this study. There was a commercial k-type TC also placed nearby (2-3 mm above the surface of the cell) to compare the readings obtained from the sensor sensing points. The length of the TC inserted in the upper part is 8 mm from the upper surface which is where the upper surface is 10 mm away from the cell surface yielding a 2 mm gap between the TC and cell surface. There is a ceramic bead bonded on to the TC at that point to block further insertion of the TC into the upper part as shown in Fig. 37. Only one TC is used as it is considered as sufficient to measure the inside temperature of the manifold in this study. Once the assembly was completed, the furnace was heated to 750 °C with a 2 °C/min heating rate and cooled down to room temperature after about 5 hours dwelling at 750 °C with the same cooling rate. The heating and cooling rate are kept small to prevent the cell from any sudden temperature changes and hence related harm.

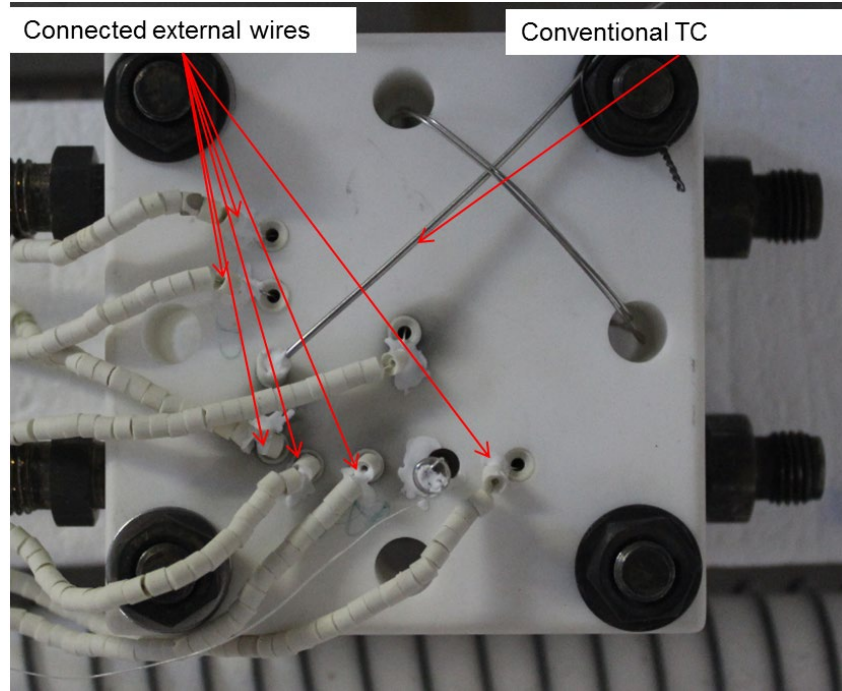


Fig. 37. Top view of the external wires attached manifold

5.5 Results and Discussions

5.5.1 Results for SBC without silver paste

Fig. 38 shows the temperature measurement obtained from each of the sensor sensing points (SSPs) and TC from the experiment using SBC without any silver paste. Nine readings from the SSPs (S1-S9) and a reading from the commercial TC are plotted. There is comparatively good agreement with the reading from these SSPs and the TC during the heating and dwelling segments compared to the cooling segment. TC provides higher readings than the SSPs throughout the experiment till failure which occurred at around 500 °C during cooling.

Fig. 39 (a) demonstrates the TC and average temperature readings of the sensing points (SSPs-ave (average over S1-S9)) from the given range as well as the temperature difference (TC–SSPs-ave) of the TC and SSPs at the averaged reading for the heating, cooling, and dwelling segments.

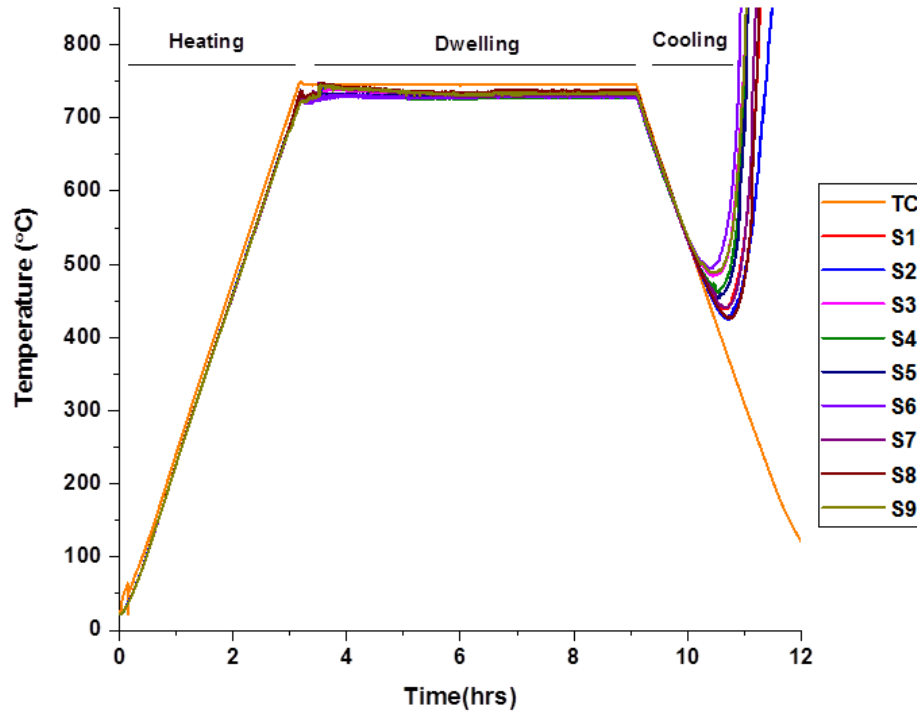


Fig. 38. Temperature measurements with spring-based connection without silver paste

There is a 14 °C temperature difference observed between the TC and SSPs-ave whilst the average cell temperature was at about 250 °C during this heating segment (H-TC, and H-SSPs ave). This is primarily presumed to be due to the higher thermal inertia of the bulk cell than the air atmosphere in the furnace as there is a thermal inertia difference expected between the cell bulk temperature and furnace inside air temperature. However, since the obtained difference increased with increasing temperature and reached 20 °C for the range between 600 °C and 700 °C, thermal inertia is not considered as the main reason as its impact should be constant. Besides the average standard deviation (SD) amongst the SSPs themselves are found to be 0.3 °C, 0.5 °C, 0.8 °C, 0.9 °C, 1.2 °C for the temperature range of 200-300 °C, 300-400 °C, 400-500 °C, 500-600 °C and 600-700 °C, respectively while it is 2 °C for dwelling. These are relatively small SD compared to the SD (such as ~9 and ~7 for the range of 200-300 °C and 500-600 °C, respectively) obtained between SSPs ave and TC for hence it can be an evident that there is common connection issue for all SSPs which results in divergence between the TC and SSPs ave readings (Fig. 39).

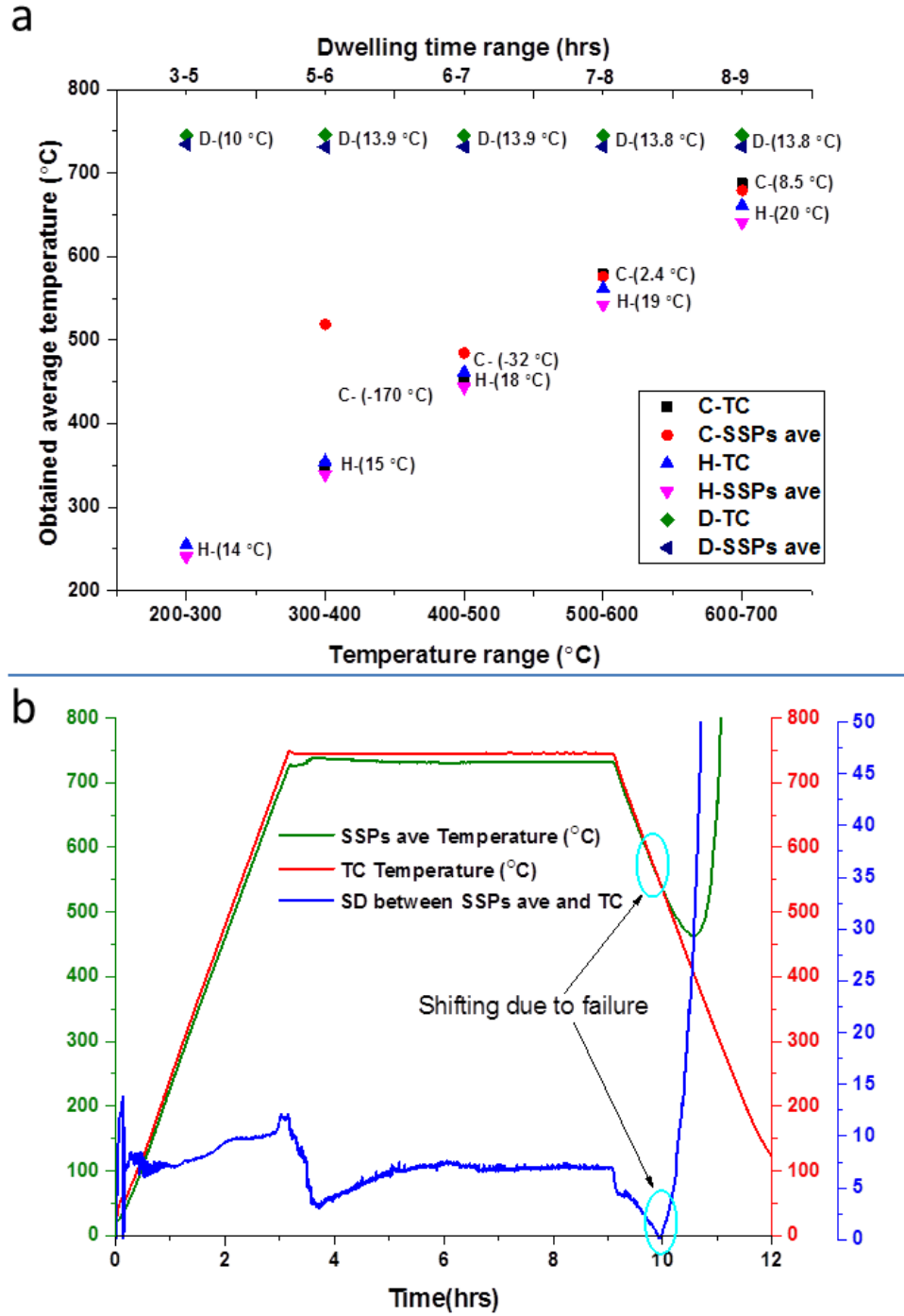


Fig. 39. (a) SSPs and TC average temperature from the given temperature range and the differences between them separately for heating, dwelling, and cooling segment with (b) SD deviation of TC and SSPs ave

The higher temperature reading obtained from the TC during dwelling is the contribution of resistance (given that the furnace is in the steady state mode) there must be thermal balance during dwelling which reduces the effect of thermal inertia.

Additionally, a constant difference, lower in magnitude (13 °C) between the TC and SSPs-ave reading is observed during dwelling (D-TC and D-SSPs ave) compared to the heating segment. These values further decrease during cooling (C-TC and C-SSPs ave) which are obtained only up to the point that failure occurred (Fig. 39 (a)). The difference between SSPs ave and TC readings shows a sharp increase from 8.5 °C to -170 °C presumably due to extremely high R_c (contact loss) leading to the SSPs' temperature increasing, despite the furnace being in the cooling mode. The order for the failure initiations of SSPs are given in the Table 6.

Table 6 Failure initiations of SSPs

SSPs	S1	S2	S3	S4	S5	S6	S7	S8	S9
Failing Time (hrs)	10:70	10:73	10:47	10:45	10:57	10:42	10:76	10:46	10:48

Failing process were found not the same for all SSPs, thus some of them failed much faster than others even the failing started at the same time or earlier than the one completing its failing process. For example failing for S4 initiated around three minutes before than S9 however as seen from the Fig. 38, the S9 started to divert or divert more than the S4. This is most likely related to the handling/preparation based error/difference of their SBC mechanism.

As shown from Fig. 39 (b) standard deviation (SD) of the monitored temperature from both SSPs-ave and TC gradually decreases from the heating to the cooling segment as $SD_{\text{heating}} (18^{\circ}\text{C}) > SD_{\text{dwelling}} (13^{\circ}\text{C}) > SD_{\text{cooling}} (8^{\circ}\text{C})$. It is clear from equation (14) that the thermal inertia of the cell is constant with the assumption that the cell possesses stable material properties during the experiment; however, the contribution of the thermal inertia can be altered or even inverted depending on the surrounding environment temperature.

Fig. 39 (b) also depicts that the SD is not constant during individual segments, as evidenced when it slightly increases by about 3-5 °C during the heating segment. While it is more stable during dwelling compared to the cooling segment and it even goes to zero which is where/when the temperature readings from SSPs ave are higher than the readings from TCs.

Thermal inertia, I , can be described as a measurement of the material's resistance to its surrounding temperature changes [160]. It can be altered depending on the materials density p (kg m^{-3}), specific heat capacity c ($\text{J kg}^{-1} \text{K}^{-1}$) and thermal conductivity k ($\text{W m}^{-1} \text{K}^{-1}$) with the given relationship between them in equation 14.

$$I = \sqrt{(ckp)} \quad (14)$$

With respect to this relationship, it is reasonable to obtain higher readings from a TC which is located at one of the gas flow channels 2-3 mm above the cell electrode (that measures the furnace atmosphere temperature) whilst the cell surface temperature is measured by the SSPs. However the difference is not constant and increases gradually with the increase in temperature while furnace heating rate and cell thermal inertia are constant (Fig. 39 (a)). It points to another source of difference made by the dissimilar resistance properties of the TC and SSPs possibly due to structural differences of the thin film sensor which has less initial resistance (Table 6).

Table 7 Initial resistance of SSPs and TC

Parameters	Resistance (Ω) before experiment
SSPs-ave (S1-S9)	25
TC	52

Importantly, the variation in the temperature difference between the TC and the SSPs-ave rises from 14 °C to 20 °C with the given varying operating temperature from 250 °C to 750 °C (Fig. 39 (a)). It indicates that there is a distinct alteration in the resistances of the TC and the SSPs-ave resulting in greater changes in the temperature readings despite a similar rate of change occurring in surrounding temperature. The properties of the electrical resistance are given by equation (15).

$$R = l\rho/A \quad (15)$$

Where, “ R ” is resistance, “ l ” is length, “ ρ ” is resistivity and “ A ” is the cross sectional area. As inferred from equation (15) the increase in resistivity leads to an increase in resistance “ R ”. This increase in resistance leads to an increase in voltage. However, it has only a small or negligible impact on the variation in temperature as the current in the thermocouples is negligibly small and controlled by high impedance amplifier(s). Additionally, according to the Seebeck theory voltage is only dependant on the parameters given in equation (16):

$$V_{emf} = \int_{T_0}^{T_1} (S_A - (-S_C)) dT \quad (16)$$

Where “ V_{emf} ” is the Seebeck potential, “ S_A ” and “ S_C ” are the Seebeck coefficients of the two thermo-element materials alumel and chromel, respectively, while T_0 is the temperature at the terminal and T_1 is the temperature at the junction.

It is apparent from equation (16) that the higher the Seebeck coefficient, the higher the corresponding Seebeck potential resulting in a higher temperature reading. Additionally the increase in thermal resistance (R_{th}) of the thermo-elements by increases in the operating temperature leads to an increase in the Seebeck coefficient [161]. However, the thermo-elements used for both measurement methods (TC and SSPs) are the same (alumel and chromel) with their wire sizes being similar in length (1 metre) and cross sectional dimensions (\varnothing 0.25 mm). The only difference between the measurements methods (TC and SSPs) is that the SSPs pattern is formed using thin film at the measurement point (on the cell only) which has a negligible impact due to its negligible size. Therefore, similar variations (increases) in R_{th} for both TC and SSPs are expected with increasing furnace temperature. Regarding the considerations above, the resistance at the connection point of the external wires to the sensor pads persists as the main reason for the divergence of the readings from SSPs-ave with the assumption that the conventional TC is functioning appropriately. Interestingly, in this SBC arrangement the increase in operating temperature contributes positively to wire connection as the compression due to the spring increases with temperature, which can lead to a better connection. This would mean less of an increase in the resistance than expected resulting in less of an increment in voltage out and corresponding temperature.

It can be assumed that spring expansion from the increase in temperature helped the attached wires and pads stay in electrical contact. Again it can be assumed that it is during cooling that the springs start to shrink and lose its spring compression capability (due to creep/plastic deformation/change in elastic modulus occurring from heat treatment). During this decreasing temperature segment contact loss is experienced between the pads and external wires. If the movement occurs parallel to the contact surface then it can damage the contact point by removing or scratching the contact elements. However, if the movement happens vertically perpendicular to the surface the author doesn't think that this will damage the surface unless it losses physical contact between the two surfaces. This failure result demonstrates the importance of the materials used for connection purposes in such a high temperature environment. In order to verify this result, another experiment was carried out by applying a very small amount of silver paste to hold the external wires' connection during the cooling segment and understand the contribution of R_c clearly.

5.5.2 Results for SBC with application of silver paste

The obtained temperature readings from SSPs and TC are depicted in Fig. 40. The experimental set up was identical to the set up for the preceding experiment without silver paste. However, during this experiment a tiny amount of silver paste was used to overcome the spring-based issues that occurred during the first experiment in the cooling segment and to identify how effectively the SBC connection performs. It was also performed to gain better knowledge about the impact of R_c on the monitored reading. Silver paste applied at the connection is the only difference from the previous set up. Having improved relationships such as smaller/constant difference between the obtained temperature readings from TC and SSPs ave can be evidence that R_c is the causal factor of the failure mechanism. The lengths of the thermoelements are not considered as important contributor due to negligible effect of the electrical resistance. The contact point is now pressure independent due to the solid body of cured silver paste. It is clear from the results illustrated in the Fig. 40 that the failure issue is resolved. In other words, even though the spring lost its elastic strain restoration (at the temperature that is over its designed service temperature) the applied silver paste was capable of holding the external wires in contact with the pads during the experiment. The temperature reading from both the

sensor sensing points and TC are in better agreement in both heating and cooling segments compared to the result obtained from previous set ups as seen in Fig. 40.

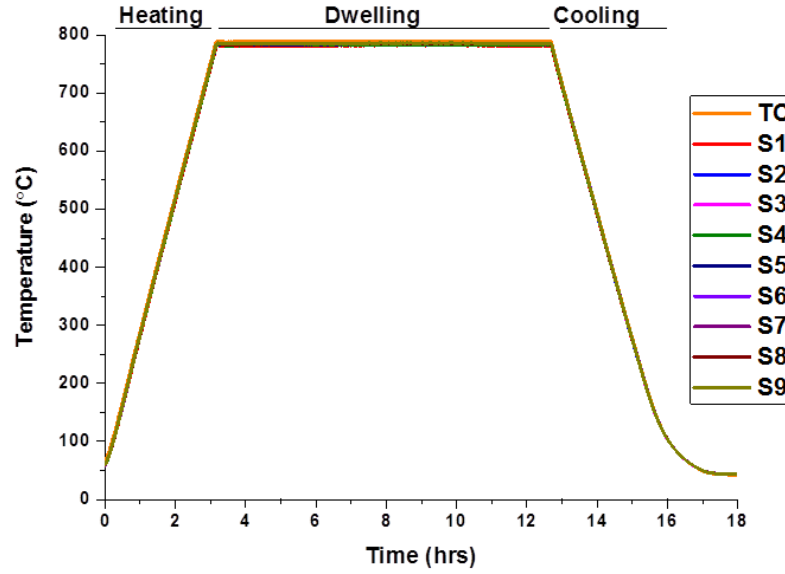


Fig. 40. Results from spring based connection with small amount of silver paste

As can be seen from Fig. 41 (a), the difference between the average temperature readings from the TC and SSPs-ave in a given temperature range is constant during each segment. A difference value of 8 °C, 6 °C and 2 °C are found for heating, dwelling, and cooling segments, respectively. While the SD among SSPs themselves are increased from 0.6 °C to 0.9 °C for the temperature range of 200-300 °C to 600-700 °C. It initially shows higher SD (0.6 °C) with less variation (0.3 °C) compared to the result obtained with the previous set up where initial SD obtained was 0.3 °C with a total variation of 0.8 °C. The different physical structure causes different initial thermoelectric properties, including R_{th} and R_c , resulting in different corresponding Seebeck potentials and finally different temperature readings. However the amount of change in thermoelectric properties during each individual segment should be similar due to the similar properties of the material of the thermoelements resulting in these constant differences.

The constant relationship between the SSPs-ave and TC average reading is also seen from Fig. 41 (b), showing SSPs-ave and TC readings and their SD changes during the experiment. The SDs are calculated at 2.5 for heating, 2 for dwelling and 1 for cooling segments.

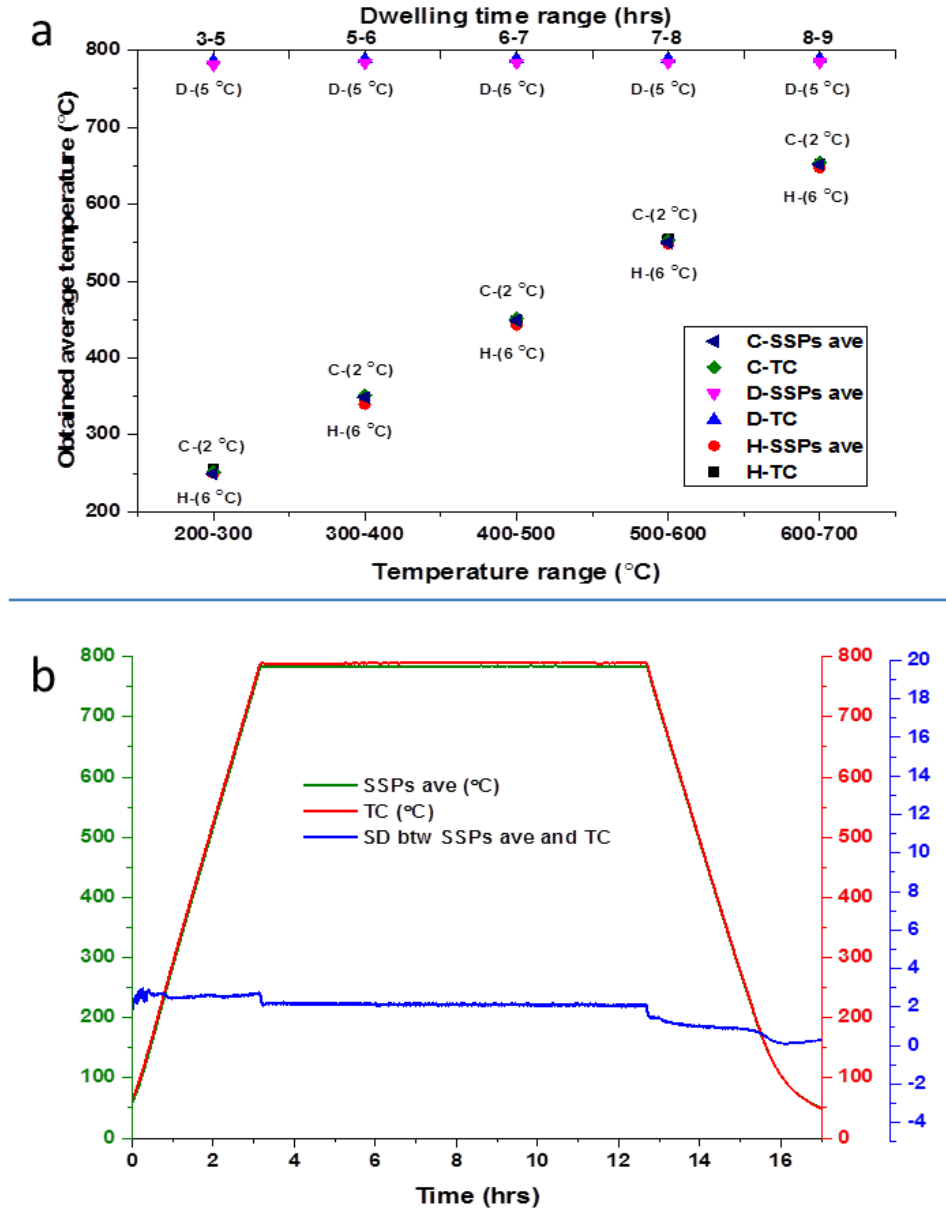


Fig. 41. SSPs and TC average temperature (a) from the given temperature range and the differences between them separately for heating, dwelling, and cooling segment with (b) SD deviation of SSPs and TC

All SD values obtained with this experimental setup are significantly less than the SD values obtained from the experiment without silver paste even though all the locations of the SSPs are exactly the same for both experiment as depicted in Fig. 39 (b).

As mentioned earlier in section 4.1, there are two factors affecting the temperature reading which are the difference in thermal inertia between the air atmosphere in the furnace and bulk cell, and resistance (R_c and R_{th}) especially at the contact point for

SSPs. Regarding the presented results and discussion carried out, the contribution of the factors that generate this diversion within the readings can be formulised by equation (17):

$$T_{TC} - T_{SSPs\ ave} = T_{TI} + T_{Rth} + T_{Rc} \quad (17)$$

Where “ T_{TC} ” is conventional TC reading, “ $T_{SSPs\ ave}$ ” is average reading from the thin film sensor (S1-S9) and “ T_{TI} ”, “ T_{Rth} ”, and “ T_{Rc} ” are the contributions due to thermal inertia, thermal resistance and contact resistance, respectively. As aforementioned the contribution of the thermal inertia and thermal resistance are similar for both set ups hence R_c is the dominant parameter for diversion of the temperature difference between TC and SSPs-ave during the experiment without silver paste. The instability issue experienced in the temperature readings with increasing furnace temperature during the experiment without silver paste seems resolved. It is inferred from the fact that the thermal inertia effect (which is constant) and the effect due to R_{th} (which similarly changes for both TC and SSPs) do not contribute to the temperature variation between TC and SSPs-ave. In other words, R_c is the only differentiating term among the physical parameters of the implemented sensor which leads to the varying divergence between readings from SSPs ave and TC.

The reason for having greater temperature differences between the readings from SSPs are and TC with increasing temperature during the previous set up without silver paste can be attributed to R_c . The electrical contact resistance (R_c) of two connected parts can be given by equation (18) [162]:

$$R_c = \{(\rho_1 + \rho_2)(1/[4na] + \alpha - 1)\} + \rho fs/Ac \quad (18)$$

Where, the “ ρ_1 ” and “ ρ_2 ” are the specific resistivity, “ n ” is the number and “ a ” is the radius of the contacting asperities, “ ρf ” is the resistance of the film between the two parts, “ α ” is the Holm radius, “ s ” is the contaminant, and “ Ac ” is the contact area. The first part of the equation is a constriction effect due to two different mediums while the second part is the effect due to contamination such as oxidation. Differing from R_{th} along conductive materials, R_c decreases with increase in operating temperature and applied contact pressure [162]. The contacting asperities are further increased with increase in pressure. This proves the presented findings from the

experiment without silver paste, as the compression of the spring is increased with elevated temperature, causing R_c to decrease together with the increase in temperature. Eventually, the increment in the resistance of the whole sensor circuit is relatively low compared to that of the expected value resulting in an increase in temperature difference between SSPs-ave and TC.

5.6 Chapter Summary

The performance of the reliability of signal acquisition via SBC with a new manifold was investigated. Electrical signals (as temperature measurements from nine different points) were acquired by applying a grid thin film sensor. External wires through the cell holder's upper part and the enlarged edge of the wires were attached to sputtered thin film sensor pads to complete electrical connection. For the first experiment without any silver paste at the connection point, failure was observed during the cooling segment due to spring-based issues, namely the loss of proportional and elastic behaviour (change in elastic modulus) from exceeding the temperature ceiling of the spring. Secondly, an experiment was run with a small amount of silver paste to overcome this issue. Since silver paste has the highest electrical conductivity among other metals and it was anticipated that when the applied paste cured it would provide enough strength to hold the external wire and connection pads in contact. Using a high temperature spring that can maintain its compression characteristics during heating and cooling is an alternate pathway to solve the failure problem. It has not been considered in this study due its high cost and limited production. Consequently, wire attachments with greater electrical and mechanical effectiveness and robustness have been achieved by the contribution of the SBC and the temperature readings have been continuously monitored throughout the experiment with second set up. A new external wire connection concept which makes applicability of thin film sensors easier for SOFC systems with minimising the disturbance to its working nature has been introduced. It is worth noting that SBC has a potential to provide significant benefits not only for establishing and maintaining electrical connection between thin film sensor and external wires but also helps smooth bonding of conductive paste materials due to its compression during the curing process of the paste.

Chapter 6:

Experimental Investigation of Temperature Distribution of SOFC Electrode

6.1. Introduction

Due to its wider working temperature range, coupled with lower cost, K-type TCs are used by many researchers for SOFC systems [152]. When using a sensing technique awareness of the uncertainty of the contributions of other heat sources including heat flux due to radiation and released or absorbed heat by electrochemical reactions that take place during SOFC operation is needed. Furthermore there are other parameters, such as, gas flow types and fed gas temperature that might affect the sensor reading depending on the proximity of those sources to the sensing devices. Therefore, there is a divergence on the reliability of temperature distribution measurement obtained by using TCs since the TCs are generally located in the flow channel. Ju *et al.* [42] claim that the measured temperature via the TCs from the flow channel, which is generally placed only 2-3 mm above the cell surface, is not only due to the cell activities itself, but rather it can be from the heat flux induced temperature inside the manifold with contributions from the gases produced, furnace heating element and cell activities.

In regards to the importance of thermal management of SOFC and the concerns on the current measurement with TCs as a sensory method, in this study the temperature distribution is measured directly from the SOFC cell surface with an implemented sensor. To test this new sensor under SOFC operation two commercial TCs have been located close to two of the SSPs for calibration purposes. The measurement from the commercial TCs and SSPs were obtained under loading and OCV conditions in order to monitor temperature distribution with varying conditions. During SOFC cell operation the response of the TCs and SSPs to temperature variations of the cell was monitored and the data obtained from both is compared in order to investigate temporal and spatial resolution of the sensors in comparison with

the TCs. To the author's best knowledge, there are no available experimental studies in the literature to validate the reliability of TCs temperature measurements.

6.2. Experimental Process

6.2.1. Materials

A 50 mm x 50 mm sized anode supported planar SOFC (FuelCellStore, USA) cell is used during the experiment. The cell consists of a 500 to 600 μm thick Ni-YSZ (Nickel-Yttria Stabilized Zirconia) anode, 7 to 10 μm thick YSZ electrolyte, and 3 to 5 μm thick GDC (Gadolinium Doped Ceria) and 30 to 60 μm thick Lanthanum strontium cobalt ferrite (LSCF) /LSCF-GDC cathode electrodes.

The homemade counter-flow designed manifold, where the features have already been explained in the previous chapter was used in this experiment. A mica based gasket with a thickness of 0.5 mm was used (Flexitallic Ltd). The cell was sandwiched between two gaskets to hinder any unwanted gas leakage. An alumina paste (Aremco products, Ceramobond-552) was applied at the junction to mount the sensor thermo-elements on the cathode. Silver meshes (PI-KEM Ltd) were used on both sides of the cell as a current collector, with a silver paste to bond the meshes on the electrodes. LabVIEW software was used for data collection (National Instruments Corporation Ltd. UK). Alumel and chromel wires, with a thickness of 0.25 mm in diameter (PI-KEM Ltd), were used as the sensor thermo-elements to form K-type TCs at each junction.

In this study, a wire formed grid architecture comprising of four alumel and four chromel (4x4) thermo-elements, resulting in sixteen independent sensing points, was used. It is proposed to evenly place the SSPs across the cell surface hence a 4x4 grid architecture is used yielding these sixteen sensing points, with the aim to achieve higher resolution. The fabricated SSPs are directly mounted on the cathode electrode by applying tiny amounts of alumina on the junctions to physically bond the sensor on to the electrode as well as preventing possible electrical interaction between sensor thermo-elements and the cathode. Therefore, the SSPs are in direct physical contact with the cathode surface via alumina, an electrically non-conductive media,

throughout the experiment. With this set up it is hoped that the sudden temperature variation caused by cell electrochemical and chemical activities are captured as soon as the heat is released. Depending on the location of the SSPs, the released heat from the cell activities can be monitored and if there is non-uniform temperature occurrence in the measuring environment this will be detected. The supplied gases, heat fluctuation in the furnace and radiation due to the furnace heating element are potential ways that temperature fluctuation on the operating SOFC cell temperature can be created. For this reason it is crucial to have a temperature sensing capability with a high temporal and spatial resolution to obtain a realistic temperature distribution related to the cell activities.

Fig. 42 shows the schematic view of the SSPs implemented on a transparent cell which is placed on the anode compartment of the manifold with silver mesh and silver thin film current collector (light blue coloured cross). Due to the limited space for current collection the thin film silver is sputtered to enlarge the active contact area to facilitate more effective monitoring of the active area temperature relationship. The locations of the SSPs, fuel and air inlets and outlets and the two commercial TCs are also shown in Fig. 42. As aforementioned it is assured that there is no electrical contact between sensor and cathode electrode and no physical contact with the current collector. The electrical connection between them was tested by using a multi-meter and there was no electrical connection observed. TC1 (thermocouple 1) and TC2 (thermocouple 2) are located close to S1 and S13, just 2-3 mm above the electrode surface, respectively. The TCs are placed in the flow channel (2-3 mm above the surface) to simulate the generally applied implementation which offers a more realistic comparison of the findings with results available in the literature. The potential electrical interference between the TCs and implemented sensor is also checked and secured before the experiment by using a multi-meter. Fuel inlet and outlet holes are represented with the dashed circle in the top-left and bottom-right respectively while air inlet and outlet holes are represented with solid circles in the bottom-left and top-right respectively in Fig. 42. The counter-flow which offers higher efficiencies compared to co-flow field configuration is achieved. The air enters from the bottom left and exits from the top right, whilst the situation is reversed for the fuel (Fig. 42).

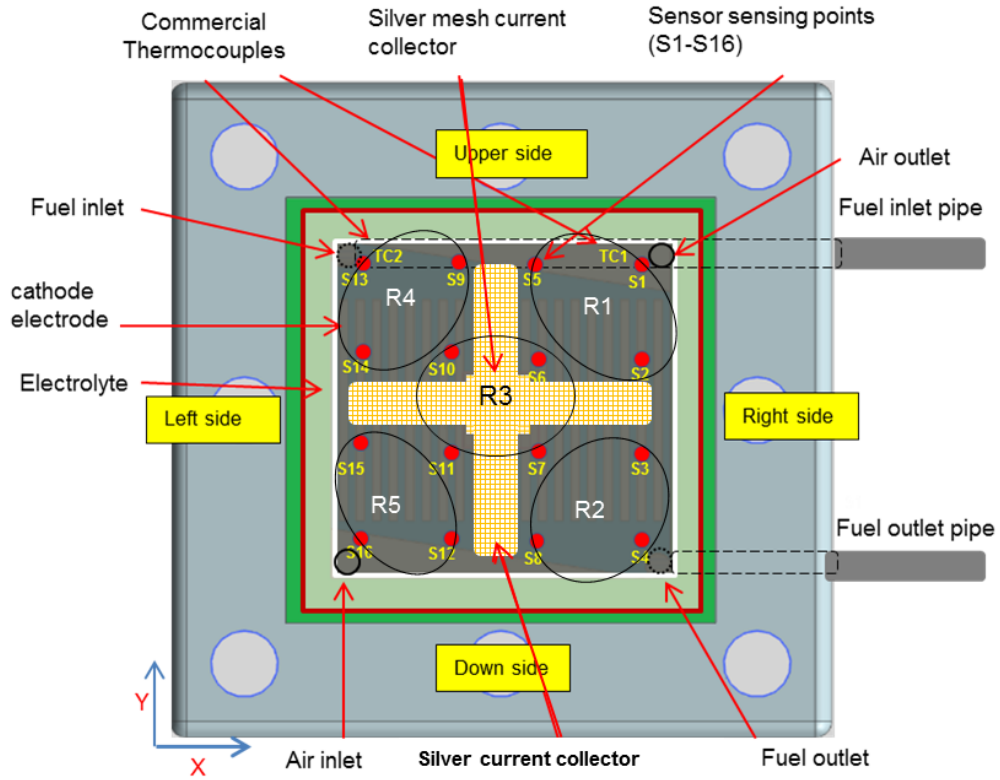


Fig. 42. Schematic representation of cell-sensor configuration

6.3. SOFC Anode Reduction and Operation

After the whole assembly was completed, including sensor and cell electrical connection, the assembled manifold was placed in a high temperature horizontal furnace as seen in Fig. 43. The horizontal furnace has two open sides on the right and on the left to insert the required pipes or/and external wires within the furnace. The open part of the furnace is closed with a sealing material (thermal fibre), though it is expected that more heat loss, via convection and conduction, can occur at the points closer to these sealed parts. As a result, there can be a temperature difference in the furnace with lower temperatures measured near the wall, or sealed part, compared to the middle part of the furnace. Expectedly the manifold and the cell inside the manifold are also affected by this temperature variation. As a result, a local temperature gradient may occur on the manifold as well as along the entire cell surface in differing ranges depending on the thermal inertia of each component. However, the impact from the working environment on the cell temperature will be considered during analysis of the monitored cell temperature under different

operating condition of a running SOFC. Since these external impacts are constant and do not change with varying operating condition, it is not difficult to distinguish these effects from the impact caused by the cell activities. The placement of the manifold in the furnace is shown in Fig. 43 where the manifold is 2.5 cm away from the left wall and is 6.5 cm away from the right wall. The reason for placing the manifold in this way is that the built in furnace temperature sensor is placed in the centre of the furnace. The factory positioned furnace sensor for sensing the inside temperature is not aligned with the cell. The possible impact from the factors correlated with the furnace specification, and design and placement of the manifold on temperature distribution is considered in the discussion following experimental action to distinguish the sources of the released heat.

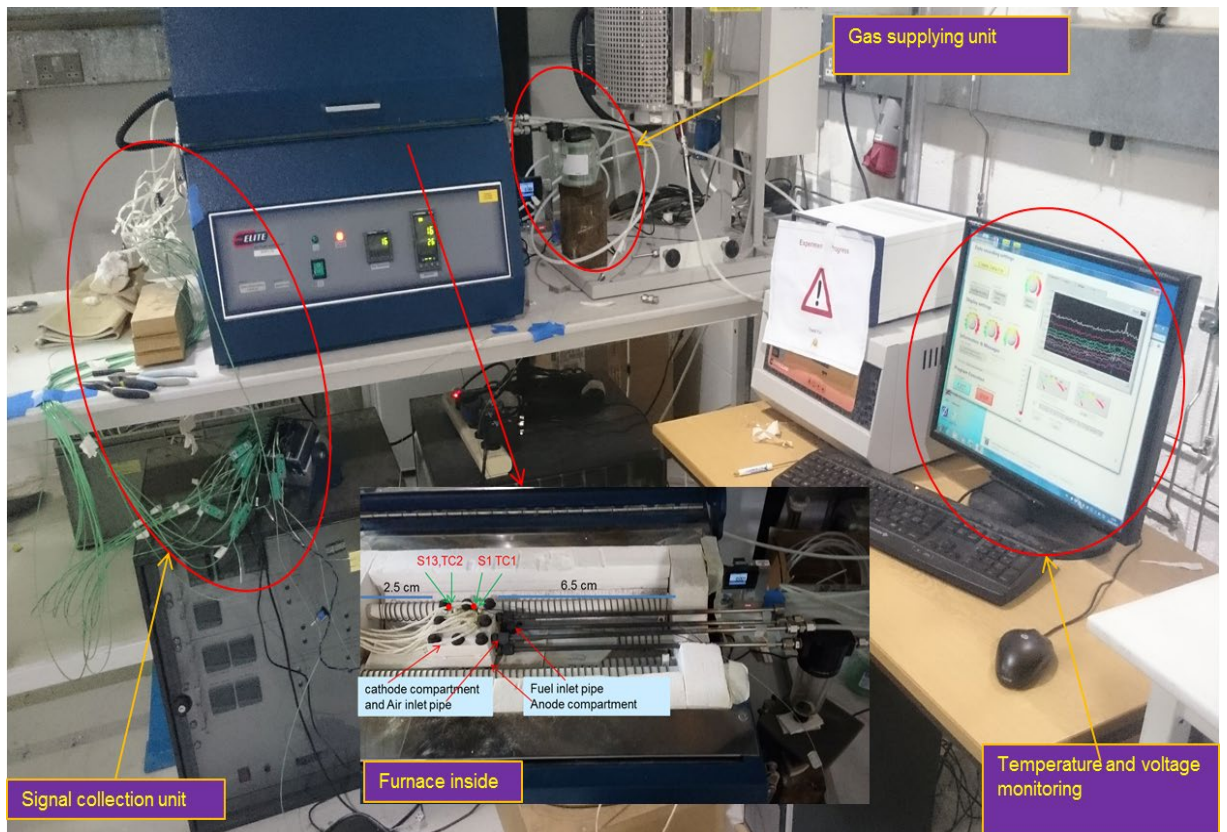


Fig. 43. Experimental set up

Once all the required gas pipes, including Nitrogen (N_2), Hydrogen (H_2) and Air, were joined with the corresponding inlets and outlets of the manifolds, the furnace was closed and sealed. The furnace temperature was increased to first $250\text{ }^{\circ}\text{C}$ ($2\text{ }^{\circ}\text{C min}^{-1}$) and dwelled for two hours at that temperature for curing purposes of the applied silver and alumina pastes. The applied paste materials alumina for sensor

wire bonding and silver for current collector bonding are required to be cured at 250 °C for two hours. Then it was increased to 750 °C (2 °C min⁻¹) to start the anode reduction process which is required prior to cell operation. The heating rate is generally kept small (less than 2 °C min⁻¹) to prevent the ceramic based cell from thermal shock related cracks due to sudden temperature changes. N₂ gas (75 mL min⁻¹) was constantly sent to the anode chamber throughout heating as well as during the experiment process to prevent any redox reaction. When the furnace temperature reached 750 °C, H₂ was sent together with N₂ at a flow rate of 50 mL min⁻¹ for the anode reduction process for a period of 10 hours. After the reduction process was completed the furnace temperature was increased to 800 °C with the same heating rate for testing the cell performance and temperature distribution under real operating conditions. All the sensor wires were connected to the data logging system where the LabVIEW programme performed the data acquisition. The data for temperature measurement and cell voltage measurement were recorded in the same interval simultaneously by the same data logging system. During the open circuit condition there is no electrochemical reactions expected to occur on both cell electrodes. Whilst during the loading condition a certain amount of electrons are allowed to transfer from anode to cathode through the external electrical circuit leading to electrochemical reactions taking place on both electrodes. The electrical wires (current collectors for anode and cathode) are connected to each other via a Potentiostat machine. The rate of the electrons allowed to travel is controlled by the Potentiostat which can apply different impedance to the circuit depending on the desired amount of electron transfer. For instance it applies a very high resistance to block electron leakage from the anode to cathode during OCV condition.

6.4. Results and Discussions

6.4.1. Temperature distribution under OCV condition:

Fig. 44 shows the temperature distribution from both SSPs (S1-S16) and TCs (TC1-S1 and TC2-S13) under OCV conditions with two different H₂ flow rates of 25 mL min⁻¹ and 50 mL min⁻¹. The experimentally obtained OCV (E_{cell} 1.07V) is reasonable compared to the theoretical OCV (E_{ner} 1.09V) which is calculated according to the

Nernst equation (Equation 19, discussed in following section) and found to be slightly higher than the experimental OCV. Furthermore a step increase is observed in both E_{cell} and E_{ner} due to the step increase in fuel flow rate as a result of increases in partial pressure of the reactant. The furnace set temperature was 800 °C and this was maintained during the experiment.

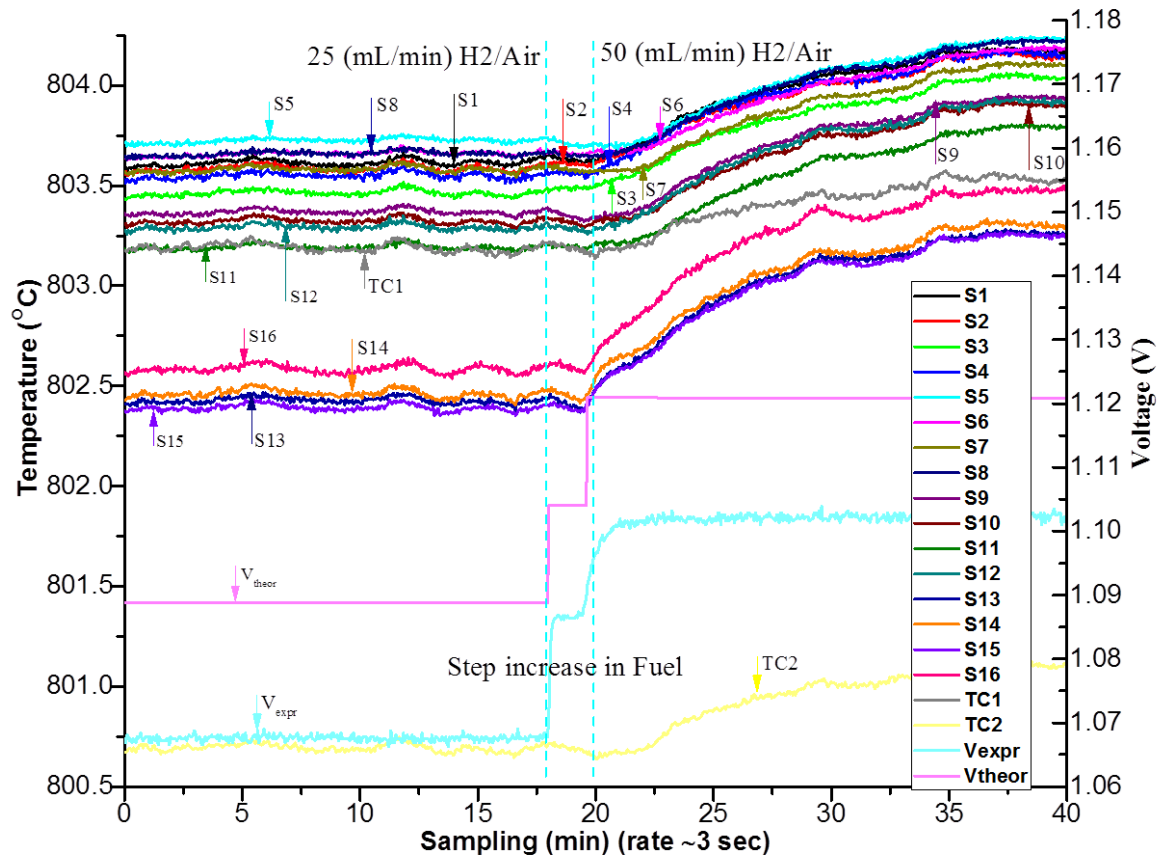


Fig. 44. Temperature monitoring from sixteen sensing point and two TCs

As it can be seen from Fig. 44, there was about a 2.5 °C difference between readings from the TCs in which the temperature of TC1 is slightly higher than 803 °C while TC2 is at about 800.5 °C with the flow rate of 25 mL min⁻¹. When the flow rate is increased from 25 mL min⁻¹ to 50 mL min⁻¹ they are both slightly increased (~0.25 °C). Whereas the maximum temperature differences in readings from the SSPs were about 1.25 °C (between S5 and S15) with the 25 mL min⁻¹ H₂ flow rate. This difference decreased to ~1 °C (again between S5 and S15) with the increased flow rate. As seen from Fig. 42 TC1 is located close to S1 and TC2 is close to S13 and the manifold is placed closer to the left side of the furnace (Fig. 43). Before the

flow rate increment, all the measurements (802.5 °C) with S13-S16 were less than the measurement obtained from the other SSPs, as they are located on the left side of the manifold which is where the fuel and air inlets are placed (Fig. 42). While the obtained temperatures readings (~803.6 °C) from S1-S8 were the highest with a small difference between each other's followed by S9-S12 with the temperature reading of ~803.25 °C. As can be seen from Fig. 44, there is a lower temperature observed from the SSPs located to left side of the cell which is where the air and fuel inlets are located than the temperature obtained from the SSPs closer to the air and fuel outlet which is the right side of the cell. This can be caused by the fuel and air cooling effect and more heat loss at the left side of the cell which is closer to the furnace wall. The similar behaviour is also seen from TC1 and TC2 where TC1, which is located to the right center of the manifold, shows a higher temperature than TC2 which is located to the left side of the manifold (closer to the fuel and inlet points). The effect due to the manifold position can be attributed to non-uniform temperature distribution between the middle part of the furnace and the points closer to the furnace wall as seen in Fig. 43.

The temperature profile of the cathode surface due to the temperature increments for each sensing point with the increase in flow rate from 25 to 50 mL min⁻¹ is illustrated in Fig. 45. To observe the increments of each SSP it is important to identify the heat sources leading to these temperature variations.

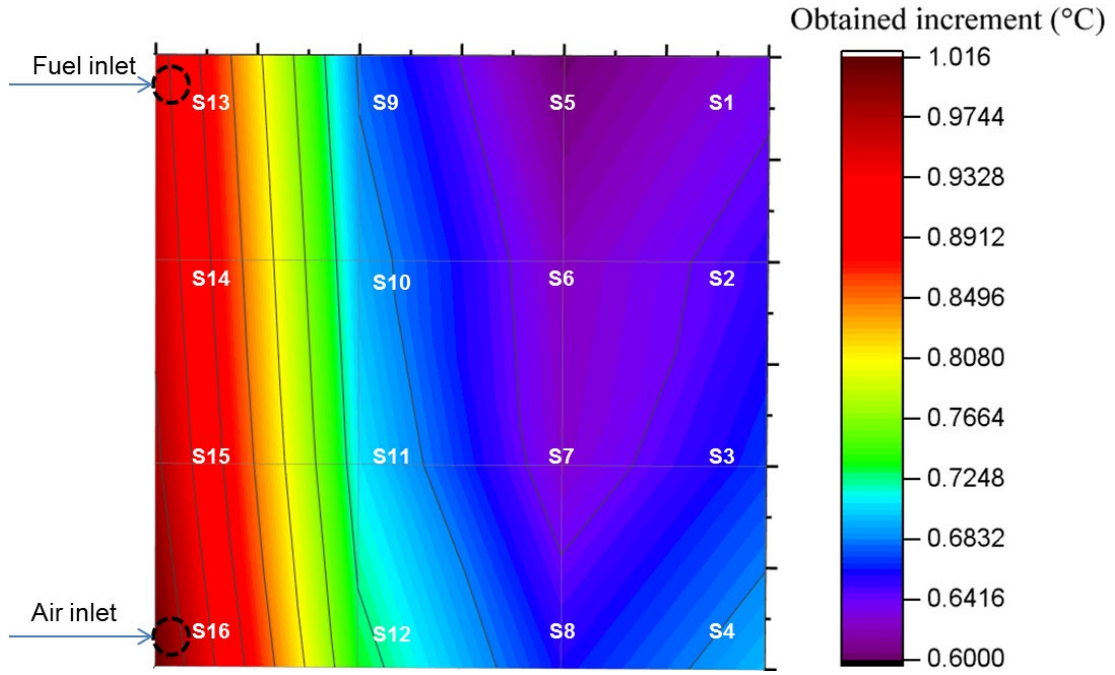


Fig. 45. Increment in temperature with the increase in flow rate under OCV condition

As seen from Fig. 45, when considering the effect of flow rate there are similar temperature increments (about 0.6 °C) obtained from S1-S12 with a small variation (~ 0.1 °C) among them. The maximum increment (1 °C), on the other hand, are monitored from S13-S16 located close to the fuel and air inlets (left side of the cell). Additionally, even though, the minimum increment (0.4 °C) is obtained with the TCs, they show a similar behaviour to the SSPs as the TC2 located near the gas inlets shows a higher increment than the TC1 located closer to the air and fuel outlets (right side). There can be three reasons for temperature increase with flow rate. The first reason is a small gas (H_2) leakage from the anode to the cathode via the gasket leading to direct oxidation of themselves with the air at the cathode side near the outer side of the cell. This is more likely at the gas inlet and outlet due to the higher pressure expected at these points. Despite the purpose built cell holders being checked in terms of gas leakages before experimentation, there is still the potential for a marginal level of gas leakage when considering SOFC operating conditions. It is proved by the result depicted in Fig. 45 as the average increments monitored from the SSPs located around gas inlets and outlets (outer side of the cell/nearby gasket) are higher than the average increments obtained from the sensing points located near the inner side of the cell (see Fig. 42 for SSPs locations). However in addition to this, the gas leakage via electrolyte is less likely or small since OCV (E_{cell}) reached

its expected value 1.1V. Nonetheless it does not mean that there is no leakage via gaskets [163]. The second reason can be the oxidation reactions taking place between the supplied H_2 and preoccupied oxygen from the anode reduction process. Even though the microstructure changes of the anode due to anode reduction where NiO is reduced to Ni has been studied [164], [165] there is no study available specifically focused on the temperature changes with reduction process in the literature. Hence it is difficult to confirm or deny this as a possibility. Another reason can be attributed to electronic current leakages as it is difficult to avoid electronic conduction of electrolytes at high operating temperatures (especially with a ceria involved electrolyte) [166]. Those electrons allow oxygen to be reduced at the cathode resulting in oxygen ions. These ions are kinetically active enough to travel to the anode at this operating temperature. There is an oxidation reaction taking place at the anode when these oxygen ions meet with hydrogen leading to a heat release. The starting point of the circle is electronic current leakages which has a direct relation with the amount of supplied fuel. The reason for the lower increment obtained from the TCs in comparison with the corresponding SSPs located near them, is due to distance to the heat sources. The most likely reason is the direct oxidation reaction that takes place in the porous cathode electrode that is first detected by the SSPs which are in direct contact with the electrode surface. It is also important to note that the response time (temporal resolution) of S13-S16 near to the inlet side to the temperature changes is 2-3 minutes quicker than TC2 which is located close to S13. The reasons for the obtained increment will be also discussed from the SOFC's thermodynamics point of view in the following section.

6.4.1.1. Thermodynamic approach to the obtained temperature variation:

As illustrated in Fig. 44 the obtained experimental OCV (E_{cell}) increased gradually with the step increase in fuel flow rate due to the increase in partial pressure. To compare E_{cell} and E_{ner} , the Nernst equation, as shown in equation 19, is performed for the theoretical calculation of the OCV. As seen from Fig. 44 there is good agreement between experimentally (E_{cell}) and theoretically (E_{ner}) obtained OCV values as they both agree with the value available in the literature [163].

$$E = E^{\circ} + \frac{RT}{nF} \ln\left(\frac{P_{H_2} \times P_{O_2}^{0.5}}{P_{H_2O}}\right) \quad (19)$$

Where, E is the operating OCV, E° is the OCV at fuel cell operating temperature and standard pressure (1 atm), n is the moles of electrons released for every mole of H_2 reacted ($2 \text{ mol } e^{-} \text{ mol}^{-1} H_2$), F and R are the Faraday and gas constant respectively, P_{H_2} , P_{O_2} and P_{H_2O} are the partial pressure of reactants and product respectively.

According to the Nernst equation, there is an inverse relation between cell voltage E_{ner} and operating temperature due to a decrease in Gibbs free energy with the increase in temperature, while it increases with the increase in reactant partial pressure [41]. The obtained result from all SSPs and TCs shown in Fig. 45 agrees with this as E_{cell} increased with the step increase in H_2 fuel/air flow rate. However there is an increase also observed in temperature and this is something that cannot be straightforwardly explained by the thermodynamic aspects of the SOFC system. Since the reason for the increase in temperature with fuel flow rate is most likely due to H_2 leakage to the cathode side generating direct oxidation of H_2 as aforementioned, which is not accounted for in the thermodynamics of SOFCs. Additionally, one of the possible reasons could be the oxidation reaction taking place at the anode side between the pre-occupied (remained from the anode reduction) oxygen and supplied H_2 as the partial pressure increased with the increase in flow rate. The effect of increased H_2 partial pressure can also be seen from the changes in E_{cell} and E_{ner} as depicted in Fig. 44. Thus, there is no simultaneous change between temperature and measured OCV. Besides, even though the OCV increased immediately, as soon as the fuel rate increased, the increase in cell temperature (from all SSPs) was only monitored within an interval of time, where this time scale will be discussed in more detail in section 6.6.1. Moreover, both E_{cell} and E_{ner} are constant or slightly decreasing which is not visible due to the small increase in temperature due to changes in Gibbs free energy as expressed in equation (20):

$$\Delta G^{\circ}_{\text{rxn},T} = \Delta H^{\circ}_{\text{rxn},T} - T \cdot \Delta S^{\circ}_{\text{rxn},T} \quad (20)$$

Where, ΔG° is Gibbs free energy, ΔH° is the enthalpy, ΔS° is the entropy and T is the operating temperature of the reaction.

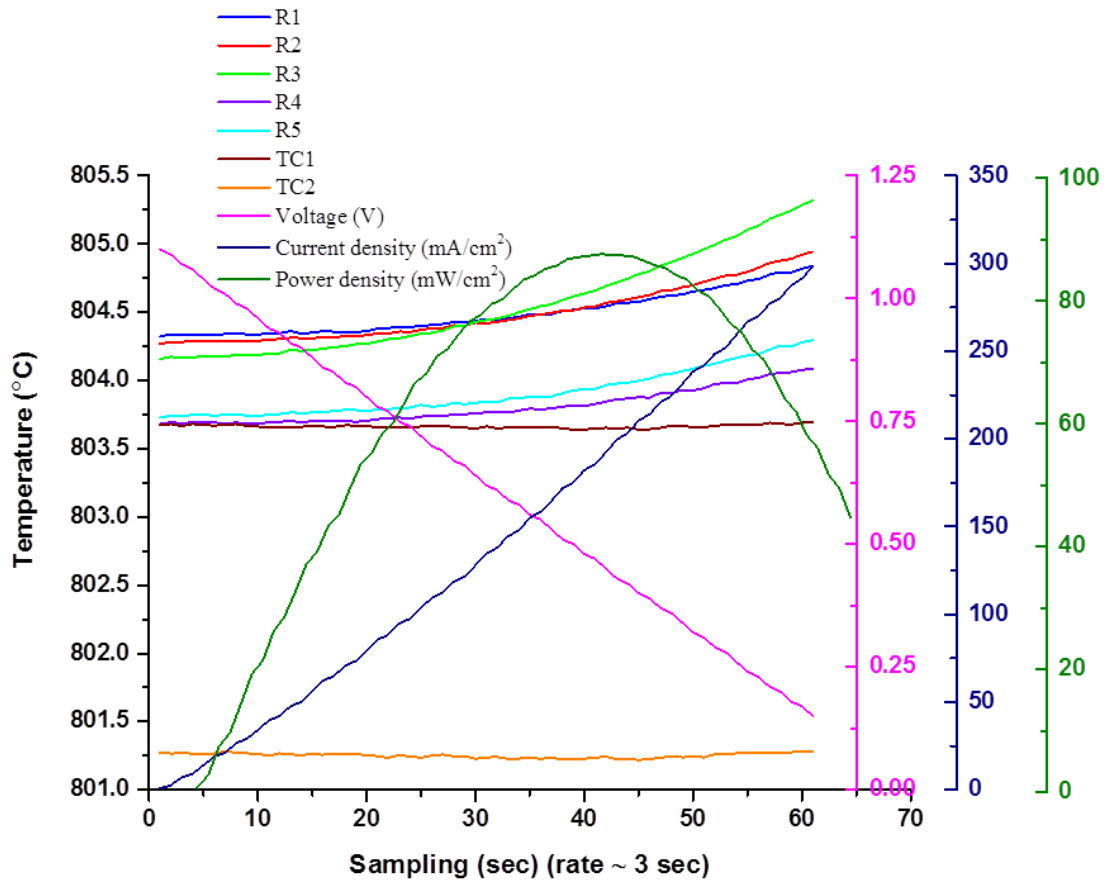


Fig. 46. Variation of local regions temperature during polarisation

There are five local regions created by obtaining the average readings from the nearest SSPs to provide a clear view of the graph. The regions (R1-R5) of the grouped SSPs correspond to R1 which is near to the air outlet, R2 is near the fuel outlet, R3 is near the current collector, R4 is near to the fuel inlet and R5 is near to the air inlet which is shown in Fig. 42 for their location and Table 7 for their group. Fig. 46 shows the temperature variation of the regions R1-R5 and conventional TCs during the polarisation where the maximum available current with the corresponding voltage and resultant power output are given. The highest increment is monitored from R3 due to higher rate of electrochemical reaction which results in more heat release while the increment is almost similar for all other regions as they are symmetric to each other in respect to the current collector. The power output, voltage

and current are represented by the coloured axes on the left side of the graph while the axis on the right side shows temperature variation.

Table 8 Regions and their corresponding SSPs

Regions	R1	R2	R3	R4	R5
Average readings Corresponding SSPs	(S1,S2,S5)	(S3,S4,S8)	(S6,S7,S10,S11)	(S9,S13,S14)	(S12,S14,S15)

As seen from Fig. 46 the temperature gradient is increased with the increase in drawn current resulting in a decrease in voltage. The maximum power density (90 mW cm^{-2}) is obtained by multiplying the corresponding cell voltage and current density under the described experimental condition and is presented in the Fig. 46. The experimental condition and the size of the current collector used are the driving factor for the obtained cell performance in the current study which is also explained in more detail in section 6.6.

It is important to note that the prediction of these kinds of small unexpected temperature increments or changes occurring on the cell surface are hard to notice by mathematical modelling which is generally carried out by considering the conventional $I-V$ curve [128]. Since the change/loss in OCV with temperature is negligible they could be attributed to a number of reasons. However, identifying the temperature dynamics along the cell surface can be vital for thermally induced stresses and their related problems that can lead to detrimental and often non-recoverable damage to the cell [31], [123], [167], [168]. The temperature profile of the cell under OCV condition is monitored and the reason for the temperature increment is found to not be related to the thermodynamics of SOFCs. Instead it is more likely due to gas leakage. The temperature increment due to cell electrochemical activities will be discussed in the next section.

6.4.2. Temperature distribution under loading conditions

Electrochemical and chemical cell reactions are the main factors leading to a temperature gradient across the cell surface due to an uneven reaction rate through the entire cell surface. In this section the temperature increment through the cell surface due to electrochemical reactions under a constant loading condition is monitored. Fig. 47 shows the temperature distribution obtained from all SSPs and TCs during loading when 750 mA current is drawn from the system. The maximum current is obtained as ~825 mA. Since running the SOFC under maximum current is not recommended, the operation is carried out by drawing 750 mA current. The experimentally obtained voltage (E_{cell}) and theoretically calculated Nernst voltage (E_{ner}) and their correlation with the monitored cathode temperature distribution are plotted in Fig. 47. The furnace set temperature was 800 °C and H_2/Air is sent with a constant flow rate of 50 mL min⁻¹ throughout the process. Other cell polarizations including ohmic, activation and concentration losses are not taken into account during the theoretical voltage calculation since these are not the focus of this study. Therefore the decrease in theoretical cell voltage named as E_{ner} is due to partial pressure changes of the fuel and oxygen used according to the Nernst equation.

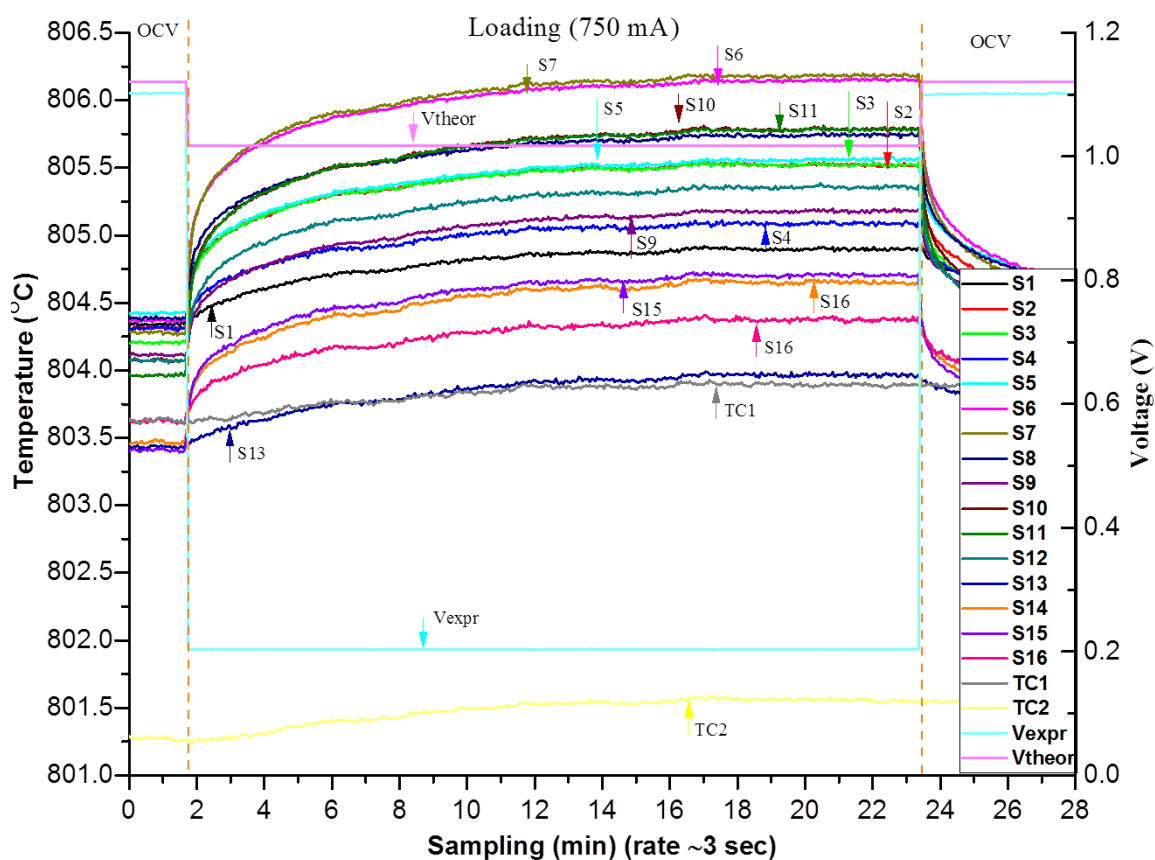


Fig. 47. Temperature distribution under constant loading condition

The temperature distributions during OCV and their changes when 750 mA (loading) is drawn from the cell are depicted in Fig. 47 with a 50 mL min^{-1} fuel flow rate. To observe the temperature distributions under both OCV and loading it is important to investigate the origin of the heat sources contributing to the temperature variation when some current is drawn from the system. Allowing the electrons to travel from the anode to the cathode, there is a clear increase in temperature due to electrochemical reactions taking place, observed from all SSPs indicating that the cell average temperature is increased. More importantly, the maximum temperature difference among the SSPs S1-S16 increased from 1°C (OCV condition) to 2.25°C when the system is loaded (between S7 and S13 see Fig. 47) while it is constant and 2.25°C for TCs as seen from Fig. 47. This is because of the higher spatial resolution of the inserted sensor compared to TCs as the measurement is obtained directly from the electrode surface with the sensor while TCs which were placed in the flow

channel obtaining the average inside temperature. The observed temperature increments of all SSPs and TCs under the loading condition are plotted in Fig. 48. The main parameter identified as the contributor to the temperature increments is the results of the exothermic electrochemical reaction, namely joule heating and heat due to resistance to ionic and electronic flow [106]. As can be seen from Fig. 48, the pattern of the measured increments of the SSPs during the loading condition has an inverse relation with the pattern obtained during OCV condition due to flow rate changes which is depicted in Fig. 45. There was the highest temperature increment obtained near gases inlets with increasing flow rate which was attributed to direct oxidation of H_2 correlated to fuel leakage. In the loading condition on the other hand higher temperature is monitored at the points where the current collector is placed which refers to the exothermic electrochemical cell reactions.

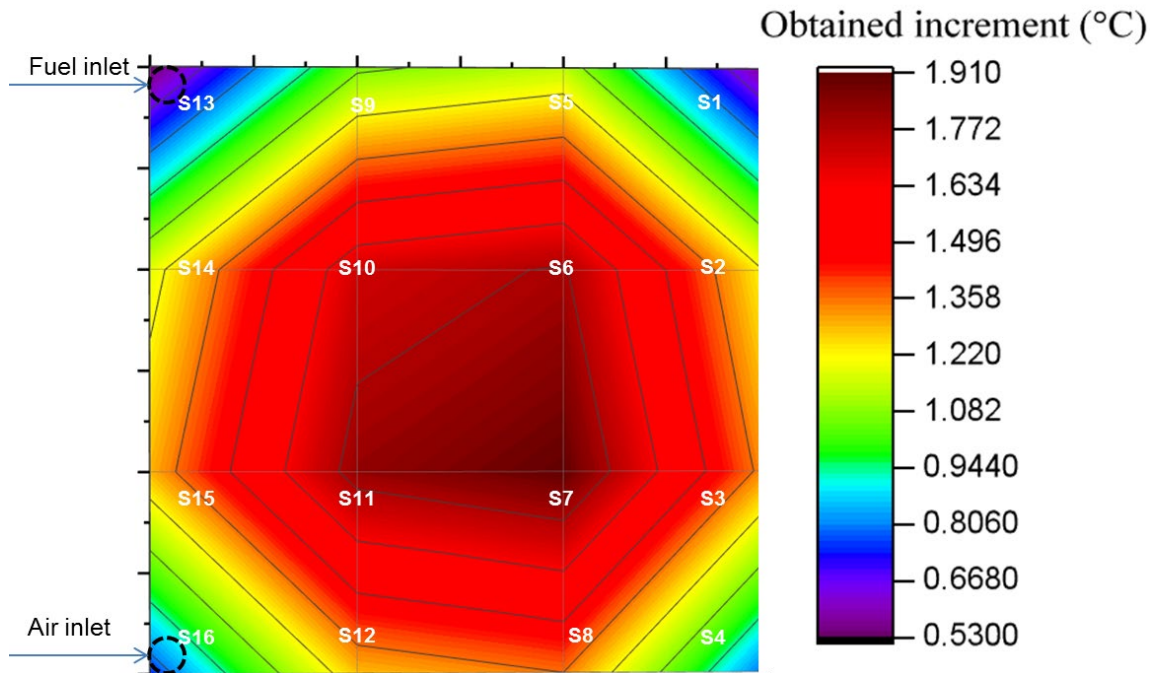


Fig. 48. Temperature distribution across the cell with loading

The SSPs which are located around the silver mesh (S6, S7, S10 and S11) show the maximum rise with an increment of approx. 1.8 °C followed by S2, S3, S5, S8, S9, S14 and S15 (which are located close to the sputtered thin film silver of the current collector). While S1 and S13 shows the minimum increment of approximately 0.5 °C followed by S4 and S16 which are located on the corner of the cathode. In other

words, the four sensing points including S1, S13, S4 and S16 which are relatively far from the contact area (between the current collector and cathode) is where more electrochemical reaction takes place [169]. On the other hand, TC1 and TC2 increased about 0.25 °C and 0.3 °C, respectively, which is less than half of the measurement obtained from SSPs S1 and S13 located close to TC1 and TC2, respectively (Fig. 47). The location of the TCs seems to be the main reason for this since they located at the flow channel hence they are affected by the fuel flow temperature.

As it can be seen from Fig. 48, there is an apparent relation observed between the contact area and the temperature increments of the cell. The maximum temperature increments are observed near the current collector as more heat release is expected from where the electrochemical exothermic reaction is taking place [158]. The effect of the heat due to Joule heating and contact resistance is less compared to the heat released due to exothermic reactions, but their contribution is most likely higher near to the current collector cell contact point [170]. Regarding this the results show that the contact area between the current collector and electrode (interconnect and electrode for a stack configuration) is found to be a noticeable contributing factor to the given temperature distribution. Regardless of the fuel inlet there is a higher temperature increment monitored from the SSPs near to the current collector. In other words the fuel flow direction affects the temperature distribution when a completely even current collection mechanism is achieved across the entire cell surface.

At the same time, the fuel flow path is also an important parameter as for temperature. It becomes the limiting factor causing overall output deterioration with the presence of an air gradient [130], [131], [171]. In order to observe the effect of the direction of the provided fuel and air flow, the SSPs which are placed on the same flow channel and have similar distance to the contact area are compared. In respect to this, S2, S6, S10 and S14 located on the second row and S3, S7, S11 and S15 located on the third row are compared. Since each couple, such as S2 and S3, are on the same flow channel and have similar distance from the contact area both should experience similar contributions from the electrochemical reaction. As seen from Fig. 48, the obtained increments for the SSPs in the second row are 0.1 °C less than the increments for their corresponding SSPs on the third row. Similar relations

are obtained for the other couples (S6-S7, S10-S11 and S14-S15). Furthermore, the temperature increments for the SSPs on the first row are less than their corresponding SSPs located on the fourth row. There can be two possible reasons for this; air fraction across the cell surface occurs in the region of the electrode and/or the cooling effect by the supplied fuel (as the fuel is sent along with N₂ leading to a total flow rate of 125 mL min⁻¹). Since the produced air has a flow rate of 50 mL min⁻¹ including only 20% O₂ (10 mL min⁻¹ O₂) provided from the bottom- left side corner (see Fig. 42 for location and Fig. 48 for temperature), therefore there is the possibility of an insufficient supply of O₂. Normally air on the cathode side is considered as the reason for cooling and moreover it is used to remove the excess heat [122], [132], [172]. Nonetheless the same amount of air and fuel were used in this study to eliminate any possible manipulation from excess air to the temperature distribution. Hence the obtained increments are naturally due to electrochemical reactions only. Regarding this finding it is worth noting that the fuel/air starvation/fraction is not only causing performance degradation but also contributing to the thermal gradient along the cell surface. According to some studies the cathodic half reaction is exothermic [107], [30]. If that is the case, this could be the reason for the SSPs which are representing a slightly higher increment in comparison with their counterpart SSPs as they could be exposed to air starvation/fraction.

Furthermore, in order to analyse the cooling effects of the produced gas, the SSPs located on the left side (S9 - S16) and the SSPs on the right side (S1 -S8) of the cell are compared by taking into account their distances to the current collector. This is evaluated as the cooling effect due to the supplied gas temperature is considered an important contributor to temperature gradient in an SOFC system [42], [43]. As seen from Fig. 48, the SSPs located on the left side of the cell show a slightly lower temperature increment than their corresponding SSPs located on the right side of the cell. For instance, S2 and S3 show slightly higher increments than their corresponding sensing points S14 and S15, respectively. This is hence deemed due to the gas cooling effect as S14 and S15 are closer to the gas inlets which are affected more than S2 and S3.

6.4.2.1. Thermodynamic analysis of the obtained temperature increment

The relationship between the operating temperature and cell voltage has already been mentioned in the above sections. Thus, in this section the corresponding temperature increment from the released heat is theoretically calculated to compare the experimentally obtained temperature variations. By taking into account the described experimental condition, the data from the experimentally obtained I - V curve is applied as the main source during the calculation. Hence, equation (22) is derived for the relationships between the I - V correlated data and the corresponding released heat from the reactions. As a result of calculation from the equation the reacted molar flow of H_2 depending on the drawn current density and the equivalent fuel flow rate at both the anode and cathode electrodes under the loading condition are determined [175]. In order to achieve this obtained current density (mA cm^{-2}) is converted to reacted flow rate and using the reaction stoichiometry of the H_2 oxidation (equation 3) then corresponding O_2 flow rate is also calculated.

$$250 \frac{\text{mAmps}}{\text{cm}^2} \left(\frac{\text{mC}}{\text{s.cm}^2} \right) \times \frac{1 \text{ mol } e^-}{96485 \text{C}} \times \frac{1 \text{ mol } H_2}{2 \text{ mol } e^-} \quad (22)$$

$$\begin{aligned} \text{Reacted molar } H_2 &= 1.3 \times 10^{-6} \left(\frac{\text{mol}}{\text{s.cm}^2} \right) \\ &\rightarrow \text{equivalent } H_2 \text{ flow rate found as } 5.2 \text{ mL min}^{-1} \end{aligned}$$

$$\begin{aligned} \text{Reacted molar } O_2 &= 0.65 \times 10^{-6} \left(\frac{\text{mol}}{\text{s.cm}^2} \right) \\ &\rightarrow \text{equivalent } O_2 \text{ flow rate found as } 2.6 \text{ mL min}^{-1} \end{aligned}$$

The total gas sent to the cathode side is 50 mL min^{-1} air which includes a 10 mL min^{-1} O_2 flow rate due to its percentage (0.2%) in air. According to the amount of obtained O_2 (2.6 mL min^{-1} out of supplied 10 mL min^{-1}) the utilisation of the O_2 is calculated as 26%. As the aforementioned O_2 is thought to be a limiting factor in this experiment, this allows investigation into the fuel starvation/fraction based effect on

temperature distribution. Besides, the utilisation of H₂ is calculated as about 10% (5.2 mL min⁻¹ reacted out of 50 mL min⁻¹ supplied amount) which is seriously low and the main reason for a relatively low power density (Fig. 46). However the main focus of this study is not directly related with the cell optimum performance, it is instead the temperature profile under the given conditions.

Table 9 flow rate of supplied gases and percentage of the excess gases

	Total gases flow rate sent (mL min ⁻¹)	Percentage of excess fuel
Anode	125 (H ₂ (50), N ₂ (75))	96%
Cathode	50 (Air)	94.8%

The molar flow of the reacted H₂ is calculated from the equation given in (22) by using the drawn current density. Regarding this, Table 9 illustrates the percentage of excess gas out of the total feed gases on both the anode and cathode chamber separately. This is important to know due to the fact that the higher the amount of excess gases the greater the likelihood of more of a cooling effect on the measured temperature increment (cooling effect has a minimal effect due to pre-heated gases). From the other side, the lower utilisation of H₂ is because of the small cell active area used which is limited by the small sized current collector (3 cm²).

The given formulas in equation (23) [106] and (24) [176] for the released corresponding heat from the electrochemical reaction and net resultant heat after the effect of heat losses is considered.

$$Q_e = R_e \Delta H_f - I_{cell} E_{cell} + \frac{I_{cell}^2}{\sigma} \quad (23)$$

$$\Delta Q = Q_e - Q_{conv} = mc_p \Delta T \quad (24)$$

$$Q_{conv} = h \times A \times \Delta T \quad [\Delta T = (T_s - T_f)] \quad (25)$$

Where the heat flux Q_e (J s⁻¹) is the released heat rate for cell area from the electrochemical reaction, R_e is the reacting molar flow, ΔH_f (J mol⁻¹) is enthalpy of the formation at the given temperature, I_{cell} (Amps cm⁻²) is the current density and

E_{cell} (V) is the voltage of the operating cell and σ is taken as the bulk ionic conductivity of the YSZ electrolyte for joule heating purposes calculated at roughly 3 Sm^{-1} [177]. ΔQ (J s^{-1}) is the net heat that increased the cell temperature, Q_{conv} (J s^{-1}) (7) is the heat lost, m (kg) is the mass of the cell, C_p is the specific heat capacity ($\text{J g}^{-1} \cdot \text{K}^{-1}$) of the cell and ΔT (K, $^{\circ}\text{C}$) is the temperature difference between the cell solid (T_s) and fuel (T_f) phase in the anode and cathode channel. Since there is two phase (solid and gas) at the point where the heat released by the electrochemical reaction and it is questionable whether temperature of these two phases are same or not. Thus, it is worth noting that the local thermal equilibrium (LTE) aspect which refers to the negligible heat transfer from the solid to the gas phase within the porous electrode is considered during the analytical calculation [178]. A heat loss via convection due to advection of the excess gases through the fuel flow channels is assumed as the only reason for heat consumption. Additionally, heat contributions of cell overpotential losses are inherently taken into account in equation (5), by using the product power of the measured cell voltage and current density, in lieu of the product of activation and concentration overpotential with current density. The joule heating term yields a value of approximately 0.024 W and is henceforth neglected in the analysis. Heat losses via conduction through the cell gasket and manifolds are not directly calculated by per-component basis, due to complexity of determining the exact contact boundaries of the components. Instead, their effects are brought to bear via time-dependent analysis of the thermal gradients, as to which body or bodies are acting as heat conducting and absorbing masses.

If it is assumed that all the released heat is consumed or coming out due to convection, then the maximum temperature difference can be calculated

$$mc_p\Delta T = \frac{0.273j}{s} \left(Q_{in} \frac{J}{s} \right) - \frac{0.033j}{s} \times \Delta T \left(Q_{out} \frac{J}{s} \right) \quad (26)$$

From equation (26) the rate of the temperature difference is calculated as $0.06 \text{ }^{\circ}\text{C s}^{-1}$ with the obtained cell properties of $m=9 \text{ g}$ and $c_p=0.5 \text{ J g}^{-1} \text{ K}^{-1}$. The calculated value is aligned well with the experimentally obtained increment ($0.062 \text{ }^{\circ}\text{C s}^{-1}$) from the SSPs especially for the first gradient shown in Fig. 49. The small difference in experimentally measured and analytically calculated increment can be attributed to the heat dissipated by convection to the gas phase within the porous electrodes which is not considered in the theoretical calculation. There are also contributions to heat

loss from conduction via the SOFC solid components which are in physical contact with the cell, such as gasket materials and ribs of manifolds, and also due to radiation, both of which are neglected during the calculation. The impact of these parameters are being more considerable by time since the heat is transferred through the whole bodies of cell manifold system. Thus there is great difference in the calculated increment rate and the rate measured when the system starts reaching the thermal equilibrium ($\tan\theta_2$ and $\tan\theta_3$). Since at this time, the generated heat is not held by the cell only instead it is held by whole body of the cell manifold arrangement. Thus the left side of equation (26) is required to be modified for realistic analytical temperature increment when the system is about reaching the thermal equilibrium. However, overall, the experimentally obtained increment is promising and shows good agreement with the analytically calculated increment. Three different transient conditions are defined for the monitored temperature variation, for a given time, depending on the gradient ($\tan\theta_1$, $\tan\theta_2$, $\tan\theta_3$) as depicted in Fig. 49. The greatest gradient ($\tan\theta_1$) is observed just after the system is loaded which is about twelve times greater than the second gradient ($\tan\theta_2$). The third gradient ($\tan\theta_3$), on the other hand, is considerably less compared to the two previous gradients as the system is almost reaching the steady-state condition during this period (Fig. 49). If the assumption is held that the cell is the sole body for heat absorbed in the time duration described by gradient $\tan\theta_1$, with $m = 9$ g, equation (8) yields a temperature increment of 30°C after 500 s, which can continue to rise with time if the rate is maintained; this is not the case from the observed experimental readings. This is manifested in the period with the gradient $\tan\theta_2$, which shows a decrease in the rate (from $\sim 62 \times 10^{-3}^\circ\text{C/s}$ to $4.5 \times 10^{-3}^\circ\text{C/s}$). The third gradient ($\tan\theta_3$), on the other hand, is extremely low compared to two previous gradients. By this time, the generated heat is held not only by the cell, but instead is held by the whole body of the cell manifold arrangement/assembly as the system is approximately reaching the steady-state condition during this period (Fig. 9). Thus, the left side of the equation (8) is required to be modified for realistic analytical temperature increment when the system is nearing the thermal equilibrium. In the literature for modelling concerning temperature increments, the obtained values are varying in the region of $60\text{-}120^\circ\text{C}$; this is mainly due to variances in experimental parameters such as fuel utilisation ($>60\%$), [179], [180] drawn current density (much

greater than the drawn current density from this experiment) and sizes and properties of cell and manifold. In particular, the manifold/interconnect is a single block in our presented work, but simulations are conducted with very thin interconnect geometry [179], [180]. It is also possible to determine the difference between the temporal resolution of the SSPs and the conventional TCs by the calculated gradients in which there is no any visible temperature increment monitored from the TCs for first and second gradients. Besides the observed spatial resolution of the SSPs for a given time range is at least six times higher than the TCs as shown in the Fig. 49.

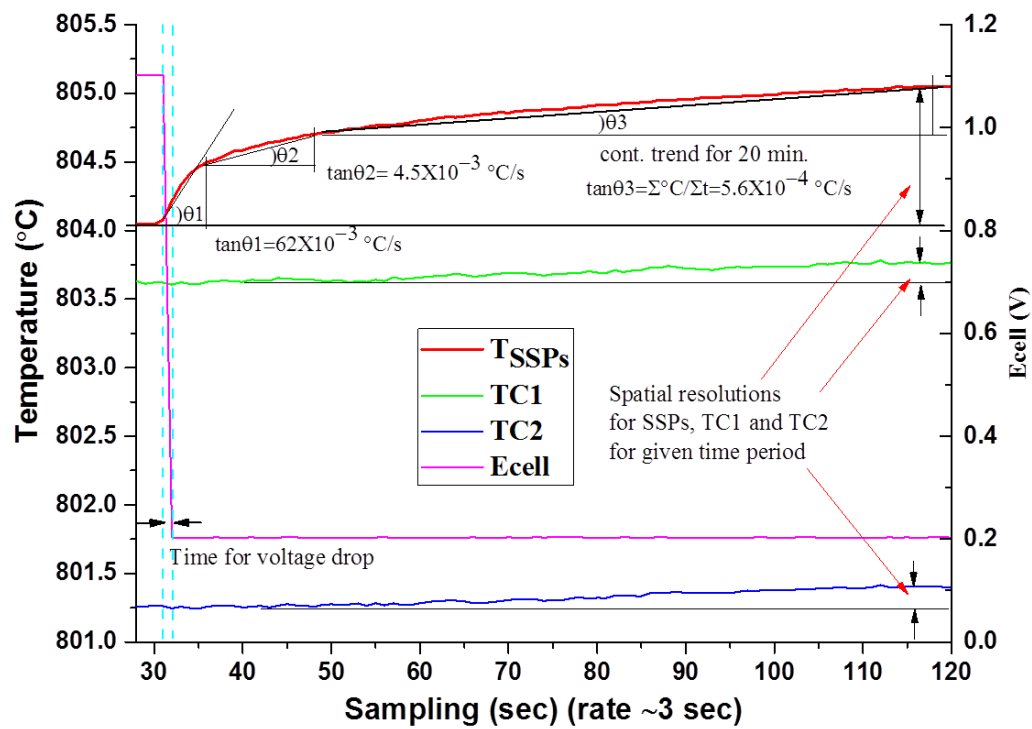


Fig. 49. Obtained average temperature increment under varying conditions

A quicker response of temperature increment is monitored from the SPPs when the system is loaded in comparison with the conventional TCs (Fig. 49). The cell voltage, E_{cell} , drops to a settled voltage of 0.2V from the operating OCV voltage of 1.1V in about 1 sec. It is difficult to talk about a precise steady state condition if there are complex and continuous heat release/sink mechanisms such as those in a SOFC. The heat release/sink mechanism of a SOFC system is affected by some complex parameters including electrochemical and chemical reactions, overpotential losses, and heat losses via radiation, convection and conduction. Therefore the period

(tan θ 1) where the varying sharp increases are monitored can be referred to as the transient condition whilst the period where the slight increase is monitored can be referred to as the partially steady state condition. As seen from Fig. 49, the temperature increment starts as soon as the system is loaded since the SSPs located directly on the cell surface and the temperature difference between holes and the solid body of the cell is negligible [178]. The observed thermal gradient along the cell surface can be considered as small and negligible, which is about 1.5 °C, this is because of the small temperature increase caused from loading due to the small sized current collector and cell. However, there is a greater difference in average temperature increments obtained from SSPs and TCs. This difference increased importantly during loading compared to the increments observed during the OCV condition. The average increments obtained from SSPs (1.25 °C) is approx. five times higher than the average increment obtained by TCs (0.25 °C) during loading. If it is assumed that of those values for the temperature increment would be further increased in constant proportion when the cell and current collector sized is enlarged, there can be a serious discrepancy between flow channel temperature and cell surface temperature. Then, this can be an important difference that can mislead the modeller if the data from TCs is used for validation purposes. This is especially true in the case of having higher thermal gradients as the gradient can further increase depending on the experimental condition, and hence it can be significantly important to have more realistic temperature measurements. Regarding the obtained temperature distribution, cell size, amount of drawn current, fuel and air flow types, cell materials, manifold or stack design, even furnace configuration are important parameters that influence the thermal gradient of the SOFC for both cell and stack level. As it is addressed in the literature [174] there is a strong relationship between those mentioned physical parameters and SOFC operating performance. With the variation of those parameters the temperature distribution can be significant as mentioned in the literature [46], [47]. In respect to this, the presented method has great potential to address the individual source of the released/sink heat during operation with having the advantages of higher spatial and temporal resolution compared to the conventional measurement obtained from the flow channel with TCs.

6.5. Chapter Summary

Temperature distribution of an anode supported SOFC and its changes under OCV and loading conditions is monitored by inserted SSPs which are in direct contact with the cathode surface. Two commercial TCs are also used to compare the measurement obtained with the SSPs from the same location in order to investigate the capability of this sensory technique in terms of temporal and spatial resolution. Under OCV conditions, temperature increments due to fuel/air flow rate increase were detected well by SSPs and TCs with only a small difference among them. There is a small temperature variation observed along the cathode surface due to the sensing point's location. The increase in the measured temperature with increase in flow rate, as attributed to the direct fuel oxidation due to small gas leakage, is observed by the SSPs located on the outer side of the cathode. On the other hand, TCs were found not to be sensitive to the temperature increments caused by cell electrochemical activities compared to the increments monitored by the SSPs under loading conditions. The obtained temperature increment is compared with that theoretically calculated by using the I - V related thermodynamic information. Good similarity is observed between the experimental and theoretical temperature increment until the sensors reach thermal balance. Current collector contact area was found as the dominant factor resulting in temperature variation under loading conditions, of course with the impact of gas cooling and flow direction effects. In respect to the findings, the measurement directly from the cell surface is considered as a more realistic way to understand the temperature phenomena of the in comparison to the TCs based measurement from the flow channel as an experimental method. Sensitive detection of the local temperature variations allows definition of the origin of the sources of either heat releases or losses. This would help to diagnose the problems induced by high operating temperature before possible system failure.

Chapter 7:

Parameters and Their Impacts on the Temperature Distribution and Thermal Gradient of SOFC

7.1 Introduction

In the previous chapter, the architecture, temperature detection capabilities of the inserted sensor are discussed by comparing the new sensor results with those obtained from conventional TCs which are located in the flow channel. The importance of the area covered by the current collection (3 cm^2) on the temperature profile of the electrode was emphasised. The area which is covered by current collection was found as a dominant parameter for the temperature gradient compared to the fuel cooling effect and the effect due to fuel leakage. The effect of the fuel flow direction on the temperature rise under both OCV and loading conditions was discussed by looking at the readings from symmetrically located SSPs in respect to current collection. The impact of the current collection mechanism as an important factor on cell temperature gradient has not been fully understood yet. In order to understand this, identifying the parameters which have an effect on the cells temperature gradient is important.

It is thought clear that the overall oxidation reaction is exothermic and released heat together with the electrical power are the reaction products [181]. The uniformity of the released heat along the electrode surface is a key parameter in ensuring a minimal thermal gradient across the cell surface. Regarding this, the impact of the fuel flow direction or its dilution [125], thermal cycling [40], and uneven material composition on the thermal gradient of SOFCs have usually been studied as the main contributors to the thermal gradient issue. However the impact of the current collection on cell performance has been the main focus in some studies [19], [182]–[184] rather than establishing the relationship between the temperature gradient and the current collection mechanism. However, as it has been addressed in the previous

chapter that the impact of current collection mechanism on overall temperature rise as well as on the thermal gradient during loading is not negligible. In addition to this, identification of this relationship provides important knowledge to clarify the anodic H_2 oxidation reaction which has not been fully understood yet due to its complex electronic and ionic transfer characteristics throughout the porous media [185].

In the current chapter, individual contributions of some key parameters such as operating temperature, fuel/air flow rate, and the loading rate on both temperature rise and thermal gradient is investigated. The temperature profile of the electrode for each contributor is also reflected which allows the identification of how the local temperature changes the varying operating parameters including fuel flow rate, drawn current and operating temperature. The time dependent response of the TCs and SSPs to variation in the corresponding parameters such as flow rate or loading rate is compared to identify the characteristics of the cell temperature regarding the obtained temporal resolutions. Once the performance is stabilised and the system reaches a reasonable equilibrium, the corresponding analytical temperature rise is calculated and compared with the experimentally obtained increment. Furthermore, the impact of the integrated sensor in terms of cell performance with the contribution of an EIS measurement for determining the cell resistance under the same operating conditions is also analysed. EIS measurement is the generally applied technique to investigate the individual contribution of polarisations by impeding the flow of electrical current in respect to time or frequency [186].

7.2 Experimental Preparation and Operating Conditions

There is two different experimental set ups used for the experiments during the current chapter. One of them is the same experimental setup used and explained in the previous chapter with the same configuration as shown in Fig. 50. The impact of the sensor on cell power output is tested with the second experimental set up. Different from the set up illustrated in Fig. 50, there is no sensor integrated on the cell during the second experiment while all other parameters are kept the same which is explained in section 7.4 in detail. Fig. 50 shows the location of the placed sensor sensing points (SSPs), TCs, current collector together with fuel/air inlet and outlets.

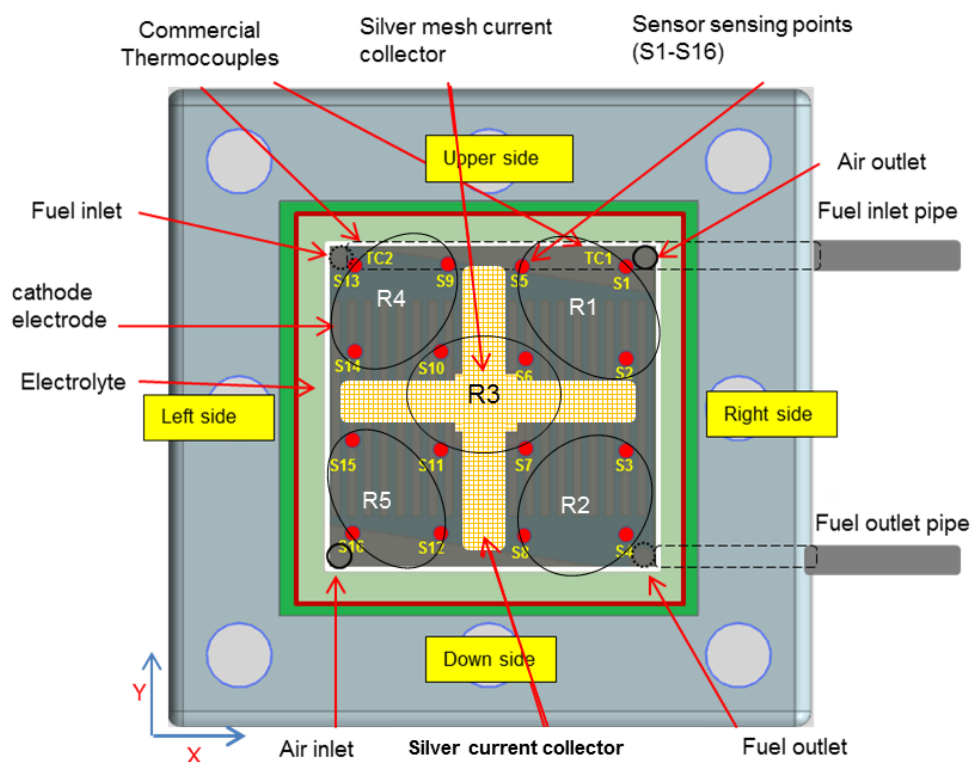


Fig. 50. Schematic view of the sensor integrated cell-manifold configuration

Meanwhile different from the previous chapter, different operating conditions including flow rates, drawn current, and furnace set temperature are applied to observe their contribution to the temperature increment in the current chapter. At the same time, variation in experimental and theoretical OCV with the corresponding cell temperature average increment (CTA) and cell temperature gradient (CTG) are monitored at 700 °C, 750 °C and 800 °C which are the operating temperature for high temperatures SOFCs with varying flow rate and loading conditions. The flow rate is changed from 50 mL min⁻¹ to 150 mL min⁻¹ to observe the impact of the amount of flow rate on the increment in CTA and CTG together with the corresponding cell performance. For similar reason, the amount of drawn current is also varied by changing the set voltage such as current drawn at 0.2 V and 0.8 V. For the second setup, on the other hand, a similar cell is used without sensor integration under one of the same operating conditions as carried out with integrated sensor in order to investigate the effect of the implemented sensor on cell performance. All the processes including correct collection attachment and anode reduction processes are similar for both experiments carried out with or without sensor integration.

7.3 Results and Discussions

7.3.1 Operating temperature effect on temperature increment and its distribution across the cell

Table 9 shows the temperature increment CTA over the set operating temperatures, CTG along the entire cell, experimentally (OCV_{expr}) and theoretically (OCV_{theor}) obtained OCVs under the condition of constant 50 mL min^{-1} fuel flow rate at 700°C , 750°C and 800°C operating temperatures. The OCV_{theor} is computed by applying the Nernst equation shown in equation (27). An obtained decrease in OCV_{theor} with the increase in operating temperature is expected due to the Nernst equation (27) as a result of the reverse relation between Gibbs free energy and temperature [175].

$$Enerst = E^\circ + \frac{RT}{nF} \ln \frac{PH_2 + PO_2}{PH_2O} \quad (27)$$

Table 10 Variations in ACT and CTG with varying operating temperature

	Increment in ACT ($^\circ\text{C}$)	Corresponding CTG($^\circ\text{C}$)	OCV expr (V)	OCV theor (V)
700°C	1.70	0.77	1.122	1.14
750°C	3.14	0.85	1.117	1.13
800°C	4.27	0.96	1.10	1.12

The value shown in Table 9 except OCV_{theor} is depicted graphically in Fig. 51 to visualise the simultaneous changes clearly. As seen from the figure OCV_{expr} reduces with the increase in operating temperature as expected. Besides, the CTA and corresponding CTG also increase with increases in operating temperature even under OCV conditions. As addressed in the previous chapter there is two possibilities that this increase can be attributed to: i) anodic oxidation reactions if there is any remaining oxygen existing; and ii) fuel crossover from anode to cathode which was considered as the case most likely happen due to observing a higher increment on the outer side of the cell.

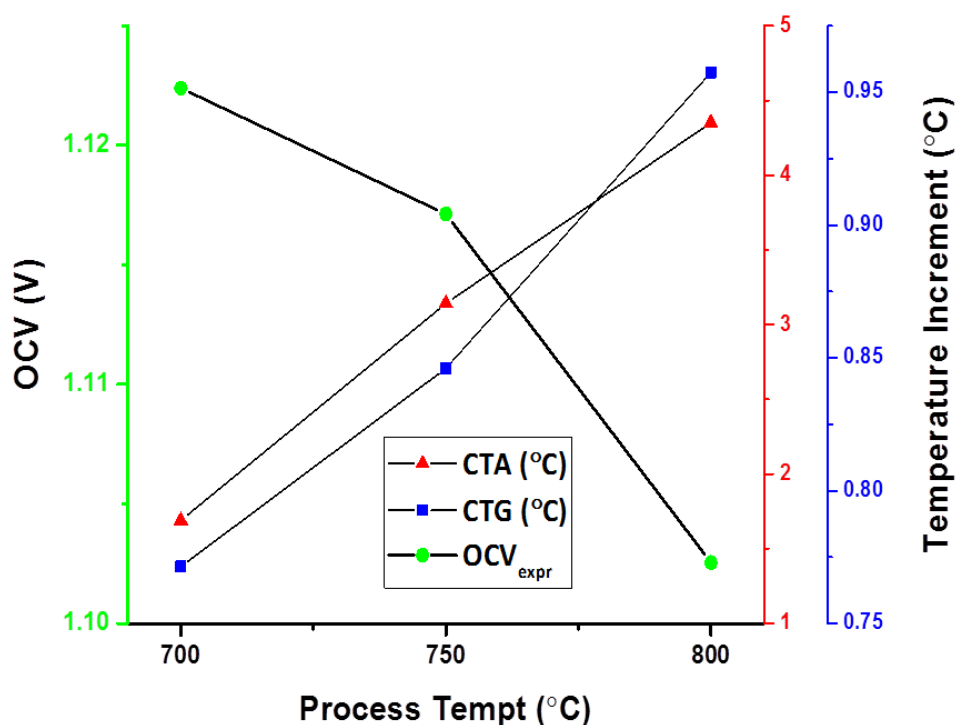


Fig. 51. OCV_{expr} , CTG and increment in CTA at varying operating temperature with 50 mL min^{-1} constant flow rate

The increments in CTA are obtained as $1.70 \text{ }^{\circ}\text{C}$, $3.14 \text{ }^{\circ}\text{C}$, and $4.27 \text{ }^{\circ}\text{C}$ while CTG is observed as 0.77 , 0.85 , and 0.96 at the operating temperatures of $700 \text{ }^{\circ}\text{C}$, $750 \text{ }^{\circ}\text{C}$, and $800 \text{ }^{\circ}\text{C}$, respectively (Table 9 and Fig. 51). However there are slight changes ($\sim 0.1 \text{ }^{\circ}\text{C}$) is monitored in the CTG with the varying operating temperature. It means that the location of the heat sources which leads to cell temperature increase are similarly affected by the contribution of the changes in operating temperature. It is clear that the operating temperature is contributing to the CTA and CTG of the electrode. It can be attributed to the changes in partial pressure of H_2 with increasing operating temperature. Since due to the ideal gas law which is where the system pressure increases (eventually partial pressure of the gas components increase) due to increasing the temperature when the volume and provided fuel flow rate are kept the same as the relationship of the parameters given in equation (28) [91].

$$PV = nR\Delta T \quad (28)$$

Where P is the pressure, V is the volume, n is the molar ratio, R is the gas constant and ΔT is the temperature difference.

The other and more important reason can be the chemical and electrochemical activities of gases (H_2) at increasing operating temperature. Regarding this, it is worth noting that the CTG is increased more when the operating temperature is increased from 750 °C to 800 °C than the CTG is obtained when the operating temperature is increased from 700 °C to 750 °C even though the total temperature variation is the same at around 50 °C for both cases. This refers to the contribution of direct H_2 oxidation reaction mechanism is enhanced with increasing operating temperature. The leaked H_2 amount is analytically calculated depending on the applied experimental condition by taking into account the corresponding CTA increment obtained.

Meanwhile, Fig. 52 shows the 3D surface mapping of the cell electrode at different operating temperatures. Before the reduction process, the monitored temperature is the furnace set temperature since there is not any increment illustrated (a zero with purple colour in the given temperature scale). However, when the reduction process is completed, there is temperature increment in the CTA with the produced fuel depending on the operating temperature during OCV where the maximum increment (~ 6 °C) is obtained at 800 °C near the fuel inlets. There is high temperature monitored nearby to the fuel and air inlets for all temperature sets which are where the fuel is fresher with higher partial pressure. Besides the inner side of the cell shows the lowest temperature for almost all cases which can be indicative that leakage is happening from the outer side of the cell via the sealing material (mica gasket).

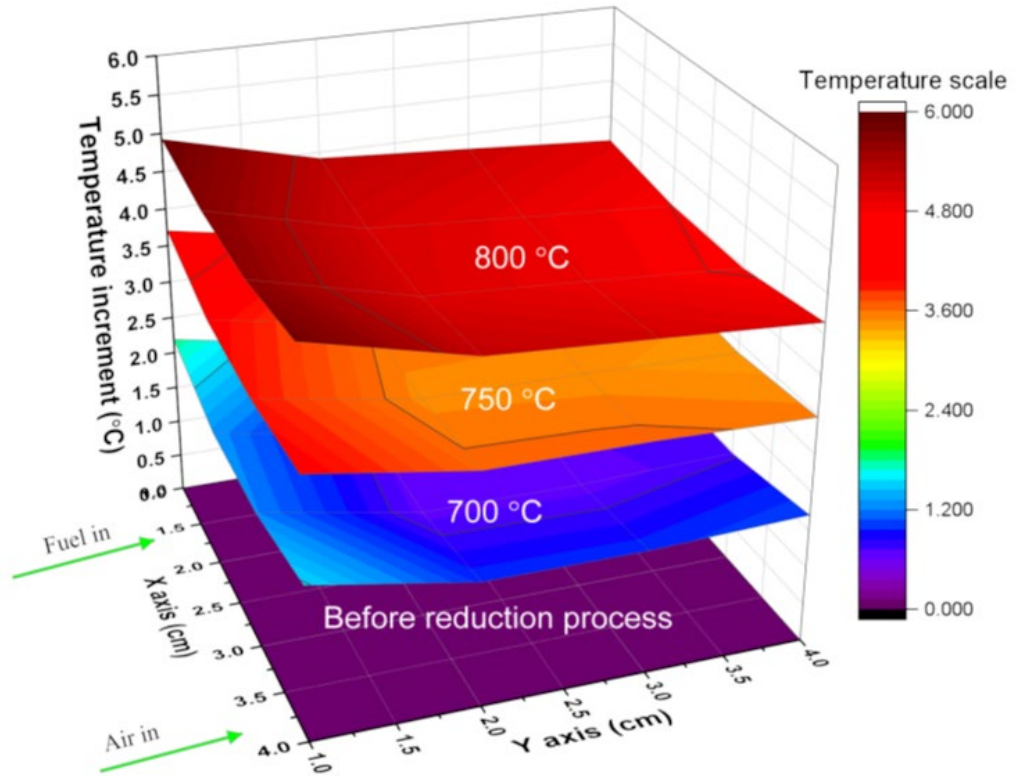


Fig. 52. Temperature distributions after anode reduction at OCV condition at different operating temperature

Once the cell anode reduction process is completed, the remaining temperature increment and their variations with varying operating temperature are investigated in this section. Fuel leakage is considered as the most probable reason for those obtained temperature increments due to the location where the maximum increment is observed for all cases. CTA increment and corresponding CTG due to varying fuel flow rate is investigated in the next section.

7.3.2 Fuel rate effects

Fig. 53 and Table 10 show the increment in CTA, CTG and OCV variation with varying flow rate at constant operating temperature. The axis and corresponding curve is in the same colour for instance the green axes is for voltage changes and OCV changes are represented by the line with green circle symbols. The furnace operating temperature is selected as 750 °C (average temperature) and furnace temperature is kept constant during the measurement. As seen from the figure and

Table 10 OCV_{expr} and OCV_{theor} are increased with increasing fuel flow rate as a result of the increase in partial pressure of the reactants due to the relation given in the Nernst equation (27).

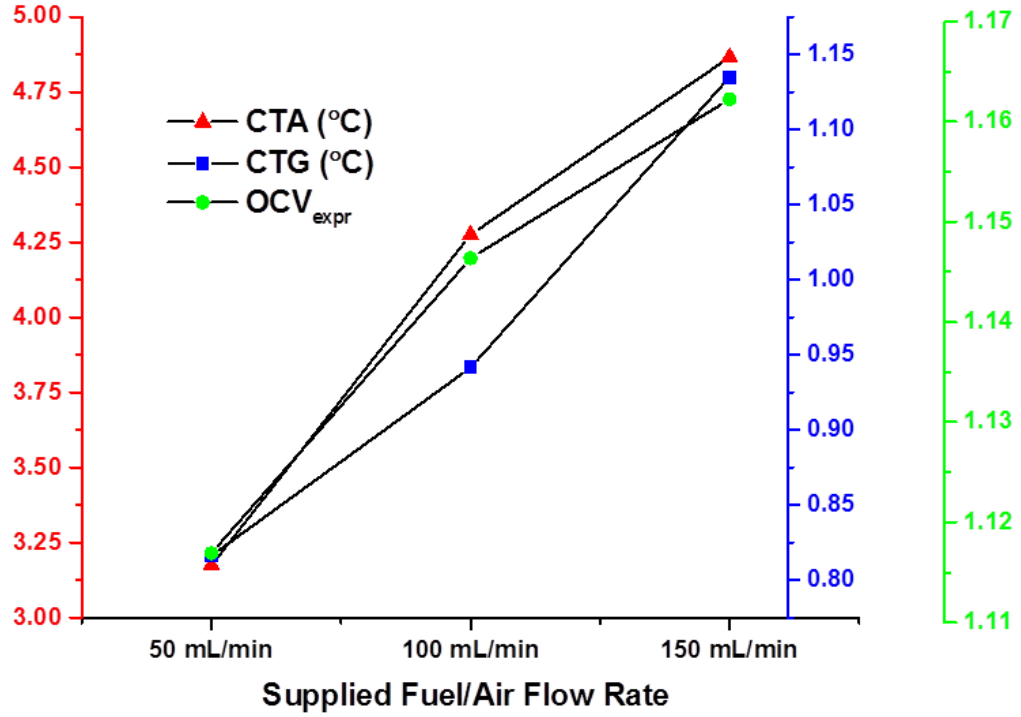


Fig. 53. Obtained CTA and CTG with OCV under varying flow rate

However, as also experienced in the previous chapter the ACT is also increasing together with OCV_{expr} . This is not an expected change according to the thermodynamics of SOFC as there is a reverse relation between Gibbs free energy and operating temperature. Thus, this is attributed to unwanted direct oxidation of H_2 with O_2 due to H_2 leakage from the anode to cathode which leads to fuel crossover losses (see equation 29) [175]. The equation shows the net voltage can be obtained after deducting the losses including η_{act} (due to activations), η_{conc} (due to concentration), η_{ohm} (due to ohmic), and η_{fuel} (due to fuel crossover). When H_2 crosses over to the cathode through the electrolyte or via sealing, oxidation can occur with the existing oxygen due to the presence of the catalyst. The catalyst is yielding no current hence this leads to undesired heat resulting in fuel wastage at both the anode and cathode.

$$OCV_{expr} = OCV_{theor} - Total\ losses(\eta_{act} + \eta_{conc} + \eta_{ohm} + \eta_{fuel}) \quad (29)$$

CTA is increased about 1.1 °C when the flow rate is doubled from 50 mL min⁻¹ to 100 mL min⁻¹ and 0.6 °C when a further 50% increase is incurred from 100 mL min⁻¹ to 150 mL min⁻¹. There is negligibly small changes monitored in CTG with varying fuel flow rate which where it increased by 0.1 °C and 0.2 °C when fuel flow rate increases from 50 mL min⁻¹ to 100 mL min⁻¹ and from 100 mL min⁻¹ to 150 mL min⁻¹, respectively (Table 10).

Table 11 Variations in CTA, CTG, OCV_{expr} and OCV_{theor} with varying flow rate

Flow rate (mL min ⁻¹)	Increment of CTA (°C)	Corresponding CTG (°C)	OCV_{expr} (V)	OCV_{theor} (V)
50	3.18	0.84	1.12	1.13
100	4.27	0.94	1.15	1.16
150	4.87	1.13	1.16	1.18

The obtained temperature profile due to fuel flow rate contribution to the CTA is similar to the profile obtained with the contribution of operation temperature as shown in Fig. 54. There is more increment observed nearby to the fuel/air inlet side while the lowest increment obtained is in the inner side of the cell for all cases due to reasons similar to those mentioned in the previous section. Even though the parameters are totally different, the reason behind their contribution is considered as fuel leakage. The increase in flow rate leads to a rise in partial pressure of reactants resulting in relatively higher amounts of gas leakage. The chemical activities are considered as the dominant factor for temperature increase with increasing fuel flow rate. The dominant factor is considered as partial pressure increase correlated gas leakage resulting in CTA increment in the case of fuel flow rate variation with constant operating temperature.

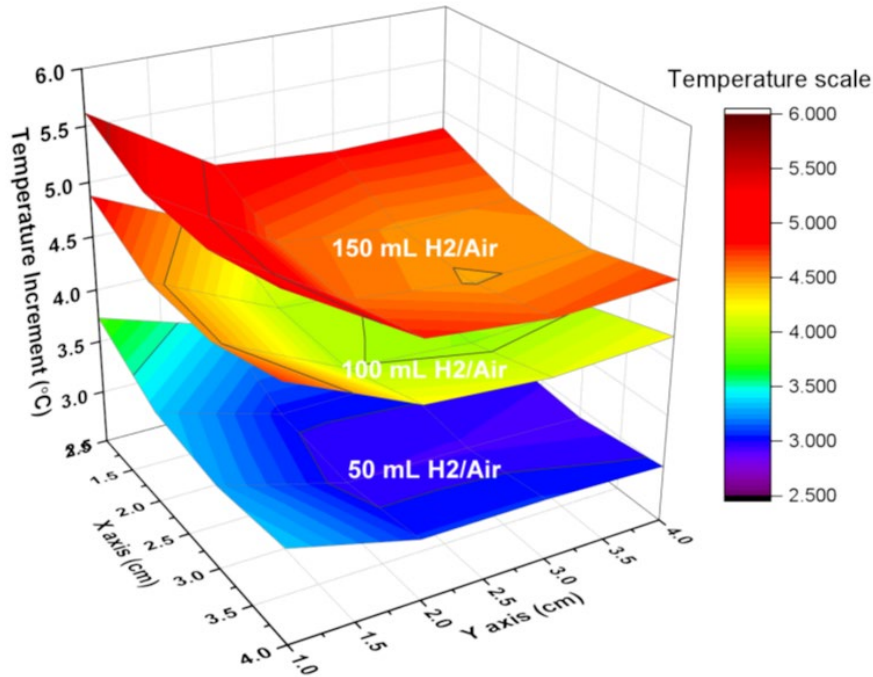


Fig. 54. Temperature profile of the cell with varying fuel rate

7.3.2.1 Thermodynamic approach to temperature increase due to anode reduction and variation in fuel flow rate

As aforementioned the reasons for the unexpected increase in cell temperature are attributed to the H_2 and free electron crossover from anode to cathode throughout the electrolyte due to their higher potential compared to the cathode. As a result of this, there is an exothermic direct H_2 oxidation reaction taking place when the leaked H_2 meets with O_2 in the presence of catalysts. Eventually heat is released which leads to the temperature rise in SOFC over the operating temperature even under OCV conditions. This is seen in the experimentally monitored results, presented in Fig. 51 with varying operating temperature and Fig. 53 for varying fuel flow rate with constant N_2 . The key parameter to determine the impact of the heat due to this direct oxidation of H_2 on the cell temperature is by calculating the molar ratio (\dot{n}_{H_2}) of leaked H_2 and its leak rate with varying flow rate. Herein, the measured temperature change is used to calculate the amount of leaked H_2 thus the corresponding enthalpy

at the given operating temperature of the oxidation reaction due to temperature changes is calculated, as given in equation (30). The released heat rate is the multiplication of the leaked flow rate with corresponding enthalpy (Equation 31).

$$\Delta H^{\circ}_{f_{H_2O,T}} = \Delta H^{\circ}_{f_{H_2O,298}} + \int_{298}^T C_p dT \quad (30)$$

$$Q_{in} = \Delta H \times \dot{n}H_2 \quad (31)$$

Where, $\Delta H^{\circ}_{f_{H_2O,T}}$ is the reaction enthalpy at operating temperature, $\Delta H^{\circ}_{f_{H_2O,298}}$ is the enthalpy at room temperature, T is the operating temperature, C_p is the heat capacity, and \dot{Q}_{in} is the heat rate generated due to direct oxidation of leaked H_2 .

The relationship between is the net heat, generated heat rate and simultaneous heat loss rate is given in equation (32).

$$\Delta Q = \int_{t_1}^{t_2} Q_{in} dt - \int_{t_1}^{t_2} Q_{out} dt (Q_{conv}) \quad (32)$$

$$\Delta Q = Q_{cell} + Q_{manifold} \quad (33)$$

$$Q_{cell} = Q_a + Q_c + Q_{el} \text{ and } Q_i = m_i c_p i \Delta T$$

$$Q_{conv} = h \times A \times \Delta T \quad (34)$$

Where, ΔQ is the heat observed by the corresponding thermal mass including cell components and manifolds (equation 33). These are separately mentioned in equation (32) due to their varying thermo-physical properties. While \dot{Q}_{conv} (equation 34) is the removed heat rate by the excess gas (air at the cathode and N_2 and H_2 at the anode flow) from the cell electrode surface via convection heat transfer which is where h is the heat transfer coefficient and A is the surface area where the heat transfer is happening. Q_i , (equation 33) on the other hand, is the heat consumed by related component of cell testing unit as “a” used for anode “c” for cathode and “el” for electrolyte, m_i (gr) is the total weight for all involved components that the heat is transferred through and c_i ($0.6 \text{ J gr}^{-1} \text{ K}^{-1}$) is the heat capacity for each involved component. ΔT is the average net temperature increment which is taken from the related experimental results (Fig. 53). Meanwhile, heat transfer coefficient, which varies depending on the conditions such as fuel flow rate and dimension of the path the fuel is passing through, is calculated as $h=6.5 \text{ Wm}^{-2}\text{K}^{-1}$ (calculating the

coefficient for cell inside is not always applicable and reliable but in our experiment the condition is quit chemically stable) by applying equation (35) and (36) as follows:

$$Nu = \frac{h \times x}{k} = 0.664 \times Re_x^{0.5} \times Pr^{0.3} \quad (35)$$

$$Re = \frac{u \times x}{\nu} \quad (36)$$

Where Nu is Nusselt number, h is convection coefficient, k is thermal conductivity of the fluid and x is length of the entire surface, Re is Reynolds number which is calculated as 38, Pr is the Prandtl number, u is velocity of the steam and ν is the kinematic viscosity of fluid (Table 11).

Table 12 Parameters used for computing heat convection coefficient

Re (dimensionless)	Thermal conductivity ($10^{-5} \text{Wm}^{-1}\text{K}^{-1}$)	Kinematic viscosity ($10^{-5} \text{m}^2 \text{s}^{-1}$)	Pr (dimensionless)	Nu (dimensionless)
38	6.8	12	0.7	3.6

The leaked H_2 amount is calculated by taking the total temperature changes ($\Delta T = 0.75^\circ \text{C}$) when the fuel flow rate is increased from 50 mL min^{-1} to 100 mL min^{-1} for a specific time period. The time required for the given temperature rise to reasonably reach an equilibrium is monitored as $\sim 1000\text{-}1250\text{s}$ (Fig. 55). Eventually, the leaked H_2 is calculated as $1.31 \times 10^{-6} \text{ mol s}^{-1}$ which is a negligibly small amount compared to the supplied H_2 amount ($37 \times 10^{-3} \text{ mol s}^{-1}$).

Once the amount of leaked H_2 is calculated under the condition of 100 mL min^{-1} at 750°C set temperature, then the possible leakage of H_2 can be analytically simulated by writing the relationship between leakage flow and pressure (equation 37) for varying fuel flow rate. Due to the increasing fuel flow rate the partial pressure of H_2 is increased which leads to higher leakage and finally results in a higher temperature increment. However, it is not always applicable for the given system especially is

there is electrochemical/chemical reactions taking places then the partial pressure of H_2 near the leaking point depends on not the fuel flow rate only.

$$\frac{F1}{F2} = \frac{h1}{h2} \quad (37)$$

Where, $F1$ and $F2$ are the leakage flow rates at pressures $h1$ and $h2$, respectively. Temperature increment, then, is analytically calculated when the fuel flow rate increased from 100 mL min^{-1} (0.57 atm (calculated partial pressure)) to 150 mL min^{-1} (0.65 atm (calculated partial pressure)) by obtaining the corresponding leaked fuel amount due to partial pressure changes (equation 12). There is a good agreement observed between the experimentally and analytically obtained temperature increments as shown in Fig. 55. The possible temperature increment is also found for 50 mL min^{-1} as $1.8 \text{ }^\circ\text{C}$ as it has the highest partial pressure changes ($\sim 0.4 \text{ atm}$) compared to the changes when the fuel is increased from 50 mL min^{-1} to 100 mL min^{-1} (0.17 atm changes) and 100 mL min^{-1} to 150 mL min^{-1} (0.08 atm). Thus, if the increment due to fuel leakage is subtracted from the total increment ($3.28 \text{ }^\circ\text{C}$ see Fig. 53) obtained with 50 mL min^{-1} , the impact of the electrochemical activities related to this temperature increment occurring during the anode reduction is found as $1.5 \text{ }^\circ\text{C}$.

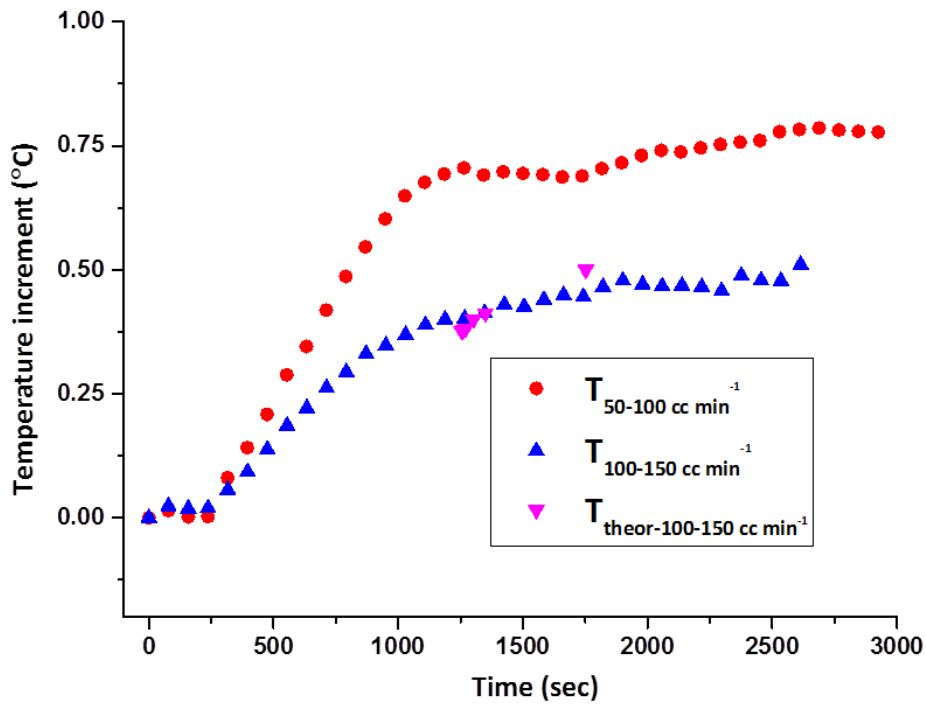


Fig. 55. Analytically and experimentally calculated temperature increment

7.3.2.2 SSPs and TCs response to the heat released by direct oxidation of leaked H_2

As illustrated in Fig. 52 and Fig. 54 there is a greater temperature increment monitored near the fuel/air inlet side compared to the outlet due to both the increases in fuel flow rate and operating temperature. This can be attributed to the occurrence of more gas leakage near to the inlet which leads to a greater direct oxidation reaction eventually resulting in higher heat release. Fig. 56 shows the cross sectional view of the location of the placed cell components: SSPs (located on the first row see Fig. 50); TCs; current collector; flow channels; and sealing materials.

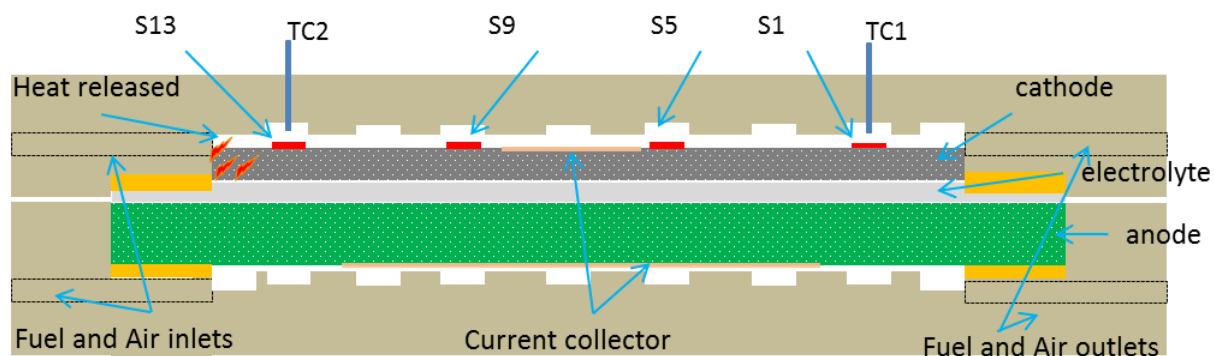


Fig. 56. Schematic view of cross section of the manifold-cell-sensor integration

The average temperature increment with varying flow rate for each sensing point S13, S9, S5, S1, TC2 and TC1 are given in Fig. 57. They are all located on the same horizontal line in the first row as seen from Fig. 50. S13 and S1 are located closer to the TCs (TC1 and TC2 respectively), these TCs being located in the flow channel approximately 2-3 mm above the electrode surface.

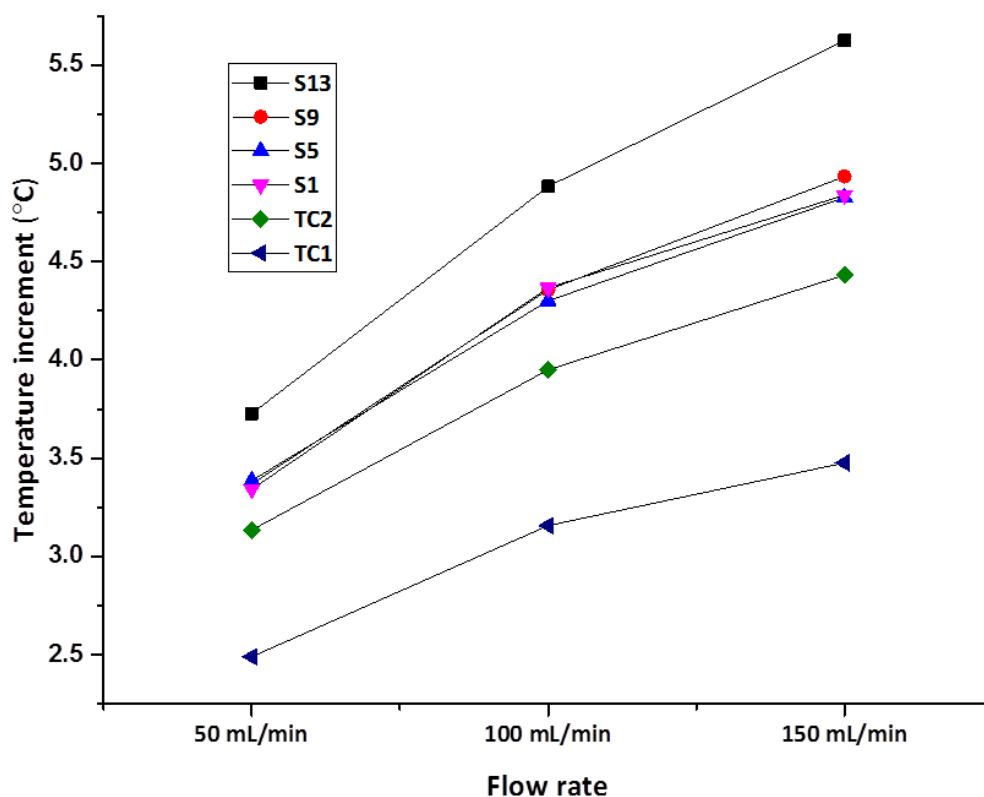


Fig. 57. Comparison of temperature increment between the TCs and SSPs

The highest temperature increment is obtained from S13 amongst the SSPs, while TC2 shows the higher increment compared to TC1. It is obvious that more gas leakage is nearby to the gases inlet resulting in these higher temperature increments due to more heat released from the oxidation reaction. S9, S5 and S1, on the other hand, show similar increments at 50 mL min^{-1} and similarly these increments increase with increasing flow rate. The increment obtained with S1 is higher than the increment obtained with TC1. Besides, obtaining a higher temperature increment from S13 and S1 compared to TC2 and TC1 refers to the cooling effect/convection heat losses. The cooling effect/heat loss via convection is more on TC2 and TC1 than S13 and S1, as more heat is transferred through the flow channel compared to the cell electrode. The direct oxidation is possibly occurring both in the porous media of the electrode and with the air in the atmosphere of the manifold near to the inlets as soon as the leaked H_2 meets O_2 . Fig. 58 illustrates the SSPs average (SSPs ave) and TCs average (TCs ave) temperature increment when the fuel flow rate is increased from 50 mL min^{-1} to 100 mL min^{-1} . The timely (300s) average increment from the SSPs (S13, S9, S5, and S1) is higher than the TCs (TC1, TC2) however the difference is almost constant. In other words, as seen from Fig. 57 and Fig. 58 the TCs are sensitive to temperature changes due to direct oxidation though the resolution is slightly less compared to the resolution obtained by the SSPs. The difference between the temperature increments obtained from the SSPs and TCs are almost constant with the varying fuel flow rate after equilibrium is reached shown in Fig. 57 as well as during transient temperature changes just after fuel rate shifts, shown in Fig. 58. This relation between SSPs and TCs is totally different from the relation they have during loading which has already been discussed in the previous chapter and further discussed in the next section of the current work. There was greater temporal and spatial resolution obtained with the SSPs than the TCs during loading while the temporal resolution between the SPPs and TCs is similar herein during OCV conditions with varying flow rate. Even though the spatial resolution is greater with SSPs than the TCs, their difference does not change considerably by the changes in flow rate under OCV conditions.

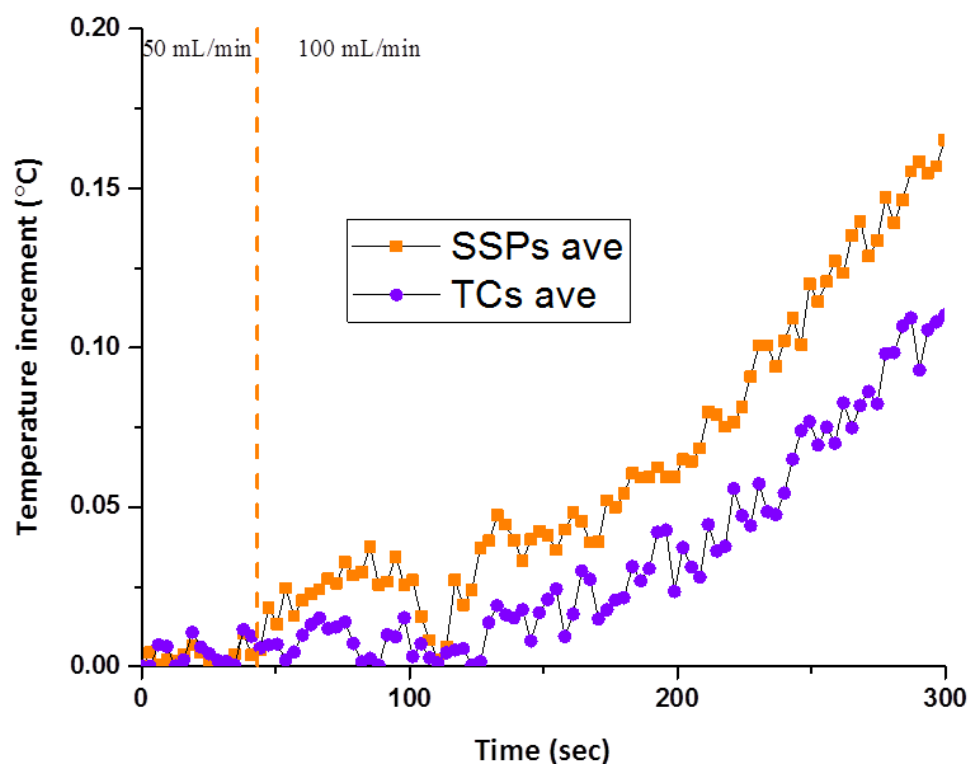


Fig. 58. Timely temperature response of SSPs and TCs to the varying flow rate

7.3.3 Loading Effect on Cell average temperature and cell temperature gradient

The increment of CTA and CTG is monitored under OCV and two different loads with a flow rate of 100 mL min^{-1} and plotted in Fig. 59. The furnace temperature is set to be constant (750°C) during the measurement process.

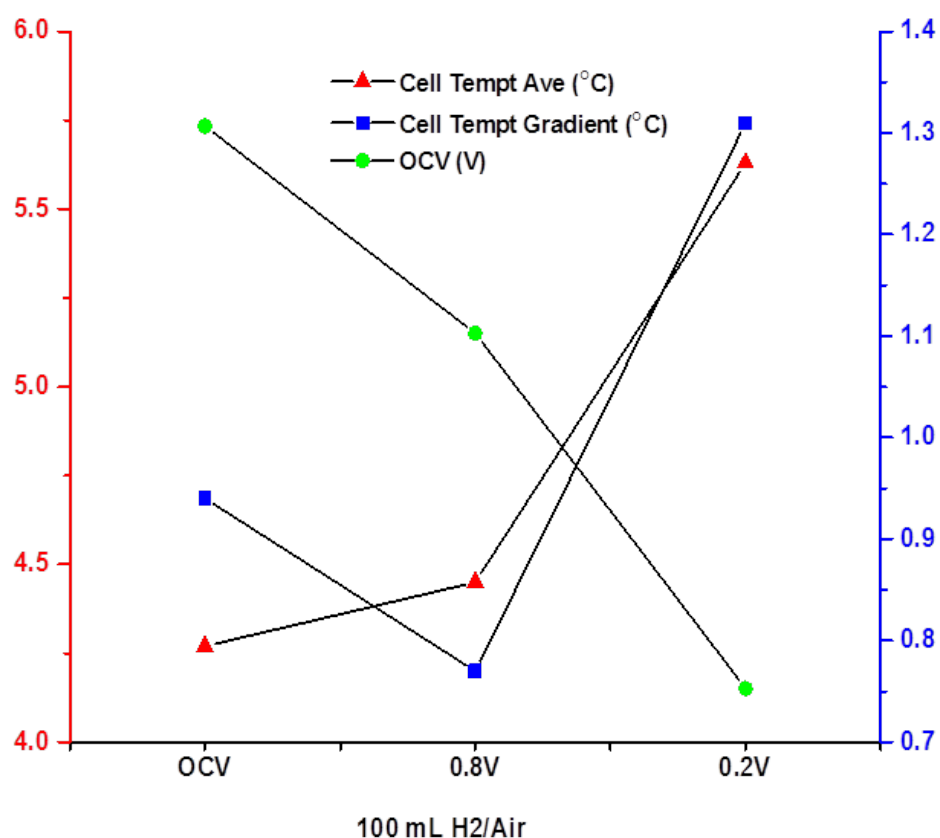


Fig. 59. Cell temperature increment with resulted gradient with corresponding voltage

The numerical values for the obtained CTA and CTG are also shown in

Table 13 shows the CTA and CTG numerical values under the condition of open circuit and two constant set voltages (0.8V and 0.2V).

Table 13 Cell temperature increment with resultant gradient under OCV and loading condition

	100 mL/min		
	OCV	0.8V (275mA)	0.2V(826mA)
CTA (°C)	4.25	4.45	5.63
CTG (°C)	0.94	0.77	1.31

The CTA and CTG have shown a similar trend with varying fuel flow rate and operating temperature under OCV conditions as analysed in the previous section. However, there is a reverse relationship observed between CTA and CTG when the system changes from OCV to the constant 0.8V loading condition. The CTA increases slightly by 0.2 °C while the CTG decreases by 0.5 °C. When the system is loaded there is heat produced due to more exothermic reactions taking place at the inner side of the cell which is where the lowest temperature has been recorded during OCV condition resulting in a relative thermal balance across the cell surface (Fig. 60). Consequently there is a decrease experienced in CTG. Whereas when more current is drawn from the system at 0.2V constant voltage then the CTG increased sharply together with the CTA from about 0.75 °C to 1.35 °C (80% change) and from about 4.5 °C to 5.55 °C (22% change), respectively. This is due to greater variation in the exothermic reactions taking place at the inner side and outer side of the cell.

The surface temperature distribution of the cell electrode under OCV and two different loading conditions is presented in Fig. 60. The highest temperature increment is obtained at the inner side of the cell whilst the lowest temperature is obtained around the fuel outlet.

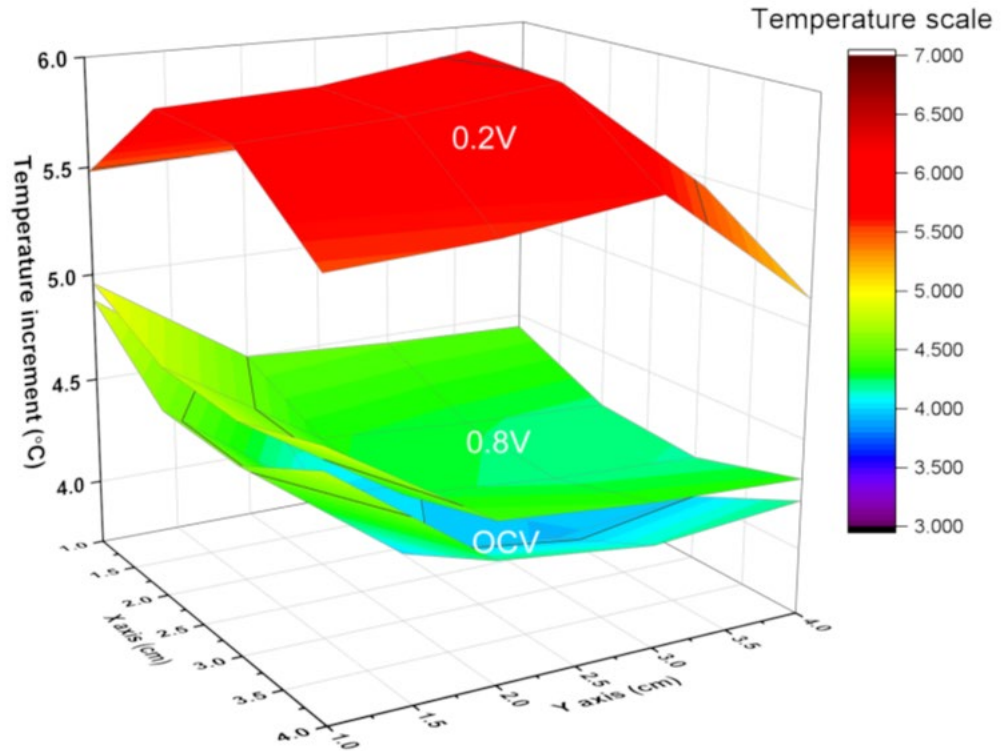


Fig. 60. Temperature profile of the cell under OCV and loading conditions

It is worth mentioning that there is shift occurring at the inner side temperature of the cell when the current is drawn from the system at 0.2V compared to the OCV condition. The inner side temperature of the cell shifts from the lowest temperature increment to the highest temperature increment. When the system reaches thermal balance after the voltage is set to 0.2V, CTG is about 1.3 °C and the cell temperature increment is increased to about 1.5 °C with loading at 100 mL min⁻¹ fuel flow rate while the shifting temperature at the inner side is obtained as 2 °C. The reason for this relative higher temperature change at the inner side of the cell is due to the cell area which is occupied by current collection. Since, the inner side of the cell is the place where the axis of the plus-shaped current collector is intersected. This addresses the importance of even distribution of the current collection mechanism. Therefore the contact point of the current collector is found to be the most critical location that a temperature induced thermal stress related hard failure issue may occur. It is important to point out the location where more heat is released to take the necessary action to remove the unwanted heat from the system to minimise the

thermal gradient. For instance, Vijay et al., [31] introduce excess air to the cathode side by incorporating a second air counter flow channel to minimise the thermal gradient, since the author assumes that there is a fuel flow direction driven temperature gradient with the co-flow type configured system. According to the obtained results herein this study, the effect of the flow direction might be a dominant factor for temperature gradient unless a non-uniform current collection mechanism, such as rib disconnection, is formed. This is further discussed in the next section.

7.3.3.1 Thermodynamic approach to temperature increase due to loading

The heat produced is as a result of the electrochemical reactions which takes place at the triple phase boundaries (TPB) at both electrode active layers [185]. The temperature increment due to loading has already been explained analytically in the previous chapter for constant loading to analyse the measured transient temperature increment. In the current chapter, specifically in this section, an analytical calculation is carried out for the equilibrium condition. When a system reaches a reasonable equilibrium condition, it is assumed that the heat released and lost heat is almost similar. The heat transfer via conduction to the other parts of the system such as manifold, gasket and mesh used for current collection is completed which helps to determine if the thermal mass absorbs the released heat (which can need modelling study to determine heat losses). The released heat from these electrochemical reactions is calculated by using equation (38) with the assumption that the electrochemical reaction is taking place at the infinite thin layer (electrode-electrolyte interfaces at the anode) [106].

$$Q_e = R_e \times \Delta H - I \times E_{cell} \quad (38)$$

Where Q_e is the released electrochemical heat, R_e is the reaction rate based on H_2 molar consumption and ΔH is the reaction enthalpy while I is the current and E_{cell} (OCV_{exp}) is the cell operating potential.

Using the given flow rate of air, the molar flow of oxygen is calculated by assuming the air is an ideal gas (equation 39). The corresponding H_2 (Re) which reacts with the transferred oxygen at the anode can be computed by using the reaction stoichiometry.

$$n = \frac{VP}{RT} = \frac{1 \text{ atm} \times 40 \text{ mL/min}}{(0.08206 \text{ L} \times \text{atm} \times \text{mol}^{-1} \times \text{K}^{-1})(1027 \text{ K})} \quad (39)$$

Where n is the molar ratio, P is the pressure, V is the flow rate T is the operating temperature and R is the gas constant.

Alternatively the molar flow of H_2 as a reactant of the oxidation reaction can also be computed by using the drawn current (with corresponding cell voltage) when equation 40 is calculated [175].

$$Re = mA \left(\frac{C}{s} \right) \times \frac{1 \text{ mol } e^-}{96485 C} \times \frac{1 \text{ mol } H_2}{2 \text{ mol } e^-} \quad (40)$$

So, obtaining/calculating the required parameters including E_{cell} , I , Re and ΔH from the experimental findings and conditions, the released heat (by using Q_e for Q_{in}) is calculated by applying the formula given in equation (31), (32) and (33). For the heat loss via convection the same parameters used in the previous section are still applicable where the heat convection coefficient was calculated as $h=6.5 \text{ Wm}^{-2}\text{K}^{-1}$.

The theoretical temperature rise is calculated for a time period of ~ 600 s, which is the time taken for the system to reach a reasonable equilibrium condition, and this rise is compared with the experimentally obtained increment as presented in Fig. 61. There is good agreement observed between the analytically obtained and experimentally measured temperature rise over the given time frame. Beyond that time (600s) the increment is negligible such as from 600s to 800s there is no considerable change monitored (which was the main reason for the assumption of reasonable steady state condition) as shown in Fig. 61.

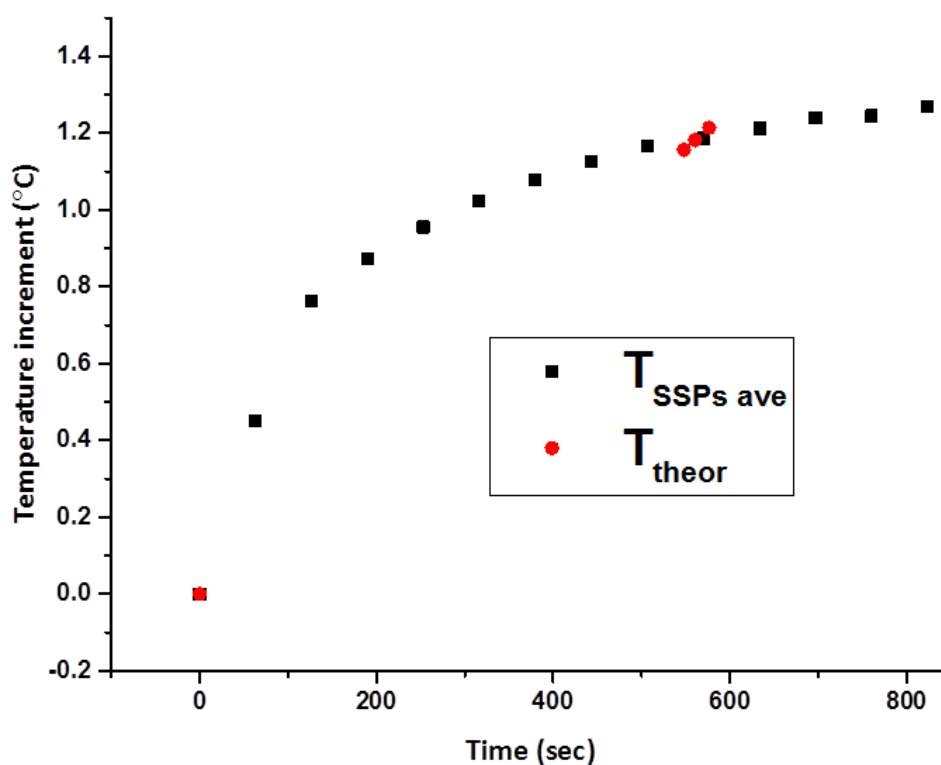


Fig. 61. Experimentally and analytically obtained temperature increment by time

It is assumed that the released heat is absorbed not only by the cell bulk if the increment is not calculated for only transient temperature changes for a short time period. The heat released due to cell activities first is absorbed by the cell body and transferred through the other components which are in physical contact with the cell till the reasonable thermal balance is reached. When the components reach thermal balance, there is heat transfer occurring from the cell-manifold system to the inside atmosphere of the furnace since the ambient temperature in the furnace is 750 °C and constant during the measurement period. Thus, only cell components are considered during transient temperature increments (as discussed in the previous chapter) while all components are involved during the calculation for the temperature rise at equilibrium. Thus the author think that the analytical calculation is more realistic for the transient condition compared to the assumed steady state condition which requires the impact of more parameters thus modelling work can provide better certainty. Since as partly mentioned the analytical calculation was carried out for a few points of time only due to unknown parameters of heat loss especially for heat loss via conduction which was ignored during analytical calculation due to its

minimum contribution for the transient condition. But still important to see that there is a good agreement obtained with the experimental data even at some point with the assumption.

Fig. 62 shows the schematic cross view of the cell-manifold configuration and the expected corresponding location where the heat is released during electrochemical reactions. The location of the SSPs are grouped as each column (see Fig. 50 for the order of SSPs in each column) and TCs are also shown, S6, S7, S10 and S11 are not seen in Fig. 62 (but seen in Fig. 50) as they are in the middle part of the corresponding arrays S5-S8 and S9-S12.

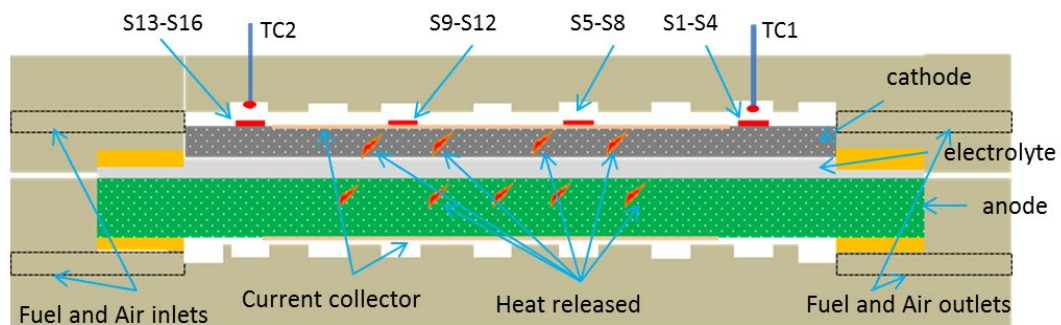


Fig. 62. Cross view of the cell-manifold configuration

Timely temperature rise from S13, TC2, SSPs_{center} (S7, S6, S10, S11 which are located in the centre of the cell near to the current collector), S1 and TC2 during loading conditions are plotted in Fig. 63. The highest reading monitored is from SSPs_{center} while S13 and S1 had a similar increase and a small rise amount compared to SSPs_{center} even though S13 is the nearest sensing point on the fuel inlet side. On the other hand, both TC1 and TC2 increase similar to each other and by a comparatively negligible amount. There is a significant difference observed in temperature increment detection capabilities of the TCs when the increments due to loadings are compared to the increment due to heat leakage. TCs are seen not sensitive enough to the temperature changes caused by the cell electrochemical activities. Different from the direct oxidation of H₂ at the cathode owing to leakage, there is H₂ oxidation and O₂ reduction half reactions taking place at the anode and cathode TPBs, respectively. Thus, the released heat is directly absorbed by the solid parts of the cell and other components which are in direct physical contact. There is

not too much heat loss occurring in the cell porous media since the temperature difference between the gas phase and solid phase of the electrode is found in the order of 10^{-2} K which is negligible [178].

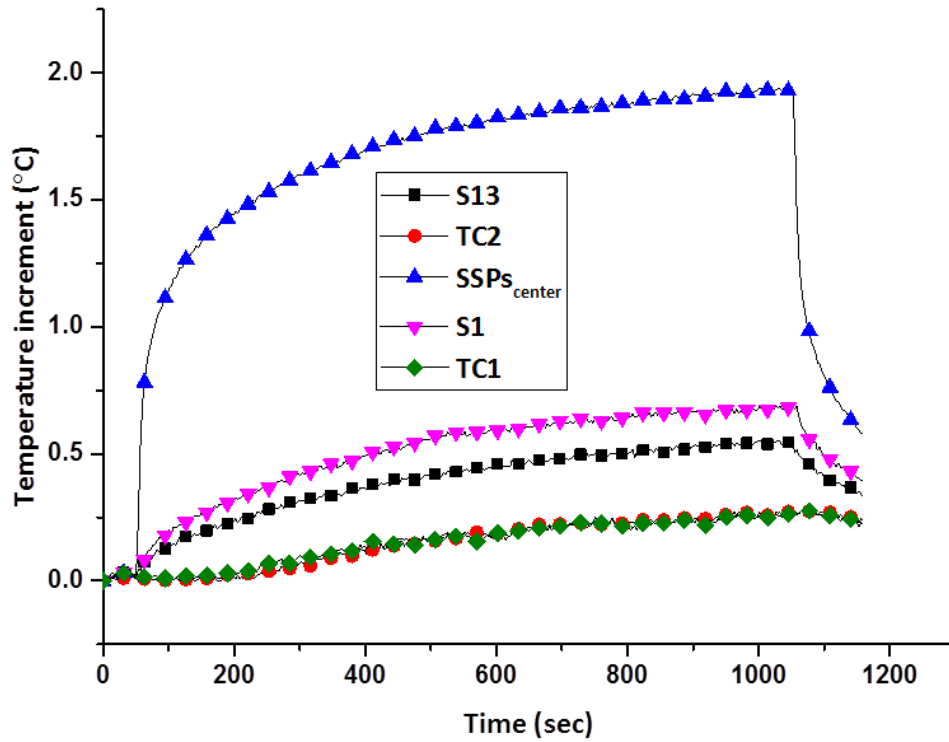


Fig. 63. Timey temperature increment of SSPs_{center}, TCs, S13, S1 at 0.2V

One of the most important observations here is that the current collection area is the most dominant factor on CTA and CTG. As presented in Fig. 60 the higher temperature increment is monitored on the inner side of the electrode which is where the current collector is placed. In the literature the temperature profile of the cell surface is shaped depending on fuel flow direction/types and reforming reactions [28], [120], [125]. There is usually more temperature increments obtained in the vicinity of the fuel/air inlet which is ascribed to the higher rate of fuel utilisation. However here in this study there is almost negligible effect from the fuel direction observed compared to the effect when there is non-uniformity in current collection. Hence from the experience of this study it has shown the importance of the

interconnect design and its contact mechanisms. Hence it is identified as a key parameter to understand/minimise the cell temperature gradient as it is extremely challenging to provide uniform electrical connection between cell electrodes and interconnect across the cell entire cell surface.

In the case of drawing 826 mA (0.2V) with 100 mL min⁻¹ of fuel/air flow rate at furnace set temperature (750 °C), the overall temperature rise is found as 5.75 °C. Table 13 shows the percentage of the parameters' contribution to the obtained temperature increment out of the given overall increment by looking at the ratio of their individual contributions. The highest contributor is observed from the unexpected gas/charge crossover related temperature increment with 45%. While the percentage of temperature increment due to electrochemical reactions (28%) and anode reduction process related reactions (27%) are almost the same depending on the increments obtained from each individual parameter. Since the current drawn is limited due to the small sized current collection area (only 20% of the total electrode active area covered for the current collection), the rate of the contribution of the cells electrochemical activation correlated increment can be further increased by expanding the size of the current collection area. By ignoring the increment (taken as a reference point) due to the anode reduction process in which the reaction mechanism is not clearly known, the rate of the contribution of the fuel leakage related and drawn current related changes to CTG is also calculated which is also shown in Table 13. In contrast with their contributions to CTA, there is a more severe CTG is occurring when the system is loaded (40%) compared to the obtained CTG due the fuel crossover (15%).

Table 14 Parameters and their impact on total temperature increment (5.5 °C)

	Heat source/sink	Location	Contribution to CTA	Contribution to CTG
Anode reduction	Source	Anode	27%	Reference point
Unexpected crossover (fuel or electrons)	Source	cathode	45%	15%
Electrochemical reaction	Source	Anode and cathode	28%	40%

It is worth noting that there is about ~ 2 °C temperature shift occurring at the inner side of the cell when the current starts to be drawn at 0.2V from the cell while CTA and CTG only changed 1.38 °C and 0.37 °C, respectively (Fig. 60). This value can be further increased depending on the operating condition which can lead to thermal shock related issues. These include cracks and delamination between cell layers, between the current collection area and the current collection free area and include other components of the SOFC system. The higher the loading amount the more severe the thermal shift and the higher the risk of thermal shock related issues [187]. It is revealed from the results that the fuel leakage related temperature rise is another contributor to the temperature increment together with cell activities. Moreover, even though its contribution varies depending on the experimental condition, its impact is not something negligible and is worth considering as a contributor for SOFC thermal gradient related issues. Thus, it is important to take into account other heat contributors to understand the realistic relationship between the temperature increments and the related performance degradation or thermal stress analysis.

Although the twelve SSPs is located on the side where the current collector is placed, those which are placed near to the centre show higher increments than the others during the loading condition as a result of uneven current density across the current collection (see Fig. 50 for their location and Fig. 60 for temperature increment). This can be caused either by the cell electrochemical activity related parameters including cell morphology, different O₂ pathway for its diffusion and difference in electrode composition locally [120], and fuel flow direction [188] or current collection area related parameters including the location, effectiveness of the connection between the electrode surface and current collector [184], [189]. According to the obtained results the effect of the location of the current collection mechanism on temperature distribution is more dominant than the other discussed parameters including fuel/air effect, flow rate and leakage related effect. The importance of the current collection mechanism on cell performance degradation has already been expressed in the literature [190], while its impact on cell temperature distribution has not been studied fully yet. However, as it has been found in this study the maximum temperature gradient occurred between the area covered for current collection and the area free from the current collection. This offers a solution to similar problems which might appear when the ribs detachment (removal of current collector from the electrode

surface) problem is experienced [187]. For instance SSPs S14 and S15 are located near to the current collector at fuel/air inlets sides which is where the higher rate of fresh fuel/air is expected compared to the location where SSPs S10 and S11 are located. However, S10 and S11 show higher increments than S14 and S15 since they are surrounded with current collection as they are close to both the horizontal and vertical side of the current collector (see Fig. 50 for their locations). Another reason can be the place where the electrical wire is connected to the current collector. As soon as the electrons reach the cathode they possibly start reacting more through the depth of the cathode rather than horizontal spreading through the placed current collector. Then the electrochemical reactions take place around the first contact point more than any other side of the electrode. This emphasizes the importance of having a uniform electrical connection (with no ribs detachment issues) between the cell electrodes and interconnects material especially in the case of stack level operation. Consequently, it has been revealed from the findings that the impact of fuel utilisation on temperature gradient is strongly dependent on the effectiveness of the current collection mechanism in terms of electrically and electronically evenness. The study has also pointed out the difficulty in distinguishing the individual impact of the mentioned parameters on SOFC temperature distribution using a conventional TCs based measurement method.

7.4 Effect of the Applied Sensor on Cell Performance

In order to demonstrate the impact of the implemented sensor on the obtained cell performance, the cell performance is experimentally observed under two similar conditions one with and without sensor integration. There is not a unique polarisation curve for all planar SOFCs as it varies depending on the operating parameters including fuel/air composition, fuel utilisation, operating temperature, and the current collection mechanism. Thus during the experiment these parameters are kept the same for both experimental conditions to make realistic comparisons. The experiment is carried out under the conditions (randomly selected) of fuel/air gases flow rate of 100 mL min^{-1} , a furnace set temperature of 750 and by setting a similar current collection mechanism. Fig. 64 shows the obtained polarisation from the experiment both with and without the sensor. The voltage and power for the cell

without the sensor is represented by the open-square and triangle symbols, respectively, while they are represented by the solid-square and triangle symbols for the cell with the sensor, respectively. The maximum obtained powers are almost the same for both cell configurations which are slightly higher than 0.25W. Besides, the current drawn is slightly higher for the cell without the sensor than the current drawn from the cell with the sensor.

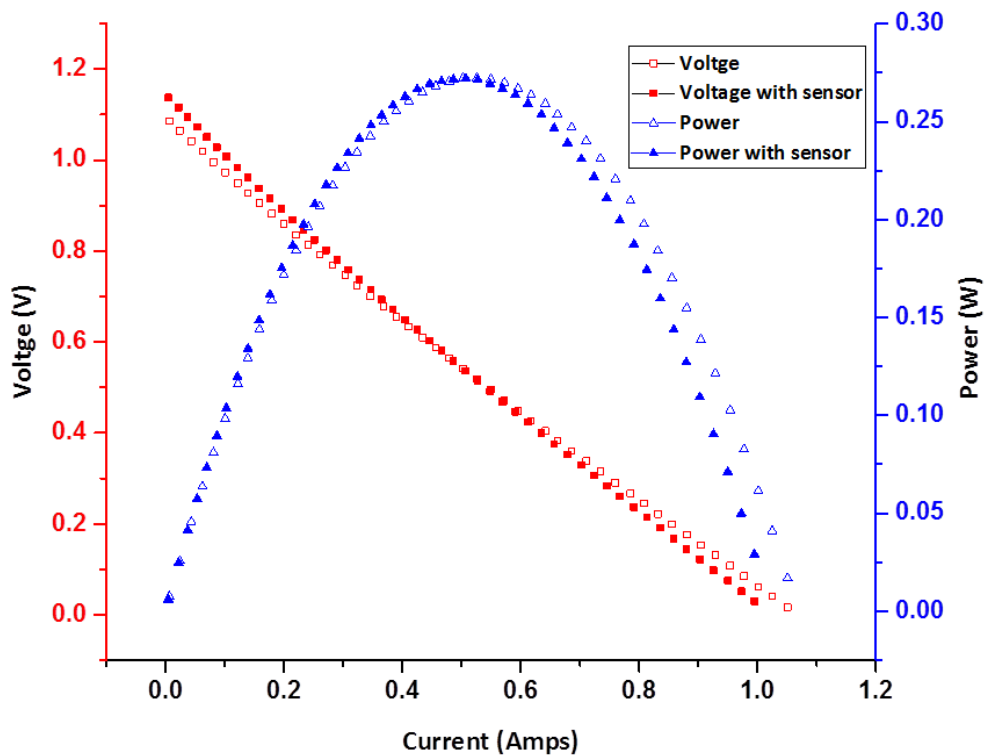


Fig. 64 Comparison of the polarisation curves

As seen from Fig. 64, there is no considerable difference between the powers obtained during the first half of the semi-circle of the polarisation curve. However, there is slightly more power obtained from the cell without the sensor during the other half of the semi-circle of the power curve. The measured voltage for the corresponding current from the cell without the sensor is more than the cell with the sensor which leads to more power output. At the beginning there is a higher voltage observed from the cell with the sensor. This can be attributed to the higher volume of the cathode with the sensor due to the applied alumina paste. Due to the behaviour of

the voltage curve which is linear for both cases, there are only ohmic losses experienced. The activation losses are negligible in the SOFC due to its high operating temperature while concentration losses can be minimised due to the limited reaction area. Since there is only a small area covered with the current collection which results in less utilisation and more excess fuel. The reason for this discrepancy between measured voltages can be ascribed to experiencing more ohmic losses from the cell with the sensor with increasing drawn current. In other words, the inserted sensor is negligibly contributing to the ohmic losses due to more resistance to ionic and electronic charges due to the applied alumina paste while there is almost a zero negative effect correlated with concentration and activation losses experienced depending on the obtained polarisation curve. This is because the sensor is mounted on the cathode surface by using alumina and those connection points has no physical contact with the current collector and are not blocking the pathway gaseous. It seems that the applied alumina is somehow positively affecting the cell potential resulting in higher open circuit voltage. The other possibility is handling based differences during the preparation process leading to this small unexpected contribution to the cell voltage which is within an acceptable error level. In order to observe the impact of the integrated sensor in terms of resistance electrochemical impedance spectra (EIS) is performed for both cells under the OCV condition. The frequency used for the EIS measurement ranged from 20k Hz to 20 Hz with a signal amplitude of 10 mV.

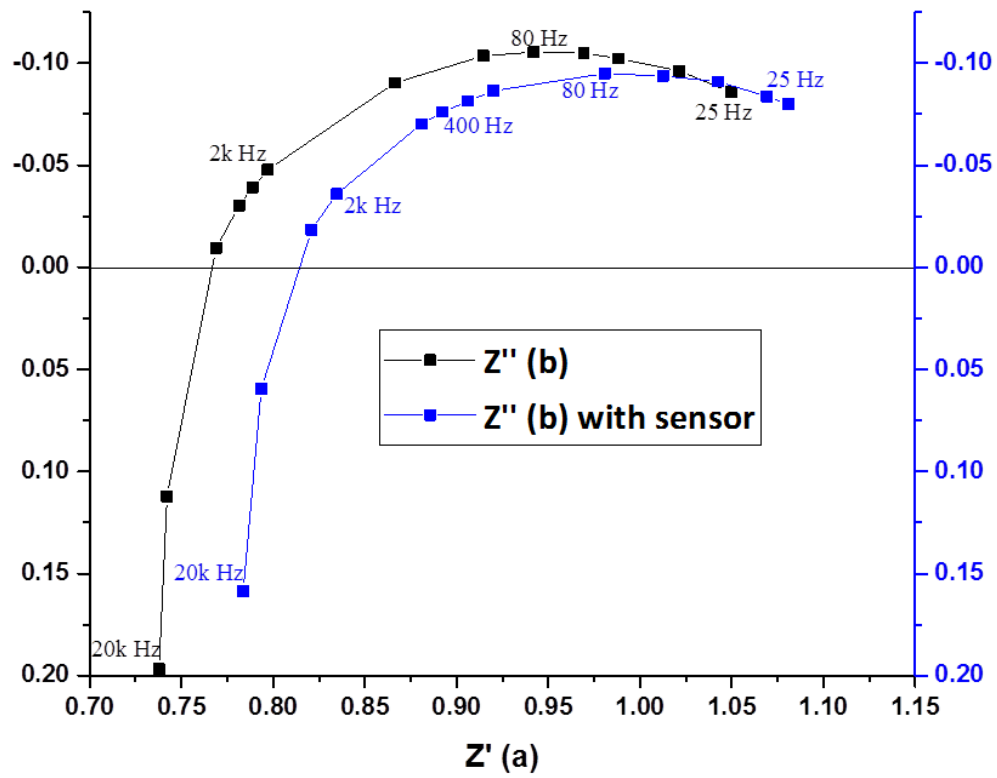


Fig. 65. The EIS data obtained from the cell with and without sensor integration

As depicted in Fig. 65, the impedance spectra of the cells with/without sensor is shown by a single suppressed semicircle. In the 1st quadrant (negative impedance) that were fitted with equivalent Randle circuits (Fig. 66) and attributed to the kinetic of electrochemical charge transfer at electrode-electrolyte interface [59]. The impedance at higher frequencies lie in the fourth quadrant (positive impedance) that relates to the stray inductance of the lead wires [191].

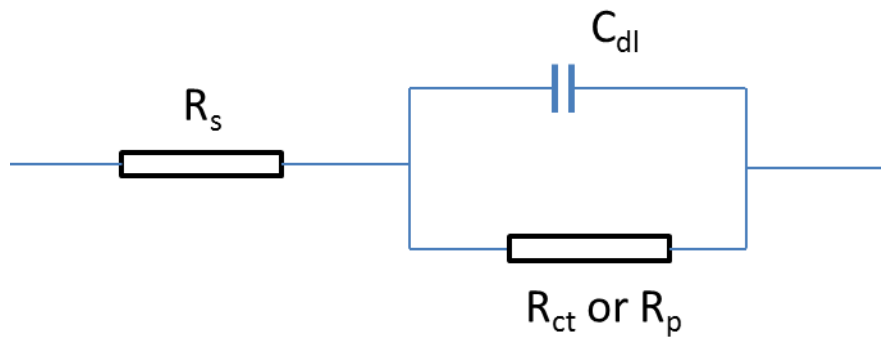


Fig. 66. Equivalent circuit for the behaviour of the obtained impedance elements shown in Fig. 65

Table 15 Experimentally obtained value for the elements given the equivalent circuit

	$R_{sbn} (\Omega)$	$R_{ct} (\Omega)$	$C_{dl} (\text{Farad})$
Without sensor	0.76	0.38	0.0034
With sensor	0.81	0.39	0.0036

Where R_s is ohmic resistance of electrical connection and electrodes, R_{ct} is the charge transfer resistor and C_{dl} is double layer capacitance at the interface.

The value of R_s of the cell with the sensor is slightly higher than that without the sensor, while both cells have similar values of R_{ct} and C_{dl} respectively. This indicates that the sensor does not affect the kinetics of the electrochemical reaction. However, it slightly increases the ohmic resistance due to the extra connection and coverage of the sensor on the electrode's surface.

7.5 Chapter Summary

The contributions of some key parameters including operating temperature, fuel flow rate, and electrochemical reactions to SOFC average temperature and temperature gradient are in-situ monitored. Additionally the findings are analytically calculated based on the aspects of SOFCs' thermodynamics. Temperature measurement is obtained via the inserted sensor via the sixteen individual sensing points directly from the cell electrode surface and via conventional TCs from the flow channel. Enough time interval was given for the cell to come to thermal balance after each action while the impact of some actions are timely monitored. The local temperature distribution as a result of non-uniform temperature increment of the cell electrode at its different parts was also monitored.

There is a temperature increment experienced with varying operating set temperature even with a constant fuel flow rate. The temperature increment is higher near to the fuel/air inlet which gradually decreases through to the fuel outlet. It is ascribed to the higher possibility of the occurrence of H_2 leakages near the inlet due to relatively higher partial pressure at the inlet leading to more direct oxidation reaction resulting in higher heat release. With the increase in temperature this makes the gas components more active and leads to an increase pressure. These both contribute to

the gas leakages resulting in more direct oxidation and finally a temperature increment. The temperature increment was also observed with the increasing flow rate under the same operating set temperature which was also attributed to undesired fuel crossover through the electrolyte resulting in direct H_2 oxidation. This can be either oxygen ions (reduced at cathode due to free electrons or the electron crossover) travelling from cathode to anode or H_2 from anode to cathode eventually leading to an exothermic reaction between O_2 and H_2 resulting in heat release to the atmosphere. According to the obtained temperature increment, the released heat and its corresponding required reactant (fuel) were calculated.

Cell electrode temperature increment due to electrochemical cell reactions and its impact on corresponding temperature distribution were monitored during loading conditions with varying drawn currents at constant furnace temperature and fuel flow rate. Experimentally obtained heat is compared with the analytically calculated value under steady state conditions. The analytical obtained increment matches well with the experimentally measured increment. The percentage of the contribution of each individual value on the increment of the cell temperature out of the total obtained increment is computed. Direct oxidation was found the most dominant parameter on temperature increment while the electrochemical reactions have the highest impact on temperature distribution.

The obtained value of the temperature increment can vary depending on the experimental condition, however the characteristics of the temperature profile and time dependency to reach reasonable equilibrium for each action remains relatively the same. There are two key points to identify the source for the experienced temperature increment during SOFC operation. First is the location where the increments are monitored and second how quick these increments occur. For instance, if there is higher temperature appearing near the inlet this does not just due to fuel utilisation instead the leakage might be the reason/contributor for the increment. Additionally, if there is a sudden increase observed this is then most likely being caused by cell electrochemical reactions. This shows the benefits provided due to the high temporal (sudden increase) and spatial resolutions (temperature profile) of the implemented sensor.

Chapter 8:

Conclusions and Future Works

8.1 Conclusions

This thesis presents the in situ monitoring of the temperature distribution of an operating SOFC and the contribution of individual parameters affecting this distribution. Regarding the objectives mentioned in chapter 1 the findings and outputs of each are addressed:

1. An understanding of SOFC working principles including governing reactions and its components and failure mechanisms was gained through a literature review. In addition to this SOFC thermodynamics and heat sources/sinks due to chemical and electrochemical reactions were investigated. These properties have found as the key parameters for understanding the temperature correlated failure mechanisms.
2. The literature review also established the state of the art of currently applied techniques for SOFC temperature monitoring together with their advantages and disadvantages. There was a great number of numerical studies carried out for temperature distribution prediction which needs to be validated with experimental studies. The optical method was found costly and required machining to access the operating cell for monitoring its temperature. There was a lack of research found in implementation of sensory methods (namely with TCs), and those that have been carried out identified temperature sensing with poor resolution. Thus it has been considered as the objective of this study to improve the implementation and resolution of the sensory method by using a new sensor with advanced implementation.
3. Based on the literature:
 - a. The challenges in monitoring SOFC temperature due to limited available space with the current experimental method for temperature measurement were identified as needing improvement. Regarding this a recently developed sensor with improved architecture was applied. In order to achieve this practical implementation of this sensor and also to

improve the resolution of the traditional experimental TC based measurement a new implementation method was required. This method was developed and introduced.

- b. In the initial implementation method, the sensor was first fabricated in film form and directly sputtered onto the cathode. Its durability on the cathode porous surface was investigated by applying a conventional external wire attachment technique to the thin film sensor. A failure due to the external wire connection was experienced which required a newly proposed connection technique.
 - c. A spring based connection was introduced as the solution for connection related issues. Two different experimental set ups were applied by using a spring to keep the external wire in continuous contact with the thin films sensor: one with only a spring whilst another one with the spring attached with a small amount of silver paste. In the first attempt without silver paste, there was an issue of no temperature reading experienced during cooling which was attributed to the loss of spring compressing capabilities. In the second attempt applying a small amount of silver paste at the connection between the spring loaded external wire and the thin film sensor pads, the problem was resolved and continuous reading was monitored throughout the experiment.
 - d. On the other hand due to the limitations for having proper protecting layer to electrically isolate the thin film sensor from the environment, a new implementation method was proposed using a wire formed sensor, applied for temperature monitoring from a running SOFC. Conventional TCs were placed with the conventional method to compare the findings with this applied new method.
4. The results show that a greater resolution was obtained with the implemented sensor compared to the resolution obtained from the conventionally applied method with TCs placed in the fuel flow channel. For instance, the spatial resolution, of the implemented sensor was found to be five times greater than the resolution obtained by conventional TCs. The findings emphasised that there can be a considerable difference between cell surface temperature and flow channel temperature. The analytical calculations were carried out to

theoretically obtain the experimentally monitored temperature of SOFC for validation purposes.

5. The temporal resolution was also improved with the applied method compared to the resolution obtained with conventional TCs. There was a transient temperature (0.5 °C) monitored during the first 60s with the sensor as soon as the system was loaded whilst no visible changes were monitored with the conventional TCs during this time.
6. The results show that the measurement with high resolution offers the ability to identify the parameters leading to a temperature increment by defining the characteristics of the monitored temperature. Fuel crossover, furnace operating temperature and cell activities were found as the contributors to cell temperature increment and also affect its distribution across the cell surface. The fuel crossover related direct oxidation was found the most dominant contributor for cell temperature average increment whilst the electrochemical reactions were found to be the most impactful parameters for temperature distribution. At this point it has been identified that high spatial resolution plays a key role for identifying the location of the heat source which helps location based identification of the source depending on the experimental condition. The temporal resolution, on the other hand, provides time dependent identification of the source especially under loading conditions.

8.2 Contributions

This thesis contributes a technique for in situ monitoring of an operating SOFC temperature distribution by using a recently developed sensory technique. The way the sensor is implemented is the key to improve its resolution while the architecture of the sensor is key to overcome the SOFC construction based challenges which reduces the number required thermo-elements that the conventional TCs are required even for the same number sensing points. There is not currently a method for SOFC temperature monitoring directly from the cell surface in the literature and hence this is considered as a novel contribution.

The research has also accordingly some and enhanced understanding of others regarding the parameters affecting temperature distribution. It has revealed that the

cell activities are not the only source for temperature increment; instead there are different parameters including fuel crossover related direct oxidation contributing to the operating cell temperature characteristics. Additionally their contributions were found not proportional to cell temperature and temperature gradient. Among the parameters the area covered by the current collection was found as the most impactful factor on temperature gradient during loading conditions with varying drawn current. Besides there was a considerable contribution observed to the cell temperature increment due to gas leakage (H_2 direct oxidation) under the applied experimental condition. However the contribution of the gas leakage correlated heat release to the temperature distribution was found not serious with varying flow rate. On the other hand fuel flow direction and gas cooling effect on temperature gradient (distribution) was found as a considerable contributor only in the case when a uniform, current collection mechanism was achieved. More specifically the current distribution across the entire cell surface was noticed as a key parameter for understanding and managing thermal gradient of SOFC.

With the presented technique there is the possibility to obtain the SOFC temperature distribution during its operation with high resolution. The temperature profile of the cell was identified under different operating conditions together with the correlated parameters. This offers the use of the sensor as a health monitoring tool that potentially could help early detection of failure mechanisms. In addition to this, some key information about the cell performance degradation can also be provided by observing the changes in temperature profile of an operating cell.

8.3 Limitations

Thin film sensor was fabricated on the cell surface directly to monitor SOFC temperature during operation. The electrical connection was successfully achieved between the patterned thin film sensor and external wires. However, the thin film sensor was not used under running SOFC without having electrically insulated and chemically inert protecting layer. The limitation identified was the possible risk for phase changes of the obtained alumina layer from aluminium oxidation when the cathode reaction takes place. The required temperature to achieve a proper alumina phase as a protecting layer is over 1000 °C which is a critically high temperature for

the cell used possibly leading to material degradation. Thus direct sputtering of alumina is required by using RF (radio frequency) sputter. However the sputter currently available in the laboratory is a DC (direct current) sputter which only works with metals. Due to unavailability of the RF sputter mechanism this has not been able to be investigated further.

This is not a big problem if the cell was not electrochemically/chemically active however it is vitally important when the cell is electrochemical/chemically active. In order to experience the performance of the sensor which is encased by the alumina layer under the earlier mentioned method, an experiment was carried out under real operating SOFC condition. There was a severe interruption from the working environment to the sensor reading monitored, and the results are explained in appendix A.1.

8.4 Future Research

This thesis offers a novel technique for monitoring the temperature distribution of SOFC during operation directly from the cell surface with a new connection mechanism. However, the implemented technique is required to be improved at some points as addressed;

1. Further experimentation using the sensor in the thin film form. When the sensor is used in thin film form it provides better resolution due to its smaller mass compared to the wired sensors. In order to achieve a durable thin film sensor on a porous media, electrically and chemically stable protection layer is vital. However, as it has been experienced from the study that due to chemical characteristics of the cell, physical deposition of the protecting layer is required. Work on this deposition method and hence further testing of the sensor in this form could then be initiated.
2. The temperature distribution has been monitored from a cell under different operating condition with a limited iteration. In order to identify individual contribution of each parameter precisely the experiment should be carried out with more iterations and variations.

3. Even though the experimental results were compared with the analytical calculation, it should also be validated by applying numerical modelling.
4. In order to observe the potential of the sensor as a health monitoring tool, it should be tested under real failure modes during a prolonged experiment or the experiment with more cycles.

Appendix

A. Thin film sensor testing under operating SOFC condition

The variation in temperature and OCV with different H_2 flow rates is shown in Fig. 67. The furnace temperature is set at about 740 °C and kept constant during the measurement. The connection configuration was similar to the configuration of the experiment with the SBC without silver paste. The measured OCV (1.05V) with the supplied flow rate is reasonable compared to the value obtained in the literature [192]. Temperature from both TCs and SSPs is in good agreement without H_2 , whereas it increases dramatically from 740 °C to about 1200 °C when 15 mL/min H_2 is presented and levelled down to the temperature ranged 800 °C -1000 °C. There is a huge temperature discrepancy that is also observed amongst the SSPs (S1-S9) themselves as the maximum temperature difference is about 250 °C between S3 and S8). When the H_2 flow is increased from 15 mL/min to 20 mL/min, simultaneous changes occur in temperature readings of SSPs while there is no discernible change observed from TCs.

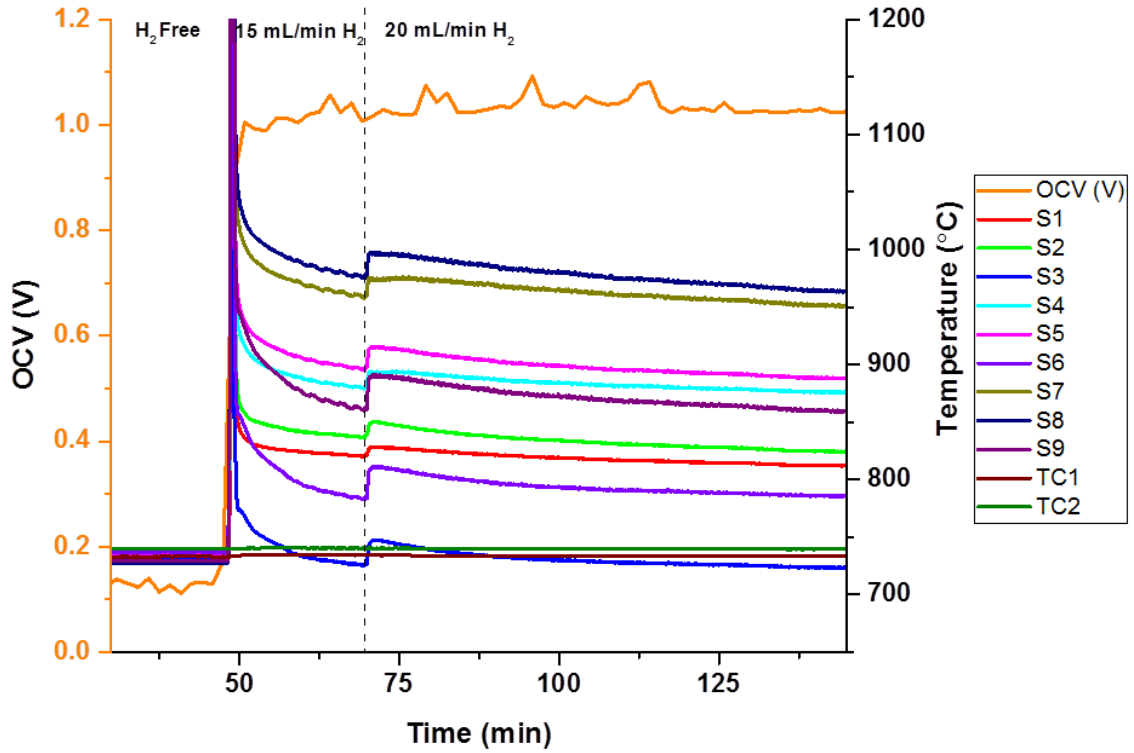


Fig. 67. Temperature response of SSPs, TC1 and TC2 to the varying fuel flow rate under OCV condition of SOFC

These abnormal temperature changes monitored from the SSPs (S1-S9) when the fuel is provided to initiate anode reduction process is correlated with electrical interaction between the sensor thermo-elements and cathode. As presented in the figure the obtained temperature from SSPs increased sharply while the temperature monitored from TCs are only increased by 2-3 °C. The simultaneous changes within the SSPs temperature readings and OCV due to presence of fuel show that there is electrical interaction between sensor thermo-elements and cell electrode materials. Since (i) there is not that high a temperature expected regarding to the SOFC's thermodynamics during reduction process, and (ii) fuel leakage or connection related issues cannot be the reason for these temperature raise while the TCs staying almost same level, this suggests that there are no severe temperature changes in the surrounding environment of the sensing points. However, there is an electrical movement or electrical field changes even at the cathode side that might occur during the anode reduction owing to electrical and chemical potential variation [59].

As a result of this, sudden and severe unexpected changes in SSPs temperature readings occur due to direct intervention of moving electrons of cathode to sensor thermo-elements as a result of poor electrical insulation. This causes significant temperature rise or drop as due to Seebeck theory only a small amount of potential (μV scale) is obtained from thermo-elements and converted to temperature reading. Thus small changes in obtained potential make significant impact on the corresponding OCV. Even though the thermo-elements are encased with alumina protecting layer, the layer is observed not sufficient to keep its insulating capability at that temperature. Thermally oxidised aluminum was used to form aluminium oxide as protecting layer. Phase changes in the protecting layer is also a possible mechanism that can cause this issue [193].

As this is also monitored by located conventional TCs even there is only small variation observed in their temperature reading. Nonetheless, again the represented temperature fluctuation from SSPs is not realistic. Besides, the results still confirm that the inserted thin film sensor is highly sensitive to small electrical changes. As it is clear that there is temperature increase expected from the SOFC due to electrochemical reaction when the cell is loaded. These temperature variations are well detected from the SSPs even though the magnitude is more than the expected value. The insulation properties and characterisation is beyond this study. Even though unrealistic temperature changes are monitored from SSPs, it is confirmed that the electrical connection is kept in contact under OCV during the operation as is the focus of this study.

B. Fuel spectra atomic percentage of the thermoelement samples for both intact and used.

Fig. 68. Atomic percentage of the intact sample for full spectrum

Fig. 69. Atomic percentage of used thermoelement

Bibliography

- [1] A. Alises and J. M. Vassallo, “Comparison of road freight transport trends in Europe. Coupling and decoupling factors from an Input-Output structural decomposition analysis,” *Transp. Res. Part A Policy Pract.*, vol. 82, pp. 141–157, 2015.
- [2] A. García-Olivares, J. Solé, and O. Osychenko, “Transportation in a 100% renewable energy system,” *Energy Convers. Manag.*, vol. 158, no. August 2017, pp. 266–285, 2018.
- [3] M. S. Dresselhaus and I. L. Thomas, “Alternative energy technologies,” *Nature*, vol. 414, no. 6861, pp. 332–7, Nov. 2001.
- [4] S. Solomon, J. S. Daniel, T. J. Sanford, D. M. Murphy, G.-K. Plattner, R. Knutti, and P. Friedlingstein, “Persistence of climate changes due to a range of greenhouse gases,” *Proc. Natl. Acad. Sci.*, vol. 107, no. 43, pp. 18354–18359, 2010.
- [5] W. R. W. Daud, R. E. Rosli, E. H. Majlan, S. A. A. Hamid, R. Mohamed, and T. Husaini, “PEM fuel cell system control: A review,” *Renew. Energy*, vol. 113, pp. 620–638, 2017.
- [6] US Department of Energy, “Hydrogen Fuel Cells,” *DOE Hydrog. Progr.*, 2006.
- [7] G. Merle, M. Wessling, and K. Nijmeijer, “Anion exchange membranes for alkaline fuel cells: A review,” *J. Memb. Sci.*, vol. 377, no. 1–2, pp. 1–35, 2011.
- [8] N. Sammes, R. Bove, and K. Stahl, “Phosphoric acid fuel cells: Fundamentals and applications,” *Curr. Opin. Solid State Mater. Sci.*, vol. 8, no. 5, pp. 372–378, 2004.
- [9] L. van Biert, M. Godjevac, K. Visser, and P. V. Aravind, “A review of fuel cell systems for maritime applications,” *J. Power Sources*, vol. 327, no. X, pp. 345–364, 2016.

- [10] Y. Wang, K. S. Chen, J. Mishler, S. C. Cho, and X. C. Adroher, "A review of polymer electrolyte membrane fuel cells: Technology, applications, and needs on fundamental research," *Appl. Energy*, vol. 88, no. 4, pp. 981–1007, 2011.
- [11] B. C. Ong, S. K. Kamarudin, and S. Basri, "Direct liquid fuel cells: A review," *Int. J. Hydrogen Energy*, vol. 42, no. 15, pp. 10142–10157, 2017.
- [12] H. Chen, Z. Song, X. Zhao, T. Zhang, P. Pei, and C. Liang, "A review of durability test protocols of the proton exchange membrane fuel cells for vehicle," *Appl. Energy*, vol. 224, no. April, pp. 289–299, 2018.
- [13] F. S. da Silva and T. M. de Souza, "Novel materials for solid oxide fuel cell technologies: A literature review," *Int. J. Hydrogen Energy*, vol. 42, no. 41, pp. 26020–26036, 2017.
- [14] M. Andersson and B. Sundén, "Technology Review – Solid Oxide Fuel Cell," Stockholm, 2017.
- [15] Y. Wang, L. Cai, T. Liu, J. Wang, and J. Chen, "An efficient strategy exploiting the waste heat in a solid oxide fuel cell system," *Energy*, vol. 93, pp. 900–907, 2015.
- [16] N. Mahato, A. Banerjee, A. Gupta, S. Omar, and K. Balani, "Progress in material selection for solid oxide fuel cell technology: A review," *Prog. Mater. Sci.*, vol. 72, pp. 141–337, 2015.
- [17] D. Tucker, M. Abreu-Sepulveda, and N. F. Harun, "SOFC Lifetime Assessment in Gas Turbine Hybrid Power Systems," *J. Fuel Cell Sci. Technol.*, vol. 11, no. 5, p. 51008, Aug. 2014.
- [18] T. Dey, D. Singdeo, A. Pophale, M. Bose, and P. C. Ghosh, "SOFC Power Generation System by Bio-gasification," *Energy Procedia*, vol. 54, pp. 748–755, 2014.
- [19] T. Li, Z. Wu, and K. Li, "A dual-structured anode/Ni-mesh current collector hollow fibre for micro-tubular solid oxide fuel cells (SOFCs)," *J. Power Sources*, vol. 251, pp. 145–151, Apr. 2014.
- [20] J.-H. Song, N. M. Sammes, S.-I. Park, S. Boo, H.-S. Kim, H. Moon, and S.-H.

- Hyun, "Fabrication and Characterization of Anode-Supported Planar Solid Oxide Fuel Cell Manufactured by a Tape Casting Process," *J. Fuel Cell Sci. Technol.*, vol. 5, no. 2, p. 21003, 2008.
- [21] E. D. Wachsman and K. T. Lee, "Lowering the temperature of solid oxide fuel cells.," *Science*, vol. 334, no. 6058, pp. 935–9, Nov. 2011.
- [22] A. Choudhury, H. Chandra, and a. Arora, "Application of solid oxide fuel cell technology for power generation - A review," *Renew. Sustain. Energy Rev.*, vol. 20, pp. 430–442, 2013.
- [23] A. Lanzini, P. Leone, M. Santarelli, P. Asinari, M. Cali, and R. Borchellini, "Performances and Degradation Phenomena of Solid Oxide Anode Supported Cells With LSM and LSCF Cathodes: An Experimental Assessment," *J. Fuel Cell Sci. Technol.*, vol. 6, no. 1, p. 11020, 2009.
- [24] U.S. Department of Energy, "Technology program plan solid oxide fuel cells," in *Solid Oxide Fuel Cell Technology Program Plan*, 2013, no. January.
- [25] M. Näslund and H. Iskov, "Accelerated lifetime testing and standardization of SOFC systems," Danish Gas Technology Centre, Hørsholm 2012, 2012.
- [26] R. Steinberger-Wilckens and L. Blum, "Overview of the development of solid oxide fuel cells at Forschungszentrum Juelich," *Int. J. Appl. Ceram. Technol.*, vol. 476, pp. 470–476, 2006.
- [27] A. Nakajo, F. Mueller, J. Brouwer, J. Van herle, and D. Favrat, "Mechanical reliability and durability of SOFC stacks. Part I : Modelling of the effect of operating conditions and design alternatives on the reliability," *Int. J. Hydrogen Energy*, vol. 37, no. 11, pp. 9249–9268, Jun. 2012.
- [28] A. Al-Masri, M. Peksen, L. Blum, and D. Stolten, "A 3D CFD model for predicting the temperature distribution in a full scale APU SOFC short stack under transient operating conditions," *Appl. Energy*, vol. 135, pp. 539–547, Dec. 2014.
- [29] B. Zitouni, G. M. Andreadis, B. M. Hocine, A. Hafsia, H. Djamel, and Z. Mostefa, "Two-dimensional numerical study of temperature field in an anode

- supported planar SOFC: Effect of the chemical reaction,” *Int. J. Hydrogen Energy*, vol. 36, no. 6, pp. 4228–4235, Mar. 2011.
- [30] K. J. Daun, S. B. Beale, F. Liu, and G. J. Smallwood, “Radiation heat transfer in planar SOFC electrolytes,” *J. Power Sources*, vol. 157, no. 1, pp. 302–310, Jun. 2006.
 - [31] P. Vijay, S. Hosseini, and M. O. Tadé, “A novel concept for improved thermal management of the planar SOFC,” *Chem. Eng. Res. Des.*, vol. 91, no. 3, pp. 560–572, Mar. 2013.
 - [32] M. Iwata, T. Hikosaka, M. Morita, T. Iwanari, and K. Ito, “Performance analysis of planar-type unit SOFC considering current and temperature distributions,” *Solid State Ionics*, vol. 132, pp. 297–308, 2000.
 - [33] M. Lockett, M. J. H. Simmons, and K. Kendall, “CFD to predict temperature profile for scale up of micro-tubular SOFC stacks,” *J. Power Sources*, vol. 131, no. 1–2, pp. 243–246, 2004.
 - [34] D. H. Jeon, “A comprehensive CFD model of anode-supported solid oxide fuel cells,” *Electrochim. Acta*, vol. 54, no. 10, pp. 2727–2736, 2009.
 - [35] N. Autissier, D. Larrain, J. Van Herle, and D. Favrat, “CFD simulation tool for solid oxide fuel cells,” *J. Power Sources*, vol. 131, no. 1–2, pp. 313–319, 2004.
 - [36] S. Celik, B. Timurkutluk, and M. D. Mat, “Measurement of the temperature distribution in a large solid oxide fuel cell short stack,” *Int. J. Hydrogen Energy*, vol. 38, no. 25, pp. 10534–10541, Aug. 2013.
 - [37] S. Hashimoto, H. Nishino, Y. Liu, K. Asano, M. Mori, Y. Funahashi, and Y. Fujishiro, “The electrochemical cell temperature estimation of micro-tubular SOFCs during the power generation,” *J. Power Sources*, vol. 181, no. 2, pp. 244–250, 2008.
 - [38] H. Guo, G. Iqbal, and B. S. Kang, “Development of an in situ surface deformation and temperature measurement technique for a solid oxide fuel cell button cell,” *Int. J. Appl. Ceram. Technol.*, vol. 7, no. 1, pp. 55–62, 2010.

- [39] R. Montanini, A. Quattrocchi, S. A. Piccolo, A. Amato, S. Trocino, S. C. Zignani, M. Lo Faro, and G. Squadrito, “Real-time thermal imaging of solid oxide fuel cell cathode activity in working condition,” *Appl. Opt.*, vol. 55, no. 25, p. 7142, 2016.
- [40] L. Barelli, G. Bidini, G. Cinti, and a. Ottaviano, “SOFC regulation at constant temperature: Experimental test and data regression study,” *Energy Convers. Manag.*, vol. 117, pp. 289–296, 2016.
- [41] V. Liso, G. Cinti, M. P. Nielsen, and U. Desideri, “Solid oxide fuel cell performance comparison fueled by methane, MeOH, EtOH and gasoline surrogate C₈H₁₈,” *Appl. Therm. Eng.*, vol. 99, pp. 1101–1109, 2016.
- [42] G. Ju, K. Reifsnider, and X. Huang, “Infrared Thermography and Thermoelectrical Study of a Solid Oxide Fuel Cell,” *J. Fuel Cell Sci. Technol.*, vol. 5, no. 3, p. 31006, 2008.
- [43] E. Ivers-Tiffée, A. Weber, and D. Herbstritt, “Materials and technologies for SOFC-components,” *J. Eur. Ceram. Soc.*, vol. 21, no. 10–11, pp. 1805–1811, 2001.
- [44] US Department of Energy, “US Energy Sector Vulnerabilities to Climate Change and Extreme Weather,” *J. Chem. Inf. Model.*, 2013.
- [45] T. Somekawa, K. Nakamura, T. Kushi, T. Kume, K. Fujita, and H. Yakabe, “Examination of a high-efficiency solid oxide fuel cell system that reuses exhaust gas,” *Appl. Therm. Eng.*, 2016.
- [46] M. Fardadi, D. F. McLarty, J. Brouwer, and F. Jabbari, “Enhanced performance of counter flow SOFC with partial internal reformation,” *Int. J. Hydrogen Energy*, vol. 39, no. 34, pp. 19753–19766, 2014.
- [47] A. Faes, A. Hessler-Wyser, A. Zryd, and J. Van Herle, “A Review of RedOx Cycling of Solid Oxide Fuel Cells Anode,” *Membranes (Basel)*, vol. 2, no. 3, pp. 585–664, Jan. 2012.
- [48] J. C. Ruiz-morales and D. Marrero-l, “Environmental Science,” vol. 3, no. 11, 2010.

- [49] M. Rokni, "Thermodynamic and thermoeconomic analysis of a system with biomass gasification, solid oxide fuel cell (SOFC) and Stirling engine," *Energy*, pp. 1–13, Feb. 2014.
- [50] R. M. Ormerod, "Solid oxide fuel cells," *Chem. Soc. Rev.*, vol. 32, no. 1, pp. 17–28, Dec. 2003.
- [51] M. Ha-Duong and R. Loisel, "Actuarial risk assessment of expected fatalities attributable to carbon capture and storage in 2050," *Int. J. Greenh. Gas Control*, vol. 5, no. 5, pp. 1346–1358, Sep. 2011.
- [52] US Department of Energy, "Report of the Hydrogen Production Expert Panel : A Subcommittee of the Hydrogen & Fuel Cell Technical Advisory Committee," 2013.
- [53] C. Sun, R. Hui, and J. Roller, "Cathode materials for solid oxide fuel cells: A review," *J. Solid State Electrochem.*, vol. 14, no. 7, pp. 1125–1144, 2010.
- [54] K. Tanwar, N. Jaiswal, D. Kumar, and O. Parkash, "Synthesis & characterization of Dy and Ca Co-doped ceria based solid electrolytes for IT-SOFCs," *J. Alloys Compd.*, vol. 684, pp. 683–690, 2016.
- [55] S. Hossain, A. M. Abdalla, S. N. B. Jamain, J. H. Zaini, and A. K. Azad, "A review on proton conducting electrolytes for clean energy and intermediate temperature-solid oxide fuel cells," *Renew. Sustain. Energy Rev.*, vol. 79, no. May, pp. 750–764, 2017.
- [56] L. Bi, E. H. Da'as, and S. P. Shafi, "Proton-conducting solid oxide fuel cell (SOFC) with Y-doped BaZrO₃electrolyte," *Electrochem. commun.*, vol. 80, no. April, pp. 20–23, 2017.
- [57] M. Shishkin and T. Ziegler, "the three-phase boundary of solid oxide fuel cell anodes by density functional theory : a critical overview," no. 2, pp. 1798–1808, 2014.
- [58] S. C. S. and K. Kendall, *High Temperature Solid Oxide Fuel Cells: Fundamentals, design and applications*. Oxford: Elsevier Advanced Technology, The Boulevard, Langford Lane, Kidlington Oxford OX5 1GB,

UK, 2003.

- [59] W. G. C. Ryan O'hayre, Suk-Won Cha, *Fuel Cell Fundamentals*. 2016.
- [60] V. Kharton, F. Marques, and a Atkinson, "Transport properties of solid oxide electrolyte ceramics: a brief review," *Solid State Ionics*, vol. 174, no. 1–4, pp. 135–149, Oct. 2004.
- [61] C. M. Dikwal, W. Bujalski, and K. Kendall, "The effect of temperature gradients on thermal cycling and isothermal ageing of micro-tubular solid oxide fuel cells," *J. Power Sources*, vol. 193, no. 1, pp. 241–248, Aug. 2009.
- [62] F. Yi, H. Chen, and H. Li, "Performance of Solid Oxide Fuel Cell With La and Cr Co-doped SrTiO₃ as Anode.," *J. fuel cell Sci. Technol.*, vol. 11, no. 3, pp. 0310061–0310064, Jun. 2014.
- [63] S. Roudeau, J. C. Grenier, and J. M. Bassat, "La 0.5 Sr 0.2 TiO 3- δ Perovskite as Anode Material for Solid Oxide Fuel Cells," *J. Fuel Cell Sci. Technol.*, vol. 11, no. 4, p. 41006, Mar. 2014.
- [64] V. a. C. Haanappel, C. Lalanne, a. Mai, and F. Tietz, "Characterization of Anode-Supported Solid Oxide Fuel Cells With Nd[sub 2]NiO[sub 4] Cathodes," *J. Fuel Cell Sci. Technol.*, vol. 6, no. 4, p. 41016, 2009.
- [65] J. Rossmesl and W. G. Bessler, "Trends in catalytic activity for SOFC anode materials," *Solid State Ionics*, 2008.
- [66] A. Sinha, D. Miller, and J. T. S. Irvine, "Development of Novel Titanium Oxycarbide Anode material for Intermediate Temperature SOFC (IT-SOFC)," *J. Mater. Chem. A*, 2016.
- [67] B. Shri Prakash, S. Senthil Kumar, and S. T. Aruna, "Properties and development of Ni/YSZ as an anode material in solid oxide fuel cell: A review," *Renew. Sustain. Energy Rev.*, 2014.
- [68] K. R. Han, Y. Jeong, H. Lee, and C. S. Kim, "Fabrication of NiO/YSZ anode material for SOFC via mixed NiO precursors," *Mater. Lett.*, 2007.
- [69] D. E. Vladikova, Z. B. Stoyanov, A. Barbucci, M. Viviani, P. Carpanese, J. A.

- Kilner, S. J. Skinner, and R. Rudkin, "Impedance studies of cathode/electrolyte behaviour in SOFC," *Electrochim. Acta*, vol. 53, no. 25, pp. 7491–7499, 2008.
- [70] D. Rembelski, J. P. Viricelle, L. Combemale, and M. Rieu, "Characterization and Comparison of Different Cathode Materials for SC-SOFC: LSM, BSCF, SSC, and LSCF," *Fuel Cells*, vol. 12, no. 2, pp. 256–264, Apr. 2012.
- [71] T. Hibino, A. Hashimoto, M. Yano, M. Suzuki, S. Yoshida, and M. Sano, "High Performance Anodes for SOFCs Operating in Methane-Air Mixture at Reduced Temperatures," *J. Electrochem. Soc.*, vol. 149, no. 2, p. A133, 2002.
- [72] S. P. Simner, M. D. Anderson, L. R. Pederson, and J. W. Stevenson, "Performance Variability of La(Sr)FeO₃ SOFC Cathode with Pt, Ag, and Au Current Collectors," *J. Electrochem. Soc.*, vol. 152, no. 9, p. A1851, 2005.
- [73] T. Hibino, S. Wang, S. Kakimoto, and M. Sano, "One-chamber solid oxide fuel cell constructed from a YSZ electrolyte with a Ni anode and LSM cathode," vol. 127, pp. 89–98, 2000.
- [74] T. Suzuki, T. Yamaguchi, Y. Fujishiro, and M. Awano, "Fabrication and characterization of micro tubular SOFCs for operation in the intermediate temperature," *J. Power Sources*, vol. 160, no. 1, pp. 73–77, Sep. 2006.
- [75] S. F. Lee and C. W. Hong, "Multi-scale design simulation of a novel intermediate-temperature micro solid oxide fuel cell stack system," *Int. J. Hydrogen Energy*, vol. 35, no. 3, pp. 1330–1338, Feb. 2010.
- [76] C. Sun, R. Hui, and J. Roller, "Cathode materials for solid oxide fuel cells: a review," *J. Solid State Electrochem.*, vol. 14, no. 7, pp. 1125–1144, Oct. 2009.
- [77] D. Ding, X. Li, S. Y. Lai, K. Gerdes, and M. Liu, "Enhancing SOFC cathode performance by surface modification through infiltration," *Energy Environ. Sci.*, 2014.
- [78] Y.-L. Lee and D. Morgan, "Ab initio and empirical defect modeling of LaMnO_{3±δ} for solid oxide fuel cell cathodes," *Phys. Chem. Chem. Phys.*,

vol. 14, no. 1, pp. 290–302, Jan. 2012.

- [79] E. Park, S. Taniguchi, T. Daio, J.-T. Chou, and K. Sasaki, “Comparison of chromium poisoning among solid oxide fuel cell cathode materials,” *Solid State Ionics*, 2014.
- [80] C.-J. Fu, K.-N. Sun, N.-Q. Zhang, and D.-R. Zhou, “Mechanism of chromium poisoning of LSM cathode in solid oxide fuel cell,” *Chem. J. Chinese Univ.*, 2007.
- [81] J. Wu and X. Liu, “Recent development of SOFC metallic interconnect,” *J. Mater. Sci. Technol.*, vol. 26, no. 4, pp. 293–305, 2010.
- [82] S. C. Singhal and K. Kendall, *High-temperature Solid Oxide Fuel Cells: Fundamentals, Design and Applications*. Oxford: Elsevier Ltd, The Boulevard, Langford Lane, Kidlington, Oxford OX5 1GB, UK, 2003.
- [83] X. Du, M. Han, and Z. Sun, “Progress in SOFC Metallic Interconnect Coating Xiaojia Du,” *ECS Trans.*, 2013.
- [84] J. Li, W. Zhang, J. Yang, D. Yan, J. Pu, B. Chi, and L. Jian, “Oxidation behavior of metallic interconnect in solid oxide fuel cell stack,” *J. Power Sources*, vol. 353, pp. 195–201, 2017.
- [85] S. Fontana, R. Amendola, S. Chevalier, P. Piccardo, G. Caboche, M. Viviani, R. Molins, and M. Sennour, “Metallic interconnects for SOFC: Characterisation of corrosion resistance and conductivity evaluation at operating temperature of differently coated alloys,” *J. Power Sources*, vol. 171, no. 2, pp. 652–662, Sep. 2007.
- [86] S. M. Jamil, M. H. D. Othman, M. a. Rahman, J. Jaafar, a. F. Ismail, and K. Li, “Recent fabrication techniques for micro-tubular solid oxide fuel cell support: A review,” *J. Eur. Ceram. Soc.*, Sep. 2014.
- [87] L. S. Mahmud, A. Muchtar, and M. R. Somalu, “Challenges in fabricating planar solid oxide fuel cells: A review,” *Renew. Sustain. Energy Rev.*, vol. 72, no. January, pp. 105–116, 2017.
- [88] R. M. Manglik and Y. N. Magar, “Heat and Mass Transfer in Planar Anode-

Supported Solid Oxide Fuel Cells : Effects of Interconnect Fuel / Oxidant Channel Flow Cross Section,” vol. 7, no. December 2015, pp. 1–10, 2016.

- [89] S. C. Singhal and K. Kendall, *PREFACE*. 2003.
- [90] M. Irshad, K. Siraj, R. Raza, A. Ali, P. Tiwari, B. Zhu, A. Rafique, A. Ali, M. Kaleem Ullah, and A. Usman, “A Brief Description of High Temperature Solid Oxide Fuel Cell’s Operation, Materials, Design, Fabrication Technologies and Performance,” *Appl. Sci.*, 2016.
- [91] J. M. Park, D. Y. Kim, J. D. Baek, Y. Yoon, P. Su, and S. H. Lee, “Effect of Electrolyte Thickness on Electrochemical Reactions and Thermo-Fluidic Characteristics inside a SOFC Unit Cell,” 2018.
- [92] P. Chinda, “The performance improvement of a thick electrode solid oxide fuel cell,” *Energy Procedia*, vol. 34, pp. 243–261, 2013.
- [93] Y. Du and N. M. Sammes, “Fabrication and properties of anode-supported tubular solid oxide fuel cells,” *J. Power Sources*, vol. 136, no. 1, pp. 66–71, Sep. 2004.
- [94] C. Zuo, M. Liu, and M. Liu, *Sol-Gel Processing for Conventional and Alternative Energy*. Boston, MA: Springer US, 2012.
- [95] V. Lawlor, S. Griesser, G. Buchinger, A. G. Olabi, S. Cordiner, and D. Meissner, “Review of the micro-tubular solid oxide fuel cell. Part I. Stack design issues and research activities,” *J. Power Sources*, vol. 193, no. 2, pp. 387–399, 2009.
- [96] Z. Han, Z. Yang, and M. Han, “Optimization of Ni-YSZ anodes for tubular SOFC by a novel and efficient phase inversion-impregnation approach,” *J. Alloys Compd.*, vol. 750, pp. 130–138, 2018.
- [97] D. Panthi and A. Tsutsumi, “Micro-tubular solid oxide fuel cell based on a porous yttria-stabilized zirconia support,” *Sci. Rep.*, vol. 4, pp. 1–6, 2014.
- [98] X. Meng, X. Gong, N. Yang, X. Tan, Y. Yin, and Z.-F. Ma, “Fabrication of Y₂O₃-stabilized-ZrO₂(YSZ)/La_{0.8}Sr_{0.2}MnO₃- α -YSZ dual-layer hollow fibers for the cathode-supported micro-tubular solid oxide fuel cells by a co-

- spinning/co-sintering technique,” *J. Power Sources*, vol. 237, pp. 277–284, Sep. 2013.
- [99] N. Q. Minh, “Solid oxide fuel cell technology - Features and applications,” *Solid State Ionics*, vol. 174, no. 1–4, pp. 271–277, 2004.
- [100] E. D. Wachsman, C. a Marlowe, and K. T. Lee, “Role of solid oxide fuel cells in a balanced energy strategy,” *Energy Environ. Sci.*, vol. 5, pp. 5498–5509, 2012.
- [101] S. Singhal, “Solid oxide fuel cells for stationary, mobile, and military applications,” *Solid State Ionics*, vol. 152–153, pp. 405–410, Dec. 2002.
- [102] B. Dziurdzia, Z. Magonski, and H. Jankowski, “Commercialisation of Solid Oxide Fuel Cells - Opportunities and forecasts,” *IOP Conf. Ser. Mater. Sci. Eng.*, vol. 104, no. 1, pp. 0–12, 2016.
- [103] N. K. Sandhu, A. R. Hanifi, A. Woldnik, T. Amiri, T. H. Etsell, J. Luo, and P. Sarkar, “Electrochemical performance of a short tubular solid oxide fuel cell stack at intermediate temperatures,” *Appl. Energy*, vol. 183, pp. 358–368, 2016.
- [104] R. Goettler, “Overview of f the Rolls-Royce SOFC SO C Technology and SECA Program,” 2009.
- [105] H. Zhu and R. J. Kee, “Thermodynamics of SOFC efficiency and fuel utilization as functions of fuel mixtures and operating conditions,” *J. Power Sources*, vol. 161, no. 2, pp. 957–964, 2006.
- [106] T. X. Ho, P. Kosinski, A. C. Hoffmann, and A. Vik, “Effects of heat sources on the performance of a planar solid oxide fuel cell,” *Int. J. Hydrogen Energy*, vol. 35, no. 9, pp. 4276–4284, May 2010.
- [107] K. Fischer and J. R. Seume, “Location and Magnitude of Heat Sources in Solid Oxide Fuel Cells,” *J. Fuel Cell Sci. Technol.*, vol. 6, no. 1, p. 11002, 2009.
- [108] M. Ishizuka, T. M. Rudy, V. V Wadekar, E. Confernces, H. Yoshida, and H. Iwai, “Thermal management in solid oxide fuel cell systems,” *Eng. Conf. Int.*,

vol. CHE2005-01, no. September, 2005.

- [109] K. Zheng, Q. Sun, and M. Ni, "Local Non-Equilibrium Thermal Effects in Solid Oxide Fuel Cells with Various Fuels," *Energy Technol.*, vol. 1, no. 1, pp. 35–41, 2013.
- [110] A. Hafsia, Z. Bariza, H. Djamel, B. M. Hocine, G. M. Andreadis, and A. Soumia, "SOFC fuel cell heat production: Analysis," *Energy Procedia*, vol. 6, pp. 643–650, 2011.
- [111] S. P. Jiang and X. Chen, "Chromium deposition and poisoning of cathodes of solid oxide fuel cells - A review," *Int. J. Hydrogen Energy*, vol. 39, no. 1, pp. 505–531, 2014.
- [112] A. Lanzini, D. Ferrero, D. Papurello, and M. Santarelli, "Reporting Degradation from Different Fuel Contaminants in Ni-anode SOFCs," *Fuel Cells*, vol. 17, no. 4, pp. 423–433, 2017.
- [113] H. T. Lim, S. C. Hwang, M. G. Jung, H. W. Park, M. Y. Park, S. S. Lee, and Y. G. Jung, "Degradation mechanism of anode-supported solid oxide fuel cell in planar-cell channel-type setup," *Fuel Cells*, vol. 13, no. 5, pp. 712–719, 2013.
- [114] M. S. Khan, S. B. Lee, R. H. Song, J. W. Lee, T. H. Lim, and S. J. Park, "Fundamental mechanisms involved in the degradation of nickel-yttria stabilized zirconia (Ni-YSZ) anode during solid oxide fuel cells operation: A review," *Ceram. Int.*, vol. 42, no. 1, pp. 35–48, 2015.
- [115] D. Yan, C. Zhang, L. Liang, K. Li, L. Jia, J. Pu, L. Jian, X. Li, and T. Zhang, "Degradation analysis and durability improvement for SOFC 1-cell stack," *Appl. Energy*, 2016.
- [116] A. Baldinelli, L. Barelli, G. Bidini, A. Di Michele, and R. Vivani, "SOFC direct fuelling with high-methane gases: Optimal strategies for fuel dilution and upgrade to avoid quick degradation," *Energy Convers. Manag.*, vol. 124, pp. 492–503, 2016.
- [117] T. Mizusawa, T. Araki, and M. Mori, "Temperature and reactive current

- distributions in microtubular solid oxide electrolysis cells,” *Int. J. Hydrogen Energy*, vol. 41, no. 32, pp. 13888–13900, 2016.
- [118] Y. Wang, Y. Shi, X. Yu, and N. Cai, “Thermal shock resistance and failure probability analysis on solid oxide electrolyte direct flame fuel cells,” *J. Power Sources*, vol. 255, pp. 377–386, 2014.
- [119] H. Mounir, M. Belaiche, A. El Marjani, and A. El Gharad, “Thermal stress and probability of survival investigation in a multi-bundle integrated-planar solid oxide fuel cells IP-SOFC (integrated-planar solid oxide fuel cell),” *Energy*, vol. 66, pp. 378–386, Mar. 2014.
- [120] P. Fan, G. Li, Y. Zeng, and X. Zhang, “Numerical study on thermal stresses of a planar solid oxide fuel cell,” *Int. J. Therm. Sci.*, vol. 77, pp. 1–10, Mar. 2014.
- [121] K. Wang, D. Hissel, M. C. Péra, N. Steiner, D. Marra, M. Sorrentino, C. Pianese, M. Monteverde, P. Cardone, and J. Saarinen, “A Review on solid oxide fuel cell models,” *Int. J. Hydrogen Energy*, vol. 36, no. 12, pp. 7212–7228, Jun. 2011.
- [122] V. Zaccaria, D. Tucker, and A. Traverso, “A distributed real-time model of degradation in a solid oxide fuel cell, part II: Analysis of fuel cell performance and potential failures,” *J. Power Sources*, vol. 327, pp. 736–742, 2016.
- [123] M. Xu, T. S. Li, M. Yang, M. Andersson, I. Fransson, T. Larsson, and B. Sundén, “Modeling of an anode supported solid oxide fuel cell focusing on thermal stresses,” *Int. J. Hydrogen Energy*, vol. 41, no. 33, pp. 14927–14940, 2016.
- [124] K. P. Recknagle, R. E. Williford, L. a. Chick, D. R. Rector, and M. a. Khaleel, “Three-dimensional thermo-fluid electrochemical modeling of planar SOFC stacks,” *J. Power Sources*, vol. 113, no. 1, pp. 109–114, 2003.
- [125] M. Fardadi, D. F. McLarty, and F. Jabbari, “Investigation of thermal control for different SOFC flow geometries,” *Appl. Energy*, vol. 178, pp. 43–55, 2016.

- [126] P. Yuan and S.-F. Liu, “Numerical Analysis of Temperature and Current Density Distribution of a Planar Solid Oxide Fuel Cell Unit with Nonuniform Inlet Flow,” *Numer. Heat Transf. Part A Appl.*, vol. 51, no. 10, pp. 941–957, 2007.
- [127] H. Schlegl and R. Dawson, “Finite element analysis and modelling of thermal stress in solid oxide fuel cells,” *Proc. Inst. Mech. Eng. Part A J. Power Energy*, vol. 231, no. 7, pp. 654–665, 2017.
- [128] Ö. Aydın, H. Nakajima, and T. Kitahara, “Reliability of the numerical SOFC models for estimating the spatial current and temperature variations,” *Int. J. Hydrogen Energy*, vol. 41, no. 34, pp. 15311–15324, 2016.
- [129] B. Morel, R. Roberge, S. Savoie, T. W. Napporn, and M. Meunier, “An Experimental Evaluation of the Temperature Gradient in Solid Oxide Fuel Cells,” *Electrochem. Solid-State Lett.*, vol. 10, no. 2, pp. B31–B33, 2007.
- [130] W. B. Guan, H. J. Zhai, L. Jin, C. Xu, and W. G. Wang, “Temperature measurement and distribution inside planar SOFC stacks,” *Fuel Cells*, vol. 12, no. 1, pp. 24–31, 2012.
- [131] O. Aydın, H. Nakajima, and T. Kitahara, “Influence of Convective Heat Transfer by Air Flow on Local Current/Temperatures along Microtubular Solid Oxide Fuel Cells In-situ Identified by Electrodesegmentation Method for Co- and Counter-flow Configurations,” *ECS Trans.*, vol. 68, no. 1, pp. 2141–2150, 2015.
- [132] O. Razbani, I. Wærnhus, and M. Assadi, “Experimental investigation of temperature distribution over a planar solid oxide fuel cell,” *Appl. Energy*, vol. 105, pp. 155–160, May 2013.
- [133] E. Guk, M. Ranaweera, V. Venkatesan, and J. S. Kim, “Performance and durability of thin film thermocouple array on a porous electrode,” *Sensors (Switzerland)*, vol. 16, no. 9, pp. 1–2, 2016.
- [134] J. B. Robinson, L. D. Brown, R. Jarvis, O. O. Taiwo, T. M. M. Heenan, J. Millichamp, T. J. Mason, T. P. Neville, R. Clague, D. S. Eastwood, C. Reinhard, P. D. Lee, D. J. L. Brett, and P. R. Shearing, “Investigating the

- effect of thermal gradients on stress in solid oxide fuel cell anodes using combined synchrotron radiation and thermal imaging,” *J. Power Sources*, vol. 288, pp. 473–481, 2015.
- [135] P. R. Ohodnicki Jr., T. D. Brown, G. R. Holcomb, J. Tylczak, A. M. Schultz, and J. P. Baltrus, “High temperature optical sensing of gas and temperature using Au-nanoparticle incorporated oxides,” *Sensors Actuators B Chem.*, vol. 202, pp. 489–499, 2014.
- [136] T. Parhizkar and S. Hafeznezhadi, “Degradation based operational optimization model to improve the productivity of energy systems, case study: Solid oxide fuel cell stacks,” *Energy Convers. Manag.*, vol. 158, no. August 2017, pp. 81–91, 2018.
- [137] D. D. Pollock, “THE THEORY AND PROPERTIES OF THERMOCOUPLE ELEMENTS,” Philadelphia, 2015.
- [138] Y. Chen, H. Jiang, W. Zhao, W. Zhang, X. Liu, and S. Jiang, “Fabrication and calibration of Pt-10%Rh/Pt thin film thermocouples,” *Meas. J. Int. Meas. Confed.*, vol. 48, no. 1, pp. 248–251, 2014.
- [139] S. T. Ali, J. Lebak, L. P. Nielsen, C. Mathiasen, P. Møller, and S. K. Kær, “Thin film thermocouples for in situ membrane electrode assembly temperature measurements in a polybenzimidazole-based high temperature proton exchange membrane unit cell,” *J. Power Sources*, vol. 195, no. 15, pp. 4835–4841, Aug. 2010.
- [140] J. D. Wrbanek, G. C. Fralick, and D. Zhu, “Ceramic thin film thermocouples for SiC-based ceramic matrix composites,” *Thin Solid Films*, vol. 520, no. 17, pp. 5801–5806, 2012.
- [141] a. Ababneh, U. Schmid, J. Hernando, J. L. S??nchez-Rojas, and H. Seidel, “The influence of sputter deposition parameters on piezoelectric and mechanical properties of AlN thin films,” *Mater. Sci. Eng. B Solid-State Mater. Adv. Technol.*, vol. 172, no. 3, pp. 253–258, 2010.
- [142] J. S. Kim, R. a. Rudkin, X. Wang, and A. Atkinson, “Constrained sintering kinetics of 3YSZ films,” *J. Eur. Ceram. Soc.*, vol. 31, no. 13, pp. 2231–2239,

2011.

- [143] A. Atkinson, J. S. Kim, R. Rudkin, S. Taub, and X. Wang, “Stress induced by constrained sintering of 3YSZ films measured by substrate creep,” *J. Am. Ceram. Soc.*, vol. 94, no. 3, pp. 717–724, 2011.
- [144] G. C. Allen, P. M. Tucker, and R. K. Wild, “Surface oxidation of nickel metal as studied by X-Ray photoelectron spectroscopy,” *Oxid. Met.*, vol. 13, no. 3, pp. 223–236, 1979.
- [145] L. C. Martin, “Applications for Surface of Thin Film Thermocouples Temperature Measurement,” in *Spin-Off Technologies for Commercial Sensor and Scientific Instrumentation*, 1994, vol. 249, pp. 1–25.
- [146] J.-F. Lei, L. C. Martin, and H. a. Will, “Advances in Thin Film Sensor Technologies for Engine Applications,” 1997.
- [147] Y. Chen, H. Jiang, W. Zhao, W. Zhang, X. Liu, and S. Jiang, “Fabrication and calibration of Pt–10%Rh/Pt thin film thermocouples,” *Measurement*, vol. 48, pp. 248–251, Feb. 2014.
- [148] I. M. Tougas, M. Amani, and O. J. Gregory, “Metallic and ceramic thin film thermocouples for gas turbine engines,” *Sensors (Switzerland)*, vol. 13, no. 11, pp. 15324–15347, 2013.
- [149] X. Cheng and X. Li, “Investigation of heat generation in ultrasonic metal welding using micro sensor arrays,” *J. Micromechanics Microengineering*, vol. 17, no. 2, pp. 273–282, Feb. 2007.
- [150] U. S. Karl Ehinger, Dieter Flach, Lothar Gellrich Eberhard Horlebein, Dr. Ralf Huck Henning Ilgner, Thomas Kayser Harald Müller, Helga Schädlich Andreas Schüssler, *Industrial temperature measurement Basics and practice*. 2013.
- [151] M. Ranaweera and J. S. Kim, “Cell integrated multi-junction thermocouple array for solid oxide fuel cell temperature sensing: N+1 architecture,” *J. Power Sources*, vol. 315, pp. 70–78, 2016.
- [152] E. Guk, M. Ranaweera, V. Venkatesan, and J.-S. Kim, “Performance and

- Durability of Thin Film Thermocouple Array on a Porous Electrode,” *Sensors*, vol. 16, no. 9, p. 1329, 2016.
- [153] Y. Wang, C. Zhang, J. Li, G. Ding, and L. Duan, “Fabrication and characterization of ITO thin film resistance temperature detector,” *Vacuum*, vol. 140, pp. 121–125, 2017.
- [154] F. Schmaljohann, D. Hagedorn, and F. Löffler, “Thin film sensors for measuring small forces,” *J. Sensors Sens. Syst.*, vol. 4, no. 1, pp. 91–95, 2015.
- [155] R. De la Torre and V. M. Sglavo, “Fabrication of Innovative Compliant Current Collector-Supported Microtubular Solid Oxide Fuel Cells,” *Int. J. Appl. Ceram. Technol.*, vol. 9, no. 6, pp. 1058–1063, Nov. 2012.
- [156] Corning Inc., “Macor data sheet,” 2001.
- [157] P. Argyropoulos, K. Scott, and W. M. Taama, “Modeling Flow Distribution for Internally Manifolded Direct Methanol Fuel Cell Stacks,” *Chem. Eng. Technol.*, vol. 23, no. 11, pp. 985–995, 2000.
- [158] P. Metzger, K. a Friedrich, H. Muller-Steinhagen, and G. Schiller, “SOFC characteristics along the flow path,” *Solid State Ionics Notes*, vol. 177, no. 19–25, pp. 2045–2051, 2006.
- [159] P. Shen, H. Fujii, T. Matsumoto, and K. Nogi, “Critical Factors Affecting the Wettability of Alpha-Alumina by Molten Aluminum,” *J. Am. Ceram. Soc.*, vol. 87, pp. 2151–2159, 2004.
- [160] J. Wang, R. L. Bras, G. Sivandran, and R. G. Knox, “A simple method for the estimation of thermal inertia,” *Geophys. Res. Lett.*, vol. 37, no. 5, pp. 1–5, 2010.
- [161] Y. Zhang, G. Zeng, R. Singh, J. Christofferson, E. Croke, J. E. Bowers, and A. Shakouri, “Measurement of Seebeck coefficient perpendicular to SiGe superlattice,” in *International Conference on Thermoelectrics, ICT, Proceedings*, 2002, vol. 2002–Janua, pp. 329–332.
- [162] M. Vogler and S. Sheppard, “Electrical Contact Resistance under High Loads and Elevated Temperatures,” *Weld. J.*, no. June, p. 231s–238s, 1993.

- [163] G. Chiodelli and L. Malavasi, "Electrochemical open circuit voltage (OCV) characterization of SOFC materials," *Ionics (Kiel)*, vol. 19, no. 8, pp. 1135–1144, 2013.
- [164] D. Vladikova, Z. Stoynov, Z. Wullemin, D. Montinaro, P. Piccardo, I. Genov, and M. Rolland, "Impedance Studies of the Reduction Process in NiO-YSZ SOFC Anodes," *ECS Trans.*, vol. 68, no. 1, pp. 1161–1168, 2015.
- [165] S. W. Cheng, C. H. Tsai, S. H. Wu, C. K. Liu, Y. N. Cheng, and R. Y. Lee, "Effects of reduction process on the electrochemical and microstructural properties for electrolyte-supported SOFC," *Int. J. Hydrogen Energy*, vol. 40, no. 3, pp. 1534–1540, 2015.
- [166] T. Matsui, M. Inaba, A. Mineshige, and Z. Ogumi, "Electrochemical properties of ceria-based oxides for use in intermediate-temperature SOFCs," *Solid State Ionics*, vol. 176, no. 7–8, pp. 647–654, 2005.
- [167] D. Bhattacharyya and R. Rengaswamy, "A Review of Solid Oxide Fuel Cell (SOFC) Dynamic Models," *Ind. Eng. Chem. Res.*, vol. 48, pp. 6068–6086, 2009.
- [168] W. Jiang, Y. Luo, W. Zhang, W. Woo, and S. T. Tu, "Effect of Temperature Fluctuation on Creep and Failure Probability for Planar Solid Oxide Fuel Cell," *J. Fuel Cell Sci. Technol.*, vol. 12, no. 5, p. 51004, 2015.
- [169] L. Jin, W. Guan, J. Niu, X. Ma, and W. G. Wang, "Effect of contact area and depth between cell cathode and interconnect on stack performance for planar solid oxide fuel cells," *J. Power Sources*, vol. 240, pp. 796–805, 2013.
- [170] M. Dillig, T. Biedermann, and J. Karl, "Thermal contact resistance in solid oxide fuel cell stacks," *J. Power Sources*, vol. 300, pp. 69–76, 2015.
- [171] M. Fardadi, F. Mueller, and F. Jabbari, "Feedback control of solid oxide fuel cell spatial temperature variation," *J. Power Sources*, vol. 195, no. 13, pp. 4222–4233, 2010.
- [172] J. Park, J. Kang, and J. Bae, "Computational analysis of operating temperature, hydrogen flow rate and anode thickness in anode-supported flat-

- tube solid oxide fuel cells,” *Renew. Energy*, vol. 54, pp. 63–69, 2013.
- [173] H. Severson and M. Assadi, “Analysis of Residual and Operational Thermal Stresses in a Planar SOFC,” *J. Fuel Cell Sci. Technol.*, vol. 10, no. 6, p. 61001, 2013.
- [174] M. Andersson, J. Yuan, and B. Sundén, “SOFC modeling considering electrochemical reactions at the active three phase boundaries,” *Int. J. Heat Mass Transf.*, vol. 55, no. 4, pp. 773–788, 2012.
- [175] G. Kaur, “Solid oxide fuel cell components: Interfacial compatibility of SOFC glass seals,” in *Solid Oxide Fuel Cell Components: Interfacial Compatibility of SOFC Glass Seals*, 2015, pp. 1–408.
- [176] M. R. Abbas, A. M. Noor, S. Rajoo, N. Ahmad, U. M. Basheer, and M. H. M. Sah, “Thermal Conductivity and Specific Heat Capacity of Different Compositions of Yttria Stabilized Zirconia-Nickel Mixtures,” *Adv. Mater. Res.*, vol. 1119, no. April, pp. 783–788, 2015.
- [177] A. Pramuanjaroenkij, S. Kakaç, and X. Yang Zhou, “Mathematical analysis of planar solid oxide fuel cells,” *Int. J. Hydrogen Energy*, vol. 33, no. 10, pp. 2547–2565, 2008.
- [178] D. L. Damm and A. G. Fedorov, “Local thermal non-equilibrium effects in porous electrodes of the hydrogen-fueled SOFC,” *J. Power Sources*, vol. 159, no. 2, pp. 1153–1157, 2006.
- [179] M. Andersson, H. Paradis, J. Yuan, and B. Sunden, “Three dimensional modeling of an solid oxide fuel cell coupling charge transfer phenomena with transport processes and heat generation,” *Electrochim. Acta*, vol. 109, pp. 881–893, 2013.
- [180] Y. Shi, H. Wang, and N. Cai, “Direct two-dimensional electrochemical impedance spectra simulation for solid oxide fuel cell,” *J. Power Sources*, vol. 208, pp. 24–34, 2012.
- [181] D. P. Xenos, P. Hofmann, K. D. Panopoulos, and E. Kakaras, “Detailed transient thermal simulation of a planar SOFC (solid oxide fuel cell) using

gPROMSTM,” *Energy*, vol. 81, pp. 84–102, 2015.

- [182] J. W. Son and H. S. Song, “Influence of current collector and cathode area discrepancy on performance evaluation of solid oxide fuel cell with thin-film-processed cathode,” *Int. J. Precis. Eng. Manuf. - Green Technol.*, vol. 1, no. 4, pp. 313–316, 2014.
- [183] Y. Guo, Y. Liu, R. Cai, D. Chen, R. Ran, and Z. Shao, “Electrochemical contribution of silver current collector to oxygen reduction reaction over Ba_{0.5}Sr_{0.5}Co_{0.8}Fe_{0.2}O_{3-δ} electrode on oxygen-ionic conducting electrolyte,” *Int. J. Hydrogen Energy*, vol. 37, no. 19, pp. 14492–14500, Oct. 2012.
- [184] A. Rolle, V. Thoréton, P. Rozier, E. Capoen, O. Mentré, B. Boukamp, and S. Daviero-Minaud, “Evidence of the Current Collector Effect: Study of the SOFC Cathode Material Ca₃Co₄O_{9+δ},” *Fuel Cells*, vol. 12, no. 2, pp. 288–301, Apr. 2012.
- [185] M. C. Doppler, J. Fleig, M. Bram, and A. K. Opitz, “Hydrogen oxidation mechanisms on Ni/yttria stabilized zirconia anodes: Separation of reaction pathways by geometry variation of pattern electrodes,” *J. Power Sources*, vol. 380, no. October 2017, pp. 46–54, 2018.
- [186] A. Bieberle and L. J. Gauckler, “State-space modeling of the anodic SOFC system Ni, H₂-H₂O|YSZ,” *Solid State Ionics*, vol. 146, no. 1–2, pp. 23–41, 2002.
- [187] L. Barelli, E. Barluzzi, and G. Bidini, “Diagnosis methodology and technique for solid oxide fuel cells: A review,” *Int. J. Hydrogen Energy*, vol. 38, no. 12, pp. 5060–5074, 2013.
- [188] Z. Zhang, J. Chen, D. Yue, G. Yang, S. Ye, C. He, W. Wang, J. Yuan, and N. Huang, “Three-dimensional CFD modeling of transport phenomena in a cross-flow anode-supported planar SOFC,” *Energies*, vol. 7, no. 1, pp. 80–98, 2014.
- [189] K. Channa R. De Silva, B. J. Kaseman, and D. J. Bayless, “Silver (Ag) as anode and cathode current collectors in high temperature planar solid oxide

- fuel cells,” *Int. J. Hydrogen Energy*, vol. 36, no. 1, pp. 779–786, Jan. 2011.
- [190] M. Kuhn, T. W. Napporn, M. Meunier, and D. Therriault, “Experimental Study of Current Collection in Single-Chamber Micro Solid Oxide Fuel Cells with Comblike Electrodes,” *J. Electrochem. Soc.*, vol. 155, no. 10, p. B994, 2008.
- [191] E. C. Shin, P. A. Ahn, H. H. Seo, J. M. Jo, S. D. Kim, S. K. Woo, J. H. Yu, J. Mizusaki, and J. S. Lee, “Polarization mechanism of high temperature electrolysis in a Ni-YSZ/YSZ/LSM solid oxide cell by parametric impedance analysis,” *Solid State Ionics*, vol. 232, pp. 80–96, 2013.
- [192] P. Tiwari and S. Basu, “Performance studies of electrolyte-supported solid oxide fuel cell with Ni-YSZ and Ni-TiO₂-YSZ as anodes,” *J. Solid State Electrochem.*, vol. 18, no. 3, pp. 805–812, 2014.
- [193] S. Dutta, J. M. Biser, R. P. Vinci, and H. M. Chan, “Solid state annealing behavior of aluminum thin films on sapphire,” *J. Am. Ceram. Soc.*, vol. 95, no. 2, pp. 823–830, 2012.